A COMPARISON OF MULTIPLE TECHNIQUES FOR THE RECONSTRUCTION OF ENTRY, DESCENT, AND LANDING TRAJECTORIES AND ATMOSPHERES

A Thesis
Presented to
The Academic Faculty

by

Grant Wells

In Partial Fulfillment
of the Requirements for the Degree
Doctor of Philosophy in the
Daniel Guggenheim School of Aerospace Engineering

Georgia Institute of Technology
May 2011

A COMPARISON OF MULTIPLE TECHNIQUES FOR THE RECONSTRUCTION OF ENTRY, DESCENT, AND LANDING TRAJECTORIES AND ATMOSPHERES

Approved by:

Dr. Robert Braun, Advisor
Daniel Guggenheim School of
Aerospace Engineering
Georgia Institute of Technology

Dr. Michael Lisano
Jet Propulsion Laboratory
California Institute of Technology

Dr. Ryan Russell
Daniel Guggenheim School of
Aerospace Engineering
Georgia Institute of Technology

Dr. Scott Striepe
Langley Research Center
National Aeronautics and
Space Administration

Date Approved: May 2011

Dr. Vitali Volovoi
Daniel Guggenheim School of
Aerospace Engineering
Georgia Institute of Technology

ACKNOWLEDGEMENTS

First, I want to thank my committee, without whom, this work would not have been possible. Second, I would like to thank Prof. Aaron Lanterman of the School of Electrical and Computer Engineering at Georgia Tech for his help in understanding how best to present the comparisons of the Kalman filters. He is a professor who is willing to take the time to help students understand something they are trying to learn even when he has no obligation to. Third, I would like to thank Rob Falck of the NASA Glenn Research Center and Steve Price of Boeing for sharing their knowledge of collocation with me (and Waldy Sjauw of the NASA Glenn Research Center for introducing me to Rob). Without our discussions, I would not have been able to finish this. Finally, yet most importantly, I want to thank my family and friends who have supported me throughout this long endeavor.

TABLE OF CONTENTS

LIST OF TABLES

LIST OF FIGURES

LIST OF SYMBOLS OR ABBREVIATIONS

Acronyms

ASI Atmospheric Structure Instrument.

BET Best Estimated Trajectory.

DSN Deep Space Network.

EDL Entry, Descent, and Landing.

EKF Extended Kalman Filter.

HASI Huygens Atmospheric Structure Instrument.

IMU Inertial Measurement Unit.

KF Kalman Filter.

MEADS Mars Entry Atmospheric Data System.

MEDLI Mars Science Laboratory Entry, Descent and Landing Instrumentation.

MER Mars Exploration Rover.

MIMU Minature Inertial Measurement Unit.

MPF Mars Pathfinder.

MSL Mars Science Laboratory.

NASA National Aeronautics and Space Administration.

NSSDC National Space Science Data Center.

PAET Planetary Atmosphere Experiments Test.

PEPP Planetary Entry Parachute Program.

PHX Mars Phoenix Lander.

PVLP Pioneer Venus Large Probe.

PVSP Pioneer Venus Small Probe.

TPS Thermal Protection System.

UKF Unscented Kalman Filter.

UTTR Utah Test and Training Range.

VLA Very Large Array.

Units

atm	atmosphere.
g_n	Earth normal surface gravitational acceleration = 9.80665 $\frac{m}{s^2}$.
Hz	hertz.
kg	kilogram.
km	kilometer.
m	meter.
mg_n	milli–g_n.
μ**g_n**	micro–g_n.
MHz	megahertz.
min	minute.
s	second.
°	degree.

Roman Symbols in Equations

$_0$	subscript denoting an initial boundary condition.
a	acceleration.
a_A	axial acceleration.
a_x	x–axis acceleration.
a_y	y–axis acceleration.
a_z	z–axis acceleration.
$\mathbf{a}$	acceleration vector.
$_c$	subscript denoting the center of a time segment.
C	cubic polynomial coefficient.
D	drag.
C_D	drag coefficient.
C_L	lift coefficient.
C_Y	side force coefficient.
$E[\ ]$	denotes the mathematical "expectation of" a quantity.
$_f$	subscript denoting a final boundary condition.
$\mathbf{f}$	nonlinear function of the state vector.
$\mathbf{F}$	Jacobian matrix of $\mathbf{f}$.
g	acceleration due to gravity.
h	altitude.
$\mathbf{h}$	nonlinear function relating the state vector to the measurement vector.
H	scale height.
$\mathbf{H}$	measurement matrix, *or* system Hamiltonian.
$_i$	subscript denoting a discrete time point, *or* subscript denoting a column of a matrix.
$_j$	subscript denoting a discrete time point, *or* subscript denoting a segment of time.

$\mathbf{I}$	identity matrix.
J	scalar objective function.
$\mathbf{J}$	multiplying matrix factor.
$_k$	subscript denoting a discrete time point.
$\mathbf{K}$	Kalman gain.
L	length of the state vector, *or* lift.
m	mass.
M	Mach number.
MW	molecular mass.
$_n$	subscript denoting a discrete time point, *or* subscript denoting a segment of time.
p	pressure.
$\mathbf{P}$	*a posteriori* error covariance matrix.
$\mathbf{P_x}$	error covariance matrix of $\mathbf{x}$.
$\mathbf{P_{xy}}$	error covariance matrix of $\mathbf{x}$ and $\mathbf{y}$.
$\mathbf{P_{yy}}$	error covariance matrix of $\mathbf{y}$.
$\mathbf{P}^-$	*a priori* error covariance matrix.
$\mathbf{Q}$	process noise matrix.
r	radius.
$\dot{r}$	time derivative of radius.
R	measurement noise matrix.
$\Re$	ideal gas constant.
s	distance along the length of a time segment.
S	aerodynamic reference area.
t	time.
T	temperature, *or* total time of interest.

$\mathbf{u}$ control vector.

v velocity.

$\dot{v}$ time derivative of velocity.

$\mathbf{v}$ measurement noise.

$\mathbf{w}$ process noise.

$w^{(mean)}$ weight for means.

$w^{(cov)}$ weight for covariances.

x element of the state vector $\mathbf{x}$.

$\dot{x}_{\text{system derivative}}$ state time derivative calculated using a differential equation.

$\dot{x}_{\text{interpolation}}$ state time derivative calculated using interpolation.

$\mathbf{x}$ state vector.

$\dot{\mathbf{x}}$ time derivative of $\mathbf{x}$.

$\mathbf{x}_{best\,estimate}$ best estimate trajectory.

$\mathbf{x}_{reference}$ reference trajectory.

$\dot{\mathbf{x}}_{reference}$ time derivative of the reference trajectory.

$\mathbf{x}_{true}$ true trajectory.

$\dot{\mathbf{x}}_{true}$ time derivative of the true trajectory.

$\hat{\mathbf{x}}^{-}$ *a priori* estimate of the state.

$\hat{\mathbf{x}}$ *a posteriori* estimate of the state.

$\dot{\hat{\mathbf{x}}}$ time derivative of the estimate of the state.

$\tilde{\mathbf{x}}^{-}$ *a priori* estimate of the state–error.

$\tilde{\mathbf{x}}$ *a posteriori* estimate of the state–error.

$\mathcal{X}$ sigma–vector.

$\mathbf{y}$ measurement vector.

$\mathbf{y}_{reference}$ measurement vector corresponding to the reference trajectory.

$\mathbf{y}_{true}$ measurement vector corresponding to the true trajectory.

$\mathbf{Y}$ side force.

$\mathcal{Y}$ measurement vector corresponding to sigma–vector $\mathcal{X}$.

Greek Symbols in Equations

α	angle of attack, *or* constant determining the spread of sigma–points around a mean.
β	sideslip angle, *or* constant constant used to incorporate prior knowledge of the distribution of $\mathbf{x}$.
γ	flight path angle.
$\dot{\gamma}$	time derivative of flight path angle.
Δ	defect at the center of a time segment.
θ	longitude.
$\dot{\theta}$	time derivative of longitude.
κ	secondary scaling parameter.
λ	scaling parameter, *or* vector of adjoint (or costate) values.
$\boldsymbol{\nu}$	vector of sensitivities associated with final condition constraints.
ρ	density.
σ	bank angle, *or* standard deviation.
ϕ	latitude, *or* scalar cost function.
$\dot{\phi}$	time derivative of latitude.
$\mathbf{\Phi}$	state transition matrix, *or* $\phi + \boldsymbol{\nu}^T \mathbf{\Psi}$.
ψ	azimuth.
$\dot{\psi}$	time derivative of azimuth.
$\mathbf{\Psi}$	vector of algebraic functions.
Ω	rotation rate of a planet or moon.

CHAPTER I

INTRODUCTION

1.1 Motivation

A very important aspect of trajectory reconstruction is to assess the accuracy of pre-flight predictions of the entry trajectory. This assessment serves a dual purpose. First, trajectory reconstruction confirms: computational models of the atmosphere, planetary gravitational models, vehicle aerodynamic characteristics, and predicted vehicle flight performance. Second, trajectory reconstruction highlights discrepancies in each of these four things. That is, entry reconstruction makes us aware of how well we know what we know, and it helps make note of where our models may not be correct.

For example, trajectory reconstruction highlighted both the anomalistic disturbance torques experienced by the Mars Exploration Rovers during entry, and trajectory reconstruction helped quantify the extent to which the Mars Phoenix Lander landed long. The torques experienced by the Mars Exploration Rovers were explained by the incomplete burning away during entry of the thermal blanket on the forebody of each spacecraft. [287] Without trajectory reconstruction, this problem would not have been identified, and mitigations could not be developed for future mission designs. While the long landing of the Mars Phoenix lander is yet unexplained, it does perhaps highlight the need for additional instrumentation on board entry vehicles and improved local atmospheric monitoring capabilities around non–terrestrial bodies that are being explored.

Typically, spacecraft entering Earth's atmosphere are well instrumented and there

exists much data with which to reconstruct the entry trajectory.[1] [278] In contrast, while numerous entry systems have flown in non–terrestrial atmospheres, often these systems are not adequately instrumented or the flight team not adequately funded to perform the statistical engineering reconstruction required to quantify performance and feedforward lessons learned into future missions. As such, entry system performance and reliability levels remain unsubstantiated and improvement in aerothermodynamic and flight dynamics modeling remains data poor. This research focuses on comparing methods for providing an accurate estimate of the atmosphere flown in and the trajectory flown by a robotic entry system. Best estimate values and uncertainties are provided, where applicable.

1.2 Objectives

This thesis compares two Kalman filter methods for obtaining information from previous entry data (i.e. from the Mars Pathfinder entry). The comparison is done in an effort to quantitatively and qualitatively compare the Kalman filter methods of reconstructing trajectories and atmospheric conditions from entry systems flight data. The first Kalman filter method used is extended Kalman filtering.[2] Extended Kalman filtering has been used extensively in trajectory reconstruction both for orbiting spacecraft and for planetary probes. It represents a standard against which to compare the other Kalman filter method. The second Kalman filter method is unscented Kalman filtering. As the literature suggested, unscented Kalman filtering offers improved performance over extended Kalman filtering, and this improved performance is demonstrated for entry, descent, and landing trajectory reconstruction. Unscented Kalman filtering has not been applied to entry, descent, and landing

[1] Genesis [69] and Stardust [68] are notable exceptions to this. Neither mission included instrumentation to provide data for trajectory reconstruction such as inertial measurement units.

[2] To some extent, most estimation methods such as Kalman filtering are fundamentally related to least squares.

trajectory reconstruction.[3]

Additionally, a formulation for trajectory reconstruction using collocation was desired, and it was desired that the trajectory simulation capabilities of collocation be evaluated. Collocation has also not been applied to entry, descent, and landing trajectory reconstruction. While collocation is not an estimation technique, it is useful for simulating entry, descent, and landing trajectories, and it may be useful for reconstructing entry, descent, and landing trajectories.

1.3 A Word on the Uniqueness of the Trajectory Reconstruction Problem

Unlike many applications where measurements are made, the states in trajectory reconstruction are generally not observable. The global positioning system on Earth makes it easy to determine our location, but it does not exist on other planets. The location of a spacecraft must often be determined by the inertial measurement unit acceleration data alone while performing entry descent, and landing from an initial state that has some uncertainty. And without certain knowledge of where it started from, the spacecraft could easily get lost until it finds the ground with its radar altimeter. The radar altimeter finds that landmark of the ground that allows the spacecraft to orient itself on the way to the surface of the planet. This is analogous to a blind man walking on the street. He knows where he started from, and he has a rough idea of where he is as he is walking. Periodically, however, he needs to find landmarks he knows along his route to verify his location. So unlike terrestrial navigation, there is no visibility of position and velocity during entry, descent, and landing.

[3]Unscented Kalman filtering has been used for the reconstruction of Mars Odyssey's aerobraking. [127, 128, 129]

1.4 Contributions

The contributions of this research, as will be discussed, are:

(1) The extended Kalman filter was originally developed for signal processing applications and only later applied to trajectory reconstruction. Similarly, unscented Kalman filtering was developed for signal processing applications, and this work represents its first application to the reconstruction of entry, descent, and landing trajectories.

(2) The reformulation of the entry, descent, and landing trajectory reconstruction problem using collocation has been demonstrated by the author. This approach dubbed "TRUC", after "trajectory reconstruction using collocation" posits that entry, descent, and landing trajectory design tools using collocation may also be used for entry, descent, and landing trajectory reconstruction. As a first step, the performance of entry, descent, and landing trajectory simulation using collocation (TSUC) has been demonstrated by the author. Additionally, a solution procedure for determining the state values that satisfy the defect constraints has been developed. This procedure allows the trajectory to be determined from the controls and parameters of the simulation in a deterministic way.[4]

(3) Trajectory reconstruction results from the unscented Kalman filter were compared against the trajectory reconstruction done using the extended Kalman filter. From this, guidance on choosing a method for the reconstruction of future trajectories was established. This guidance included trajectory reconstruction using collocation based on its expected capabilities.

[4]The review of the literature for this research indicates that collocation has not been used for entry, descent, and landing trajectory reconstruction, so this solution procedure has not been used for entry, descent, and landing trajectory reconstruction using collocation.

CHAPTER II

BACKGROUND AND MOTIVATION

In the following sections, an overview of methods for reconstructing atmospheric information from observations is provided. Next, a historical review is presented of the trajectory reconstruction work performed for several planetary probe missions. While primarily focused on Mars, Venus, and Earth-return missions, the Galileo (Jupiter) and Huygens (Titan) missions are also discussed. Emphasis is placed on the reconstruction of trajectories and atmospheres from inertial measurements of the motion of a planetary probe entering a body's atmosphere.

2.1 Measurement Techniques

A number of methods for measuring the variations of density and pressure with altitude in an atmosphere have been devised. Descriptions of some of those which have been used to survey the Earth's atmosphere were reported by Hanessian [113], Kondratyev [159], and Peterson [204]. Early on, it was noted that one of the primary objectives of robotic probes was to characterize non–terrestrial atmospheres, not only in terms of composition, but by finding temperature, pressure, and density profiles. [238] As Alvin Seiff [317], of the NASA Ames Research Center, wrote in a NASA technical note:

> One of the early objectives of space probes sent to Mars and Venus will be to determine the characteristics of the atmospheres on those planets for scientific purposes. Characteristics of interest include profiles of gas density, temperature, and pressure above the planet surface, and chemical composition of the atmosphere. Because of practical limitations, it

> is doubtful that the first probes will convey a very complete picture of the atmosphere, and a good initial objective will be to define the above properties broadly, although certainly the more that can be learned from an early probe the better. [238]

Given the dynamics of an atmosphere, real-time "weather reports" are needed to make the most accurate predictions of a planetary probe's entry trajectory and landing site. Knowledge of the atmospheric entry conditions also aids in the design of the spacecraft [220]. A summary of the different methods that can be used to determine various atmospheric properties are listed in Table 1. The following sections will present an overview of various methods for obtaining information on planetary and natural satellite atmospheres.

Table 1: Methods for determining atmospheric properties.

Method	Composition	Density	Temperature	Pressure	Wind Speed
Radio occultation		✓*	✓*	✓*	
Photometric occultation		✓*	✓*	✓*	
Spectroscopic measurements	✓		✓		
In situ measurements	✓	✓	✓	✓	✓
Doppler tracking		✓			✓
Inertial measurement units		✓	✓*	✓	

*When observations are combined with composition information obtained from another method.

2.1.1 Remote Sensing

Radio Occultation Occultation is the interruption of photons from some source such as a star, planet, or spacecraft due to a passing celestial body such as a planet (see Figure 1). Radio occultation refers specifically to the occultation of a radio signal from a spacecraft due to the atmosphere of a planet interposed between the source of the radio signal and the receiver. The interposing celestial body might be Mars between Earth and Mariner 4 [89] or Venus between Earth and Mariner 5 [90, 91]. The atmosphere of the celestial body refracts the signal, and a refractivity profile for the atmosphere is established. From the atmospheric refractivity profile, one can

retrieve, in sequence, profiles of the atmospheric density (given the composition), pressure, and temperature [319]. For radio signals, the Doppler shift of the radio signal is used to determine the refractivity profile rather than the "bending" of the signal [132] since the amount of bending is small. From the atmospheric refractive index, one can retrieve, in sequence, profiles of the atmospheric density, pressure, and temperature [319]. Information on atmospheric turbulence can also be obtained with single-frequency radio occultation, but turbulence is better determined from dual-frequency observations [315].

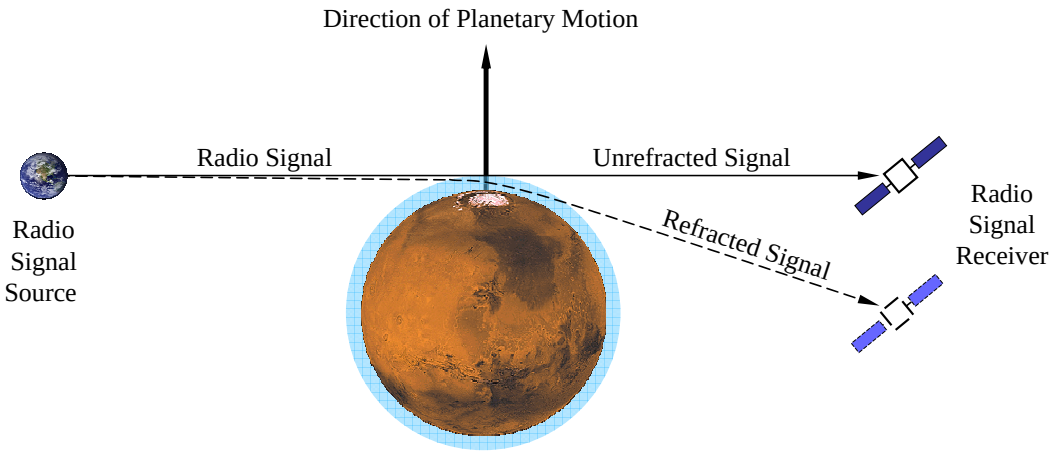

Figure 1: Radio occultation by Mars of a signal sent from Earth.

Before the atmospheric refractivity profile can be used to obtain the density profile of the atmosphere, the composition of the atmosphere must be determined. The atmospheric composition can be determined using ground-based spectroscopic observations for many gases. An atmospheric profile of number density can then be determined using the refractivity and composition through the use of empirical relations from refractivity experiments with gas mixtures. Knowing the composition, it is a simple step to go from the number density profile to the mass density profile of the atmosphere. Pressure then follows from the hydrostatic equation (to be discussed

further in § 2.1.4), and temperature then follows from pressure and the ideal gas equation of state.

Radio occultation measurements of temperature and pressure are limited by signal power and critical refraction. For example, on the Mariner 5 mission to Venus, loss of lock on the 423.3 MHz channel occurred 0.3 min after encounter. At this time, the lowest point on the ray passed 35 km above the surface where the pressure of the Venusian atmosphere was approximately 6 atm. No information about the atmosphere was determined below this altitude. The depth to which the radio signal probed before the loss of lock occurred was limited by the power of Mariner 5's transmitter. However, even with unlimited radio signal power, obtaining data down to the surface would not have been possible because of critical refraction. (Critical refraction occurs in atmospheric regions where the radius of curvature of a horizontal ray due to refraction becomes equal to, or smaller than, the distance from the top of the atmosphere to the planetary center of mass. No rays can probe tangentially through such regions since they are effectively bent to intersect with the planet.) The critical refractive properties of the atmosphere of Venus became known when the Venera 4 lander made its direct measurements on October 18, 1967 (one day prior to the Mariner 5 occultation experiments). [90] Radio occultation measurements were also used during the Viking missions to obtain atmospheric temperature and pressure profiles [92].

Photometric Occultation Photometric occultation is generally used to determine the shape of planetary bodies that lack an atmosphere such as moons and asteroids. However, when stars are occulted by planetary atmospheres such as the occultation of Regulus (α-Leonis) on July 7, 1959 by Venus [58], refractive observations can be combined with additional observations to obtain temperature and pressure profiles

for the atmosphere (see Figure 2). The additional information necessary includes atmospheric composition, surface temperature from microwave observations, and other remote temperature measurements to provide anchor points for the temperature profile. Occultation of stars passing behind natural satellite and planetary atmospheres also allows spectroscopic measurements to be made.

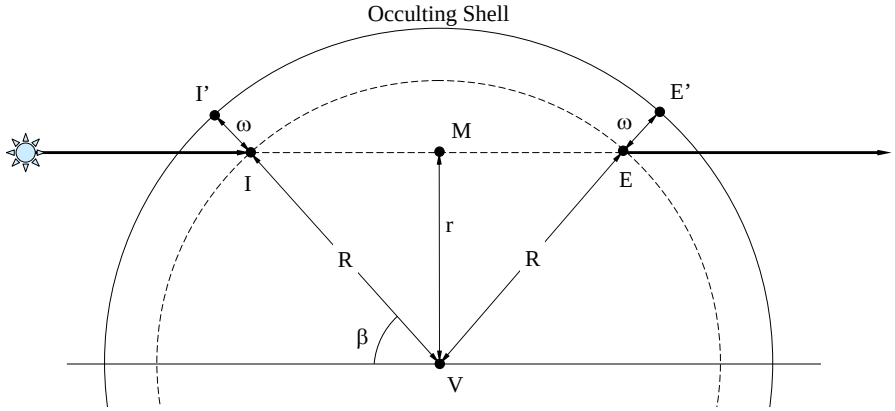

Figure 2: The effect of atmospheric refraction on the duration of occultation. At the time of apparent ingress (I) and egress (E), the apparent radius is $R = VI = VE$ corresponds to the observed duration of the occultation. The apparent radius is less than the true radius of the occulting shell, and the difference (ω) is due to refraction. [58]

Spectroscopic Measurements Occultation of stars passing behind natural satellite and planetary atmospheres also allows comparisons to be made of the star's spectra with and without an intervening atmosphere to see where absorption in the electromagnetic spectrum occurs. Spectroscopic measurements of sunlight reflected from natural satellite and planetary bodies allows their composition to be determined. [220, 28] Spectroscopic measurements can be used to characterize the composition of both an atmosphere and a rocky body. For example, water, carbon dioxide, and ozone all have strong, easily identifiable absorption bands at infrared wavelengths.

2.1.2 In Situ Measurements

The best measurements of atmospheric properties are made in situ and then transmitted to Earth. The first in situ measurements of atmospheric composition were made on October 18, 1967 by Venera 4 on Venus [197, 155, 177]. Similar measurements were made in Jupiter's atmosphere by Galileo on December 7, 1995 [318, 185], and on Titan by Huygens on January 14, 2005 [150, 235]. On Mars, Mars 6 observed the presence of inert gases (suspected to be carbon dioxide and argon) on March 12, 1974 [189, 124] and specific abundances for gases were measured by Viking 1 on July 20, 1976 [198, 194]. Instruments for atmospheric measurements used on several robotic probe missions are listed in Table 2 on page 10 for missions performing entry at celestial bodies beyond the Asteroid Belt, Table 3 on page 11 for missions performing entry at Venus, Table 4 on page 13 for missions performing entry at Earth, and Table 5 on page 16 for missions performing entry at Mars.

Table 2: Instruments (or types of measurements) for obtaining atmospheric information used on several robotic missions performing entry at celestial bodies beyond the Asteroid Belt.

	Galileo [318, 248, 244]	Huygens [150]
Accelerometers	✓	✓
Gyroscopes		
Pressure sensor	✓	✓
Temperature sensor	✓	✓
Mass spectrometer	✓	✓
Gas chromatograph		✓
Shock layer radiometer		
Trace species detector		
Cloud sensors	✓	✓
Aerosol analyzer		✓
Net flux radiometer	✓	
Solar flux sensors		
Lightning detectors	✓	
Hydrogen-Helium ratio	✓	
Energetic particles	✓	
Wind speed	✓	✓
Descent imager		✓
Surface science		✓

In situ measurements have included temperature, pressure, wind speed, and composition. Measuring temperature and pressure on the surface of a planet is relatively straightforward. Landing a spacecraft onto the surface of another planet, however, is fraught with complications. Additionally, once the lander has landed, it must survive long enough to make the measurements and transmit the data back to Earth.

On Venus, with its high temperature and high pressure environment, for example, the greatest challenge is having the spacecraft survive until it reaches the surface. Venera 7 was the first spacecraft to successfully return data from the surface of Venus [22, 134]. The density of Venus' atmosphere makes possible in situ measurements of temperature and pressure while descending on a parachute with minimal impact from the effects of the spacecraft's descent through the atmosphere. Vega 1 and Vega 2 were able to measure atmospheric temperature and pressure from 0 km to 63 km above ground level [59].

Table 3: Instruments (or types of measurements) for obtaining atmospheric information used on several robotic missions performing entry at Venus.*

	Venera	Pioneer Venus Large Probe	Pioneer Venus Small Probes	Vega
Accelerometers	✓	✓[50]	✓[50]	✓
Gyroscopes	✓[147]			✓[59]
Pressure sensor	✓[17]	✓[50]	✓[50]	✓[169]
Temperature sensor	✓[17]	✓[50]	✓[50]	✓[169]
Mass spectrometer	✓	✓		✓
Gas chromatograph	✓	✓		✓
Shock layer radiometer				
Trace species detector	✓			✓
Cloud sensors	✓	✓	✓	✓
Aerosol analyzer	✓			✓
Net flux radiometer		✓	✓	
Solar flux sensors	✓	✓		✓
Lightning detectors	✓			✓
Hydrogen-Helium ratio				
Energetic particles				
Wind speed	✓	✓	✓	✓
Descent imager				
Surface science	✓			✓

*The instruments used by Venera, Vega, Pioneer Venus Large Probe, and Pioneer Venus Small Probes are provided in reference [240] except where noted.

In-flight measurements of atmospheric temperature and pressure are complicated because, at supersonic and hypersonic speeds, an instrument may not directly measure freestream conditions.[1] Experiments involving a number of forms of observations, such as acceleration, spectral distribution and intensity of shock-layer radiation, oscillation frequency, etc., were proposed in [238], and the experiments were developed in more detail in [249] and [205].

The most comprehensively instrumented probe flown on Earth was the Planetary Atmosphere Experiments Test (PAET) vehicle [250] (see Figure 3), which was built to carry instruments for making the observations discussed in the previous paragraph. The PAET instruments included temperature sensors, pressure sensors, accelerometers, a mass spectrometer, and a radiometer (to aid in the determination of atmospheric composition) (see Figure 4 and Figure 5). Future generations of the PAET atmospheric structure instrument flew on Viking 1 and Viking 2 (2nd generation), Pioneer Venus (3rd generation), and Galileo (4th generation). [248] The atmospheric structure instrument consisted of accelerometers, temperature sensors, and pressure sensors.

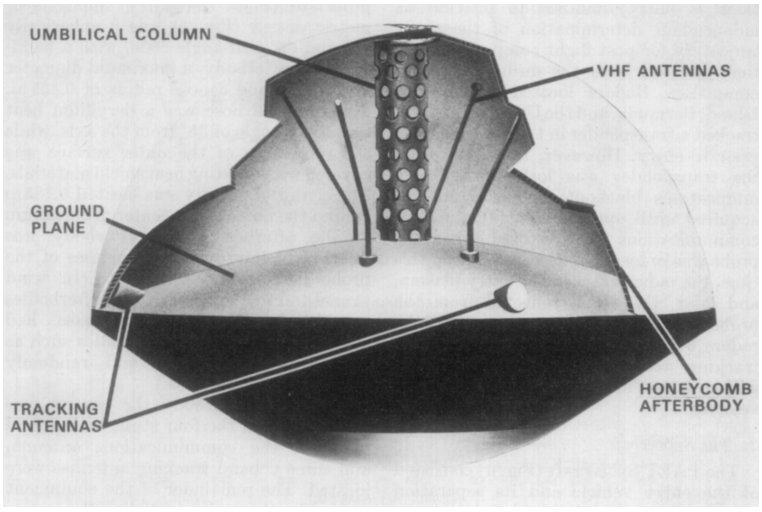

Figure 3: Cut-away view of the PAET vehicle. [250]

[1] Density can also be determined from pressure and velocity measurements during entry. [326, 192]

Table 4: Instruments (or types of measurements) for obtaining atmospheric information used on several robotic missions performing entry at Earth.

	PAET [250, 240]	Genesis [69]	Stardust [68]
Accelerometers	✓		
Gyroscopes			
Pressure sensor	✓		
Temperature sensor	✓		
Mass spectrometer	✓		
Gas chromatograph			
Shock layer radiometer	✓		
Trace species detector	✓		
Cloud sensors			
Aerosol analyzer			
Net flux radiometer			
Solar flux sensors			
Lightning detectors			
Hydrogen-Helium ratio			
Energetic particles			
Wind speed			
Descent imager			
Surface science			

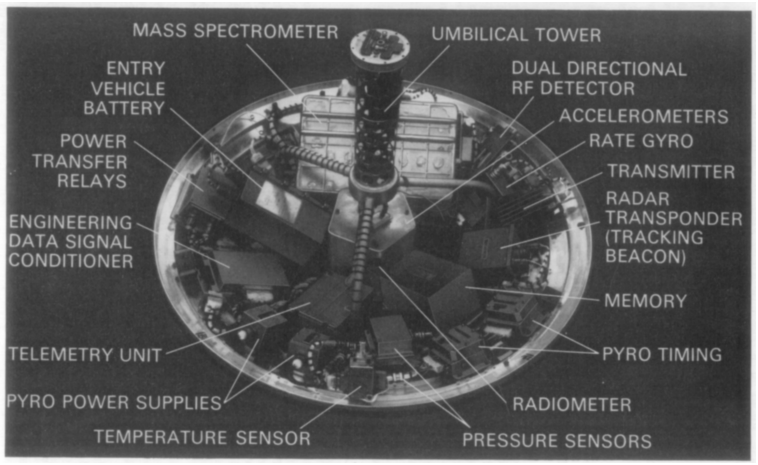

Figure 4: Interior view of the PAET vehicle. [250]

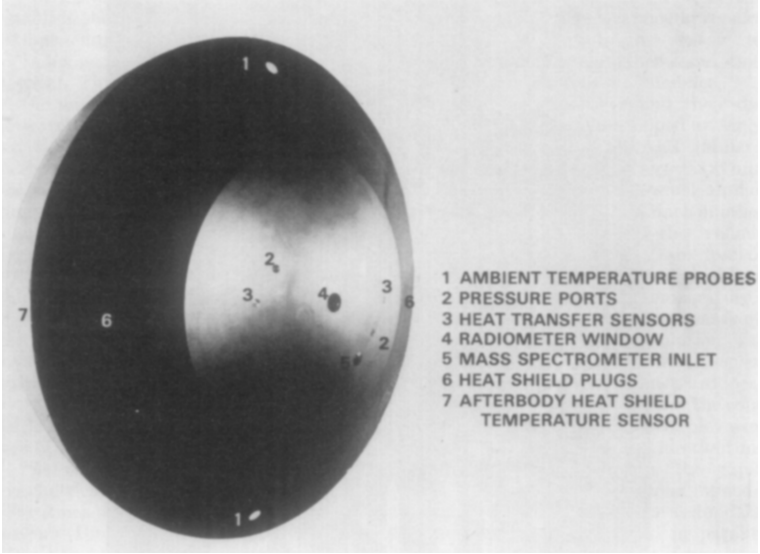

Figure 5: Sensor ports on the PAET vehicle. [250]

In 1967, a study was conducted on the design of a thoroughly instrumented probe (see Figure 6) to determine the properties of the Martian atmosphere [101], but it was not built. Nevertheless, several robotic missions have made in situ measurements on Mars. The Mars 6 descent vehicle made temperature and pressure measurements as it descended [16] . The temperature measurements were biased due to entry heating, but could be used to obtain the stagnation point temperature [85, 325]. Viking 1 and 2, Mars Pathfinder, the Mars Exploration Rovers, and Mars Phoenix Lander have all made in situ measurements on Mars, although the Mars Exploration Rovers did not make in situ measurements of temperature and pressure, and Mars Pathfinder only measured surface properties.

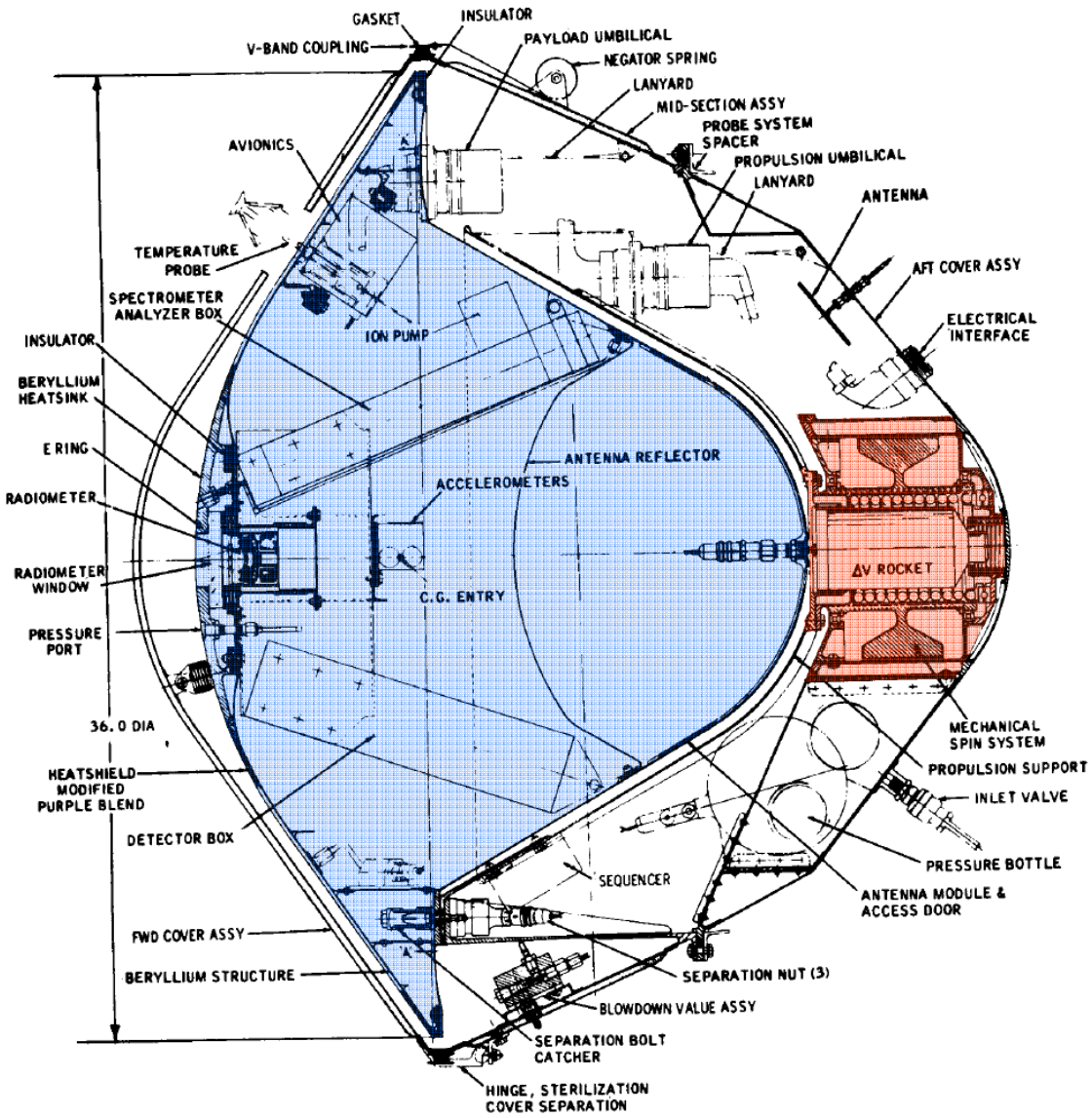

Figure 6: Design proposed in 1967 for a probe to determine the atmospheric properties of the Martian atmosphere. The probe is enclosed inside a shell that spins up the probe for stabilization and is jettisoned prior to entry. [101] The Δv rocket and the mechanical spin system are in the middle, right portion of the figure.

The Mars Science Laboratory (MSL) will have a suite of instrumentation embedded in the heatshield of the entry vehicle. Called MEDLI for "Mars Science Laboratory Entry, Descent and Landing Instrumentation," the instrumentation will

measure temperature, pressure, and recession of the thermal protection system. The data collected will aid in the understanding of the aerodynamics, aerothermodynamics, flight dynamics, and material response of the thermal protection system, as well as permit more accurate aerodynamics, atmosphere, and trajectory reconstruction.[2] [196]

Table 5: Instruments (or types of measurements) for obtaining atmospheric information used on several robotic missions performing entry at Mars.

	Mars 6 [261]	Viking 1 and 2	Mars Pathfinder [267]	Mars Exploration Rovers [53, 11]	Mars Phoenix Lander [255]
Accelerometers	✓	✓[240]	✓	✓	✓
Gyroscopes		✓[239]		✓	✓
Pressure sensor	✓	✓[239]	✓		✓
Temperature sensor	✓	✓[239]	✓		✓
Mass spectrometer	✓[124]	✓[240]			✓
Gas chromatograph		✓[240]			
Shock layer radiometer					
Trace species detector					
Cloud sensors			✓	✓[46]	✓
Aerosol analyzer					
Net flux radiometer					
Solar flux sensors					
Lightning detectors					
Hydrogen-Helium ratio					
Energetic particles					
Wind speed			✓		✓
Descent imager				✓	
Surface science		✓	✓		✓

2.1.3 Doppler Tracking

Doppler tracking uses the Doppler shift of a radio signal from a spacecraft to determine the velocity of the spacecraft and other state and model parameters. Atmospheric

[2]Essentially, the actual entry flight of a spacecraft represents the best opportunity to collect data on the performance of the flight vehicle since the actual flight conditions cannot always be simulated in tests on Earth. Hence, data for model validation may be lacking. The improved models can then be used for designing future spacecraft. For example, aerodynamic heating uncertainties can be greater than 50%, especially near the shoulders of aeroshells. Such uncertainties require thicker, heavier aeroshells than may be necessary. Additionally, pressure data taken in–flight will help resolve the separation of aerodynamic coefficient uncertainties with uncertainties in the atmospheric conditions.

wind profiles can also be determined from Doppler tracking.[3] Generally, the source of the radio signal is a spacecraft descending to the surface of a planet or natural satellite. There may be one or more receivers of the signal. Often, the NASA Deep Space Network (DSN) or the Very Large Array (VLA) constitute the Earth-based receiver. If there is a second spacecraft in the vicinity of the celestial body of interest (such as with paired orbiter-lander or flyby-lander missions), it may be used as another receiver. Two receivers in different locations allows two components of the lander's velocity to be determined.

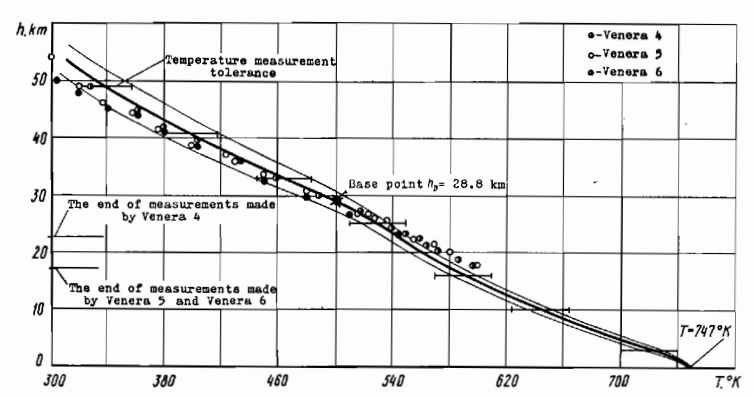

Figure 7: Temperature profile of Venus' atmosphere based on measured temperatures and altitudes from Doppler tracking. [22]

Doppler tracking was used extensively as part of exploration missions to Venus. Doppler tracking was used to determine the velocity of the Venera and Vega landers (see Figure 7) [155, 22, 6, 7, 8, 316, 18] and to obtain profiles of the atmospheric winds [155, 7, 8, 154, 153]. Doppler tracking was also used during the Pioneer Venus mission to obtain more than one component of the spacecraft's velocity. [14] At Mars, Doppler tracking was used during Mars 6 flyby-lander mission [16] and the Viking orbiter-lander missions [182]. Changes in the speed of the Galileo probe at Jupiter

[3]Wind measurements generally require a separate ground station in addition to sensors at altitude in the atmosphere. Doppler tracking is the most straightforward method for use at non–terrestrial planets and natural satellites with atmospheres [133]

caused by zonal winds also created a small but measurable effect in Galileo's relay carrier frequency. [14]

2.1.4 Inertial Measurement Units

Properties of planetary and natural satellite atmospheres can also be determined from observations made by an entry vehicle passing through the atmosphere. Considerable attention has been focused on knowledge of the acceleration experienced by a body, having known aerodynamic characteristics (with known uncertainties associated with them) and entering an atmosphere on a ballistic trajectory. [205] Measurements of the motion of the entry vehicle can be used to construct the density and pressure structure of the atmosphere.[4] [205] The motion of an entry body is generally measured using inertial measurement units (IMUs). An inertial measurement unit contains accelerometers for measuring the translational motion of the entry vehicle, and it may also contain gyroscopes for measuring rotational motion.

Detailed procedures for obtaining the density and pressure profiles of a planetary atmosphere from measurements of accelerations experienced by a vehicle making a ballistic entry into the atmosphere of a planet are given in [238, 204]. Atmospheric temperature profiles can also be determined given composition information. Early work focused on a spherical entry bodies [47, 204, 205, 120], though some work involved conical bodies [262] including the fourth flight of the NASA Planetary Entry Parachute Program (PEPP) [263].

Atmospheric density (ρ) is determined from the axial acceleration (a_A) experienced by the entry vehicle assuming: the vehicle's aerodynamic properties (i.e. drag coefficient (C_D) and aerodynamic reference area (S)), the speed of the entry vehicle (v), and its mass (m) are all known.[5]

[4]However, the uncertainties of the spacecraft's aerodynamic coefficients and the uncertainties of the atmospheric conditions cannot be separated unless separate measurements are made of either the actual flight atmospheric conditions or the pressure distribution around the spacecraft in–flight.

[5]The speed of the entry vehicle (v) is known from the reconstruction of the spacecraft's trajectory

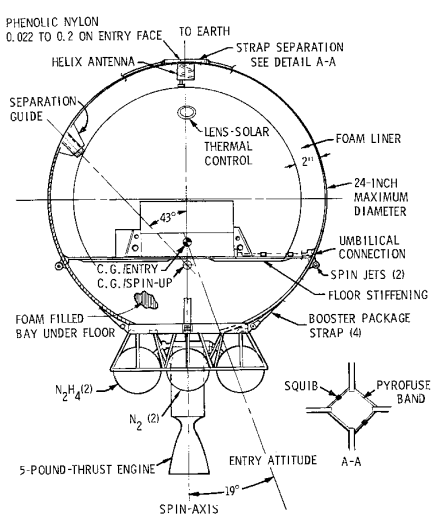

Figure 8: A spherical entry vehicle proposed in reference [120] for obtaining Martian atmospheric profiles of density and pressure. Both the engine and the spin jets were to be jettisoned prior to entry.

$$ma = \frac{1}{2}\rho v^2 C_D S \tag{1}$$

$$\rho = \frac{2ma}{v^2 C_D S} \tag{2}$$

Vehicle drag coefficients are not greatly affected by the composition of the atmosphere in which a vehicle flies [130], so the composition of the atmosphere can be neglected when finding the atmosphere's density profile. Typically for ballistic entry vehicles flying at zero angle of attack, the axial acceleration (a_A) is used in equation 2.

$$\rho = \frac{2ma_A}{v^2 C_D S} \tag{3}$$

The atmospheric pressure (p) profile can be determined by integrating the hydrostatic equation, which can be expressed in terms of the velocity (v) and flight path

from the accelerometer data.

angle (γ) of the entry vehicle.

$$dp = -\rho g dh \tag{4}$$

$$p = -\int_{\infty}^{h} \rho g dh \tag{5}$$

and

$$dh = -(v \sin\gamma) dt \tag{6}$$

$$p = \int_{0}^{t} \rho g v \sin\gamma dt \tag{7}$$

The atmospheric temperature (T) profile can then be determined by using the ideal gas equation of state if the molecular mass (MW) of the atmosphere is known.

$$p = \rho \frac{\Re}{MW} T \tag{8}$$

$$T = \frac{p}{\rho \frac{\Re}{MW}} \tag{9}$$

2.1.5 Light Detection and Ranging

Light Detection and Ranging (LIDAR), also known as Laser Detection and Ranging (LADAR), can be used to determine position and velocity and is expected to improve real–time navigation significantly for pinpoint landing [3] and remotely piloted vehicles [2]. LIDAR can also be used to obtain various atmospheric information [178] including: measuring wind speeds [254, 93], carbon dioxide concentration in the atmosphere [254], molecular species temperature and pressure [179], measurement of gas and aerosol profiles [4, 221], and trace gas concentration [44].

2.1.6 Descent Imaging

The Descent Imager / Spectral Radiometer (DISR) provided images during part of the descent of the Huygens probe to the surface of Saturn's natural satellite Titan. Altitude, attitude information ("tip and tilt", as well as rotation), and wind velocity [146] can be determined from descent imaging. By imaging the same surface feature at different altitudes, descent imaging can also serve to verify the reconstruction of altitude from inertial measurement units [146], even if the size of the surface feature is not known. If the size of the surface feature is known, the altitude estimation is more accurate. Clouds, fog, and dust can limit the use of descent imaging depending on what part of the spectrum the image is taken from. Higher resolution images enhance the accuracy of reconstruction, and allow reconstruction to begin at higher altitudes. However, higher resolution images require more memory space to store, present a higher computational burden for in–flight processing, and take longer to transmit to Earth.

2.1.7 Magnetometer Measurements

Magnetometers can measure the strength and direction of a magnetic field. Since the magnetic field at any point around Earth is relatively unique, magnetometer measurements can be used to determine altitude and latitude [257, 258] by matching the magnetometer measurements to a model of the Earth's magnetic field. Spacecraft attitude [26, 52, 51, 216, 211, 215, 214] and changes in attitude [51, 289] can also be determined. In order for magnetometer measurements to be used, the planet or natural satellite of interest must have a significant and *mapped* magnetic field. Earth, Jupiter, Ganymede, Saturn, Uranus, and Neptune are the only solar system bodies with appreciable magnetic fields. The use of magnetometer measurements also requires an up–to–date model of the magnetic field, and magnetic fields are subject to change. For example, as of 2009, the Earth's magnetic north pole was moving from

Canada to Russia at the rate of approximately 64 kilometers per year. [173] This is approximately four times faster than its rate of movement at the beginning of the 20th century.

2.2 Reconstructed Mission Data

A survey of several robotic planetary probe missions was conducted to determine if there was a standard method of trajectory reconstruction for entry, descent, and landing. This standard method would then be used to evaluate the two methods under investigation in this research[6] for possible application to trajectory reconstruction. Generally, the entry, descent, and landing trajectory reconstructions were performed by either directly integrating the accelerometer data obtained during entry or by using Kalman filtering[7] in conjunction with the accelerometer data. In some cases, both direct integration and Kalman filtering were used for trajectory reconstruction. For other missions, radar tracking data was used and a description of how the data was processed to reconstruct the trajectory is not explicitly stated, even though some form of data reduction or filtering was probably used. Though direct integration was the most widely used method of trajectory reconstruction, extended Kalman filtering was selected as the standard to evaluate the two new techniques against as it provides an estimate of uncertainty, which direct integration does not.

A summary of the methods used to reconstruct the trajectory of each spacecraft are listed in Table 6 on page 29 for missions performing entry at Venus, Table 7 on page 31 for missions performing entry at Earth, and Table 8 on page 42 for missions performing entry at Mars, and Table 9 on page 45 for missions performing entry at celestial bodies beyond the Asteroid Belt. The following paragraphs briefly discuss each mission or series of missions.

[6]The two methods under investigation in this research being: (1) the unscented Kalman filter (UKF) and (2) trajectory reconstruction (TRUC). This thesis compares these two methods with extended Kalman filtering for reconstructing entry, descent, and landing trajectories.

[7]Usually with the extended Kalman filter form of the Kalman filter.

2.2.1 Venus Missions

Venera The sixteen Venera missions to Venus consisted of: flyby spacecraft (Venera 1 and 2), probes (Venera 3, 4, 5, and 6), landers (Venera 7 and 8), orbiters (Venera 15 and 16), and orbiter-lander pairs (Venera 9, 10, 11, 12, 13, and 14). Data was returned from Venera 4, 5, and 6, but contact was lost before any of these spacecraft reached the surface of Venus. Venera 7 (see Figure 9) was the first spacecraft to return data from another planet when it landed on Venus on December 15, 1970. Venera 7 operated for 23 minutes after landing. [134] Sufficient data was returned to construct profiles of atmospheric temperature and pressure. [22] Follow-on missions provided additional data confirming the Venera 7 measurements. By the end of the Venera missions, sufficient data had been received to construct profiles of Venus' atmospheric temperature, pressure, density, and winds using a combination of accelerometer measurements, in situ measurements, and Doppler / radar tracking.

It is assumed that the trajectories of the Venera landers were reconstructed deterministically using direct integration as the method is not always generally discussed in the literature (cf. [17], [19], [147]). Applying filtering to the reconstruction of the Venera–lander trajectories is discussed in reference [21]. However, reference [21] was published over a year after the last Venera–lander (Venera 14) was launched (November 4, 1981), so it is not clear if filtering was later applied to the reconstruction of the Venera trajectories.

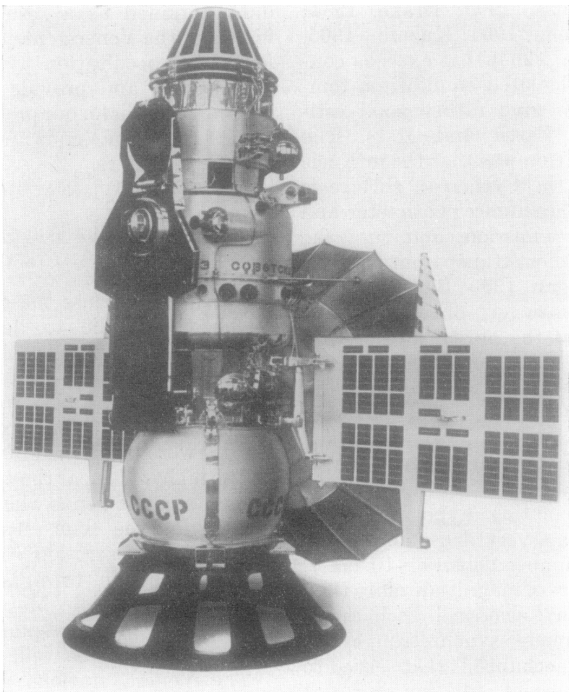

Figure 9: The Venera 7 spacecraft. [177]

Figure 10: The Venera 7 entry capsule. [Image credit: NSSDC]

Pioneer Venus The Pioneer Venus missions consisted of an orbiter and four probes: one "large" probe (see Figure 12) and three small probes (see Figure 13) (the "north,"

"night," and "day" probes). Each probe entered Venus' atmosphere at a different location (see Figure 11). The orbiter was launched before the probes and inserted into Venus orbit on December 4, 1978. The landers entered Venus' atmosphere on December 9, 1978.

Temperature and pressure data were received from all four probes. The data allowed the construction of temperature, pressure, density, and wind profiles for Venus' atmosphere. [247] However, temperature data from all four probes ceased at approximately 12.5 km altitude, so the temperature was extrapolated from that altitude to the surface. [246]

A post-flight investigation determined the cause of the data loss to be a short in an electrical connection for the atmosphere structure instrument and the net flux radiometer. Kapton insulation and kynar shrink tubing were used for these electrical connections, and these materials dissolve after prolonged exposure to sulfuric acid. [251] The data loss occurred at the same time as other anomalies in several other probe instruments. There was also an increase in ambient light seen by the nephelometers at the time of the anomaly. [246]

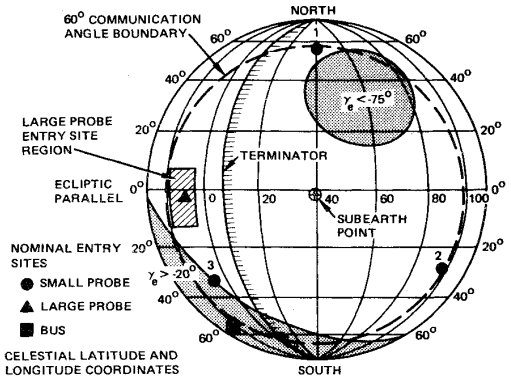

Figure 11: Pioneer Venus entry sites as seen from Earth. [73]

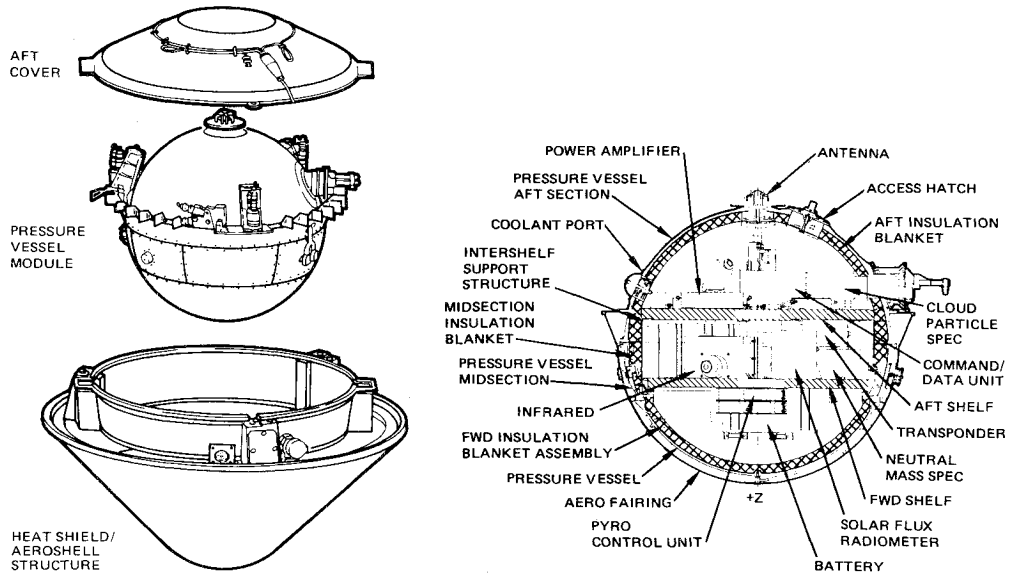

(a) Exploded view. (b) Internal view.

Figure 12: Pioneer Venus Large Probe. [73]

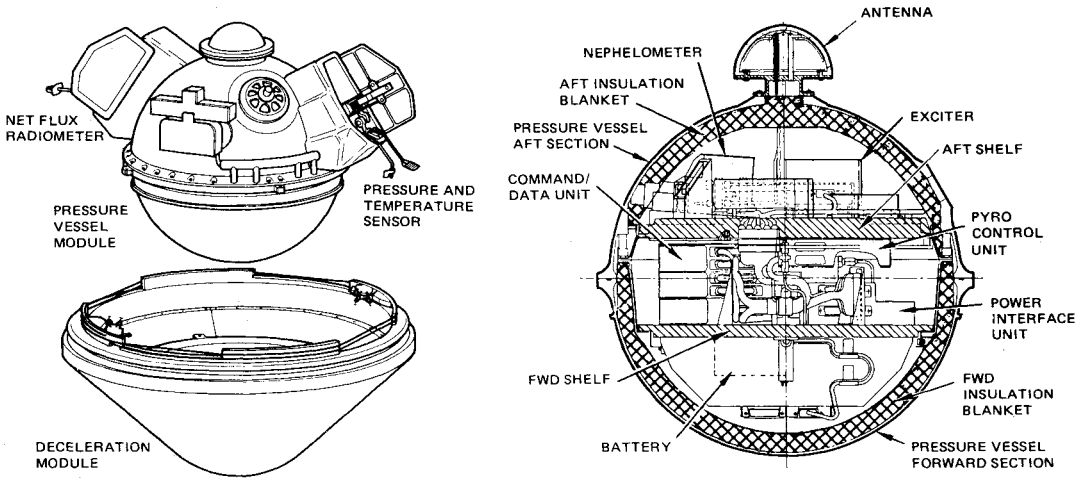

(a) Exploded view. (b) Internal view.

Figure 13: Pioneer Venus Small Probe. [73]

The entry trajectory reconstruction process presented in reference [86] for the Pioneer Venus probes evolved from simulation studies and error analysis results. Initially two types of methods were considered. These methods differ principally in the manner by which spacecraft state predictions were obtained. One method, termed the "conventional method," obtained a state prediction by integrating the computed

forces based on an *a priori* atmospheric and aerodynamic model. The conventional method employed a Bayesian batch estimator. [87, 86] In the other method, referred to as the "deterministic method," the state predictions were obtained by integrating the measured accelerations from some predetermined set of initial conditions. A form of the deterministic method [303] was successfully employed by the Viking Project to reconstruct the two Viking lander entries through the Martian atmosphere. [86] References [303] and [230] utilize Kalman filtering algorithms, and the same algorithm was employed for the Pioneer Venus probes in the deterministic method. [86] Similar options for trajectory reconstruction are discussed in references [301, 302, 303, 230].

Vega The Vega 1 and 2 missions flew by Venus on their way to an encounter with Halley's Comet in 1986. At Venus, each Vega spacecraft deployed a lander inside a spherical aeroshell (see Figure 14). Each lander deployed a balloon that drifted near an altitude of 53.6 km. [232] The balloons and landers recorded temperature and pressure data. The data from the landers were used to construct atmospheric profiles of temperature, pressure, and density. [59, 169] Atmospheric density profiles calculated using the ideal gas equation and from accelerometer measurements were in good agreement with each other. [169] Vertical wind speed profiles were also constructed from Doppler measurements [153], and a reference model for minimum, mean, and maximum zonal winds was created from the data [190]. No mention is made of data filtering, so it is presumed that direct integration was used with the accelerometer measurements. However, some data filtering of data reduction may have been used with the Doppler tracking data.

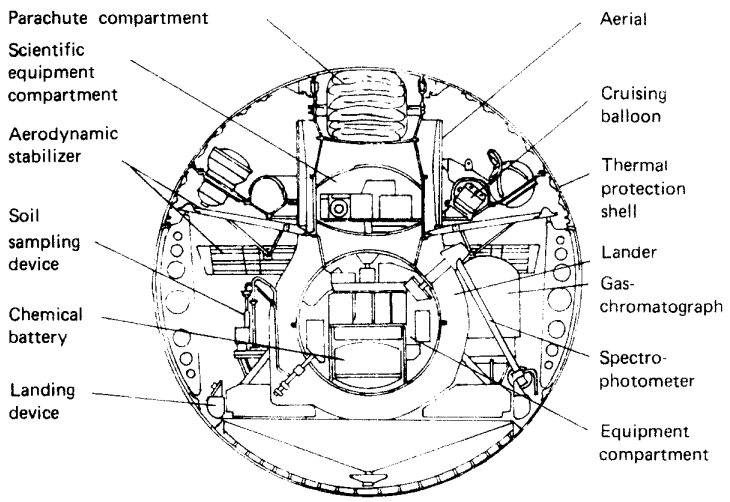

Figure 14: Vega entry vehicle. The lander is contained inside the spherical aeroshell. [160]

Table 6: Trajectory reconstruction methods and atmospheric information obtained from several robotic missions performing entry at Venus.

	Venera[b]	Pioneer Venus Large Probe[d]	Pioneer Venus Small Probes[f]	Vega[g]
Trajectory Reconstruction Method				
Radar Tracking	✓			✓
Direct Integration[a]	✓[c]			✓
Kalman Filter		✓[e]	✓	
Atmosphere Reconstruction				
Density Profile	✓	✓	✓	✓
Pressure Profile	✓	✓	✓	✓
Temperature Profile	✓	✓	✓	✓
Winds	✓	✓	✓	✓

[a]If accelerometer data was available for trajectory reconstruction and extended Kalman filtering is not specifically mentioned, it is assumed that direct integration was the method used for trajectory reconstruction.

[b]References [155, 147, 316, 19, 18, 20, 153].

[c]Applying filtering to the reconstruction of the Venera–lander trajectories is discussed in reference [21]. However, reference [21] was published over a year after the last Venera–lander (Venera 14) was launched (November 4, 1981), so it is not clear that filtering was later applied to the reconstruction of the Venera trajectories.

[d]References [87, 246, 247].

[e]The entry trajectory reconstruction process presented in reference [86] for the Pioneer Venus probes evolved from simulation studies and error analysis results. Initially two types of methods were considered. These methods differ principally in the manner by which spacecraft state predictions were obtained. One method, termed the "conventional method," obtained a state prediction by integrating the computed forces based on an textita priori atmospheric and aerodynamic model. The conventional method employed a Bayesian batch estimator. [87, 86] In the other method, referred to as the "deterministic method," the state predictions were obtained by integrating the measured accelerations from some predetermined set of initial conditions. A form of the deterministic method [303] was successfully employed by the Viking Project to reconstruct the two Viking lander entries through the Martian atmosphere. [86] References [303] and [230] utilize Kalman filtering algorithms, the same algorithm was employed for the Pioneer Venus probes in the deterministic method. [86]

[f]References [87, 246, 247].

[g]References [160, 59, 153, 169].

2.2.2 Earth-return Missions

Genesis and Stardust The Genesis and Stardust spacecraft were not equipped with onboard sensor data for a traditional trajectory reconstruction. Instead, a best estimated trajectory was calculated using the final navigation state vector at entry interface and tracking data from the UTTR tracking stations. Atmospheric density and wind profiles were obtained from balloon data prior to entry.[8] [69, 68]

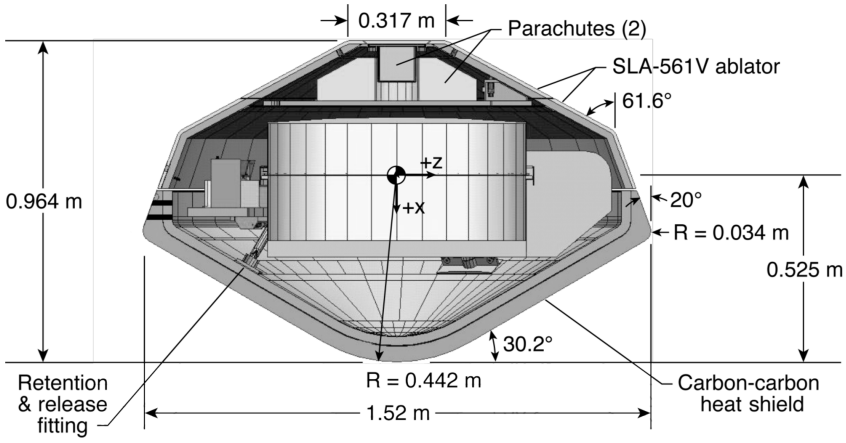

(a) Genesis. [65]

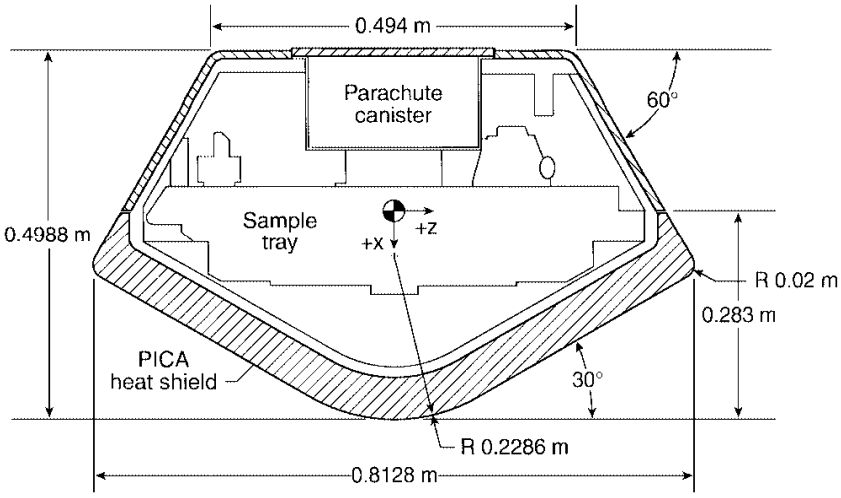

(b) Stardust. [66]

Figure 15: The Genesis and Stardust sample return capsules.

[8]Four hours prior to entry for Genesis [69], and two hours prior to entry for Stardust [68].

Table 7: Trajectory reconstruction methods and atmospheric information obtained from several robotic missions performing entry at Earth.

	PAET[b]	Genesis[c]	Stardust[e]
Trajectory Reconstruction Method			
Radar Tracking	✓	✓[d]	✓[f]
Direct Integration[a]	✓		
Kalman Filter			
Atmosphere Reconstruction			
Density Profile	✓	✓	✓
Pressure Profile	✓		
Temperature Profile	✓		
Winds		✓	✓

[a]If accelerometer data was available for trajectory reconstruction and extended Kalman filtering is not specifically mentioned, it is assumed that direct integration was the method used for trajectory reconstruction.

[b]PAET was discussed in § 2.1.2.

[c]Reference [69].

[d]No onboard sensor data for a traditional trajectory reconstruction was available from Genesis. Instead, a best estimated trajectory was calculated using the final navigation state vector at entry interface and tracking data from the UTTR tracking stations. Atmospheric density and wind profiles were obtained from balloon data four hours prior to entry. [69]

[e]Reference [68].

[f]As with Genesis, no onboard sensor data for a traditional trajectory reconstruction was available from Stardust. Instead, a best estimated trajectory was calculated using the final navigation state vector at entry interface and tracking data from the UTTR tracking stations. Atmospheric density and wind profiles were obtained from balloon data two hours prior to entry. [68]

2.2.3 Mars Missions

Mars 3 & Mars 6 Mars 6 (see Figure 16) was one of the *Mars*–series spacecraft (Mars 1 through 7) launched by the Soviet Union from 1962 to 1973. Mars 1 came within approximately 193,000 km of Mars, but its communication system failed when it was 106,760,000 km from Earth. Mars 2 and 3 arrived at Mars on November 27, 1971 and December 2, 1971, respectively. Mars 2 crashed on Mars at approximately 45°S, 302°W. Having entered the atmosphere at too steep of an angle it crashed into the surface before its parachute system was activated. [203] Mars 3

achieved the first soft landing on Mars at approximately 45°S, 158°W, but ceased operating after 20 seconds on the surface [183], perhaps because of the violent Martian dust storm taking place when it landed. [108]

Mars 4, 5, 6, and 7 arrived at Mars in February and March of 1974. Mars 4 arrived first on February 10, 1974. Passing as close as 2200 km altitude, it took several photographs as it flew by Mars. Mars 5 arrived on February 12, 1974 and was placed into a highly elliptical orbit around Mars with an eccentricity of 0.74974 and a periapsis altitude of 5150 km. Mars 7 arrived next on March 9, 1974. Unfortunately, an on board systems failure caused its lander to fly by Mars at an altitude of 1300 km. Mars 6 arrived at Mars on March 12, 1974. [189]

The descent velocity of Mars 6 was determined using the Doppler shift in the signal transmitted to the orbiter up until the descent vehicle reached a speed between 60 m/s and 65 m/s when communication ceased. The relative velocity measurement was used to determine the maximum deceleration experienced by the descent vehicle. The analysis of the Doppler shift was performed on Earth using recorded data [16], and references [222, 152] present further analysis of the Mars 6 transmissions. Reference [152] includes estimates of the atmospheric temperature, pressure, and density profiles, as well as a wind profile from 0.2 km to approximately 7.5 km above the landing site. Accelerometer measurements were also made and used for the trajectory reconstruction. [16] No discussion was found of any data reduction or filtering techniques used for the reconstruction, so it is presumed that direct integration of the accelerometer measurements was used to reconstruct the trajectory.

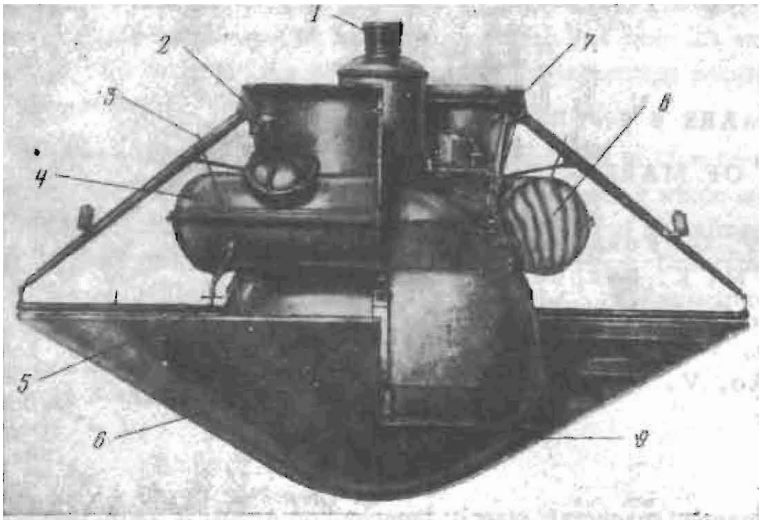

Figure 16: The Mars 6 entry vehicle. 1) motor for separating the entry capsule, 2) motor for ejecting the draw parachute, 3) antennas for communication with the orbiter, 4) parachute container, 5) radio-altimeter antenna, 6) aerodynamic deceleration cone, 7) instruments and equipment of the automatic control system, 8) main parachute, and 9) the lander. [261]

The Mars 6 descent vehicle made temperature and pressure measurements as it descended. The temperature measurements were biased due to entry heating, but the pressure measurements provided a means of estimating atmospheric temperature during descent. [16] Temperature and pressure profiles from 20 km to 0 km altitude (above the landing site at 23.9°S, 19.5°W) were constructed. [261]

Mars 6 also carried a mass spectrometer. Measurements were made of atmospheric composition. The mass spectrometer data were stored on board during the descent and scheduled to be transmitted after landing. However, communications ceased before the data could be transmitted. The current to the vacuum pump was transmitted as an engineering parameter, however. The current data showed a steep increase. It was hypothesized that this indicated the presence of an inert gas which could not be removed by the pump. [126] Carbon dioxide was hypothesized to make up no less than 75% of the Martian atmosphere since the pump's electric current data

fell around the 35% argon / 65% carbon dioxide calibration curve for the pump. [124]

Viking The Viking missions consisted of two orbiter-lander pairs (see Figure 17). Viking 1 landed in the Chryse Planitia region at 22.5°N, 48.0°W on July 20, 1976 [259], and Viking 2 landed in the Utopia Planitia region at 47.89°N, 225.86°W on September 3, 1976 [193]. The Viking landers had a reaction control system [123], and center of gravity placement was used to trim the Viking aeroshells at an angle of attack of –11.1° [76]. The landers made measurements of the structure of the atmosphere during entry and descent using accelerometers, pressure, and temperature sensors (see Figure 18).

Profiles of atmospheric density, temperature, and pressure were established using atmospheric deceleration measurements, as well as direct measurements of temperature and pressure below approximately 20 km altitude. [79, 243, 239, 242, 156, 157] Kalman filtering was used in the reconstruction process. [121, 79] A mass spectrometer measured the physical and chemical properties of the atmosphere of Mars beginning at an altitude near 200 km. [194] Preliminary data determined the abundance of gases in the Martian atmosphere to be: 95% carbon dioxide, 0.1% to 0.4% oxygen, 2% to 3% nitrogen, and 1% to 2% argon. [198]

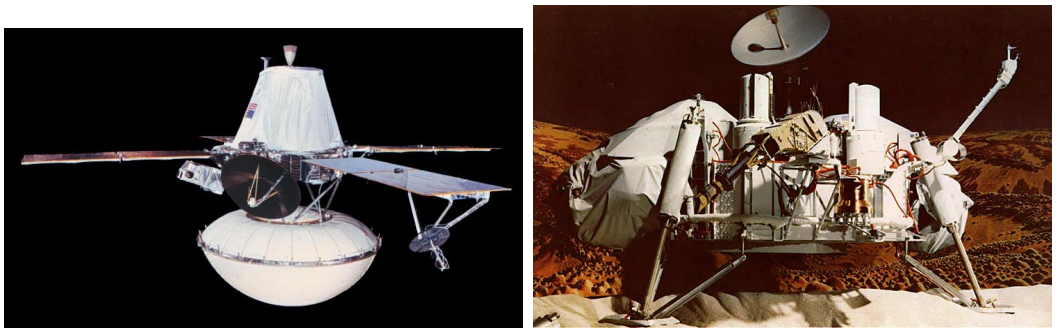

(a) Orbiter. (b) Lander.

Figure 17: The Viking 1 spacecraft. [Image credit: NSSDC]

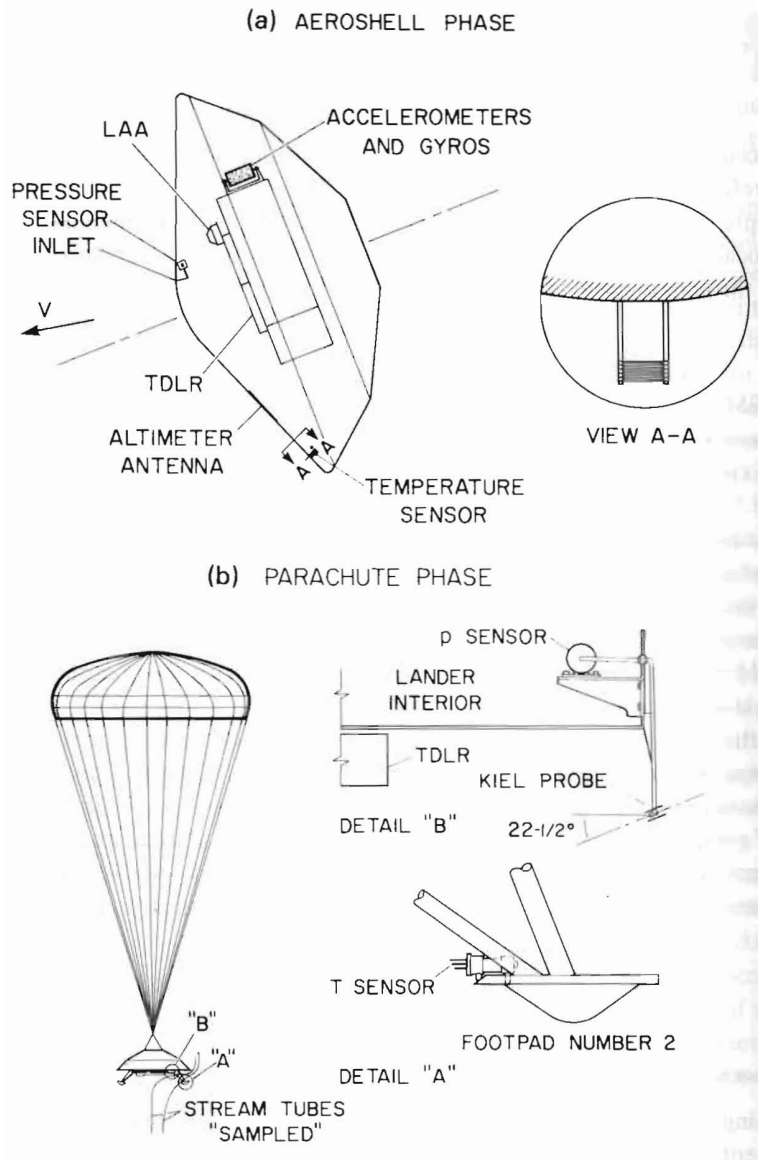

Figure 18: Locations of the Viking atmosphere structure instruments. [239]

Mars Pathfinder Mars Pathfinder (see Figure 19) was launched on December 4, 1996 and landed on Mars on July 4, 1997. [299] Three scientific instruments collected data: (1) the Imager for Mars Pathfinder [256], (2) the α–proton x–ray spectrometer (APXS) [224], and (3) an atmospheric structure investigation / meteorology package (ASI/MET) [252]. The atmospheric structure investigation / meteorology package

contained the accelerometers that provided the acceleration data for Pathfinder's trajectory reconstruction. Low–pass filters in the accelerometer electronics attenuated signal frequencies above 5 Hz to suppress the effects of noise and spacecraft dynamic motion. [252] Mars Pathfinder also deployed a small rover named *Sojourner*, which carried the α–proton x–ray spectrometer. [106, 105, 285]

Profiles of atmospheric density, temperature, and pressure were constructed, along with a best estimate trajectory. Best estimate trajectories were constructed by (1) directly integrating accelerometer data [237, 175, 313, 314], (2) using a linearized Kalman filter applied to both accelerometer data and radar altimeter data [49], and (3) using a combination of accelerometer and altimeter measurements using sequential filtering and smoothing techniques [270, 269].

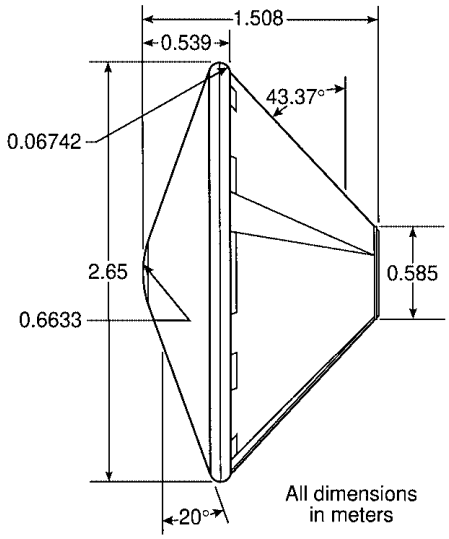

Figure 19: Dimensions of the Mars Pathfinder Aeroshell. [269, 103]

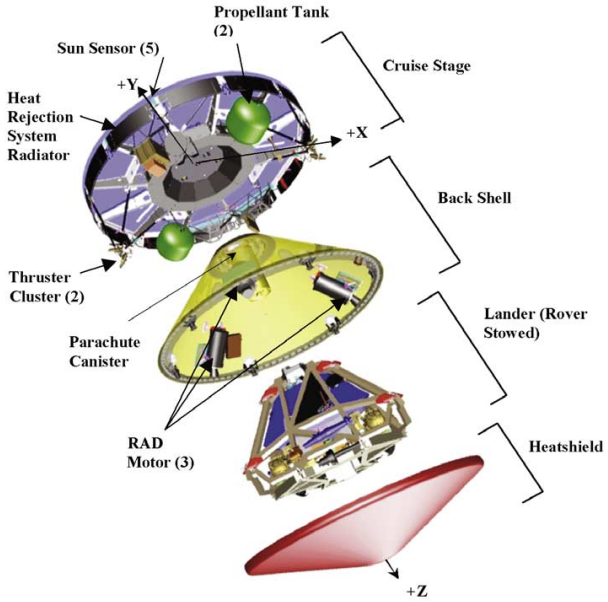

Figure 20: Diagram of the Mars Exploration Rover spacecraft. [53]

Mars Exploration Rovers The Mars Exploration Rover (MER) mission consisted of two identical spacecraft (see Figure 20): Spirit and Opportunity. The Spirit (MER A) spacecraft was launched on June 10, 2003. On January 4, 2004, Spirit landed in Gusev Crater (14.59°S, 175.3°E) on Mars. The Opportunity (MER B) spacecraft was launched on July 7, 2003. On January 25, 2004, Opportunity landed in Meridiani Planum (1.98°S, 5.94°W) on Mars. [70]

Spirit and Opportunity's entry, descent, and landing sequence was similar to that used for the Mars Pathfinder mission. [269] Each spacecraft decelerated with its aeroshell and heatshield, then deployed a supersonic parachute, jettisoned its heatshield, and used retrorockets to minimize its velocity above the surface of Mars. The lander was then separated from the backshell and dropped to the surface protected by airbags (see Figure 21). Once the motion of the lander ceased, the Spirit rover was deployed to make in situ science measurements.

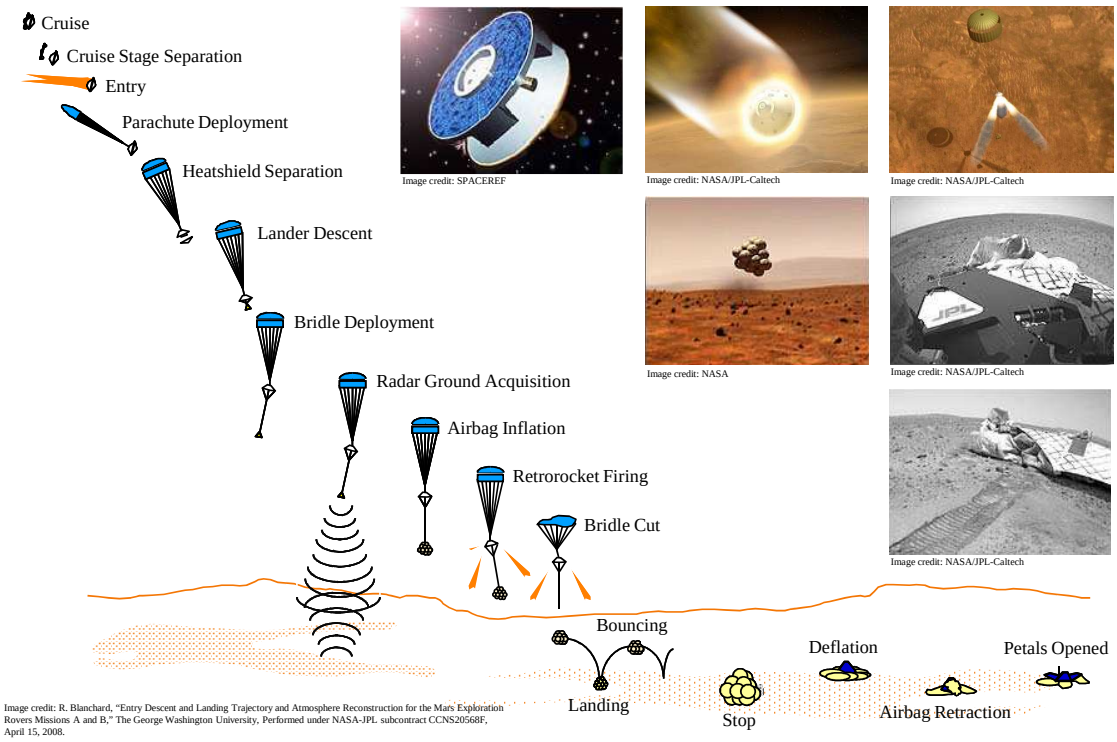

Figure 21: Entry, descent, and landing sequence for the Mars Exploration Rovers. [33]

Each MER spacecraft was equipped with two Litton LN–200S inertial measurement units. One inertial measurement unit was located in the backshell of the spacecraft's aeroshell, and the other inertial measurement unit was located in the rover. [53] Both inertial measurement units included 3–axis accelerometers and gyroscopes. The data obtained by the inertial measurement units has been archived in the NASA Planetary Data System. [148] The inertial measurement units have a dynamical range of 80 g_n ($g_n = 9.80665\ \frac{m}{s^2}$) with a 2.4 mg_n, resolution, and noise levels of 1.6 mg_n. The MER inertial measurement units obtained measurements at a frequency of 400 Hz. This data rate produced more data than the spacecraft could effectively use, so the inertial measurement unit data was summed yielding measurements at an effective frequency of 8 Hz. This change in the effective data rate reduced the effective noise to 300 μg_n. [53] In comparison, the effective noise for the Mars Pathfinder mission

accelerometers was less than 5 mg_n [175].

Post–flight analysis of the Mars Exploration Rover inertial measurement units demonstrated that the y–axis accelerometer was rotated by 0.31528° and the x–axis accelerometer was rotated by 0.10886° relative to the principle body axes. These values were determined such that the attitude oscillation was centered on 0° (no bias in the mean normal acceleration signals) for the oscillations near the parachute deployment condition. The total rotation of the backshell inertial measurement unit axes was $\frac{1}{3}°$. [253]

IMU output processing was performed on the spacecraft for all of the 8 Hz measurements. Due to memory limitations on-board the spacecraft, the frequency of the saved data varied depending on the EDL phase. Some of the transformed data was transmitted to Mars Global Surveyor during the EDL sequence. The radio link between Spirit and Mars Global Surveyor was somewhat intermittent due to the relative motion of the spacecraft and the real–time nature of the data transmission. The interrupted communication caused some of this data to be lost. Fortunately, the data returned during entry, descent, and landing and the stored data sent back after landing are complementary in many cases. Specifically for Spirit, the two data streams were both at 4 Hz, but on alternating 8 Hz timesteps, which resulted in an effective 8 Hz data set (minus the data lost over the radio link). [148] Despite the difficulties in transmitting the inertial measurement unit data, the trajectories were reconstructed using inertial measurement unit data and profiles of atmospheric density, temperature, and pressure were constructed. [312]

To construct the pressure and temperature profiles, a boundary condition at either the top or bottom of the atmosphere must be used. This boundary condition can come from a measurement by a temperature or pressure sensor (which the Mars Exploration Rovers did not have), typically at the bottom of the atmosphere. Alternatively (though more approximate), the pressure at the threshold altitude of the density data

can be estimated by extrapolating the estimated density profile upward assuming a constant scale height (H) (i.e. isothermally) to obtain a boundary condition for the hydrostatic equation at the top of the atmosphere: [250, 243, 247, 245, 175, 312]

$$p_{threshold} = (\rho g H)_{threshold} \tag{10}$$

Post–flight reconstruction revealed anomalistic disturbance torques during the entries of the Mars Exploration Rovers. Due to the accessibility of the remains of Opportunity's aeroshell, the Opportunity rover took pictures of its aeroshell on the surface. These photographs showed that portions of the aeroshell thermal blanket assembly still remained. [287] This blanket assembly was designed to burn off very early in the entry. However, the thermal blanket design was carried over from the Mars Pathfinder mission, which experienced significantly more heating during entry due to Pathfinder's higher entry velocity. [64]

Profiles of atmospheric density, temperature, and pressure were constructed, along with a best estimate trajectory. Best estimate trajectories were constructed by (1) directly integrating accelerometer data with initial condition modifications to match altimeter and landing site measurements [33], (2) using a linearized Kalman filter applied to the accelerometer data [308], and (3) directly integrating accelerometer data coupled with a Monte Carlo analysis[9] to quantify uncertainty [312].[10]

[9]Reference [312] assumed: (1) normally distributed uncertainties for the trajectory, (2) uncertainties in the entry state that were the same as Mars Pathfinder's entry state uncertainties, and (3) a fixed uncertainty of 0.01 $\frac{m}{s^2}$ for the axial acceleration based on an analysis of pre–entry data.

[10]Additionally, reference [61] discusses possible methodologies for use in reconstructing the entry, descent, and landing trajectories of the Mars Exploration Rovers including: least–squares, weighted least–squares, sequential–batch least–squares, and extended Kalman filtering. However, no later papers (references [62, 70, 64, 63]) discuss applying these methods as part of the reconstruction. Reference [62] compares preliminary post-landing reconstruction data such as peak deceleration and the time of heatshield jettison with the pre–flight predictions. Reference [70] discusses pre–mission trajectory analysis. Reference [64] also compares preliminary post-landing reconstruction data such as peak deceleration and the time of heatshield jettison with the pre–flight predictions. And reference [64] discusses each stage of the Mars Exploration Rovers' entry, descent, and landing scenario.

Mars Phoenix Lander The Mars Phoenix Lander (see Figure 22) was launched on August 4, 2007 [255] and landed on Mars on May 25, 2008 [67]. Profiles of atmospheric density, temperature, and pressure were constructed, along with a best estimate trajectory by smoothing the inertial measurement unit data using a moving average and then directly integrating the data. [34, 311]

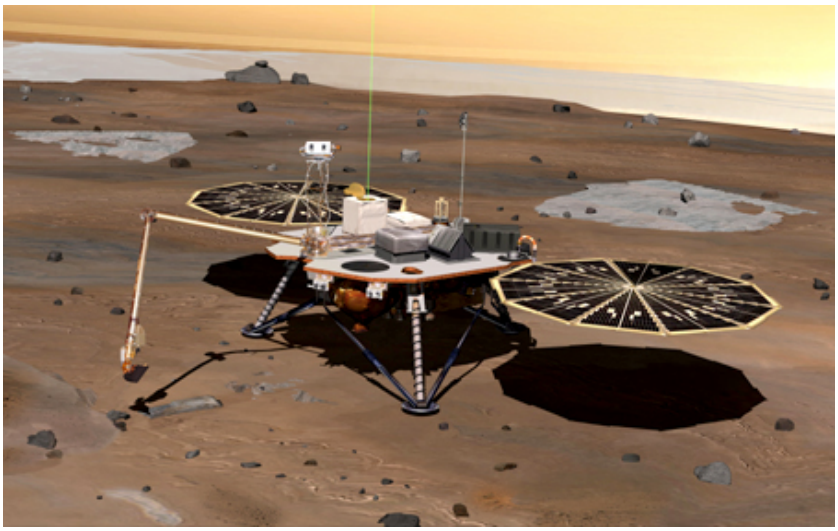

Figure 22: An artist's conception of the Mars Phoenix Lander on the surface of Mars. [Image credit: NASA / JPL]

Table 8: Trajectory reconstruction methods and atmospheric information obtained from several robotic missions performing entry at Mars.

	Mars 6[b]	Viking 1 and 2[c]	Mars Pathfinder[e]	Mars Exploration Rovers[f]	Mars Phoenix Lander[h]
Trajectory Reconstruction Method					
Radar Tracking	✓				
Direct Integration[a]	✓		✓	✓	✓
Kalman Filter		✓	✓	✓	
Atmosphere Reconstruction					
Density Profile	✓	✓	✓	✓	✓
Pressure Profile	✓	✓	✓	✓	✓
Temperature Profile	✓	✓	✓	✓	✓
Winds	✓	✓[d]		✓[g]	✓

[a]If accelerometer data was available for trajectory reconstruction and extended Kalman filtering is not specifically mentioned, it is assumed that direct integration was the method used for trajectory reconstruction.

[b]References [16, 152].

[c]References [243, 79].

[d]Parachute phase winds were also reconstructed in reference [241].

[e]References [237, 175, 269, 313, 314, 49].

[f]References [312, 33, 308].

[g]Atmospheric wind profiles at the time of the Mars Exploration Rover landings were reconstructed in reference [286] using data from the Thermal Emission Spectrometer aboard the Mars Global Surveyor spacecraft.

[h]Reference [34].

2.2.4 Galileo (Jupiter)

The Galileo probe and orbiter were launched by the Space Shuttle *Atlantis* on October 18, 1989 and arrived in the Jovian system on December 7, 1995. The need for an entry probe aspect of the Galileo mission to Jupiter arose in part from an inability to obtain sufficient information by remote sensing to adequately constrain models of formation and evolution of the outer planets. [318] The Galileo probe entered the atmosphere of Jupiter on December 7, 1995 [27], and began directly sampling the Jovian atmosphere at the 0.42 bar pressure level [318] after the descent module had jettisoned the aeroshell (see Figure 23). The probe signal was lost near the 24 bar pressure level at 61.4 minutes after entry. [318] The data collected by the Galileo probe enabled the reconstruction of the trajectory and the atmosphere. Atmospheric profiles

of density, pressure, and temperature were reconstructed using both accelerometer data and in situ measurements made during Galileo's descent on its parachute. [244] Reference [244] does not discuss any data reduction or filtering, so it is assumed that direct integration of the accelerometer data was used to reconstruct the trajectory. Doppler measurements were restricted to the line of sight between the Galileo probe and orbiter [14] and tracking of the probe carrier frequency by the Very Large Array [318]. This data allowed the construction of a wind speed profile between the 0.49 bar and the 24 bar pressure levels. [14, 15]

Figure 23: Aeroshell of the Galileo probe. [Image credit: NASA]

2.2.5 Huygens (Titan)

The Huygens probe (see Figure 24) was built and operated by the European Space Agency as part of the Cassini–Huygens international science mission to the Saturnian system. Cassini–Huygens was launched on October 15, 1997 and entered orbit around Saturn on July 1, 2004. The Huygens probe separated from the Cassini orbiter on December 25, 2004, entered Titan's atmosphere on January 14, 2005, and landed in the Xanadu region. [163]

The atmosphere was first detected at approximately 1500 km when atmospheric

drag exceeded the threshold of sensitivity of the accelerometers in Huygens' atmospheric structure instrument. [95] The data collected by Huygens' atmospheric structure instrument [94] allowed the reconstruction of the probe's trajectory, as well as density, pressure, and temperature profiles by means of (1) direct integration with least squares fitting between the entry and descent phases [151, 149, 165, 13] and (2) Kalman filtering of accelerometer data [1, 277, 279, 150]. A wind profile was constructed using descent imagery [146] from approximately 55 km altitude to the surface of Titan. [288] A wind profile was also constructed using Doppler tracking data [32], and this profile was used to model the spinning, coning, and tilting of Huygens during descent [74].

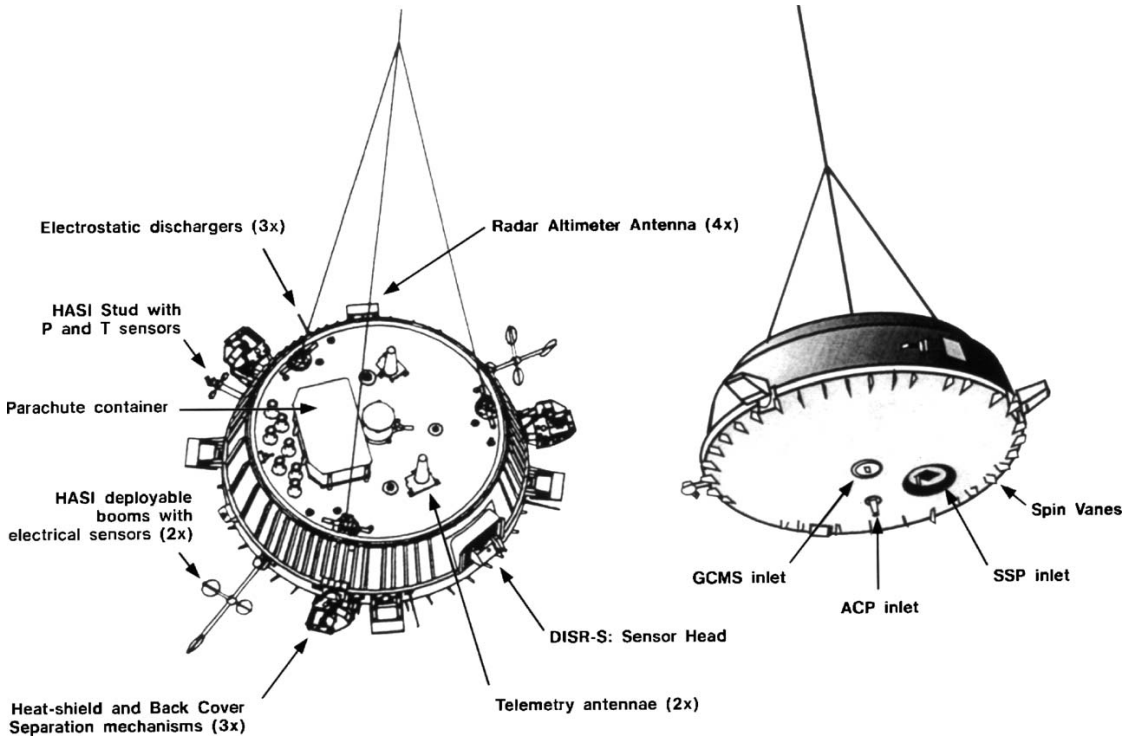

Figure 24: Sensor locations on the Huygens probe. [235]

Table 9: Trajectory reconstruction methods and atmospheric information obtained from several robotic missions performing entry at celestial bodies beyond the Asteroid Belt.

	Galileo[b]	Huygens[d]
Trajectory Reconstruction Method		
Radar Tracking	✓[c]	
Direct Integration[a]		✓
Kalman Filter		✓
Atmosphere Reconstruction		
Density Profile	✓	✓
Pressure Profile	✓	✓
Temperature Profile	✓	✓
Winds	✓	✓

[a]If accelerometer data was available for trajectory reconstruction and extended Kalman filtering is not specifically mentioned, it is assumed that direct integration was the method used for trajectory reconstruction.

[b]Density, pressure, and temperature profiles may be found in reference [244]. The wind profile may be found in reference [14].

[c]Whether or not direct integration or Kalman filtering was used for Galileos trajectory reconstruction is not clear from the literature. In addition to accelerometer data, Doppler tracking data from the Very Large Array was used for reconstruction.

[d]References [95, 150, 1]. A wind profile was constructed using descent imagery in reference [288].

CHAPTER III

STUDY OBJECTIVES AND METHODS

3.1 Study Objectives

This chapter begins with a discussion of the origins of estimation theory including the first great advance by Karl Friedrich Gauss [97] for determining the orbits of celestial bodies. The three branches of estimation are then introduced: (1) smoothing, (2) filtering, and (3) prediction. Some applications of the techniques of estimation to signal processing are then discussed. The Kalman filter (KF) is discussed in detail with emphasis being placed on the extended Kalman filter due to its application to trajectory reconstruction, as discussed in the previous chapter. An alternative Kalman filter for possible application to entry, descent, and landing trajectory reconstruction is then introduced. Then, collocation is discussed along with a formulation for trajectory reconstruction using collocation, as well as trajectory simulation using collocation.

3.2 Estimation

The origin of estimation theory dates back at least to the time of Kepler [102], if not to earlier astronomers, and their attempts to "fit" orbits to celestial observations. However, the analytical tool that was needed to cope with these orbit determination problems did not appear until Gauss [97, 265] presented his least-squares method. [180]

In 1809, the German mathematician Johann Karl Friedrich Gauss wrote his classic treatise *Theoria Motus Corporum Coelestium in Sectionibus Conicis Solem Ambientium* [97] (*Theory of the Motion of the Heavenly Bodies Moving about the Sun in Conic Sections*). In *Theoria Motus*, Gauss made the following statement while discussing

the problem of determining the orbital elements of a celestial body from available measurement data [264]:

> If the astronomical observations and other quantities, on which the computations of orbits is based, were absolutely correct, the elements also, whether deduced from three or four observations, would be strictly accurate (so far indeed as the motion is supposed to take place exactly according to the laws of Kepler), and, therefore, if other observations were used, they might be confirmed, but not corrected. But since all our measurements and observations are nothing more than approximations to the truth, the same must be true of all calculations resting upon them, and the highest aim of all computations made concerning concrete phenomena must be to approximate, as nearly as practicable, to the truth. But this can be accomplished in no other way than by a suitable combination of more observations than the number absolutely requisite for the determination of the unknown quantities. This problem can only be properly undertaken when an approximate knowledge of the orbit has been already attained, which is afterwards to be corrected so as to satisfy all the observations in the most accurate manner possible. [97]

The next notable advances in estimation theory came in 1941 from Kolmogorov [158] and in 1949 from Wiener [309]. Though Wiener's theory was extended by Zadeh in 1950 [320], later work was greatly stimulated in large measure by the filter theory results of Swerling in 1959 [281, 280], Kalman in 1960[1] and 1961 [143, 144], and Kalman and Bucy in 1961 [145]. The work of Kalman has made the greatest impact on estimation theory for both the discrete and continuous time problems. Kalman (and later, Kalman in collaboration with Bucy) treated the filtering and prediction

[1] Stratonovich in 1960 also independently obtained the Kalman filter equations. [275, 276, 142]

problems in detail, and they laid the foundation for further work in smoothing. [180]

The following paragraphs discuss three aspects of estimation: (1) smoothing, (2) filtering, and (3) prediction. They are included for the reader's information, so that they are aware that estimation is broader than the sequential filtering used in this research. For the trajectory reconstruction work in this research, sequential filtering is used, as this is useful for both post–processing of data and real–time processing of data.

Smoothing Smoothing is the process of estimating the state of a system within the time span of measured data. The estimate of the state is generally based on all the measurements available. Three types of smoothing are of interest:[2]

1. In **fixed–interval smoothing**, the time span of the data is fixed, and the estimate of the state is sought for specified times within the fixed time interval of the data. For example, suppose that for some state, measurements span a 10–second period (from 0 seconds to 10 seconds). No new measurements are made, and an estimate of the state for any time from 0 to 10 seconds is made using the 10 seconds of data.

2. In **fixed–point smoothing**, the point in time at which the estimate of the state is sought is fixed. The accumulation of new data may increase the time span of the data. For example, suppose that for some state, measurements are taken every second. Initially the data spanned 10 seconds (from 0 seconds to 10 seconds). Also, suppose the point in time at which an estimate of the state is desired is the 5 second point. The first estimate of the state is made using the initial 10 seconds of data. When the next measurement is taken at 11 seconds, the estimate of the state at the time of 5 seconds will be updated.

[2]These definitions of the different types of smoothing have been taken from reference [109].

The estimate of the state at the time of 5 seconds continues to be updated as new measurements accumulate.

3. In **fixed–lag smoothing**, estimates of the state are sought at some time that is a fixed amount (the *fixed-lag*) from the end of the time span. All the measurements are used to calculate the estimate. As new measurements are accumulated (i.e. the time span of the measurements increases), the estimates of the state are computed for times that are still a fixed amount of time from the end of the time span. For example, suppose that for some state, measurements initially spanned 10 seconds (from 0 seconds to 10 seconds) with a measurement made at each second. If the lag is 2 seconds, then the first estimate of the state will be calculated for the time of 8 seconds. When the first new measurement is taken one second later, the second estimate will be for the time of 9 seconds (with 11 seconds of data). The third estimate will be for the time of 10 seconds (with 12 seconds of data), and so on.

For smoothing, the optimal filter consists of two filters: the forward filter and the backward filter. [98, 213] The forward filter smooths the data from the initial time to the time of interest, while the backward filter smooths the data from the end of the time span to the time of interest. Each filter produces an estimate of the state at the specified time. Together these filters use all the data to estimate the state of the system at the specified time. The forward and backward estimates of the state at the specified time have uncorrelated errors since the process noise and measurement noise are both assumed to be *white noise*[3]. A combination of the forward and backward estimates (which meets a specified set of conditions defining optimality) yields what is termed "the optimal estimate" of the state at the specified time. [98]

[3] *White noise* is defined to be a stationary random process having a constant spectral density function. The term "white" is a carryover from optics, where *white light* is light containing all visible frequencies. [39]

Filtering Filtering is the process of estimating the state of a system at the time of the last measurement made of the system. Filtering is most useful for removing extraneous noise from a signal.

Prediction Prediction is the process of estimating the state of a system after the time of the last measurement made of the system. Prediction is most useful when measurements of a system's state cannot be made.

3.2.1 The Kalman Filter

Harold Sorenson has asserted "that the Kalman filter represents the most widely applied and demonstrably useful result to emerge from ... 'modern control theory'." [266] Put forth in 1960 [143], the Kalman filter is an optimal, recursive filter for linear systems that does not require the storage of all past data. An update of the state estimate of a system only requires the previously calculated estimate of the state and the new measurements. [115] This makes the Kalman filter computationally efficient. The following paragraphs will describe the Kalman filter[4] and setup the discussion of the nonlinear versions of the Kalman filter.

The State Vector and the Process and Measurement Equations The state of a system is a vector $\mathbf{x}_k$ which describes the motion of a system at a specific point in time. (The subscript k denotes a discrete time point.) Typically, the state $\mathbf{x}_k$ is unknown, so we use a set of measurements (or observations) $\mathbf{y}_k$ to estimate it. Given an initial state $\mathbf{x}_0$, future states can be found using the *process equation*:

$$\mathbf{x}_{k+1} = \mathbf{\Phi}_{k+1,k}\mathbf{x}_k + \mathbf{w}_k \tag{11}$$

[4]This discussion of the Kalman filter is an expanded combination (with more mathematical detail) of the discussions found in references [116] and [99]. There are lots of ways to derive the Kalman filter [228, 278] (see, for instance, References [282], [307], [5], [162], [223], and [40]).

where $\mathbf{\Phi}_{k+1,k}$ is the *state transition matrix* taking the state $\mathbf{x}_k$ from time k to time $k+1$. The process noise $\mathbf{w}_k$ is assumed to be additive, white, and Gaussian, with zero mean and with a covariance matrix defined by

$$E[\mathbf{w}_n \mathbf{w}_k^T] = \begin{cases} \mathbf{Q}_k & n = k \\ \mathbf{0} & n \neq k \end{cases} \tag{12}$$

The measurements (or observations) $\mathbf{y}_k$ can be expressed as a function of the state $\mathbf{x}_k$ using the *measurement equation*:

$$\mathbf{y}_k = \mathbf{H}_k \mathbf{x}_k + \mathbf{v}_k \tag{13}$$

where $\mathbf{y}_k$ is the measurement at time k and $\mathbf{H}_k$ is the *measurement matrix*. The measurement noise $\mathbf{v}_k$ is assumed to be additive, white, and Gaussian, with zero mean and with a covariance matrix defined by

$$E[\mathbf{v}_n \mathbf{v}_k^T] = \begin{cases} \mathbf{R}_k & n = k \\ \mathbf{0} & n \neq k \end{cases} \tag{14}$$

In addition, the measurement noise $\mathbf{v}_k$ is uncorrelated with the process noise $\mathbf{w}_k$.

The Kalman filtering problem consists of jointly solving the process and measurement equations for the unknown state in an optimum manner. Suppose that a measurement $\mathbf{y}_k$ on a linear dynamical system, described by equations (11) and (13), has been made at time k. The information contained in the new measurement $\mathbf{y}_k$ can be used to update the estimate of the state $\mathbf{x}_k$.

The Estimate of the State Let $\hat{\mathbf{x}}_k^-$ denote the *a priori* estimate of the state (i.e. the estimate of the state *before* the measurement was made) that is already available at time k. With a linear estimator as the objective, we may express the *a posteriori* estimate $\hat{\mathbf{x}}_k$ (i.e. the estimate of the state *after* the measurement was made) as a

linear combination of the *a priori* estimate $\hat{\mathbf{x}}_k^-$ and the new measurement $\mathbf{y}_k$ as

$$\hat{\mathbf{x}}_k = \mathbf{J}_k \hat{\mathbf{x}}_k^- + \mathbf{K}_k \mathbf{y}_k \tag{15}$$

where the multiplying matrix factors $\mathbf{J}_k$ and $\mathbf{K}_k$ are to be determined. Graphically, the *a priori* estimate of the state $\hat{\mathbf{x}}_k^-$ and the *a posteriori* estimate of the state $\hat{\mathbf{x}}_k$ are depicted in Figure 25. To find these two matrices, we first define the *a priori* and *a posteriori state–error vectors* ($\tilde{\mathbf{x}}_k^-$ and $\tilde{\mathbf{x}}_k$, respectively) as

$$\tilde{\mathbf{x}}_k^- = \mathbf{x}_k - \hat{\mathbf{x}}_k^- \tag{16}$$

$$\tilde{\mathbf{x}}_k = \mathbf{x}_k - \hat{\mathbf{x}}_k \tag{17}$$

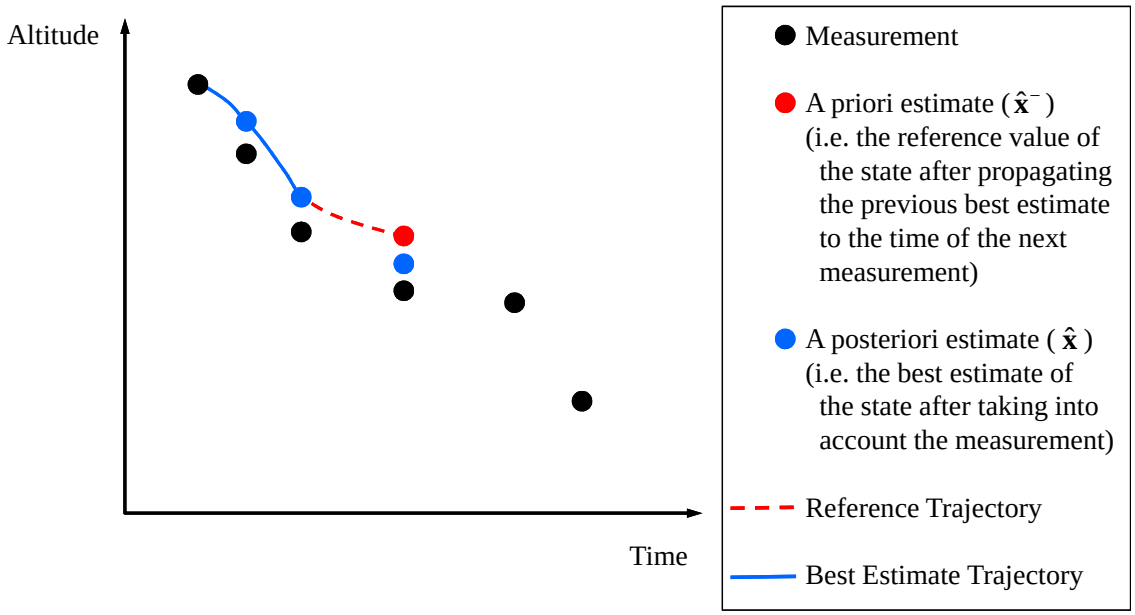

Figure 25: Graphical depiction of the *a priori* estimate of the state, the *a posteriori* estimate of the state, the reference trajectory, and the best estimate trajectory.

Second, we solve equation (16) for the *a priori* state estimate and substitute it into equation (15). Doing this, we have

$$\hat{\mathbf{x}}_k = \mathbf{J}_k\hat{\mathbf{x}}_k^- + \mathbf{K}_k\mathbf{y}_k \tag{18a}$$

$$= \mathbf{J}_k(\mathbf{x}_k - \tilde{\mathbf{x}}_k^-) + \mathbf{K}_k\mathbf{y}_k \tag{18b}$$

$$\hat{\mathbf{x}}_k = \mathbf{J}_k\mathbf{x}_k - \mathbf{J}_k\tilde{\mathbf{x}}_k^- + \mathbf{K}_k\mathbf{y}_k \tag{18c}$$

Third, we substitute the measurement equation (equation (13)) into equation (18c) for the measurement $\mathbf{y}_k$ giving

$$\hat{\mathbf{x}}_k = \mathbf{J}_k\mathbf{x}_k - \mathbf{J}_k\tilde{\mathbf{x}}_k^- + \mathbf{K}_k\mathbf{y}_k \tag{19a}$$

$$= \mathbf{J}_k\mathbf{x}_k - \mathbf{J}_k\tilde{\mathbf{x}}_k^- + \mathbf{K}_k(\mathbf{H}_k\mathbf{x}_k + \mathbf{v}_k) \tag{19b}$$

$$\hat{\mathbf{x}}_k = \mathbf{J}_k\mathbf{x}_k + \mathbf{K}_k\mathbf{H}_k\mathbf{x}_k - \mathbf{J}_k\tilde{\mathbf{x}}_k^- + \mathbf{K}_k\mathbf{v}_k \tag{19c}$$

Fourth, we substitute this expression (equation (19c)) for the *a posteriori* estimate of the state $\hat{\mathbf{x}}_k$ into the *a posteriori* state–error vector ($\tilde{\mathbf{x}}_k$ as given in equation (17)) giving

$$\tilde{\mathbf{x}}_k = \mathbf{x}_k - \hat{\mathbf{x}}_k \tag{20a}$$

$$= \mathbf{x}_k - (\mathbf{J}_k\mathbf{x}_k + \mathbf{K}_k\mathbf{H}_k\mathbf{x}_k - \mathbf{J}_k\tilde{\mathbf{x}}_k^- + \mathbf{K}_k\mathbf{v}_k) \tag{20b}$$

$$= \mathbf{x}_k - \mathbf{J}_k\mathbf{x}_k - \mathbf{K}_k\mathbf{H}_k\mathbf{x}_k + \mathbf{J}_k\tilde{\mathbf{x}}_k^- - \mathbf{K}_k\mathbf{v}_k \tag{20c}$$

$$\tilde{\mathbf{x}}_k = \mathbf{x}_k(\mathbf{I} - \mathbf{J}_k - \mathbf{K}_k\mathbf{H}_k) + \mathbf{J}_k\tilde{\mathbf{x}}_k^- - \mathbf{K}_k\mathbf{v}_k \tag{20d}$$

Fifth, we examine the expectation of the inner product of the *a posteriori* state–error vector $\tilde{\mathbf{x}}_k$ and the measurements $\mathbf{y}_i^T$: $E[\tilde{\mathbf{x}}_k\mathbf{y}_i^T]$. We know, by the principle of orthogonality (given below), that

$$E[\tilde{\mathbf{x}}_k\mathbf{y}_i^T] = \mathbf{0} \text{ for } i = 1, 2, ..., k-1 \tag{21}$$

since the *a posteriori* state–error vector $\tilde{\mathbf{x}}_k$ is defined as the difference between the

state $\mathbf{x}_k$ and the *a posteriori* state estimate $\hat{\mathbf{x}}_k$, and the *a posteriori* state estimate $\hat{\mathbf{x}}_k$ is contained in the space spanned by the measurements $(\mathbf{y}_1, \mathbf{y}_2, ..., \mathbf{y}_k)$. Therefore, the *a posteriori* state–error vector $\tilde{\mathbf{x}}_k$ must be orthogonal to the space spanned by the measurements $(\mathbf{y}_1, \mathbf{y}_2, ..., \mathbf{y}_i$ for $i = 1, 2, ..., k-1)$, and so the inner product of the *a posteriori* state–error vector $\tilde{\mathbf{x}}_k$ and the measurements $(\mathbf{y}_1, \mathbf{y}_2, ..., \mathbf{y}_i$ for $i = 1, 2, ..., k-1)$ is zero.

Principle of Orthogonality Let the stochastic processes $\{\mathbf{x}_k\}$ and $\{\mathbf{y}_k\}$ be of zero means, that is

$$E[\mathbf{x}_k] = 0 \text{ for all } k$$

$$E[\mathbf{y}_k] = 0 \text{ for all } k$$

If either

1. the stochastic process $\{\mathbf{x}_k\}$ and $\{\mathbf{y}_k\}$ are jointly Gaussian, or
2. the optimal estimate $\hat{\mathbf{x}}_k$ is restricted to be a linear function of the measurements, and the cost function is the mean–square error

then the optimum estimate $\hat{\mathbf{x}}_k$, given the measurements $\mathbf{y}_1, \mathbf{y}_2, ..., \mathbf{y}_k$, is the orthogonal projection of $\mathbf{x}_k$ onto the space spanned by the measurements.

Sixth, expanding the expectation given in equation (21) by substituting in equation (20d) for the *a posteriori* state–error vector $\tilde{\mathbf{x}}_k$, we have

$$E[\tilde{\mathbf{x}}_k \mathbf{y}_i^T] = E[(\mathbf{x}_k(\mathbf{I} - \mathbf{J}_k - \mathbf{K}_k\mathbf{H}_k) + \mathbf{J}_k\tilde{\mathbf{x}}_k^- - \mathbf{K}_k\mathbf{v}_k)\mathbf{y}_i^T] \tag{22a}$$

$$\mathbf{0} = E[\mathbf{x}_k\mathbf{y}_i^T(\mathbf{I} - \mathbf{J}_k - \mathbf{K}_k\mathbf{H}_k) + \mathbf{J}_k\tilde{\mathbf{x}}_k^-\mathbf{y}_i^T - \mathbf{K}_k\mathbf{v}_k\mathbf{y}_i^T] \tag{22b}$$

$$\mathbf{0} = E[\mathbf{x}_k\mathbf{y}_i^T(\mathbf{I} - \mathbf{J}_k - \mathbf{K}_k\mathbf{H}_k)] + E[\mathbf{J}_k\tilde{\mathbf{x}}_k^-\mathbf{y}_i^T] - E[\mathbf{K}_k\mathbf{v}_k\mathbf{y}_i^T] \tag{22c}$$

$$\mathbf{0} = (\mathbf{I} - \mathbf{J}_k - \mathbf{K}_k\mathbf{H}_k)E[\mathbf{x}_k\mathbf{y}_i^T] + \mathbf{J}_kE[\tilde{\mathbf{x}}_k^-\mathbf{y}_i^T] - \mathbf{K}_kE[\mathbf{v}_k\mathbf{y}_i^T] \tag{22d}$$

Now, we substitute in the measurement equation (equation (13)) into the last term of equation (22d) for the measurement $\mathbf{y}_i$ giving

$$\mathbf{0} = (\mathbf{I} - \mathbf{J}_k - \mathbf{K}_k\mathbf{H}_k)E[\mathbf{x}_k\mathbf{y}_i^T] + \mathbf{J}_kE[\tilde{\mathbf{x}}_k^-\mathbf{y}_i^T] - \mathbf{K}_kE[\mathbf{v}_k\mathbf{y}_i^T] \tag{23a}$$

$$\mathbf{0} = (\mathbf{I} - \mathbf{J}_k - \mathbf{K}_k\mathbf{H}_k)E[\mathbf{x}_k\mathbf{y}_i^T] + \mathbf{J}_kE[\tilde{\mathbf{x}}_k^-\mathbf{y}_i^T] - \mathbf{K}_kE[\mathbf{v}_k(\mathbf{H}_i\mathbf{x}_i + \mathbf{v}_i)^T] \tag{23b}$$

$$\mathbf{0} = (\mathbf{I} - \mathbf{J}_k - \mathbf{K}_k\mathbf{H}_k)E[\mathbf{x}_k\mathbf{y}_i^T] + \mathbf{J}_kE[\tilde{\mathbf{x}}_k^-\mathbf{y}_i^T] - \mathbf{K}_kE[\mathbf{v}_k\mathbf{H}_i\mathbf{x}_i^T] + \mathbf{K}_kE[\mathbf{v}_k\mathbf{v}_i^T] \tag{23c}$$

Examining the last term in equation (23c), we note that $E[\mathbf{v}_k\mathbf{v}_i^T] = 0$ by equation (14), which reduces equation (23c) to

$$\mathbf{0} = (\mathbf{I} - \mathbf{J}_k - \mathbf{K}_k\mathbf{H}_k)E[\mathbf{x}_k\mathbf{y}_i^T] + \mathbf{J}_kE[\tilde{\mathbf{x}}_k^-\mathbf{y}_i^T] - \mathbf{K}_kE[\mathbf{v}_k\mathbf{H}_i\mathbf{x}_i^T] \tag{24}$$

Examining the last term in equation (24), we note that there is no expectation that the meaurement noise is correlated with the process, so $E[\mathbf{v}_k\mathbf{H}_i\mathbf{x}_i^T] = 0$, and this reduces equation (24) to

$$\mathbf{0} = (\mathbf{I} - \mathbf{J}_k - \mathbf{K}_k\mathbf{H}_k)E[\mathbf{x}_k\mathbf{y}_i^T] + \mathbf{J}_kE[\tilde{\mathbf{x}}_k^-\mathbf{y}_i^T] \tag{25}$$

By invoking the principle of orthogonality again as we did for equation (21), the expectation in the last term of equation (25) becomes equal to zero: $E[\tilde{\mathbf{x}}_k^-\mathbf{y}_i^T] = 0$, and we have

$$\mathbf{0} = (\mathbf{I} - \mathbf{J}_k - \mathbf{K}_k\mathbf{H}_k)E[\mathbf{x}_k\mathbf{y}_i^T] \tag{26}$$

Since equation (26) is true by orthogonality and $E[\mathbf{x}_k \mathbf{y}_i^T] \neq 0$, the multiplying matrix factors $\mathbf{J}_k$ and $\mathbf{K}_k$ must satisfy the condition

$$\mathbf{0} = \mathbf{I} - \mathbf{J}_k - \mathbf{K}_k \mathbf{H}_k \tag{27}$$

Hence, we may express $\mathbf{J}_k$ as a function of $\mathbf{K}_k$

$$\mathbf{J}_k = \mathbf{I} - \mathbf{K}_k \mathbf{H}_k \tag{28}$$

and by substituting this condition on the multiplying matrix factors into equation (15), we now have for the *a posteriori* estimate of the state

$$\hat{\mathbf{x}}_k = \mathbf{J}_k \hat{\mathbf{x}}_k^- + \mathbf{K}_k \mathbf{y}_k \tag{29a}$$

$$= (\mathbf{I} - \mathbf{K}_k \mathbf{H}_k) \hat{\mathbf{x}}_k^- + \mathbf{K}_k \mathbf{y}_k \tag{29b}$$

$$= \hat{\mathbf{x}}_k^- - \mathbf{K}_k \mathbf{H}_k \hat{\mathbf{x}}_k^- + \mathbf{K}_k \mathbf{y}_k \tag{29c}$$

$$\hat{\mathbf{x}}_k = \hat{\mathbf{x}}_k^- + \mathbf{K}_k \mathbf{y}_k - \mathbf{K}_k \mathbf{H}_k \hat{\mathbf{x}}_k^- \tag{29d}$$

which we finally reduce to

$$\hat{\mathbf{x}}_k = \hat{\mathbf{x}}_k^- + \mathbf{K}_k (\mathbf{y}_k - \mathbf{H}_k \hat{\mathbf{x}}_k^-) \tag{30}$$

and we call the multiplying matrix factor $\mathbf{K}_k$ the *Kalman gain.*

The Kalman Gain We would like to define the Kalman gain $\mathbf{K}_k$ such that the trace of the error covariance matrix $\mathbf{P}_k$ is minimized. This is equivalent to minimizing the length of the state–error vector. To do this, we must first obtain an expression for the error covariance matrix $\mathbf{P}_k$, so we can minimize its trace. The error covariance matrix $\mathbf{P}_k$ is defined as

$$\mathbf{P}_k = E[\tilde{\mathbf{x}}_k \tilde{\mathbf{x}}_k^T] \tag{31}$$

We know the definition of the *a posteriori* state–error vector $\tilde{\mathbf{x}}_k$ from equation (17). However, in order to define an expression for the error covariance matrix $\mathbf{P}_k$, it is easier to start with equation (20d) and substitute in the expression for the multiplying matrix factor $\mathbf{J}_k$ from equation (28). Doing this, we have

$$\tilde{\mathbf{x}}_k = \mathbf{x}_k(\mathbf{I} - \mathbf{J}_k - \mathbf{K}_k\mathbf{H}_k) + \mathbf{J}_k\tilde{\mathbf{x}}_k^- - \mathbf{K}_k\mathbf{v}_k \tag{32a}$$

$$= \mathbf{x}_k(\mathbf{I} - (\mathbf{I} - \mathbf{K}_k\mathbf{H}_k) - \mathbf{K}_k\mathbf{H}_k) + (\mathbf{I} - \mathbf{K}_k\mathbf{H}_k)\tilde{\mathbf{x}}_k^- - \mathbf{K}_k\mathbf{v}_k \tag{32b}$$

$$= \mathbf{x}_k(\mathbf{I} - \mathbf{I} + \mathbf{K}_k\mathbf{H}_k - \mathbf{K}_k\mathbf{H}_k) + (\mathbf{I} - \mathbf{K}_k\mathbf{H}_k)\tilde{\mathbf{x}}_k^- - \mathbf{K}_k\mathbf{v}_k \tag{32c}$$

$$= \mathbf{x}_k \cdot \mathbf{0} + (\mathbf{I} - \mathbf{K}_k\mathbf{H}_k)\tilde{\mathbf{x}}_k^- - \mathbf{K}_k\mathbf{v}_k \tag{32d}$$

$$\tilde{\mathbf{x}}_k = (\mathbf{I} - \mathbf{K}_k\mathbf{H}_k)\tilde{\mathbf{x}}_k^- - \mathbf{K}_k\mathbf{v}_k \tag{32e}$$

Substituting equation (32e) into the error covariance matrix $\mathbf{P}_k$ definition (equation (31)), we have

$$\mathbf{P}_k = E[\tilde{\mathbf{x}}_k\tilde{\mathbf{x}}_k^T] \tag{33a}$$

$$= E[\{(\mathbf{I} - \mathbf{K}_k\mathbf{H}_k)\tilde{\mathbf{x}}_k^- - \mathbf{K}_k\mathbf{v}_k\}\{(\mathbf{I} - \mathbf{K}_k\mathbf{H}_k)\tilde{\mathbf{x}}_k^- - \mathbf{K}_k\mathbf{v}_k\}^T] \tag{33b}$$

$$\begin{aligned} = E[&(\mathbf{I} - \mathbf{K}_k\mathbf{H}_k)\tilde{\mathbf{x}}_k^-(\tilde{\mathbf{x}}_k^-)^T(\mathbf{I} - \mathbf{K}_k\mathbf{H}_k)^T \\ &- \mathbf{K}_k\mathbf{v}_k(\tilde{\mathbf{x}}_k^-)^T(\mathbf{I} - \mathbf{K}_k\mathbf{H}_k)^T \\ &- (\mathbf{I} - \mathbf{K}_k\mathbf{H}_k)\tilde{\mathbf{x}}_k^-\mathbf{v}_k^T\mathbf{K}_k^T \\ &+ \mathbf{K}_k\mathbf{v}_k\mathbf{v}_k^T\mathbf{K}_k^T] \end{aligned} \tag{33c}$$

$$\begin{aligned} = (\mathbf{I} - \mathbf{K}_k\mathbf{H}_k)&\cdot E[\tilde{\mathbf{x}}_k^-(\tilde{\mathbf{x}}_k^-)^T]\cdot(\mathbf{I} - \mathbf{K}_k\mathbf{H}_k)^T \\ &- \mathbf{K}_k\cdot E[\mathbf{v}_k(\tilde{\mathbf{x}}_k^-)^T]\cdot(\mathbf{I} - \mathbf{K}_k\mathbf{H}_k)^T \\ &- (\mathbf{I} - \mathbf{K}_k\mathbf{H}_k)\cdot E[\tilde{\mathbf{x}}_k^-\mathbf{v}_k^T]\cdot\mathbf{K}_k^T \\ &+ \mathbf{K}_k\cdot E[\mathbf{v}_k\mathbf{v}_k^T]\cdot\mathbf{K}_k^T \end{aligned} \tag{33d}$$

By definition

$$\mathbf{P}_k^- = E\left[\tilde{\mathbf{x}}_k^-(\tilde{\mathbf{x}}_k^-)^T\right] \tag{34}$$

and from equation (14), we know

$$E\left[\mathbf{v}_k\mathbf{v}_k^T\right] = \mathbf{R}_k \tag{35}$$

Additionally, we have no expectation that the measurement noise $\mathbf{v}_k$ is correlated with the *a priori* state–error vector $\tilde{\mathbf{x}}_k^-$, so

$$E\left[\tilde{\mathbf{x}}_k^-\mathbf{v}_k^T\right] = \mathbf{0} \tag{36a}$$

$$E\left[\mathbf{v_k}(\tilde{\mathbf{x}}_k^-)^T\right] = \mathbf{0} \tag{36b}$$

Using equations (34), (35), (36a), and (36b), we have for the error covariance matrix $\mathbf{P}_k$

$$\mathbf{P}_k = E\left[\tilde{\mathbf{x}}_k\tilde{\mathbf{x}}_k^T\right] \tag{37a}$$

$$\begin{aligned}
&= (\mathbf{I}-\mathbf{K}_k\mathbf{H}_k)\cdot E[\tilde{\mathbf{x}}_k^-(\tilde{\mathbf{x}}_k^-)^T]\cdot(\mathbf{I}-\mathbf{K}_k\mathbf{H}_k)^T \\
&\quad - \mathbf{K}_k\cdot E[\mathbf{v}_k(\tilde{\mathbf{x}}_k^-)^T]\cdot(\mathbf{I}-\mathbf{K}_k\mathbf{H}_k)^T \\
&\quad - (\mathbf{I}-\mathbf{K}_k\mathbf{H}_k)\cdot E[\tilde{\mathbf{x}}_k^-\mathbf{v}_k^T]\cdot\mathbf{K}_k^T \\
&\quad + \mathbf{K}_k\cdot E[\mathbf{v}_k\mathbf{v}_k^T]\cdot\mathbf{K}_k^T
\end{aligned} \tag{37b}$$

$$\begin{aligned}
&= (\mathbf{I}-\mathbf{K}_k\mathbf{H}_k)\cdot\mathbf{P}_k^-\cdot(\mathbf{I}-\mathbf{K}_k\mathbf{H}_k)^T \\
&\quad - \mathbf{K}_k\cdot\mathbf{0}\cdot(\mathbf{I}-\mathbf{K}_k\mathbf{H}_k)^T \\
&\quad - (\mathbf{I}-\mathbf{K}_k\mathbf{H}_k)\cdot\mathbf{0}\cdot\mathbf{K}_k^T \\
&\quad + \mathbf{K}_k\cdot\mathbf{R}_k\cdot\mathbf{K}_k^T
\end{aligned} \tag{37c}$$

$$\mathbf{P}_k = (\mathbf{I}-\mathbf{K}_k\mathbf{H}_k)\mathbf{P}_k^-(\mathbf{I}-\mathbf{K}_k\mathbf{H}_k)^T + \mathbf{K}_k\mathbf{R}_k\mathbf{K}_k^T \tag{37d}$$

To minimize the trace of the error covariance matrix $\mathbf{P}_k$, we must take the partial

derivative of the trace of the error covariance matrix $\mathbf{P}_k$ with respect to the Kalman gain $\mathbf{K}_k$, equate it to zero, and solve for the Kalman gain $\mathbf{K}_k$.

$$\frac{\partial}{\partial \mathbf{K}_k}[\text{trace}(\mathbf{P}_k)] = \mathbf{0} \tag{38a}$$

$$\frac{\partial}{\partial \mathbf{K}_k}[\text{trace}(\mathbf{P}_k)] = \frac{\partial}{\partial \mathbf{K}_k}[\text{trace}\{(\mathbf{I} - \mathbf{K}_k\mathbf{H}_k)\mathbf{P}_k^-(\mathbf{I} - \mathbf{K}_k\mathbf{H}_k)^T + \mathbf{K}_k\mathbf{R}_k\mathbf{K}_k^T\}] \tag{38b}$$

$$\mathbf{0} = 2(\mathbf{I} - \mathbf{K}_k\mathbf{H}_k)\mathbf{P}_k^- \frac{\partial}{\partial \mathbf{K}_k}\left[\text{trace}\left\{(\mathbf{I} - \mathbf{K}_k\mathbf{H}_k)^T\right\}\right] + 2\mathbf{K}_k\mathbf{R}_k \tag{38c}$$

$$\mathbf{0} = -2(\mathbf{I} - \mathbf{K}_k\mathbf{H}_k)\mathbf{P}_k^-\mathbf{H}_k^T + 2\mathbf{K}_k\mathbf{R}_k \tag{38d}$$

$$\mathbf{0} = -(\mathbf{I} - \mathbf{K}_k\mathbf{H}_k)\mathbf{P}_k^-\mathbf{H}_k^T + \mathbf{K}_k\mathbf{R}_k \tag{38e}$$

$$\mathbf{0} = -\mathbf{P}_k^-\mathbf{H}_k^T + \mathbf{K}_k\mathbf{H}_k\mathbf{P}_k^-\mathbf{H}_k^T + \mathbf{K}_k\mathbf{R}_k \tag{38f}$$

$$\mathbf{P}_k^-\mathbf{H}_k^T = \mathbf{K}_k\mathbf{H}_k\mathbf{P}_k^-\mathbf{H}_k^T + \mathbf{K}_k\mathbf{R}_k \tag{38g}$$

$$\mathbf{P}_k^-\mathbf{H}_k^T = \mathbf{K}_k(\mathbf{H}_k\mathbf{P}_k^-\mathbf{H}_k^T + \mathbf{R}_k) \tag{38h}$$

$$\mathbf{K}_k = \mathbf{P}_k^-\mathbf{H}_k^T(\mathbf{H}_k\mathbf{P}_k^-\mathbf{H}_k^T + \mathbf{R}_k)^{-1} \tag{38i}$$

The value of the Kalman gain $\mathbf{K}_k$ given by equation (38i) minimizes the trace of the error covariance matrix $\mathbf{P}_k$, which is equivalent to minimizing the length of the *a posteriori* state–error vector $\tilde{\mathbf{x}}_k$.

The Error Covariance Update We can use the optimal Kalman gain $\mathbf{K}_k$ given by equation (38i) along with equation (37d) to obtain a simplified expression for the error covariance matrix $\mathbf{P}_k$. To do this, we first show that the $\mathbf{K}_k\mathbf{R}_k\mathbf{K}_k$ term in equation (37d) is equivalent to $(\mathbf{I} - \mathbf{K}_k\mathbf{H}_k)\mathbf{P}_k^-(\mathbf{K}_k\mathbf{H}_k)^T$. Beginning with the optimal Kalman gain $\mathbf{K}_k$ from equation (38i), we post–multiply by $(\mathbf{H}_k\mathbf{P}_k^-\mathbf{H}_k^T + \mathbf{R}_k)\mathbf{K}_k^T$, [5] and we have

$$\mathbf{K}_k = \mathbf{P}_k^- \mathbf{H}_k^T (\mathbf{H}_k \mathbf{P}_k^- \mathbf{H}_k^T + \mathbf{R}_k)^{-1} \tag{39a}$$

$$\mathbf{K}_k (\mathbf{H}_k \mathbf{P}_k^- \mathbf{H}_k^T + \mathbf{R}_k) \mathbf{K}_k^T = \mathbf{P}_k^- \mathbf{H}_k^T (\mathbf{H}_k \mathbf{P}_k^- \mathbf{H}_k^T + \mathbf{R}_k)^{-1} (\mathbf{H}_k \mathbf{P}_k^- \mathbf{H}_k^T + \mathbf{R}_k) \mathbf{K}_k^T \tag{39b}$$

$$\mathbf{K}_k \mathbf{H}_k \mathbf{P}_k^- \mathbf{H}_k^T \mathbf{K}_k^T + \mathbf{K}_k \mathbf{R}_k \mathbf{K}_k = \mathbf{P}_k^- \mathbf{H}_k^T \mathbf{K}_k^T \tag{39c}$$

$$\mathbf{K}_k \mathbf{R}_k \mathbf{K}_k = -\mathbf{K}_k \mathbf{H}_k \mathbf{P}_k^- \mathbf{H}_k^T \mathbf{K}_k^T + \mathbf{P}_k^- \mathbf{H}_k^T \mathbf{K}_k^T \tag{39d}$$

$$= \mathbf{P}_k^- \mathbf{H}_k^T \mathbf{K}_k^T - \mathbf{K}_k \mathbf{H}_k \mathbf{P}_k^- \mathbf{H}_k^T \mathbf{K}_k^T \tag{39e}$$

$$= \mathbf{P}_k^- (\mathbf{K}_k \mathbf{H}_k)^T - \mathbf{K}_k \mathbf{H}_k \mathbf{P}_k^- (\mathbf{K}_k \mathbf{H}_k)^T \tag{39f}$$

$$\mathbf{K}_k \mathbf{R}_k \mathbf{K}_k = (\mathbf{I} - \mathbf{K}_k \mathbf{H}_k) \mathbf{P}_k^- (\mathbf{K}_k \mathbf{H}_k)^T \tag{39g}$$

Now, expanding equation (37d) and substituting in equation (39g), we have

$$\mathbf{P}_k = (\mathbf{I} - \mathbf{K}_k \mathbf{H}_k) \mathbf{P}_k^- (\mathbf{I} - \mathbf{K}_k \mathbf{H}_k)^T + \mathbf{K}_k \mathbf{R}_k \mathbf{K}_k^T \tag{40a}$$

$$= (\mathbf{I} - \mathbf{K}_k \mathbf{H}_k) \mathbf{P}_k^- - (\mathbf{I} - \mathbf{K}_k \mathbf{H}_k) \mathbf{P}_k^- (\mathbf{K}_k \mathbf{H}_k)^T + \mathbf{K}_k \mathbf{R}_k \mathbf{K}_k^T \tag{40b}$$

$$= (\mathbf{I} - \mathbf{K}_k \mathbf{H}_k) \mathbf{P}_k^- - \underbrace{(\mathbf{I} - \mathbf{K}_k \mathbf{H}_k) \mathbf{P}_k^- (\mathbf{K}_k \mathbf{H}_k)^T}_{\mathbf{K}_k \mathbf{R}_k \mathbf{K}_k^T} + \mathbf{K}_k \mathbf{R}_k \mathbf{K}_k^T \tag{40c}$$

$$= (\mathbf{I} - \mathbf{K}_k \mathbf{H}_k) \mathbf{P}_k^- - \mathbf{K}_k \mathbf{R}_k \mathbf{K}_k^T + \mathbf{K}_k \mathbf{R}_k \mathbf{K}_k^T \tag{40d}$$

$$\mathbf{P}_k = (\mathbf{I} - \mathbf{K}_k \mathbf{H}_k) \mathbf{P}_k^- \tag{40e}$$

Equation (37d) is called the "Joseph form" [110, 43] of the error covariance matrix $\mathbf{P}_k$. It generally has better numerical behavior for maintaining both symmetry and positive semi–definiteness than the simpler form given by equation (40e). For example, suppose there is a large uncertainty in the initial estimate. In this case, the *a priori* error covariance matrix $\mathbf{P}_k^-$ starts out with large values along the main diagonal. If this large initial uncertainty is then followed by a precise measurement at the initial time step, the *a posteriori* error covariance matrix $\mathbf{P}_k$ calculated using the simplified form: $\mathbf{P}_k = (\mathbf{I} - \mathbf{K}_k\mathbf{H}_k\mathbf{P}_k^-)$ approximates the indeterminate form: $0 \times \infty$. The natural symmetry of the Joseph form (equation (37d)), however, has better numerical behavior in such cases.

Propagation of the State Estimate and the Error Covariance In most of the preceding paragraphs, we have discussed how to use measurements to update the estimates of the state and the error covariance. To propagate the state estimate and the error covariance in time to the next measurement requires the use of the state transition matrix.

$$\hat{\mathbf{x}}_k^- = \mathbf{\Phi}_{k,k-1}\hat{\mathbf{x}}_{k-1} \tag{41}$$

$$\mathbf{P}_k^- = \mathbf{\Phi}_{k,k-1}\mathbf{P}_{k-1}\mathbf{\Phi}_{k,k-1}^T + \mathbf{Q}_{k-1} \tag{42}$$

Where

$$\mathbf{\Phi}_{k,k-1} = \mathbf{I} + \mathbf{F}\Delta t \tag{43}$$

$$\mathbf{F} = \left.\frac{\partial \mathbf{f}}{\partial \mathbf{x}}\right|_{\mathbf{x}=\mathbf{x}_{k-1}} \tag{44}$$

and $\mathbf{F}$ is the Jacobian of the system and Δt is the time between the k–th and $(k-1)$–th measurements.[321] Alternatively, the error covariance matrix $\mathbf{P}$ can be propagated using the expression for its time derivative below. [100]

$$\dot{\mathbf{P}}_k = \mathbf{F}_{k-1}\mathbf{P}_{k-1} + \mathbf{P}_{k-1}\mathbf{F}_{k-1}^T + \mathbf{Q}_{k-1} \tag{45}$$

A summary of the Kalman filter is given in Table 10.

Table 10: Summary of the Kalman filter.

State space model:

$$\mathbf{x}_{k+1} = \mathbf{\Phi}_{k+1,k}\mathbf{x}_k + \mathbf{w}_k \tag{46}$$
$$\mathbf{y}_k = \mathbf{H}_k\mathbf{x}_k + \mathbf{v}_k \tag{47}$$

where $\mathbf{w}_k$ and $\mathbf{v}_k$ are independent, zero-mean, Gaussian noise processes with covariance matrices $\mathbf{Q}_k$ and $\mathbf{R}_k$, respectively.

Initialization: For $k = 0$, set $\hat{\mathbf{x}}_0$ and $\mathbf{P}_0$ to their initial values.

Computation: For $k = 1, 2, ...$, compute:

State estimate propagation

$$\hat{\mathbf{x}}_k^- = \mathbf{\Phi}_{k,k-1}\hat{\mathbf{x}}_{k-1} \tag{48}$$

State transition matrix

$$\mathbf{\Phi}_{k,k-1} = \mathbf{I} + \mathbf{F}\Delta t \tag{49}$$

Error covariance propagation

$$\mathbf{P}_k^- = \mathbf{\Phi}_{k,k-1}\mathbf{P}_{k-1}\mathbf{\Phi}_{k,k-1}^T + \mathbf{Q}_{k-1} \tag{50}$$

Kalman gain matrix

$$\mathbf{K}_k = \mathbf{P}_k^-\mathbf{H}_k^T(\mathbf{H}_k\mathbf{P}_k^-\mathbf{H}_k^T + \mathbf{R}_k)^{-1} \tag{51}$$

State estimate update

$$\hat{\mathbf{x}}_k = \hat{\mathbf{x}}_k^- + \mathbf{K}_k(\mathbf{y}_k - \mathbf{H}_k\hat{\mathbf{x}}_k^-) \tag{52}$$

Error covariance update

$$\mathbf{P}_k = (\mathbf{I} - \mathbf{K}_k\mathbf{H}_k)\mathbf{P}_k^-(\mathbf{I} - \mathbf{K}_k\mathbf{H}_k)^T + \mathbf{K}_k\mathbf{R}_k\mathbf{K}_k^T \text{ (Joseph form) or} \tag{53}$$
$$\mathbf{P}_k = (\mathbf{I} - \mathbf{K}_k\mathbf{H}_k)\mathbf{P}_k^- \text{ (simplified form)} \tag{54}$$

Applications The Kalman filter and the extended Kalman filter (discussed below) have been used in many applications for filtering signals and data. Many real-time processing applications such as radar tracking [56] (and specifically maneuvering target trajectories [31, 166]), flow rate measurements [292], on-line failure detection in nuclear power plant instrumentation [291], filtering electrocardiogram signals [233],

power station control systems [304], ocean modeling [80, 81], and many, many more in virtually all engineering disciplines. These applications have all used Kalman filtering because rapid estimates are needed, and the Kalman filter does not require the storage of past data. This is especially useful for applications where a continuous stream of data is arriving in real-time.

Additional applications with more fixed data streams include the orbit determination of Voyager at Jupiter [45], the estimation and prediction of immeasurable variables [174], bathymetric and oceanographic applications [35], and the trajectory reconstruction of spacecraft atmospheric flight. The application of the Kalman filter to trajectory reconstruction occurs via the extended Kalman filter.

3.2.2 The Extended Kalman Filter

While originally formulated for linear systems, the usefulness of the Kalman filter has been extended to nonlinear systems in the form of the extended Kalman filter (EKF).[5] The extension to nonlinear systems is possible because the Kalman filter is formulated in terms of difference equations for discrete time systems. [117] The extended Kalman filter has been widely used for trajectory reconstruction. The following text describes the extended Kalman filter and discusses some of its applications.

Three Trajectories Consider the trajectory of a vehicle. There is the true trajectory, which is not knowable since all uncertainty in the motion of the spacecraft cannot be eliminated. Without incorporating measurements of the vehicle's motion, the best approximation of the true trajectory is the reference trajectory. The reference trajectory is created by modeling the motion of the spacecraft. Finally, the best estimate of the trajectory can be determined by applying the extended Kalman filter to the reference trajectory and measurements of the vehicle's motion. The true,

[5]The essential idea of the extended Kalman filter was proposed by Stanley F. Schmidt, and it has been called the "Kalman–Schmidt" filter. [111]

reference, and best estimate trajectories are related as shown in Figure 26. The assumed initial state of the vehicle is different from its true initial state because of uncertainty in the initial position and initial velocity of the vehicle. Note that the reference trajectory and the best estimate trajectory begin at the same initial state.

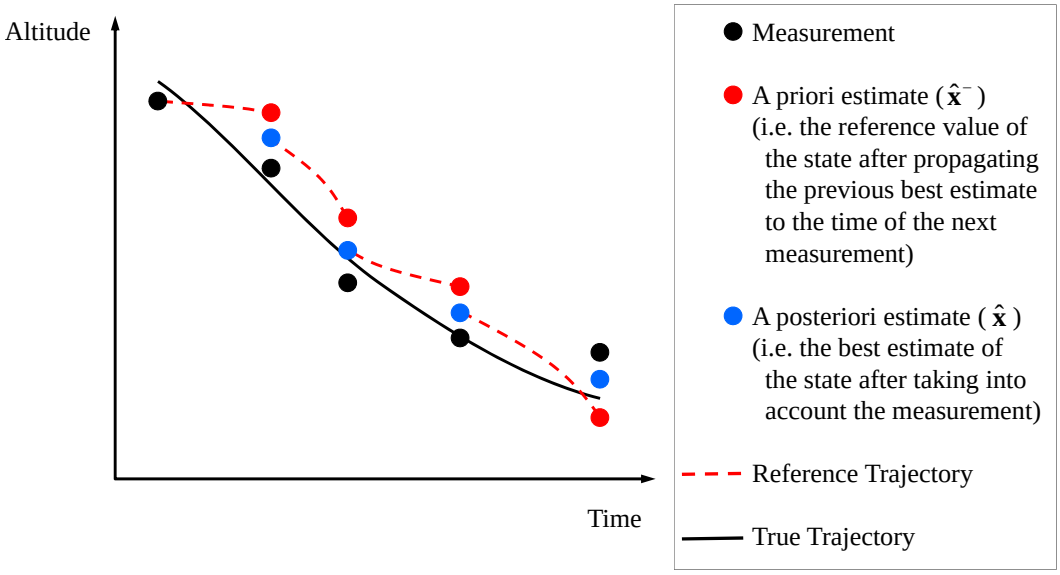

Figure 26: The true, reference, and best estimate trajectories. [187]

State Space Model The state of a system is governed by a set of nonlinear differential equations [322] of the form

$$\dot{\mathbf{x}}_{true} = \mathbf{f}(\mathbf{x}_{true}) + \mathbf{w} \tag{55}$$

where $\mathbf{x}_{true}$ is the state vector of the system, $\dot{\mathbf{x}}_{true}$ is its derivative, and $\mathbf{f}(\mathbf{x}_{true})$ is a nonlinear function of those states. The process noise $\mathbf{w}$ is assumed to be additive, white, and Gaussian, with zero mean and with a covariance matrix $\mathbf{Q}$.

Similarly, the measurements (or observations) $\mathbf{y}_{true}$ can be expressed as a nonlinear function of the state $\mathbf{x}_{true}$ [322] using an equation of the form

$$\mathbf{y}_{true} = \mathbf{h}(\mathbf{x}_{true}) + \mathbf{v} \tag{56}$$

where $\mathbf{y}_{true}$ is the measurement at time k and $\mathbf{h}(\mathbf{x}_{true})$ is a nonlinear function relating the states to the measurements. The measurement noise $\mathbf{v}$ is assumed to be additive, white, and Gaussian, with zero mean and with a covariance matrix $\mathbf{R}$.

The problem given by equations (55) and (56) represents a nonlinear estimation problem. However, if a reference trajectory exists that is sufficiently close to the true trajectory, then the deviations between the reference and true trajectories may be well approximated by a linear model obtained by truncating a Taylor series expansion of the deviations. [283, 24]

The state deviation vector $\mathbf{x}$ and the measurement deviation vector $\mathbf{y}$ are defined by

$$\mathbf{x} = \mathbf{x}_{true} - \mathbf{x}_{reference} \tag{57a}$$

$$\mathbf{y} = \mathbf{y}_{true} - \mathbf{y}_{reference} \tag{57b}$$

Neglecting the noise term, when equation (55) is expanded about the reference trajectory using a Taylor series, we have

$$\dot{\mathbf{x}}_{true} = \mathbf{f}(\mathbf{x}_{true}) \tag{58a}$$

$$\mathbf{f}(\mathbf{x}_{true}) = \mathbf{f}(\mathbf{x}_{reference}) + \left(\frac{\partial \mathbf{f}}{\partial \mathbf{x}}\right)_{reference} (\mathbf{x}_{true} - \mathbf{x}_{reference}) + \dots \tag{58b}$$

$$\mathbf{f}(\mathbf{x}_{true}) = \mathbf{f}(\mathbf{x}_{reference}) + \left(\frac{\partial \mathbf{f}}{\partial \mathbf{x}}\right)_{reference} (\mathbf{x}_{true} - \mathbf{x}_{reference}) \tag{58c}$$

$$\mathbf{f}(\mathbf{x}_{true}) - \mathbf{f}(\mathbf{x}_{reference}) = \left(\frac{\partial \mathbf{f}}{\partial \mathbf{x}}\right)_{reference} (\mathbf{x}_{true} - \mathbf{x}_{reference}) \tag{58d}$$

$$\dot{\mathbf{x}}_{true} - \dot{\mathbf{x}}_{reference} = \left(\frac{\partial \mathbf{f}}{\partial \mathbf{x}}\right)_{reference} (\mathbf{x}_{true} - \mathbf{x}_{reference}) \tag{58e}$$

$$\dot{\mathbf{x}} = \underbrace{\left(\frac{\partial \mathbf{f}}{\partial \mathbf{x}}\right)_{reference}}_{\triangleq \mathbf{F}} \mathbf{x} \tag{58f}$$

$$\dot{\mathbf{x}} = \mathbf{F}\mathbf{x} \tag{58g}$$

where the matrix $\mathbf{F}$ is called the Jacobian matrix of $\mathbf{f}$. [9]

A similar process can be followed for the measurement equation. Once again neglecting the noise term, when equation (56) is expanded about the reference measurement using a Taylor series, we have

$$\mathbf{y}_{true} = \mathbf{h}(\mathbf{x}_{true}) \tag{59a}$$

$$\mathbf{h}(\mathbf{x}_{true}) = \mathbf{h}(\mathbf{x}_{reference}) + \left(\frac{\partial \mathbf{h}}{\partial \mathbf{x}}\right)_{reference} (\mathbf{x}_{true} - \mathbf{x}_{reference}) + \dots \tag{59b}$$

$$\mathbf{h}(\mathbf{x}_{true}) = \mathbf{h}(\mathbf{x}_{reference}) + \left(\frac{\partial \mathbf{h}}{\partial \mathbf{x}}\right)_{reference} (\mathbf{x}_{true} - \mathbf{x}_{reference}) \tag{59c}$$

$$\mathbf{h}(\mathbf{x}_{true}) - \mathbf{h}(\mathbf{x}_{reference}) = \left(\frac{\partial \mathbf{h}}{\partial \mathbf{x}}\right)_{reference} (\mathbf{x}_{true} - \mathbf{x}_{reference}) \tag{59d}$$

$$\mathbf{y}_{true} - \mathbf{y}_{reference} = \left(\frac{\partial \mathbf{h}}{\partial \mathbf{x}}\right)_{reference} (\mathbf{x}_{true} - \mathbf{x}_{reference}) \tag{59e}$$

$$\mathbf{y} = \underbrace{\left(\frac{\partial \mathbf{h}}{\partial \mathbf{x}}\right)_{reference}}_{\triangleq \mathbf{H}} \mathbf{x} \tag{59f}$$

$$\mathbf{y} = \mathbf{H}\mathbf{x} \tag{59g}$$

Note that equation (58g) takes the form of a homogeneous linear system of differential equations. [78] The solution of this homogeneous linear system takes the form

$$\mathbf{x}_{k+1} = \mathbf{\Phi}_{k+1,k}\mathbf{x}_k \tag{60}$$

Including the noise terms, the solution to equation (58g) and equation (59g) together form the same problem we encountered with the linear Kalman filter (see equation (11) on page 50 and equation (13) on page 51).

$$\mathbf{x}_{k+1} = \mathbf{\Phi}_{k+1,k}\mathbf{x}_k + \mathbf{w}_k \tag{61a}$$

$$\mathbf{y}_k = \mathbf{H}_k\mathbf{x}_k + \mathbf{v}_k \tag{61b}$$

Where

$$\mathbf{\Phi}_{k+1,k} = \mathbf{I} + \mathbf{F}\Delta t \tag{62}$$

$$\mathbf{F} = \left.\frac{\partial \mathbf{f}}{\partial \mathbf{x}}\right|_{\mathbf{x}=\mathbf{x}_k} \tag{63}$$

and $\mathbf{F}$ is the Jacobian of the system and Δt is the time between the $(k+1)$–th and k–th measurements.[321] Note that this is where the linearization comes into the extended Kalman filter, as the full expression for the state transition matrix $\mathbf{\Phi}$ shown below has been truncated to only include the linear terms.

$$\mathbf{\Phi}_{k+1,k} = \mathbf{I} + \mathbf{F}\Delta t + \frac{F^2 t^2}{2!} + \frac{F^3 t^3}{3!} + \dots \tag{64}$$

Hence, by using the deviations from a reference trajectory, we are able to linearize the problem given by equations (55) and (56). This allows us to extend the Kalman filter to nonlinear problems. A summary of the extended Kalman filter is given in Table 11 on page 68. The parameters for the extended Kalman filter are given in Appendix C.

Table 11: Summary of the extended Kalman filter.

State space model:

$$\mathbf{x}_{k+1} = \mathbf{\Phi}_{k+1,k}\mathbf{x}_k + \mathbf{w}_k \tag{65}$$

$$\mathbf{y}_k = \mathbf{H}_k\mathbf{x}_k + \mathbf{v}_k \tag{66}$$

where $\mathbf{w}_k$ and $\mathbf{v}_k$ are independent, zero-mean, Gaussian noise processes with covariance matrices $\mathbf{Q}_k$ and $\mathbf{R}_k$, respectively.

Definitions: For $k = 1, 2, ...$, compute:

$$\mathbf{F} = \left.\frac{\partial \mathbf{f}}{\partial \mathbf{x}}\right|_{\mathbf{x}=\mathbf{x}_k} \tag{67}$$

$$\mathbf{H} = \left.\frac{\partial \mathbf{h}_k}{\partial \mathbf{x}_k}\right|_{\mathbf{x}=\mathbf{x}_k^-} \tag{68}$$

Initialization: For $k = 0$, set $\hat{\mathbf{x}}_0$ and $\mathbf{P}_0$ to their initial values.

Computation: For $k = 1, 2, ...$, compute:

State estimate propagation

$$\dot{\hat{\mathbf{x}}}_k = \mathbf{f}_k(\hat{\mathbf{x}}_k) \tag{69}$$

State transition matrix

$$\mathbf{\Phi}_{k,k-1} = \mathbf{I} + \mathbf{F}\Delta t \tag{70}$$

Error covariance propagation

$$\mathbf{P}_k^- = \mathbf{\Phi}_{k,k-1}\mathbf{P}_{k-1}\mathbf{\Phi}_{k,k-1}^T + \mathbf{Q}_{k-1} \tag{71}$$

Kalman gain matrix

$$\mathbf{K}_k = \mathbf{P}_k^-\mathbf{H}_k^T(\mathbf{H}_k\mathbf{P}_k^-\mathbf{H}_k^T + \mathbf{R}_k)^{-1} \tag{72}$$

State estimate update

$$\hat{\mathbf{x}}_k = \hat{\mathbf{x}}_k^- + \mathbf{K}_k(\mathbf{y}_k - \mathbf{H}_k\hat{\mathbf{x}}_k^-) \tag{73}$$

Error covariance update

$$\mathbf{P}_k = (\mathbf{I} - \mathbf{K}_k\mathbf{H}_k)\mathbf{P}_k^-(\mathbf{I} - \mathbf{K}_k\mathbf{H}_k)^T + \mathbf{K}_k\mathbf{R}_k\mathbf{K}_k^T \text{ (Joseph form) or} \tag{74}$$

$$\mathbf{P}_k = (\mathbf{I} - \mathbf{K}_k\mathbf{H}_k)\mathbf{P}_k^- \text{ (simplified form)} \tag{75}$$

3.3 Methods Possibly Applicable to Entry, Descent, and Landing Trajectory Reconstruction

Kalman filters are a type of dynamic Bayesian[6] network. [229] Bayesian data analysis has been used successfully in fault diagnosis for systems in steady–state [167], and it has been applied successfully to dynamic systems in the form of the Kalman filter as discussed earlier in § 3.2.1 on page 62. There exist many other variations of the Kalman filter besides the original and extended forms discussed previously. The following paragraphs will discuss some of these variations, as well as some other approaches to filtering and what has been called, by Russell and Norvig [229], "probabilistic reasoning over time".

After 1960, Kalman's original linear filter [143] (see § 3.2.1) brought forth many variations, the most notable of which is the extended Kalman filter (see § 3.2.2). Other variations include: the linearized Kalman filter [188], the iterated extended Kalman filter [212], second–order extended Kalman filter, singular evolutive extended Kalman filter [208, 207, 206], the ensemble Kalman filter [82, 83, 168], and the class of sigma–point Kalman filters. Sigma–point Kalman filters are the collective name used for those Kalman filters which use samples from the probability distribution of the state (i.e. sigma–points) to obtain an update of the state. [170, 171, 172, 217, 218] They include the unscented Kalman filter [141], the central difference filter [234], and the divided difference filter [195, 125].

Most of the variations of the Kalman filter are attempts to "extend" the capabilities of Kalman's original linear filter to nonlinear problems. Nevertheless, the extended Kalman filter has achieved great success when applied to nonlinear problems. Improvement was still possible, though, leading others to alter it and make further refinements.

[6] "Bayesian" after Thomas Bayes (1702–1761) who was a Presbyterian minister and mathematician. He "is best known for Bayes rule for computing the *a posteriori* probability of an event" (italics added) [298] in *An Essay towards Solving a Problem in the Doctrine of Chances*. [25]

One thing difficult for the "extended" Kalman filters to overcome, however, was the linearization of the nonlinear problems before they could be used with the "extended" Kalman filters. In 1995, Julier, Uhlmann, and Durrant–Whyte gave a new perspective with their *unscented transformation* [141]. The unscented transformation was the first truly revolutionary change in applying Kalman filters to nonlinear problems. The unscented Kalman filter has seen wide use within the aerospace community for the reconstruction of Mars Odyssey's aerobraking [127, 128, 129], for reconstructing the path of a sailplane [284], for determining in–flight the angular relationship of the body axes and the navigation axes for strapdown inertial measurement units [200], for terrain–referenced navigation [181], for locating and tracking targets [209, 227, 324, 323], for estimating the attitude of a pico satellite [260], for estimating the lift force on an F–15 aircraft with a damaged stabilator [42], and for the gyroless attitude control of multi–body satellites [88], to name a few applications. Outside the aerospace community, applications include: model–based hand tracking [273], speech processing [96], anti–lock brakes [161], brake–actuated manipulators [57], and monitoring structural behavior [48]. The unscented transformation has also been applied to both particle filters [294] and batch filters [201], and like the extended Kalman filter, it has an "iterated" version [23]. For these reasons, unscented Kalman filtering has been selected as one of the methods to evaluate for its utility when applied to the trajectory reconstruction of entry, descent, and landing trajectories, and it is discussed in more detail in § 3.3.1 on page 73.

Other filters include: the Beneš filter [29], the Daum filter [55], and particle filters [10]. The Beneš filter applies to continuous–time problems involving Wiener processes. Wiener processes are the processes that govern Brownian motion. [271] The Daum filter applies to continuous–time problems of variables with exponential distributions. The Daum filter may be said to include the continuous–time Kalman filter in the sense that the Gaussian distribution is the exponential of a quadratic function.

Particle filters, like ensemble Kalman filters, propagate a Monte Carlo set of points from the probability distribution of the state.[7] Where ensemble Kalman filters use the Monte Carlo points (the "ensemble") as an alternative means of calculating and updating covariances, particle filters employ importance sampling to determine which particles (or samples) continue to propagate. Particles judged to be the most important may end up having many copies of themselves continue to propagate, and as a result, all of the samples may eventually become copies of just a single particle. By increasing the number of samples, it is possible to stave off particle homogeneity. However, this is often undesirable due to the computational burden associated with additional samples. Another approach is to use an alternative importance sampling scheme "to move particles to areas of high observational likelihood" [293]. To this end, particle filters may employ Markov Chain Monte Carlo steps or Kalman filters in the importance sampling scheme. Sigma–point particle filters [293] and, in particular, the unscented particle filter can outperform standard particle filters [294].

The particle filter was not selected to be one of the methods used for this investigation for two reasons. First, the unscented particle filter can outperform standard particle filters and the unscented Kalman filter has already been selected for this investigation, and second, the computational load for particle filters can be much higher than Kalman filters depending on the number of particles used.[8] Additionally, one method with which the computational load is expected to be high, trajectory reconstruction using collocation (discussed in detail in § 3.3.2 beginning on page 79), has already been selected for this investigation.

Two additional methods that might be used for the trajectory reconstruction of entry, descent, and landing trajectories include artificial neural networks [176, 131]

[7] While sigma–point filters also propagate a set of points, these points are not chosen at random as would be done in a Monte Carlo method. [140]

[8] One study found the computational load for a particle filter using 25,000 particles to be approximately 100 times higher than the unscented Kalman filter. [84]

and direct collocation coupled with an optimizer [36]. Artificial neural networks were rejected as a possibility because their use would require many data sets for training and reconstructed entry trajectory data is readily available for only four Mars missions, one Jupiter mission, and one Titan mission. Simulated data sets could be made, but then the artificial neural network would be trained to model the simulation tool and not the actual flight of the planetary probe.

In regard to the collocation method, collocation converts[9] an optimal control problem into a set of algebraic constraints. [122, 114, 225] The set of algebraic constraints can then be solved numerically, giving a solution to the original problem. Often, optimal control problems have both state variables and control variables. Collocation discretizes[10] both the control variables and the state variables using an implicit integration method that represents the state variables as piecewise cubic polynomials.[11] These piecewise cubic polynomials form a set of discrete algebraic constraints.

For an entry trajectory, the total trajectory time can be discretized into segments based on the measurement times of an inertial measurement unit. Because of this, it may be possible to reconstruct an entry, descent, and landing trajectory based on the algebraic constraints from using collocation. This approach would allow the same collocation tools used to design a flight mission to also be used for the reconstruction process[12] And that is the primary reason why it was selected to be part of this study. [36] Additionally, when used in a Monte Carlo simulation with a trajectory simulation posed as an initial value problem, collocation may allow estimates of state uncertainty to be obtained. [228]

[9]The word "transcribes", rather than "converts", is often used to describe the process of problem reformulation.

[10]Frequently, this way of discretization is known as "Direct Collocation and Nonlinear Programming". [122]

[11]Higher order polynomials can be used. Reference [225] recommends third–, fifth–, or seventh–order polynomials.

[12]An example of a trajectory design tool that uses collocation is Optimal Trajectories by Implicit Simulation (OTIS). [199, 300, 226]

3.3.1 The Unscented Kalman Filter

Description The unscented Kalman filter represents the next improvement in Kalman filters. Where the extended Kalman filter provides an approximation to optimal nonlinear estimation [118] using linearization, the unscented Kalman filter does not use linearization. Instead, it deals directly with the nonlinear problem. Since extended Kalman filtering is often used for trajectory reconstruction as discussed in Chapter 2, the unscented Kalman filter represents an obvious choice as an additional method to be applied to the reconstruction of entry, descent, and landing trajectories.

The unscented Kalman filter (UKF) was first proposed by Julier, Uhlmann, and Durrant–Whyte in 1995 [141] as an alternative to the extended Kalman filter for nonlinear problems. Further development work was done by Julier and Uhlmann [137, 138, 135, 140, 136, 139], as well as by van der Merwe, Wan, and Nelson [305, 306, 294, 295, 296, 297, 293].[13]

The basic difference between the extended Kalman filter and the unscented Kalman filter stems from the manner in which Gaussian random variables are represented for propagation through the system dynamics. [118] The uncertainty distribution of the state is propagated through a linearization in the extended Kalman filter, and the extended Kalman filter requires calculating first–order sensitivities of the dynamic equations (Jacobians). In contrast, the unscented Kalman filter uses a set of sample points from the state's uncertainty distribution. These sample points are called *sigma–points*. They capture the mean and variance of the uncertainty of the state, and they can be propagated through a nonlinear system. The result is that the unscented Kalman filter achieves second–order accuracy rather than the extended Kalman filter's first–order accuracy.[14] The unscented Kalman filter's improvement in

[13]This discussion of the unscented Kalman filter is largely taken from reference [119] with additional material from reference [293].

[14]The variance estimate for the extended Kalman filter can be much greater than theory would predict. [236]

accuracy is said to be obtained with no additional computational cost over that of the extended Kalman filter. [195, 125] Although it has been said that the algorithmic complexity is arguably less favorable [228] it can be demonstrated, for purely linear problems, that the Jacobian–less unscented formulation yields equivalent results to the linear Kalman filter. [170] A flowchart of the algorithm is shown in Figure 27.

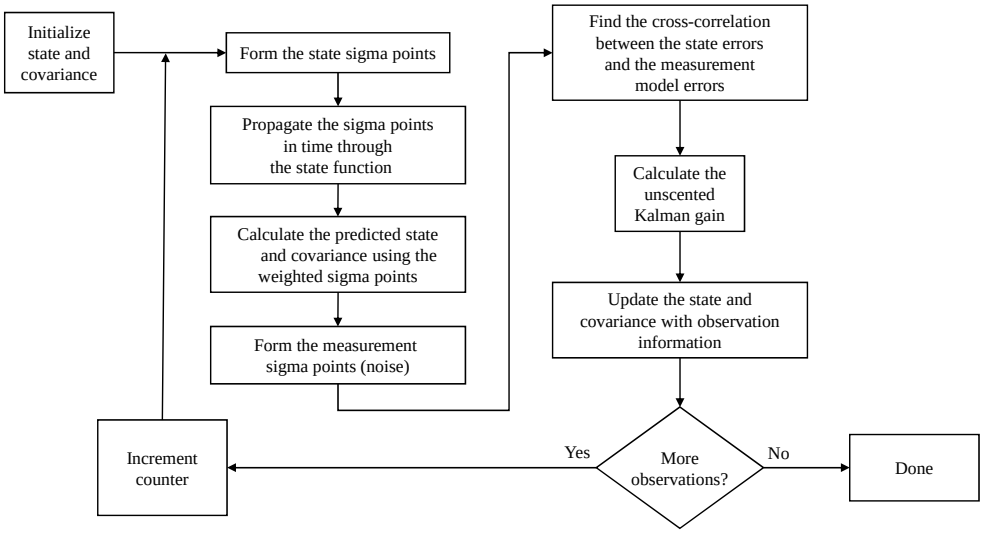

Figure 27: The unscented Kalman filter algorithm. [219]

The Nonlinear Process and Measurement Equations The state of a system is a vector $\mathbf{x}_k$ which describes the motion of a system at a specific point in time. (The subscript k denotes a discrete time point.) Typically, the state $\mathbf{x}_k$ is unknown, so we use a set of measurements (or observations) $\mathbf{y}_k$ to estimate it. Given an initial state $\mathbf{x}_0$, future states can be found using the nonlinear *process equation*:

$$\mathbf{x}_{k+1} = \mathbf{f}(\mathbf{x}_k) + \mathbf{w}_k \tag{76}$$

where $\mathbf{f}$ is a nonlinear function taking the state $\mathbf{x}_k$ from time k to time $k+1$. The process noise $\mathbf{w}_k$ is assumed to be additive, white, and Gaussian, with zero mean and with a covariance matrix defined by

$$E[\mathbf{w}_n \mathbf{w}_k^T] = \begin{cases} \mathbf{Q}_k & n = k \\ \mathbf{0} & n \neq k \end{cases} \tag{77}$$

The measurements (or observations) $\mathbf{y}_k$ can be expressed as a nonlinear function of the state $\mathbf{x}_k$ using the *measurement equation*:

$$\mathbf{y}_k = \mathbf{h}(\mathbf{x}_k) + \mathbf{v}_k \tag{78}$$

where $\mathbf{y}_k$ is the measurement at time k and $\mathbf{h}$ is the nonlinear function transforming the state $\mathbf{x}$ into the measurement $\mathbf{y}$. The measurement noise $\mathbf{v}_k$ is assumed to be additive, white, and Gaussian, with zero mean and with a covariance matrix defined by

$$E[\mathbf{v}_n \mathbf{v}_k^T] = \begin{cases} \mathbf{R}_k & n = k \\ \mathbf{0} & n \neq k \end{cases} \tag{79}$$

In addition, the measurement noise $\mathbf{v}_k$ is uncorrelated with the process noise $\mathbf{w}_k$.

The Unscented Transformation The unscented transformation is a method for calculating the statistics of a random variable which undergoes a nonlinear transformation. [138] Consider the propagation of the state $\mathbf{x}$ of dimension L through the nonlinear functions given in equations (76) and (78). Assume $\mathbf{x}$ has a mean $\bar{\mathbf{x}}$ and an error covariance matrix $\mathbf{P}_k$. To calculate the statistics, we form a matrix $\mathcal{X}$ of $2L+1$ *sigma–vectors* $\mathcal{X}_i$ according to

$$\mathcal{X}_0 = \hat{\mathbf{x}}_{k-1} \tag{80a}$$

$$\mathcal{X}_i = \hat{\mathbf{x}}_{k-1} + \left(\sqrt{(L+\lambda)\mathbf{P}_{\mathbf{x}}}\right)_i \qquad i = 1, \ldots, L \tag{80b}$$

$$\mathcal{X}_i = \hat{\mathbf{x}}_{k-1} - \left(\sqrt{(L+\lambda)\mathbf{P}_{\mathbf{x}}}\right)_i \qquad i = L+1, \ldots, 2L \tag{80c}$$

These sigma–vectors are propagated through the process equation to obtain

$$\mathcal{X}_{k|k-1} = \mathbf{f}(\mathcal{X}_{k-1}) \tag{81}$$

Before computing the *a priori* estimate of the state $\hat{\mathbf{x}}_k^-$, we compute the weights for the sample mean and covariance with

$$w_0^{(mean)} = \frac{\lambda}{L+\lambda} \tag{82a}$$

$$w_i^{(mean)} = \frac{1}{2(L+\lambda)} \qquad i = 1, \ldots, 2L \tag{82b}$$

$$w_0^{(cov)} = \frac{\lambda}{L+\lambda} + 1 - \alpha^2 + \beta \tag{82c}$$

$$w_i^{(cov)} = \frac{1}{2(L+\lambda)} \qquad i = 1, \ldots, 2L \tag{82d}$$

where

- L is the dimension of $\mathbf{x}$.
- $\lambda = \alpha^2(L+\kappa) - L$ is a scaling parameter.
- $\sqrt{(L+\lambda)\mathbf{P_x}}$ is the matrix square root of $(L+\lambda)\mathbf{P_x}$.[15]
- α is a constant that determines the spread of the sigma–points around the mean $\bar{\mathbf{x}}$. It is usually set to a small positive value: $10^{-4} \leq \alpha \leq 1$.
- κ is a secondary scaling parameter which is usually set to 0 or $3 - L$. If κ is chosen such that $\kappa = 3 - L$ then the kurtosis of one state of the sigma–points agrees with that of the Gaussian distribution. [141, 140]
- β is used to incorporate prior knowledge of the distribution of $\mathbf{x}$. For Gaussian distributions, $\beta = 2$ is optimal. [136]

[15]The matrix square root may be obtained using Cholesky decomposition. [30, 274] An important note on the square root of the error covariance matrix $\mathbf{P}_k$ from reference [140]: If the matrix square root $\mathbf{A}$ of $\mathbf{P}$ is of the form $\mathbf{P} = \mathbf{A}^T\mathbf{A}$, then the sigma–vectors are formed from the *rows* ($i = 1, \ldots, L$) of $\mathbf{A}$. However, for a square root $\mathbf{A}$ of $\mathbf{P}$ that is of the form $\mathbf{P} = \mathbf{A}\mathbf{A}^T$, then the sigma–vectors are formed from the *columns* ($i = 1, \ldots, L$) of $\mathbf{A}$.

The *a priori* estimate of the state $\hat{\mathbf{x}}_k^-$ and the error covariance matrix $\mathbf{P}_k^-$ can now be calculated using

$$\hat{\mathbf{x}}_k^- = \sum_{i=0}^{2L} w_i^{(mean)} \mathcal{X}_{i,k|k-1} \tag{83}$$

$$\mathbf{P}_k^- = \sum_{i=0}^{2L} w_i^{(cov)} \left(\mathcal{X}_{i,k|k-1} - \hat{\mathbf{x}}_k^-\right) \left(\mathcal{X}_{i,k|k-1} - \hat{\mathbf{x}}_k^-\right)^T + \mathbf{Q}_k \tag{84}$$

We follow a similar process to obtain an estimate for the measurement $\hat{\mathbf{y}}_k^-$ and the covariances ($\mathbf{P}_{\mathbf{y}_k\mathbf{y}_k}$ and $\mathbf{P}_{\mathbf{x}_k\mathbf{y}_k}$) necessary to calculate the unscented Kalman gain $\mathbf{K}_k$.

$$\mathcal{Y}_{k|k-1} = \mathbf{h}(\mathcal{X}_{k|k-1}) \tag{85}$$

$$\hat{\mathbf{y}}_k^- = \sum_{i=0}^{2L} w_i^{(mean)} \mathcal{Y}_{i,k|k-1} \tag{86}$$

$$\mathbf{P}_{\mathbf{y}_k\mathbf{y}_k} = \sum_{i=0}^{2L} w_i^{(cov)} \left(\mathcal{Y}_{i,k|k-1} - \hat{\mathbf{y}}_k^-\right) \left(\mathcal{Y}_{i,k|k-1} - \hat{\mathbf{y}}_k^-\right)^T + \mathbf{R}_k \tag{87}$$

$$\mathbf{P}_{\mathbf{x}_k\mathbf{y}_k} = \sum_{i=0}^{2L} w_i^{(cov)} \left(\mathcal{X}_{i,k|k-1} - \hat{\mathbf{x}}_k^-\right) \left(\mathcal{Y}_{i,k|k-1} - \hat{\mathbf{y}}_k^-\right)^T \tag{88}$$

$$\mathbf{K}_k = \mathbf{P}_{\mathbf{x}_k\mathbf{y}_k} \mathbf{P}_{\mathbf{y}_k\mathbf{y}_k}^{-1} \tag{89}$$

Knowing the unscented Kalman gain $\mathbf{K}_k$, we can update the estimates of the state $\hat{\mathbf{x}}_k$ and the error covariance $\mathbf{P}_k$.

$$\hat{\mathbf{x}}_k = \hat{\mathbf{x}}_k^- + \mathbf{K}_k(\mathbf{y}_k - \hat{\mathbf{y}}_k^-) \tag{90}$$

$$\mathbf{P}_k = \mathbf{P}_k^- - \mathbf{K}_k \mathbf{P}_{\mathbf{y}_k\mathbf{y}_k} \mathbf{K}_k^T \tag{91}$$

A summary of the unscented Kalman filter is given in Table 12 on page 78. The parameters for the unscented Kalman filter are given in Appendix D.

Table 12: Summary of the unscented Kalman filter.

State space model:

$$\mathbf{x}_{k+1} = \mathbf{f}(\mathbf{x}_k) + \mathbf{w}_k \tag{92}$$

$$\mathbf{y}_k = \mathbf{h}(\mathbf{x}_k) + \mathbf{v}_k \tag{93}$$

where $\mathbf{w}_k$ and $\mathbf{v}_k$ are independent, zero-mean, Gaussian noise processes with covariance matrices $\mathbf{Q}_k$ and $\mathbf{R}_k$, respectively.

Initialization: For $k = 0$, set $\hat{\mathbf{x}}_0$ and $\mathbf{P}_0$ to their initial values.

Computation: For $k = 1, 2, ...$, compute:

Sigma–points

$$\mathcal{X}_0 = \hat{\mathbf{x}}_{k-1} \tag{94a}$$

$$\mathcal{X}_i = \hat{\mathbf{x}}_{k-1} + \left(\sqrt{(L+\lambda)\mathbf{P}_{k-1}}\right)_i \qquad i = 1, \ldots, L \tag{94b}$$

$$\mathcal{X}_i = \hat{\mathbf{x}}_{k-1} - \left(\sqrt{(L+\lambda)\mathbf{P}_{k-1}}\right)_i \qquad i = L+1, \ldots, 2L \tag{94c}$$

Weights

$$w_0^{(mean)} = \frac{\lambda}{L+\lambda} \tag{95a}$$

$$w_i^{(mean)} = \frac{1}{2(L+\lambda)} \qquad i = 1, \ldots, 2L \tag{95b}$$

$$w_0^{(cov)} = \frac{\lambda}{L+\lambda} + 1 - \alpha^2 + \beta \tag{95c}$$

$$w_i^{(cov)} = \frac{1}{2(L+\lambda)} \qquad i = 1, \ldots, 2L \tag{95d}$$

Time-update equations

$$\mathcal{X}_{k|k-1} = \mathbf{f}(\mathcal{X}_{k-1}) \tag{96}$$

$$\hat{\mathbf{x}}_k^- = \sum_{i=0}^{2L} w_i^{(mean)} \mathcal{X}_{i,k|k-1} \tag{97}$$

$$\mathbf{P}_k^- = \sum_{i=0}^{2L} w_i^{(cov)} \left(\mathcal{X}_{i,k|k-1} - \hat{\mathbf{x}}_k^-\right)\left(\mathcal{X}_{i,k|k-1} - \hat{\mathbf{x}}_k^-\right)^T + \mathbf{Q}_k \tag{98}$$

Measurement-update equations

$$\mathcal{Y}_{k|k-1} = \mathbf{h}(\mathcal{X}_{k|k-1}) \tag{99}$$

$$\hat{\mathbf{y}}_k^- = \sum_{i=0}^{2L} w_i^{(mean)} \mathcal{Y}_{i,k|k-1} \tag{100}$$

$$\mathbf{P}_{\mathbf{y}_k\mathbf{y}_k} = \sum_{i=0}^{2L} w_i^{(cov)} \left(\mathcal{Y}_{i,k|k-1} - \hat{\mathbf{y}}_k^-\right)\left(\mathcal{Y}_{i,k|k-1} - \hat{\mathbf{y}}_k^-\right)^T + \mathbf{R}_k \tag{101}$$

$$\mathbf{P}_{\mathbf{x}_k\mathbf{y}_k} = \sum_{i=0}^{2L} w_i^{(cov)} \left(\mathcal{X}_{i,k|k-1} - \hat{\mathbf{x}}_k^-\right)\left(\mathcal{Y}_{i,k|k-1} - \hat{\mathbf{y}}_k^-\right)^T \tag{102}$$

$$\mathbf{K}_k = \mathbf{P}_{\mathbf{x}_k\mathbf{y}_k}\mathbf{P}_{\mathbf{y}_k\mathbf{y}_k}^{-1} \tag{103}$$

$$\hat{\mathbf{x}}_k = \hat{\mathbf{x}}_k^- + \mathbf{K}_k(\mathbf{y}_k - \hat{\mathbf{y}}_k^-) \tag{104}$$

$$\mathbf{P}_k = \mathbf{P}_k^- - \mathbf{K}_k\mathbf{P}_{\mathbf{y}_k\mathbf{y}_k}\mathbf{K}_k^T \tag{105}$$

3.3.2 Trajectory Reconstruction Using Collocation (TRUC)

Introduction Although, the reconstruction of an entry trajectory can be posed as a continuous two-point boundary value problem.[16] Posing trajectory reconstruction as an initial value problem allows collocation to obtain estimates of state uncertainty, as well as estimates of the state. [228]

Optimal Control In the optimal control problem[17], a control history is sought that takes a set of states $\mathbf{x}$ from specified initial conditions $\mathbf{x}_0$ to a desired final state $\mathbf{x}_f$ subject to a set of constraints, while minimizing a performance index J. The states are defined by a system of differential equations given by

$$\dot{\mathbf{x}} = \mathbf{f}(\mathbf{x}, \mathbf{u}, t) \tag{106}$$

where

- $\mathbf{x}$ is the state vector.
- $\mathbf{u}$ is the control vector.
- $\mathbf{f}$ is a function of the state and control vectors.

The desired final boundary conditions $\mathbf{x}_f$ are specified by a vector of algebraic functions $\mathbf{\Psi}$ of the states at the final time t_f

$$\mathbf{\Psi}(\mathbf{x}_f) = \mathbf{0} \tag{107}$$

In addition to satisfying the constraints on the final state, an optimal control history is sought that minimizes the scalar performance function

[16] The atmospheric entry point represents one boundary condition, and the entry state is known very well (i.e. it is a good initial boundary condition) from interplanetary spacecraft navigation information. The landing site location can be determined extremely accurately (i.e. it is an excellent final boundary condition) from radio triangulation with orbiting spacecraft. Additionally, using images of the lander's position on the surface of the planet, the lander's position relative to known topographical features can be determined.

[17] The following description of optimal control and collocation is taken from references [60] and [114].

$$J = \phi(\mathbf{x}_f) \tag{108}$$

where ϕ is a scalar cost function based on the final state.

One approach to solving the optimal control problem is to adjoin both the system differential equations (equation (106)) and the constraints on the final state (equation (107)) to the scalar performance function (equation (108)) creating a new augmented cost function

$$J = \phi + \boldsymbol{\nu}^T \boldsymbol{\Psi} + \int_{t_0}^{t_f} \boldsymbol{\lambda}^T (\mathbf{f}(\mathbf{x}, \mathbf{u}, t) - \dot{\mathbf{x}}) \mathrm{d}t \tag{109}$$

where

- $\boldsymbol{\nu}$ is a vector of sensitivities associated with the final condition constraints.
- $\boldsymbol{\lambda}$ is a vector of adjoint (or costate) values.

The following necessary conditions from the calculus of variations must be verified for optimality of the augmented cost function.

$$\dot{\boldsymbol{\lambda}} = \frac{\partial \mathbf{H}^T}{\partial \mathbf{x}} \tag{110}$$

$$\boldsymbol{\lambda}|_{t_f} = \frac{\partial \boldsymbol{\Phi}^T}{\partial \mathbf{x}_f} \tag{111}$$

$$\frac{\partial \mathbf{H}^T}{\partial \mathbf{u}} = \mathbf{0} \tag{112}$$

where

- $\mathbf{H} = \boldsymbol{\lambda}^T \mathbf{f}$ is the system Hamiltonian.
- $\boldsymbol{\Phi} = \phi + \boldsymbol{\nu}^T \boldsymbol{\Psi}$.

Equations (110) through (112) are collectively referred to as the Euler–Lagrange equations in the calculus of variations. Their solution must also satisfy equation (106)

subject to the specified initial conditions and the final condition constraints. These equations constitute a two–point boundary value problem whose solution provides an indirect solution to the original optimal control problem. However, this method of solving the optimal control problem is very sensitive to the initial guess of the adjoint values. In contrast, collocation can transcribe the optimal control problem into a set of algebraic constraints that can be used to solve the optimal control problem without making use of the Euler–Lagrange equations, even though the Euler–Lagrange equations can still be used.

Collocation Collocation is a method of solving the differential equations in an optimal control problem by transcribing the differential equations into a set of algebraic constraints.[18] The set of algebraic constraints can then be solved numerically using a constrained optimization method, giving a solution to the original problem. Often, optimal control problems have both state variables and control variables. Collocation discretizes both the control variables and the state variables using an implicit integration method that represents the state variables as piecewise cubic polynomials.

The total time of interest T is discretized into n segments with $n+1$ nodes, and the time between nodes T_j (i.e. the length of time segment j) may vary. Within each segment of time, the piecewise cubic polynomials constitute an approximate integration formula for the state differential equations. This formulation for the approximate integration of the system of equations transforms them into a set of discrete algebraic constraints imposed within each time segment. Using Hermite interpolation, cubic polynomials are defined for each state within each time segment using the values of the states at the nodes and the state time derivatives at the nodes. The values of the states are then selected such that the interpolated derivatives agree with the differential equations at the center of each time segment.

[18] Collocation, as discussed here, has been successfully used for trajectory design, so it was chosen for trajectory reconstruction.

The basic procedure can be derived as follows. Let each state x be represented by cubic polynomials of the form

$$x = C_0 + C_1 s + C_2 s^2 + C_3 s^3 \tag{113}$$

on each time segment j where, to simplify the argument, the segment length is one and $0 \leq s \leq 1$. Let

$$x_j|_{s=0} = x_{j0} \tag{114a}$$

$$x_j|_{s=1} = x_{jf} \tag{114b}$$

$$\left.\frac{\mathrm{d}x_j}{\mathrm{d}s}\right|_{s=0} = \dot{x}_{j0} \tag{114c}$$

$$\left.\frac{\mathrm{d}x_j}{\mathrm{d}s}\right|_{s=1} = \dot{x}_{jf} \tag{114d}$$

where

- x_{j0} is the value of state x at the beginning of time segment j.
- x_{jf} is the value of state x at the end of time segment j.
- $\dot{x}_{j0}$ is the value of the time derivative of state x at the beginning of time segment j.
- $\dot{x}_{jf}$ is the value of the time derivative of state x at the end of time segment j.

Differentiating equation (113) and evaluating it at $s = 0$ and $s = 1$ gives

$$\begin{bmatrix} 1 & 0 & 0 & 0 \\ 0 & 1 & 0 & 0 \\ 1 & 1 & 1 & 1 \\ 0 & 1 & 2 & 3 \end{bmatrix} \begin{bmatrix} C_0 \\ C_1 \\ C_2 \\ C_3 \end{bmatrix} = \begin{bmatrix} x_{j0} \\ \dot{x}_{j0} \\ x_{jf} \\ \dot{x}_{jf} \end{bmatrix} \tag{115}$$

Inverting the 4×4 matrix in equation (115) gives

$$\begin{bmatrix} C_0 \\ C_1 \\ C_2 \\ C_3 \end{bmatrix} = \begin{bmatrix} 1 & 0 & 0 & 0 \\ 0 & 1 & 0 & 0 \\ -3 & -2 & 3 & -1 \\ 2 & 1 & -2 & 1 \end{bmatrix} \begin{bmatrix} x_{j0} \\ \dot{x}_{j0} \\ x_{jf} \\ \dot{x}_{jf} \end{bmatrix} \tag{116}$$

Now, using equation (116), evaluating equation (113) at the center of each time segment (i.e. $s = \frac{1}{2}$), and with the time segment length denoted by T_j, we have the interpolated value of the state at the center of the time segment x_c to be

$$x_{jc} = \frac{1}{2}(x_{j0} + x_{jf}) + \frac{T_j}{8}(\dot{x}_{j0} - \dot{x}_{jf}) \tag{117}$$

Similarly, for the derivative at the center of the time segment

$$\dot{x}_{jc} = -\frac{3}{2T_j}(x_{j0} - x_{jf}) - \frac{1}{4}(\dot{x}_{j0} + \dot{x}_{jf}) \tag{118}$$

Define the defect at the center of the time segment as

$$\Delta = (\dot{x}_{jc})_{\text{system derivative}} - (\dot{x}_{jc})_{\text{interpolation}} \tag{119}$$

where

- Δ is the *defect*, which is the difference between the state time derivative calculated using the differential equations defining the state (equation (106)) and the state time derivative calculated using interpolation (equation (118)).
- $(\dot{x}_{jc})_{\text{system derivative}}$ is the state time derivative calculated using the differential equations defining the state (equation (106)).
- $(\dot{x}_{jc})_{\text{interpolation}}$ is the state time derivative calculated using interpolation (equation (118)).
- $\dot{x}_{j0}$ and $\dot{x}_{jf}$ are calculated from the state equation (equation (106)).

The values of x_{j0} and x_{jf} are varied to drive the defect Δ to zero and provide an accurate approximation of the solution. The defects for each time segment constitute a set of nonlinear algebraic constraints, which are a function of the states and controls at each node of the time segments.

Application to Trajectory Reconstruction For the trajectories in this research, a three-degree-of-freedom simulation was used. The translational motion is described by the state equation given in equation (120)[19] and the expressions for the state derivatives are given in equations (121) through (209)). [60]

$$\dot{\mathbf{x}} = \mathbf{f}(\mathbf{x}) = \begin{bmatrix} \dot{r} \\ \dot{\phi} \\ \dot{\theta} \\ \dot{v} \\ \dot{\gamma} \\ \dot{\psi} \end{bmatrix} \tag{120}$$

$$\dot{r} = v \sin\gamma \tag{121}$$

$$\dot{\phi} = \frac{v \cos\gamma \cos\psi}{r} \tag{122}$$

$$\dot{\theta} = \frac{v \cos\gamma \sin\psi}{r \cos\phi} \tag{123}$$

$$\begin{aligned} \dot{v} = {} & \frac{1}{m}(Y \sin\beta - D \cos\beta) \\ & - g \sin\gamma \\ & + \Omega^2 r \cos\phi(\sin\gamma \cos\phi - \cos\gamma \sin\phi \cos\psi) \end{aligned} \tag{124}$$

[19]The state variables radius r, latitude ϕ, and longitude θ give the three components of position, and the state variables velocity v, flight path angle γ, and azimuth ψ give the three components of velocity.

$$\begin{aligned}\dot{\gamma} = &\frac{1}{mv}(L\cos\sigma - D\sin\beta\sin\sigma - Y\cos\beta\sin\sigma) \\ &+ \left(\frac{v}{r} - \frac{g}{v}\right)\cos\gamma \\ &+ 2\Omega\cos\phi\sin\psi \\ &+ \frac{\Omega^2 r}{v}\cos\phi(\cos\gamma\cos\phi + \sin\gamma\sin\phi\cos\psi)\end{aligned} \tag{125}$$

$$\begin{aligned}\dot{\psi} = &\frac{1}{mv\cos\gamma}(L\sin\sigma + D\sin\beta\cos\sigma + Y\cos\beta\cos\sigma) \\ &+ \frac{v\cos\gamma}{r}\sin\psi\tan\phi \\ &- 2\Omega(\cos\phi\cos\psi\tan\gamma - \sin\phi) \\ &+ \frac{\Omega^2 r}{v\cos\gamma}\cos\phi\sin\phi\sin\psi\end{aligned} \tag{126}$$

where

- C_D is the drag coefficient of the spacecraft. It is a function of the angle of attack α and Mach number M of the of the spacecraft: $C_D = C_D(\alpha, M)$.
- C_L is the lift coefficient of the spacecraft. It is a function of the angle of attack α and Mach number M of the spacecraft: $C_L = C_L(\alpha, M)$.
- C_Y is the side force coefficient of the spacecraft. It is a function of the side-slip angle β and Mach number M of the spacecraft: $C_Y = C_Y(\beta, M)$.
- D is the aerodynamic drag force acting on the spacecraft. $D = \frac{1}{2}\rho v^2 S C_D$ where the drag coefficient C_D is a function of the angle of attack α and Mach number M of the spacecraft: $C_D = C_D(\alpha, M)$.
- g is the local acceleration of gravity at the spacecraft's position.
- L is the aerodynamic lift force acting on the spacecraft. $L = \frac{1}{2}\rho v^2 S C_L$ where

the lift coefficient C_L is a function of the angle of attack α and Mach number M of the spacecraft: $C_L = C_L(\alpha, M)$.

- m is the mass of the spacecraft.
- M is the Mach number of the spacecraft.
- r is the spacecraft's local radius measured from the center of the planet at which entry is taking place.
- S is the aerodynamic reference area of the spacecraft.
- t is time.
- v is the spacecraft's velocity.
- Y is the aerodynamic side force acting on the spacecraft. $Y = \frac{1}{2}\rho v^2 S C_Y$ where the side force coefficient C_Y is a function of the side-slip angle β and Mach number M of the spacecraft: $C_Y = C_Y(\beta, M)$.
- α is the angle of attack of the spacecraft.
- β is the side–slip angle of the spacecraft.
- γ is the spacecraft's flight path angle, which is positive above the local horizontal.
- θ is the spacecraft's longitude.
- ρ is the local atmospheric density at the spacecraft's position.
- σ is the bank angle of the spacecraft.
- ϕ is the spacecraft's latitude.
- ψ is the spacecraft's azimuth, which is positive when measured clockwise from north.

- Ω is the rotation rate of the planet at which entry is taking place.

and these variables may be categorized into state variables and parameters as shown in Table 13. Note that there are no control variables, as the angle of attack α, the side–slip angle β, and the bank angle σ for the spacecraft will be set to zero for the duration of the trajectory to be consistent with the process models of the two Kalman filters and compare the three methods on an equal basis.

Table 13: Categorization of the variables into state variables and parameters for trajectory reconstruction using collocation.

State Variables	Parameters
r	C_D
ϕ	C_L
θ	C_Y
v	D
γ	g
ψ	L
	m
	S
	Y
	α
	β
	ρ
	σ
	Ω

As stated above, the total trajectory time can be discretized into segments based on the measurement times of an inertial measurement unit. If there are n measurements taken, then there are n nodes and $n-1$ time segments. For each time segment j $(1 \leq j \leq n-1)$, the state time derivatives at the center of each time segment $(\dot{x}_{jc})_{\text{system derivative}}$ can be calculated using the differential equations above (equations (121) through (209)), and the interpolated values of the state time derivatives at the center of each time segment $(\dot{x}_{jc})_{\text{interpolation}}$ can be calculated using equation (118) as follows.

$$\dot{r}_{jc} = -\frac{3}{2T_j}(r_{j0} - r_{jf}) - \frac{1}{4}(\dot{r}_{j0} + \dot{r}_{jf}) \tag{127a}$$

$$\dot{\phi}_{jc} = -\frac{3}{2T_j}(\phi_{j0} - \phi_{jf}) - \frac{1}{4}(\dot{\phi}_{j0} + \dot{\phi}_{jf}) \tag{127b}$$

$$\dot{\theta}_{jc} = -\frac{3}{2T_j}(\theta_{j0} - \theta_{jf}) - \frac{1}{4}(\dot{\theta}_{j0} + \dot{\theta}_{jf}) \tag{127c}$$

$$\dot{v}_{jc} = -\frac{3}{2T_j}(v_{j0} - v_{jf}) - \frac{1}{4}(\dot{v}_{j0} + \dot{v}_{jf}) \tag{127d}$$

$$\dot{\gamma}_{jc} = -\frac{3}{2T_j}(\gamma_{j0} - \gamma_{jf}) - \frac{1}{4}(\dot{\gamma}_{j0} + \dot{\gamma}_{jf}) \tag{127e}$$

$$\dot{\psi}_{jc} = -\frac{3}{2T_j}(\psi_{j0} - \psi_{jf}) - \frac{1}{4}(\dot{\psi}_{j0} + \dot{\psi}_{jf}) \tag{127f}$$

Hence, the defects at the center of each time segment j are

$$\Delta_{r,j} = (\dot{r}_{jc})_{\text{system derivative}} - (\dot{r}_{jc})_{\text{interpolation}} \tag{128a}$$

$$\Delta_{\phi,j} = (\dot{\phi}_{jc})_{\text{system derivative}} - (\dot{\phi}_{jc})_{\text{interpolation}} \tag{128b}$$

$$\Delta_{\theta,j} = (\dot{\theta}_{jc})_{\text{system derivative}} - (\dot{\theta}_{jc})_{\text{interpolation}} \tag{128c}$$

$$\Delta_{v,j} = (\dot{v}_{jc})_{\text{system derivative}} - (\dot{v}_{jc})_{\text{interpolation}} \tag{128d}$$

$$\Delta_{\gamma,j} = (\dot{\gamma}_{jc})_{\text{system derivative}} - (\dot{\gamma}_{jc})_{\text{interpolation}} \tag{128e}$$

$$\Delta_{\psi,j} = (\dot{\psi}_{jc})_{\text{system derivative}} - (\dot{\psi}_{jc})_{\text{interpolation}} \tag{128f}$$

Note that there are (6 states) $\times$ ($n-1$ time segments) defect equations, and there are six state variables whose initial and final values ($\mathbf{x}_{j0}$ and $\mathbf{x}_{jf}$) for the time segment[20] are varied to drive the defects ($\Delta_{r,j}$, $\Delta_{\phi,j}$, $\Delta_{\theta,j}$, $\Delta_{v,j}$, $\Delta_{\gamma,j}$, and $\Delta_{\psi,j}$) to zero.[21]

The initial boundary condition is $\mathbf{x}_{10}$, and $\mathbf{x}_{jf} = \mathbf{x}_{j+1,\,0}$ for $1 \le j \le n-1$ (i.e. for two consecutive time segments, the final state of the first time segment is the initial

[20]Except for the first time segment, where the initial conditions of the problem give the initial value of the state.

[21]However, for practical computational reasons, it may not be possible to actually enforce that each defect equal zero, so a tolerance of 10^{-6} has been set on the defects for this research.

state of the second time segment). If we number the states by time node rather than by using initial "$_0$" and final "$_f$" subscripts, we have

$$\mathbf{x} = \begin{bmatrix} r_2 \\ \phi_2 \\ \theta_2 \\ v_2 \\ \gamma_2 \\ \psi_2 \\ \vdots \\ r_n \\ \phi_n \\ \theta_n \\ v_n \\ \gamma_n \\ \psi_n \end{bmatrix} \tag{129}$$

as the vector of state variables $\mathbf{x}$ that are varied to drive the defects Δ to zero.

In addition to driving the defects Δ to zero to satisfy the equations of motion, for the trajectory reconstruction, it is desirable to minimize the sum of the squares of the residual error between the calculated body frame accelerations and the measured accelerations from the inertial measurement unit (equation (132)). Since the inertial measurement units measure accelerations in the body frame, the aerodynamic forces experienced by the spacecraft must be transformed to the body frame. This can be accomplished by using a transformation matrix $[A \rightarrow B]$ to transform the aerodynamic forces from the aerodynamic frame to the body frame.

$$[A \rightarrow B] = \begin{bmatrix} \cos\alpha\cos\beta & \sin\alpha\sin\sigma - \cos\alpha\sin\beta\cos\sigma & -\cos\alpha\sin\beta\sin\sigma - \sin\alpha\cos\sigma \\ \sin\beta & \cos\beta\cos\sigma & \cos\beta\sin\sigma \\ \sin\alpha\cos\beta & -\sin\alpha\sin\beta\cos\sigma - \cos\alpha\sin\sigma & \cos\alpha\cos\sigma - \sin\alpha\sin\beta\sin\sigma \end{bmatrix} \tag{130}$$

Using this matrix, for the calculated body frame accelerations, we have for each measurement time

$$\mathbf{a} = \begin{bmatrix} a_{\mathrm{x}} \\ a_{\mathrm{y}} \\ a_{\mathrm{z}} \end{bmatrix} = [A \rightarrow B] \begin{bmatrix} D \\ Y \\ L \end{bmatrix} \frac{1}{m} \tag{131}$$

The objective function for the accelerations $J_{\text{acceleration}}$ may be expressed as

$$J_{\text{acceleration}} = \sum_{i=1}^{n} \|\mathbf{a}_{\text{calculated}} - \mathbf{a}_{\text{measured}}\|_i^2 \tag{132}$$

where the objective is to minimize the sum of the squares of the difference between the calculated acceleration $\mathbf{a}_{\text{calculated}}$ and measured acceleration $\mathbf{a}_{\text{measured}}$ at each measurement time i for all the measurements n.

A summary of trajectory reconstruction using collocation as described above is given in Table 14 on page 91. Note that controls $\mathbf{u}$ are required for the more general problem, so in the context of the general problem, they appear in the state equation $\dot{\mathbf{x}} = \mathbf{f}(\mathbf{x}, \mathbf{u})$, and they would also be varied to obtain an optimal solution as shown in Table 14.

Table 14: Summary of trajectory reconstruction using collocation (TRUC).

Given:

$$\dot{\mathbf{x}} = \mathbf{f}(\mathbf{x}, \mathbf{u}) \tag{133}$$

Minimize:

$$J_{\text{acceleration}} = \sum_{i=1}^{n} \|\mathbf{a}_{\text{calculated}} - \mathbf{a}_{\text{measured}}\|_i^2 \tag{134}$$

Subject to:

$$\Delta = (\dot{x}_{jc})_{\text{system derivative}} - (\dot{x}_{jc})_{\text{interpolation}} = 0 \tag{135}$$

where the n measurements are taken in the time span, and the time span is divided into $n-1$ time segments j by the measurement times. The defects Δ above are calculated at the center of each time segment for each state variable with

$$(\dot{x}_{jc})_{\text{system derivative}} = \dot{x}|_{t_{jc}} \tag{136}$$

$$(\dot{x}_{jc})_{\text{interpolation}} = -\frac{3}{2}(x_{j0} - x_{jf}) + \frac{1}{4}(\dot{x}_{j0} + \dot{x}_{jf}) \tag{137}$$

by varying: the state vector $\mathbf{x}$ and the control vector $\mathbf{u}$.

Reconstructing the Trajectory Examining this trajectory reconstruction problem further reveals that there are several possible approaches to reconstructing the trajectory by solving the algebraic constraints from collocation.

1. One way:

   (a) All the unknown states would be adjusted simultaneously based on the optimization method chosen. (If this is the beginning of the optimization, all the unknown states would be initialized to some initial guess.)

   (b) The defect constraint of each time segment (equation (128)) would be checked to see if it is satisfied.

   (c) If the defect constraints are not satisfied, then the states would be adjusted again, and the defect constraints checked again.

   (d) If the defect constraints are satisfied, then the objective function (equation (132)) would be computed based on those states.

   (e) The new computed value of the objective function would be compared against the best minimum value found so far.

   (f) If the new computed value of the objective function was lower than the best minimum value found so far, then it would be saved, along with the values of the states, and the next iteration would begin.

   (g) This process would be repeated until the iteration limit was reached, or the unknown states were no longer significantly changing.

2. A second way, would use two sets of state variables at each node with unknown state variables, where one set is the final state for the preceding node, and the next set is the initial state for the following node. This way would require continuity constraints at each node to verify that the two sets of state variables

at each node with unknown state variables were close enough to be within the tolerance limit for continuity.

(a) All the unknown states would be adjusted simultaneously based on the optimization method chosen. (If this is the beginning of the optimization, all the unknown states would be initialized to some initial guess.)

(b) The defect constraint of each time segment (equation (128)) would be checked to see if it is satisfied.

(c) The continuity constraint at each node would be checked to see if it is satisfied.

(d) If the either the defect constraints are not satisfied, or the continuity constraints are not satisfied, then the states would be adjusted again, and the defect and continuity constraints checked again.

(e) If the defect constraints and continuity constraints are satisfied, the objective function (equation (132)) would be computed based on those states.

(f) The new computed value of the objective function would be compared against the best minimum value found so far.

(g) If the new computed value of the objective function was lower than the best minimum value found so far, then it would be saved, along with the values of the states, and the next iteration would begin.

(h) This process would be repeated until the iteration limit was reached, or the unknown states were no longer significantly changing.

3. A third way, could use either of the above methods with the initial state used as an additional unknown in the optimization, and add a constraint to satisfy the initial condition.

4. A fourth way, assuming no information on uncertainty was desired, could use any of the above methods with a fixed initial condition and a fixed final condition.

And there are probably many more variations that could be proposed by changing subtle features. And while they may result in small improvements in minimizing the objective function given in Table 14, the computational effort involved in obtaining that small gain is likely to not be worth the effort.

An Alternative Method So let us propose an alternative method for finding the state values at each node in a deterministic fashion that does not require an optimizer. Using it will not necessarily result in minimizing the objective function (equation (132)) proposed above, and in fact, the objective function is not necessary for its implementation. In its essence, it is simply an integration of the trajectory[22], and therefore, a simulation not a true reconstruction.[23] However, this is not to be dismissed. Chapters 4 and 5 will show that it is enough like integration, that if the values of the controls are defined at every node in the entire trajectory, this research posits that it is not necessary to vary the states at each node as independent variables in an optimization process, as they can be determined directly from the values of the controls and the parameters of the problem.[24] This result means that only the controls have to be independent variables in an optimization (or nonlinear programming) process used to solve an entry, descent, and landing trajectory reconstruction problem transcribed by collocation into a set of algebraic constraints. This reduction in the

[22]The equivalence of Runge–Kutta methods and collocation methods has already been established. [12]

[23]Modeling the problem here on an equal basis with the Kalman filters is equivalent to simulating the trajectory using collocation.

[24]If you accept that integration is being done, then you also understand that there is only one valid solution. With only one valid solution, then, if you do a reconstruction using a method as described above, you will sacrifice the validity of the solution in order to obtain a lower value of the objective function.

number of independent variables greatly reduces the solution space that must be searched.

Now, let us describe the solution procedure.

Recall that there are no control variables, as the angle of attack α, the side–slip angle β, and the bank angle σ for the spacecraft are set to zero for the duration of the trajectory to be consistent with the process models of the two Kalman filters, so the three methods can be compared on an equal basis. Consider the defects in the first ($j = 1$) time segment shown below in equation (138).

$$\Delta_{r,1} = (\dot{r}_{1,c})_{\text{system derivative}} - (\dot{r}_{1,c})_{\text{interpolation}} \tag{138a}$$

$$\Delta_{\phi,1} = (\dot{\phi}_{1,c})_{\text{system derivative}} - (\dot{\phi}_{1,c})_{\text{interpolation}} \tag{138b}$$

$$\Delta_{\theta,1} = (\dot{\theta}_{1,c})_{\text{system derivative}} - (\dot{\theta}_{1,c})_{\text{interpolation}} \tag{138c}$$

$$\Delta_{v,1} = (\dot{v}_{1,c})_{\text{system derivative}} - (\dot{v}_{1,c})_{\text{interpolation}} \tag{138d}$$

$$\Delta_{\gamma,1} = (\dot{\gamma}_{1,c})_{\text{system derivative}} - (\dot{\gamma}_{1,c})_{\text{interpolation}} \tag{138e}$$

$$\Delta_{\psi,1} = (\dot{\psi}_{1,c})_{\text{system derivative}} - (\dot{\psi}_{1,c})_{\text{interpolation}} \tag{138f}$$

The defects of the first time segment are a function of the interpolated system derivatives at the center of the time segment and the system derivatives at the center of the time segment from the equations of motion given in equations (121) through (209). The system derivatives from the equations of motion are a function of the state, and by examining the expressions for the interpolated system derivatives in equation (139), we see that they also are only a function of the state, specifically the final value of the state for the time segment since the initial state is specified from the initial conditions of the problem.

$$\dot{r}_{1,c} = -\frac{3}{2T_1}(r_{1,0} - r_{1,f}) - \frac{1}{4}(\dot{r}_{1,0} + \dot{r}_{1,f}) \tag{139a}$$

$$\dot{\phi}_{1,c} = -\frac{3}{2T_1}(\phi_{1,0} - \phi_{1,f}) - \frac{1}{4}(\dot{\phi}_{1,0} + \dot{\phi}_{1,f}) \tag{139b}$$

$$\dot{\theta}_{1,c} = -\frac{3}{2T_1}(\theta_{1,0} - \theta_{1,f}) - \frac{1}{4}(\dot{\theta}_{1,0} + \dot{\theta}_{1,f}) \tag{139c}$$

$$\dot{v}_{1,c} = -\frac{3}{2T_1}(v_{1,0} - v_{1,f}) - \frac{1}{4}(\dot{v}_{1,0} + \dot{v}_{1,f}) \tag{139d}$$

$$\dot{\gamma}_{1,c} = -\frac{3}{2T_1}(\gamma_{1,0} - \gamma_{1,f}) - \frac{1}{4}(\dot{\gamma}_{1,0} + \dot{\gamma}_{1,f}) \tag{139e}$$

$$\dot{\psi}_{1,c} = -\frac{3}{2T_1}(\psi_{1,0} - \psi_{1,f}) - \frac{1}{4}(\dot{\psi}_{1,0} + \dot{\psi}_{1,f}) \tag{139f}$$

So the six defects given in equation (138) constitute a set of six equations in six unknowns. To solve this set of equations:

First, we set the final state for the segment equal to the initial state for the segment. The initial state is a convenient guess for the final state.

$$\mathbf{x}_f = \mathbf{x}_0 \tag{140}$$

as a consequence of this, the time derivatives of the initial and final states are also equal.

$$\dot{\mathbf{x}}_f = \dot{\mathbf{x}}_0 \tag{141}$$

Then, we substitute the formula for the interpolated derivative at the center of the time segment into the defect vector equation, set the defect vector equal to zero, and solve for the time segment's final state.

$$\mathbf{x}_f = \mathbf{x}_0 + \frac{2T}{3}\left((\dot{\mathbf{x}}_c)_{\text{system derivative}} + \frac{1}{4}(\dot{\mathbf{x}}_0 + \dot{\mathbf{x}}_f)\right) \tag{142}$$

Using this final state, we can calculate the new final values of the time derivatives for the time segment.

$$\dot{\mathbf{x}}_f = \mathbf{f}(\mathbf{x}_f) \tag{143}$$

Using the known values of the initial state and its time derivatives, along with the

values of the final state and its time derivatives calculated above, we can calculate the interpolated value of the state at the center of the time segment.

$$\mathbf{x}_c = \frac{1}{2}(\mathbf{x}_0 + \mathbf{x}_f) + \frac{T}{8}(\dot{\mathbf{x}}_0 - \dot{\mathbf{x}}_f) \tag{144}$$

We then calculate its interpolated derivative

$$\dot{\mathbf{x}}_c = -\frac{3}{2T}(\mathbf{x}_0 - \mathbf{x}_f) - \frac{1}{4}(\dot{\mathbf{x}}_0 + \dot{\mathbf{x}}_f) \tag{145}$$

and its system derivative.

$$(\dot{\mathbf{x}}_c)_{\text{system derivative}} = \mathbf{f}(\mathbf{x}_c) \tag{146}$$

And, now, we can calculate the new defect vector for the time segment.

$$\boldsymbol{\Delta} = (\dot{\mathbf{x}}_c)_{\text{system derivative}} - (\dot{\mathbf{x}}_c)_{\text{interpolation}} \tag{147}$$

We can then repeat this process until all the elements of the defect vector are driven to zero.[25] This procedure can then be repeated for each time segment until the last node is reached. Alternatively, if we consider the defects for the entire trajectory as constituting a system of $6 \times (n-1)$–equations in $6 \times (n-1)$–unknowns, the state at each node could be set to the initial state, and the procedure could be implemented on the entire trajectory at once. A summary of this solution procedure is given in Table 15 on page 98.

Additionally, this research posits that for entry, descent, and landing trajectory design with both states and controls using collocation, the solution procedure given in Table 15 could be used to calculate the states that allow the defect constraints from collocation to be met at each iteration of the optimization, while using only the control variables as the independent variables of the optimization.

[25] Or below our defect tolerance.

Table 15: The solution procedure to obtain states that meet the defect constraints of collocation when given a set values for the controls. This procedure can be used when performing trajectory simulation using collocation (TSUC) or trajectory reconstruction using collocation (TRUC).

Given:

$$\dot{\mathbf{x}} = \mathbf{f}(\mathbf{x}) \tag{148}$$

and an initial condition $\mathbf{x}_0$.

Initialization: For $j = 1$, set $\mathbf{x}_{1,f} = \mathbf{x}_{1,0}$ and $\dot{\mathbf{x}}_{1,f} = \dot{\mathbf{x}}_{1,0}$.

Computation: For each time segment $j = 1, 2, ...$, compute:

An update to the final value of the state

$$\mathbf{x}_{jf} = \mathbf{x}_0 + \frac{2T_j}{3}\left((\dot{\mathbf{x}}_{jc})_{\text{system derivative}} + \frac{1}{4}(\dot{\mathbf{x}}_{j0} + \dot{\mathbf{x}}_{jf})\right) \tag{149}$$

The final value of the state time derivative

$$\dot{\mathbf{x}}_{jf} = \mathbf{f}(\mathbf{x}_{jf}) \tag{150}$$

The interpolated state at the center of the time segment

$$\mathbf{x}_{jc} = \frac{1}{2}(\mathbf{x}_{j0} + \mathbf{x}_{jf}) + \frac{T_j}{8}(\dot{\mathbf{x}}_{j0} - \dot{\mathbf{x}}_{jf}) \tag{151}$$

Its interpolated derivative

$$(\dot{\mathbf{x}}_{jc})_{\text{interpolation}} = -\frac{3}{2T_j}(\mathbf{x}_{j0} - \mathbf{x}_{jf}) - \frac{1}{4}(\dot{\mathbf{x}}_{j0} + \dot{\mathbf{x}}_{jf}) \tag{152}$$

And its system derivative

$$(\dot{\mathbf{x}}_{jc})_{\text{system derivative}} = \mathbf{f}(\mathbf{x}_{jc}) \tag{153}$$

The new defect vector

$$\boldsymbol{\Delta}_j = (\dot{\mathbf{x}}_{jc})_{\text{system derivative}} - (\dot{\mathbf{x}}_{jc})_{\text{interpolation}} \tag{154}$$

Then repeat this process until all the elements of the defect vector for time segment j are driven to zero.

Finally, repeat this procedure for each time segment j until the final state at the last node has been found.*

---

*Though the sequential formulation above is used here, it is possible, to implement this solution method in a simultaneous manner by solving for all the unknown states at once, rather than repeating it for each time segment. However, due to the presence of the initial condition, that is not necessary though it would allow parallelization that would speed up the computation.

CHAPTER IV

TRAJECTORY RECONSTRUCTION OF A SAMPLE PROBLEM

As stated earlier, extended Kalman filtering (EKF) has been used extensively in trajectory reconstruction both for orbiting spacecraft and for planetary probes. It forms the standard to which the unscented Kalman filtering (UKF) will be compared. Additionally, trajectory simulation using collocation (TSUC) is conducted. The two Kalman filters are used to reconstruct the entry, descent, and landing trajectory of a sample problem similar to Mars Pathfinder, while collocation is used to simulate it. The purpose of this sample problem is to understand the capabilities of the Kalman filters when the true trajectory is known, and to compare the results from trajectory simulation using collocation using the solution procedure of Table 15 to the Monte Carlo simulation conducted using explicit integration of the dynamics.

4.1 Description of the Sample Problem

As a sample problem, a *Mars Pathfinder*–like vehicle entry at Mars was simulated, so the trajectory could be reconstructed. The sample problem's entry conditions are given in Table 16 and the acceleration time history is given Figure 28. The sample problem was created in the same simulation environment as the one the trajectory reconstructions were performed in. However, noise was added to the accelerations obtained from the true trajectory of the sample problem to simulate noisy acceleration data from an inertial measurement unit. The mean noise level for the simulated acceleration measurements was 0 μg with a standard deviation of 1500 μg, and the measurement frequency was 32 Hz. The sample problem entry vehicle did not jettison

any mass during entry, and parachute deployment occurred at approximately 142 s. The simulation was ended when the altitude of the entry vehicle reached 0.268 km. Plots of the altitude, velocity, and flight path angle time histories are given in Figures 29, 30, and 31, respectively. The density profile of the Martian atmosphere for the sample problem is shown in Figure 117.

Table 16: The values of the sample problem's state variables at entry.

State Variable	Mean	Uncertainty (1σ)
Radius	3 522 200 m	1 000 m
Aerocentric latitude	22.630 3°N	0.1°
Longitude	337.997 6°E	0.1°
Inertial velocity	7 264.2 $\frac{\text{m}}{\text{s}}$	1.0 $\frac{\text{m}}{\text{s}}$
Inertial flight path angle	-14.061 4°	0.1°
Inertial azimuth	253.148 1°	0.1°

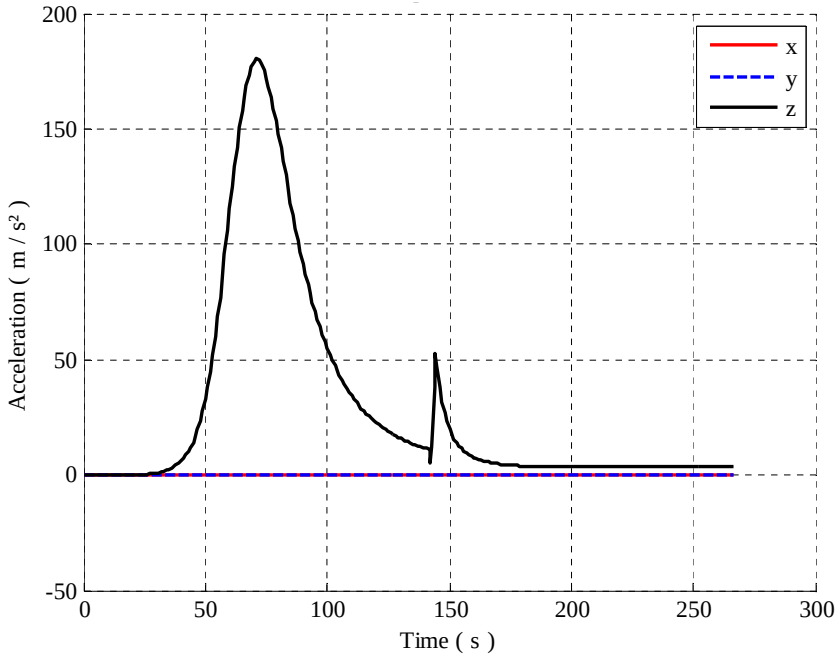

Figure 28: Sample problem acceleration time history.

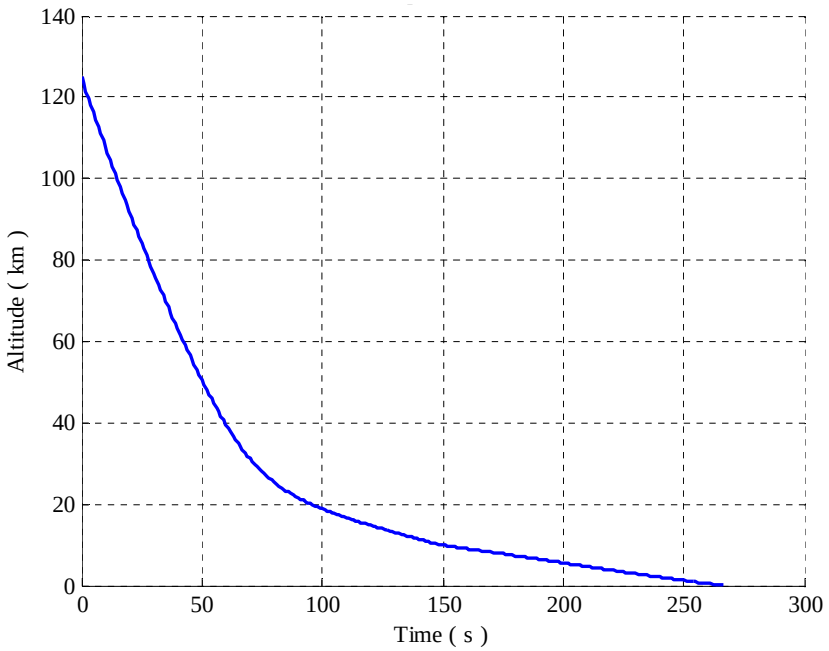

Figure 29: Sample problem altitude time history.

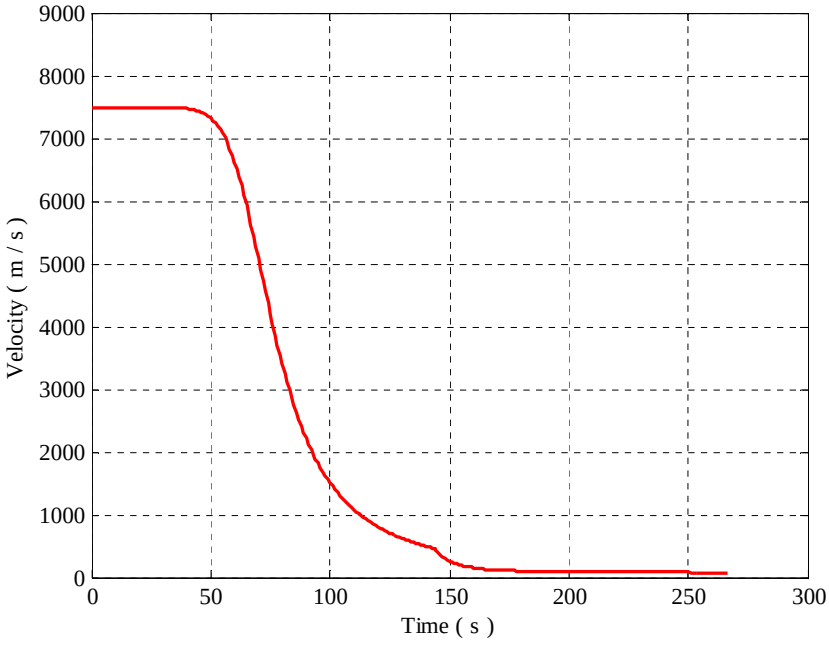

Figure 30: Sample problem velocity time history.

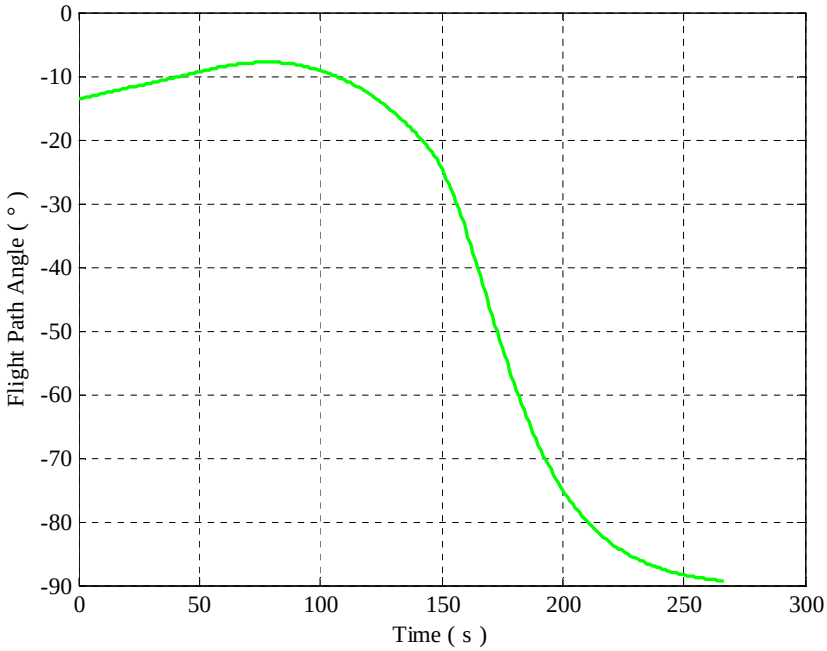

Figure 31: Sample problem flight path angle time history.

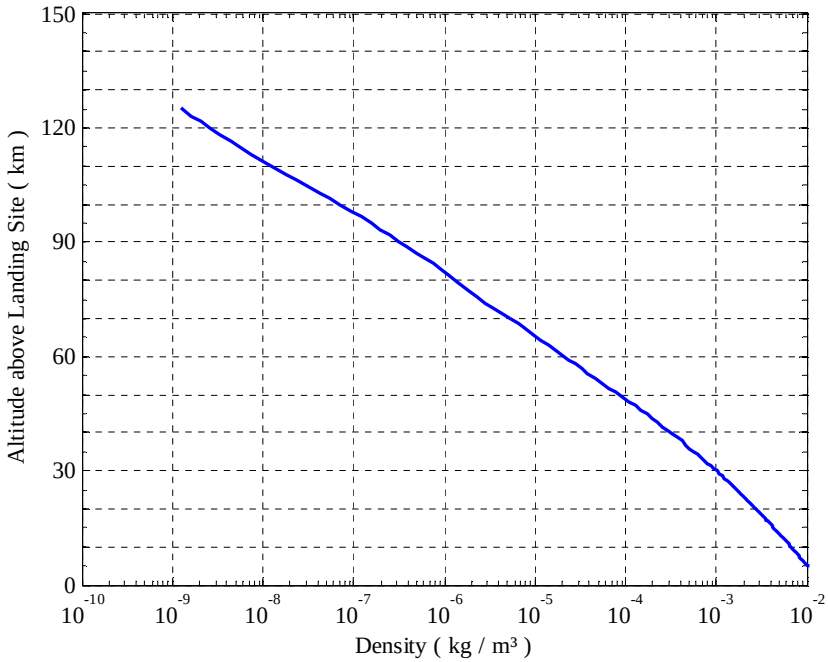

Figure 32: Sample problem atmospheric density profile.

4.2 Trajectory Performance for the Sample Problem

Each of the Kalman filters discussed in Chapter 3 was used to reconstruct the trajectory of the simulated sample problem, and the trajectory was simulated using collocation.

4.2.1 Altitude

The reconstruction of the sample problem altitude is shown in Figure 33. Each of the Kalman filters discussed in Chapter 3 appear to agree well with the simulated sample problem, and the residuals of the time history of the sample problem altitude and the reconstructions shown in Figure 33 are shown in Figure 34. Note the increasing divergence of the extended Kalman filter from the simulated sample problem beginning near the time of parachute deployment. The unscented Kalman filter maintains good agreement with the simulated sample problem, even though it deviates slightly from the simulation near the end of the trajectory. TSUC also maintains good agreement with the simulated sample problem.

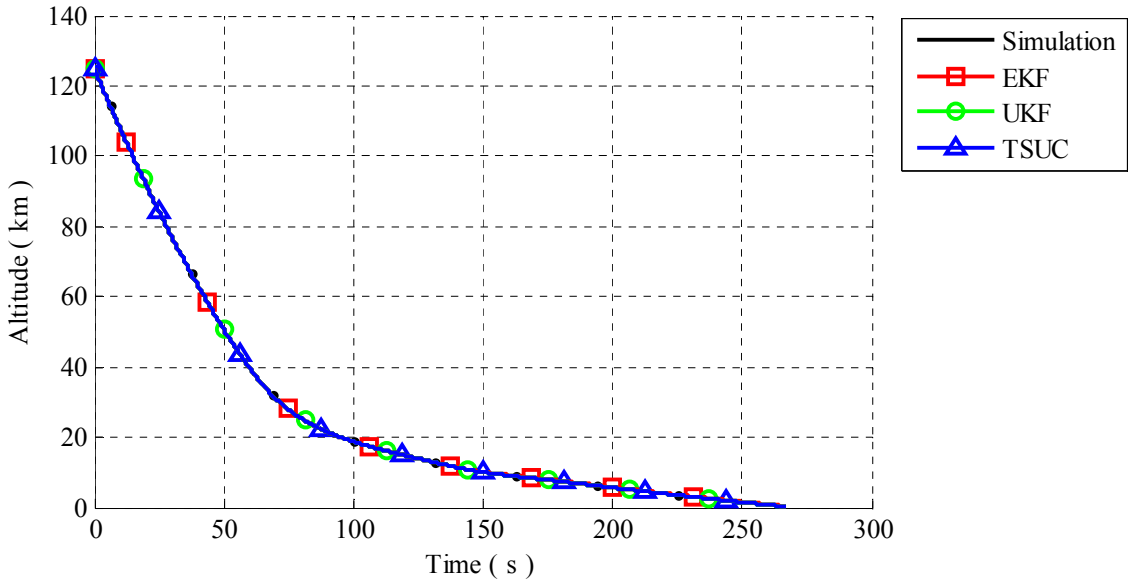

Figure 33: The time history of the sample problem altitude is reconstructed and simulated.

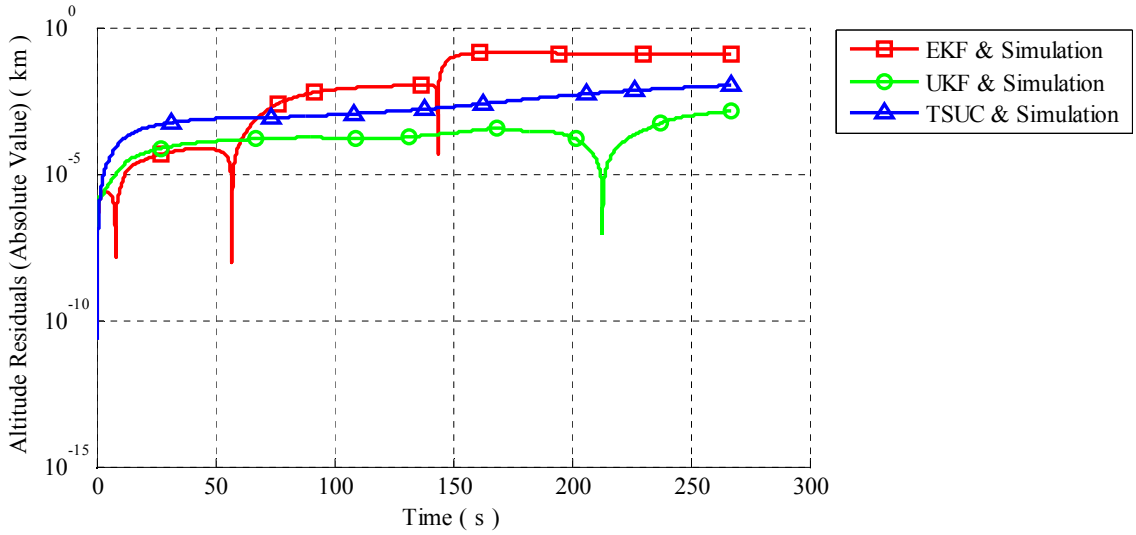

Figure 34: The residuals of the time history of the sample problem altitude shown in the previous figure.

4.2.2 Velocity

The reconstruction of the sample problem velocity is shown in Figure 35. Both Kalman filters discussed in Chapter 3 appear to agree well with the simulated sample problem, and the residuals of the time history of the sample problem velocity and the reconstructions shown in Figure 35 are shown in Figure 36. Note the divergence of the extended Kalman filter from the simulated sample problem velocity beginning near the time of parachute deployment and the subsequent recovery approximately 50 seconds later. The recovery is most likely due to the spacecraft reaching terminal velocity on the parachute, as the terminal velocity is the same regardless of the method used for reconstruction. The unscented Kalman filter maintains good agreement with the simulated sample problem's velocity throughout the entire trajectory. TSUC also maintains good agreement with the simulated sample problem.

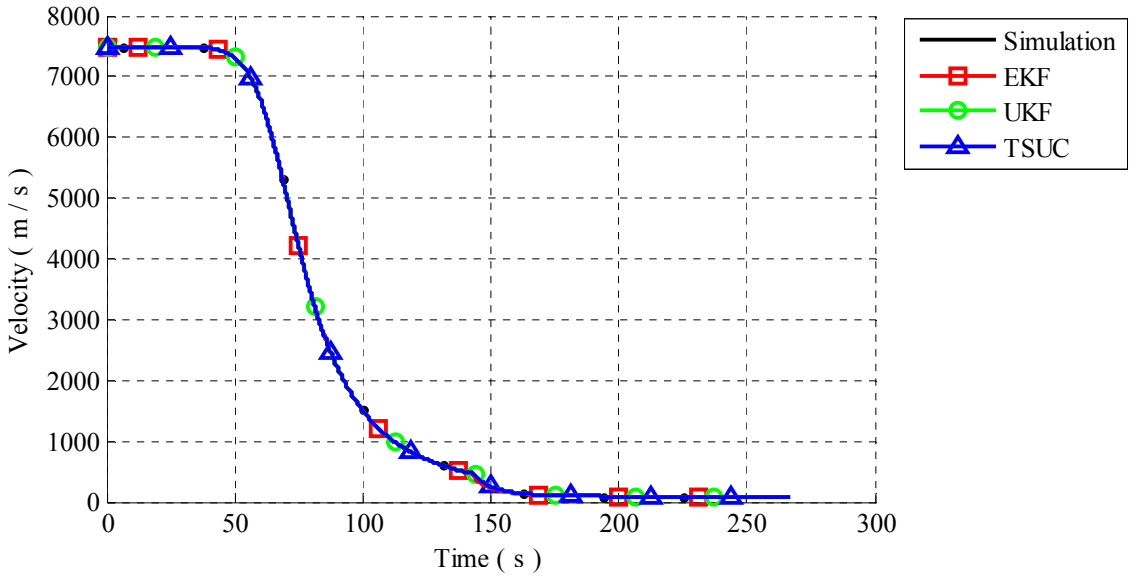

Figure 35: The time history of the sample problem velocity is reconstructed and simulated.

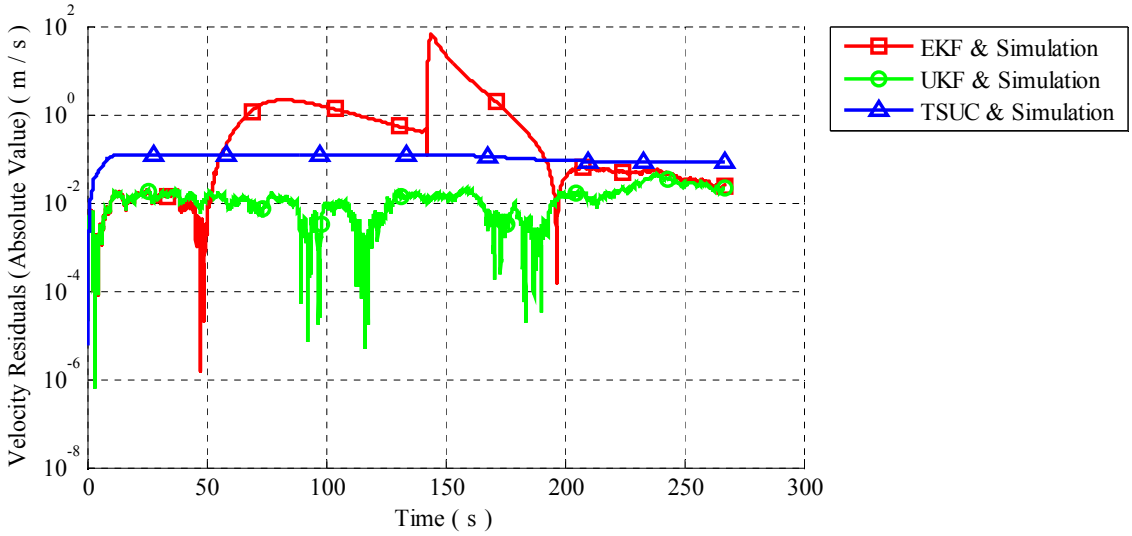

Figure 36: The residuals of the time history of the sample problem velocity shown in the previous figure.

4.2.3 Flight Path Angle

The reconstruction of the sample problem flight path angle is shown in Figure 37. Both Kalman filters discussed in Chapter 3 appear to agree well with the simulated

sample problem, and the residuals of the time history of the sample problem flight path angle and the reconstructions shown in Figure 37 are shown in Figure 38. Note the divergence of the extended Kalman filter from the simulated sample problem flight path angle beginning near the time of parachute deployment and the subsequent recovery near the end of the trajectory. The unscented Kalman filter maintains good agreement with the simulated sample problem's flight path angle throughout the entire trajectory with some slight variation. TSUC also maintains good agreement with the simulated sample problem

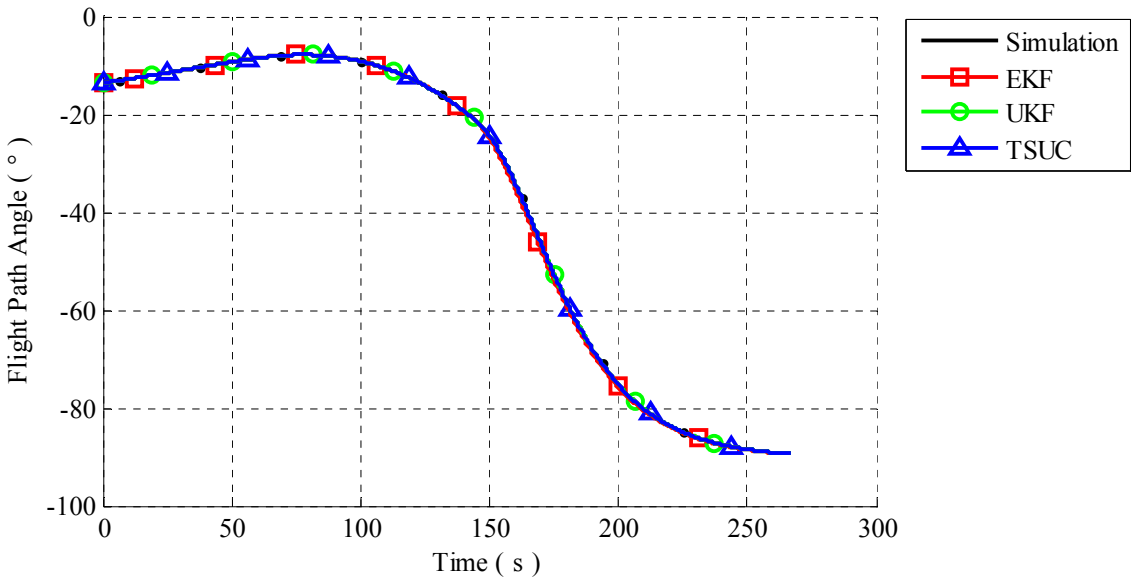

Figure 37: The time history of the sample problem flight path angle is reconstructed and simulated.

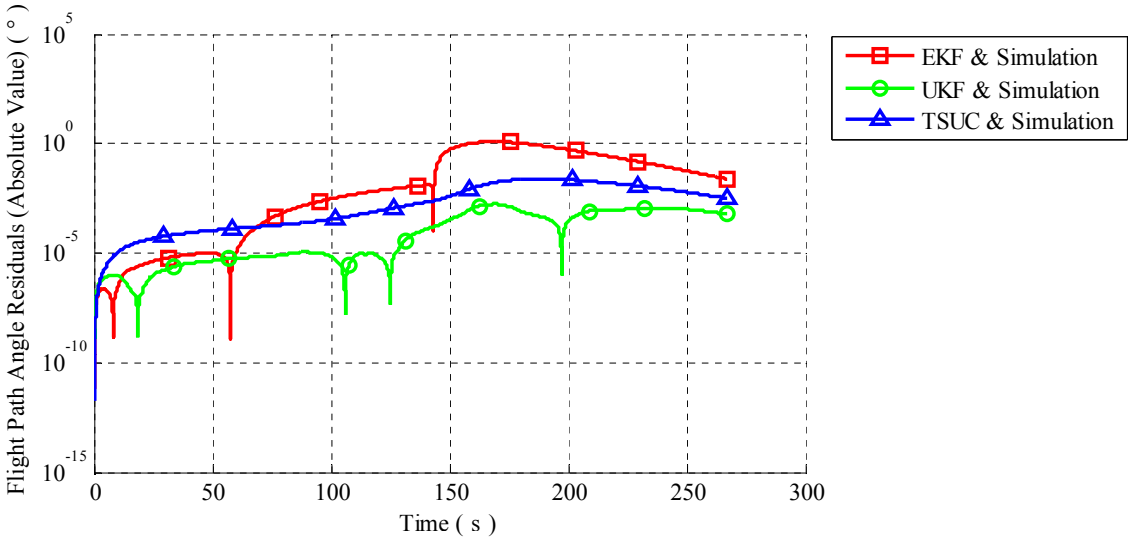

Figure 38: The residuals of the time history of the sample problem flight path angle shown in the previous figure.

4.3 Monte Carlo Solution Space for the Sample Problem

Next, a 10,000 run Monte Carlo simulation was performed by sampling from the initial condition distributions shown in Table 16 on page 100. For each trajectory run in the Monte Carlo simulation, the sample problem acceleration data was integrated from the chosen initial condition. This was done in an attempt to characterize the mean and uncertainty of the solution space, so that they could be compared with the predictions from the methods discussed in Chapter 3.[1] The extended Kalman filter results and the unscented Kalman filter results from the previous section are compared here with the mean of the Monte Carlo solution space for the sample problem dynamics.[2] Both Kalman filters were expected to predict the mean trajectory well, and this was indeed the case. Regarding the uncertainty around their best

[1]Note that for this comparison, the initial conditions for the extended Kalman filter and the unscented Kalman filter were the mean initial conditions as discussed in Chapter 3. The initial conditions for the TSUC Monte Carlo were sampled at random from the entry state distributions given in Table 16.

[2]In the next section, each Monte Carlo run will be done with the Kalman filters, rather than just with the dynamics.

estimates of the (mean) trajectory, the extended Kalman filter did not perform as well as the unscented Kalman filter, though this result was expected based on the literature. TSUC's simulation of the uncertainty around the mean trajectory also compared well with the Monte Carlo simulation.

A Note on Monte Carlo Simulations In the real world, there are many more sources of error that should be included in Monte Carlo simulations. Beyond the entry state, uncertainty exists in such things as:

- The dynamics model
- The gravitational model
- The atmospheric model including density, pressure, temperature, and winds
- The aerodynamic coefficients of the spacecraft
- The mass of the spacecraft
- The location of the center of mass of the spacecraft
- The moment of inertias of the spacecraft

However, as there was no error from these sources in the sample problem's true trajectory, there is no need to account for them in the Monte Carlo simulations for the sample problem. Because the sample problem trajectory was run in the same simulation as the reconstructions, uncertainty from any of the sources listed above would have to be explicitly added. The only noise added was the noise added to the acceleration data, as discussed earlier.

4.3.1 Altitude

The mean altitude from the Monte Carlo simulation is shown in Figure 39 with the best estimate (mean) altitude from the Kalman filters and TSUC's mean. Both

Kalman filters appear to agree well with the mean Monte Carlo altitude, and the residuals of the altitude time histories shown in Figure 39 relative to the mean Monte Carlo altitude are shown in Figure 40. Note the increasing divergence of the extended Kalman filter from the mean Monte Carlo altitude beginning near the time of parachute deployment. The unscented Kalman filter continues to maintain good agreement with the mean Monte Carlo altitude, even though they deviate slightly from the mean Monte Carlo altitude near the end of the trajectory. TSUC's simulation also compared well with the Monte Carlo simulation.

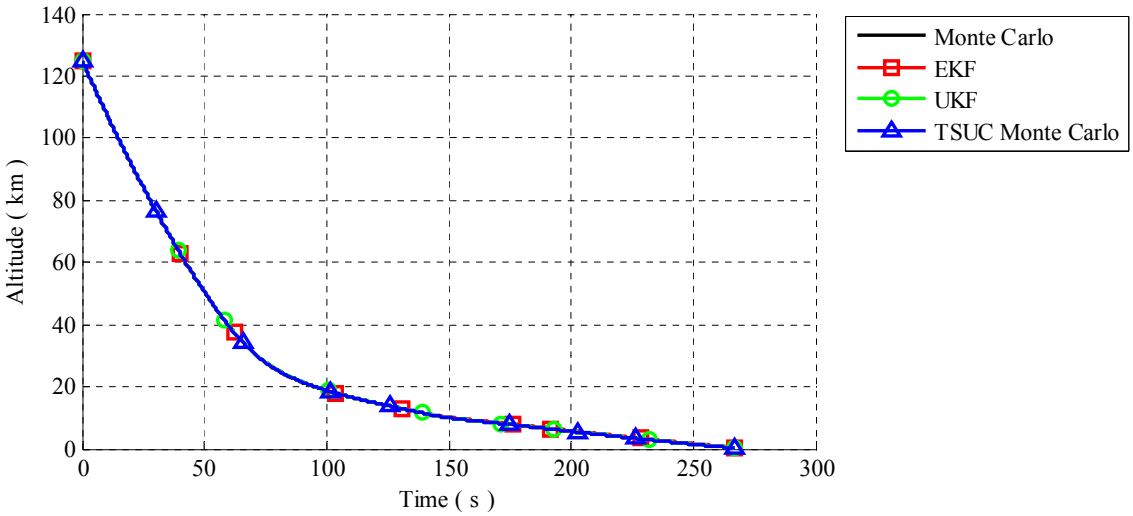

Figure 39: The mean altitude from the Monte Carlo simulation is shown with the best estimate (mean) altitude from the Kalman filters and TSUC's mean.

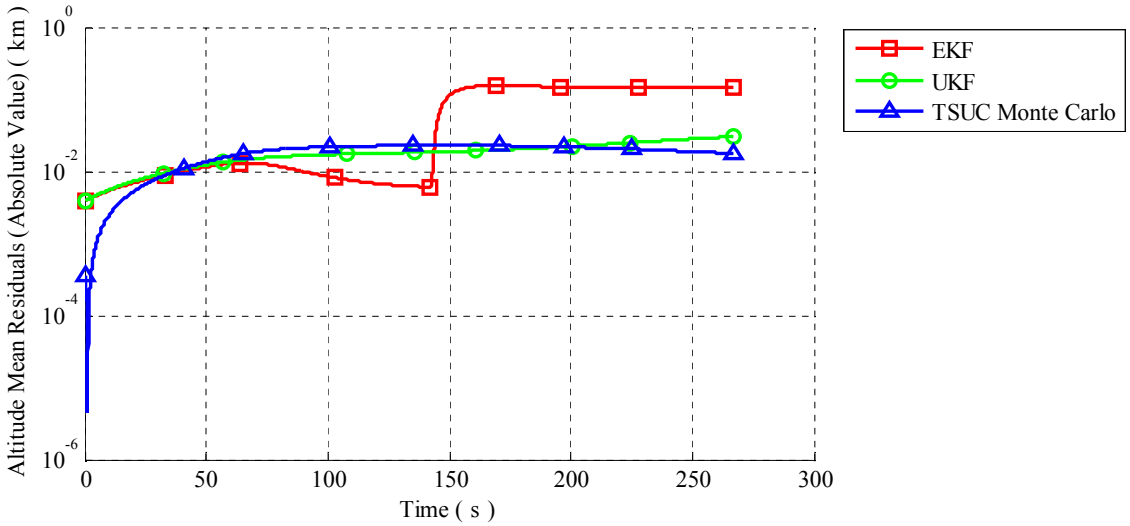

Figure 40: The residuals of the altitude time histories shown in the previous figure relative to the mean Monte Carlo altitude.

The 3σ uncertainty for altitude from the Monte Carlo simulation is shown in Figure 41 with the propagated 3σ uncertainty for altitude from the Kalman filters. The prediction of the 3σ uncertainty for altitude by the methods discussed in Chapter 3 agree well with the uncertainty for altitude from the Monte Carlo simulation for approximately the first 60 seconds of the trajectory. At that point, the extended Kalman filter's prediction begins to diverge from the Monte Carlo simulation and decreases until it settles near the initial value of the 3σ uncertainty for altitude. The unscented Kalman filter continues to maintain good agreement with the Monte Carlo simulation's 3σ uncertainty for altitude throughout the entire trajectory. TSUC also agrees well with the Monte Carlo. The residuals of the 3σ uncertainty for altitude shown in Figure 41 relative to the Monte Carlo simulation's 3σ uncertainty for altitude are shown in Figure 42.

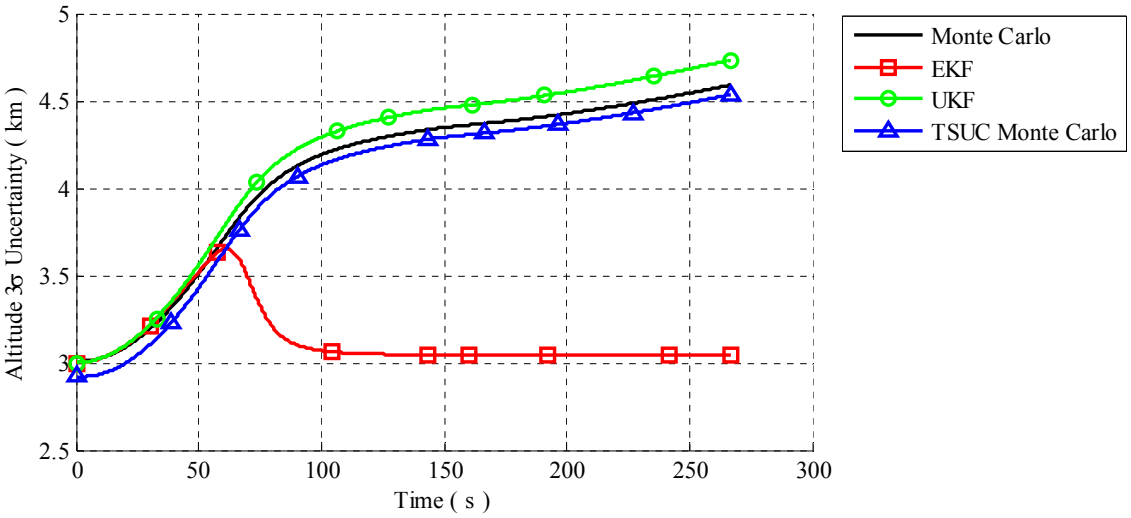

Figure 41: The 3σ uncertainty for altitude from the Monte Carlo simulation is shown with the propagated 3σ uncertainty for altitude from the Kalman filters and TSUC's 3σ uncertainty.

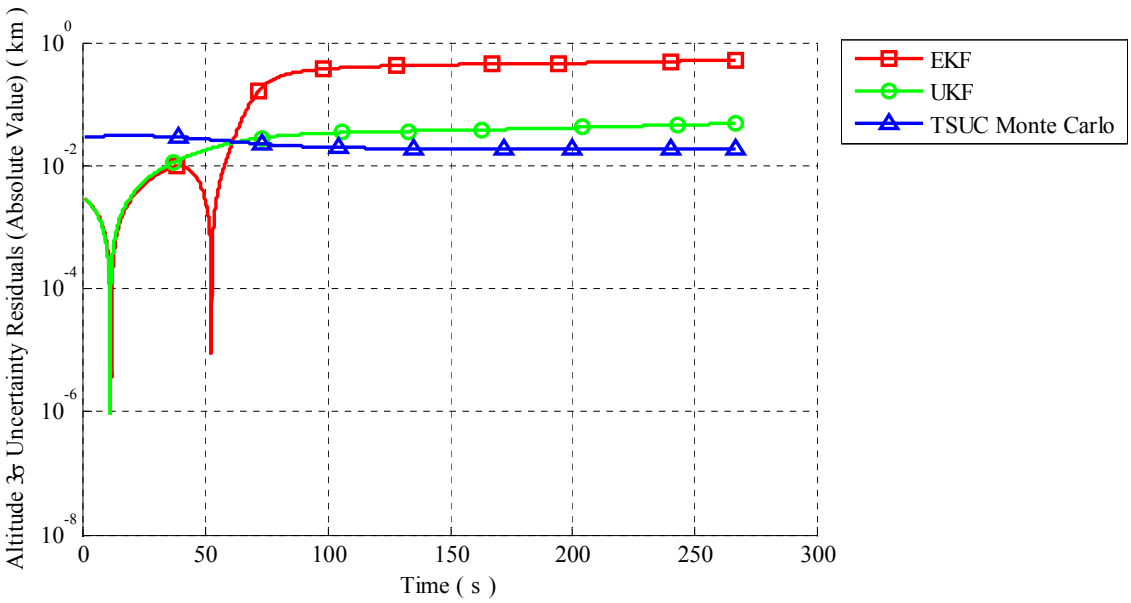

Figure 42: The residuals of the 3σ uncertainty for altitude shown in the previous figure relative to the Monte Carlo simulation's 3σ uncertainty for altitude.

4.3.2 Velocity

The mean velocity from the Monte Carlo simulation is shown in Figure 43 with the best estimate (mean) velocity from the Kalman filters. Both Kalman filters discussed in Chapter 3 appear to agree well with the mean Monte Carlo velocity, and the residuals of the velocity time histories shown in Figure 43 relative to the mean Monte Carlo velocity are shown in Figure 44. Note the divergence of the extended Kalman filter from the mean Monte Carlo velocity beginning near the time of parachute deployment and the subsequent recovery approximately 50 seconds later. The recovery is most likely due to the spacecraft reaching terminal velocity on the parachute, as the terminal velocity is the same regardless of the method used for reconstruction. The unscented Kalman filter and TSUC maintain good agreement with the mean Monte Carlo velocity throughout the entire trajectory.

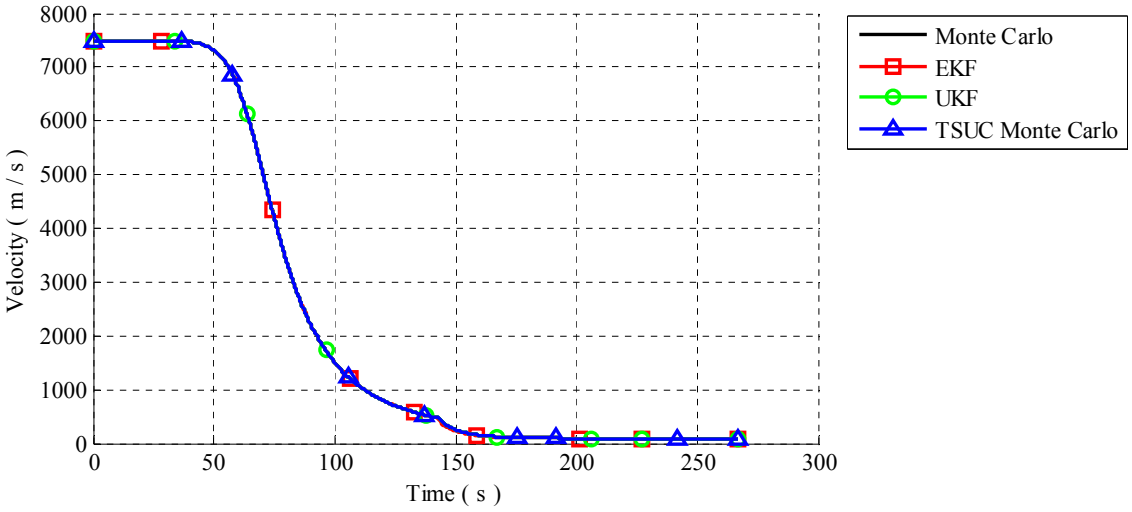

Figure 43: The mean velocity from the Monte Carlo simulation is shown with the best estimate (mean) velocity from the Kalman filters and TSUC's mean.

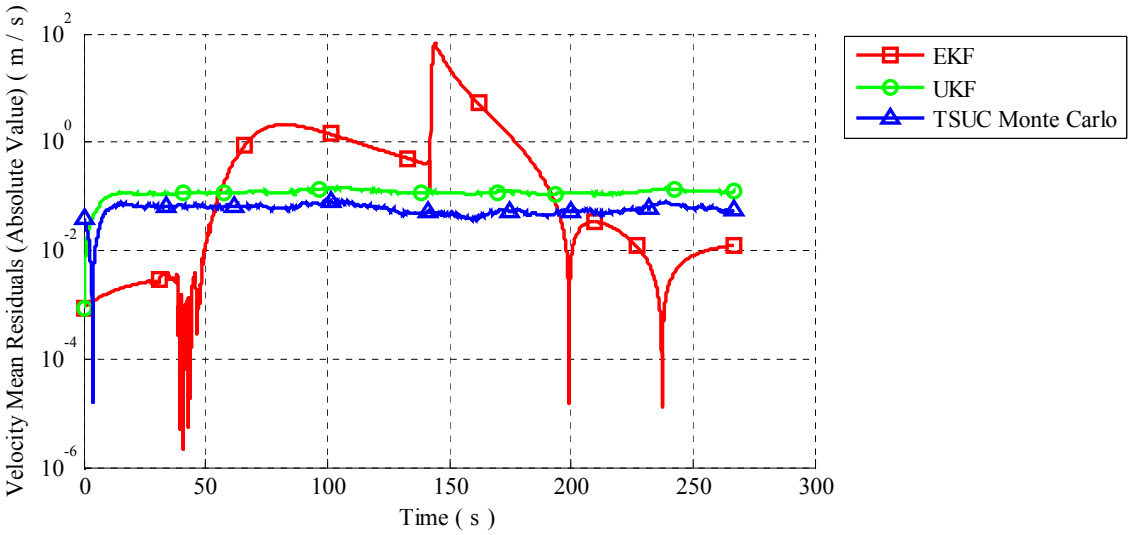

Figure 44: The residuals of the velocity time histories shown in the previous figure relative to the mean Monte Carlo velocity.

The 3σ uncertainty for velocity from the Monte Carlo simulation is shown in Figure 45 with the propagated 3σ uncertainty for velocity from the Kalman filters. The prediction of the 3σ uncertainty for velocity by the Kalman filters discussed in Chapter 3 agree well with the uncertainty for velocity from the Monte Carlo simulation for approximately the first 35 seconds of the trajectory. At that point, the extended Kalman filter's prediction begins to diverge from the Monte Carlo simulation and decreases until it settles near zero. The unscented Kalman filter continues to maintain good agreement with the Monte Carlo simulation's 3σ uncertainty for velocity throughout the entire trajectory. TSUC also agrees well with the Monte Carlo. The residuals of the 3σ uncertainty for velocity shown in Figure 45 relative to the Monte Carlo simulation's 3σ uncertainty for velocity are shown in Figure 46.

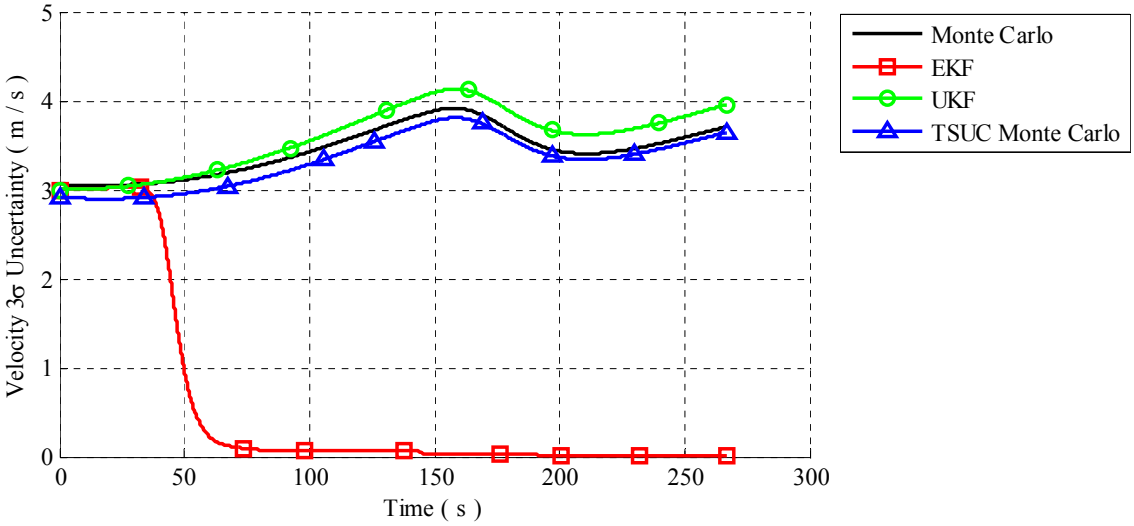

Figure 45: The 3σ uncertainty for velocity from the Monte Carlo simulation is shown with the propagated 3σ uncertainty for velocity from the Kalman filters and TSUC's 3σ uncertainty.

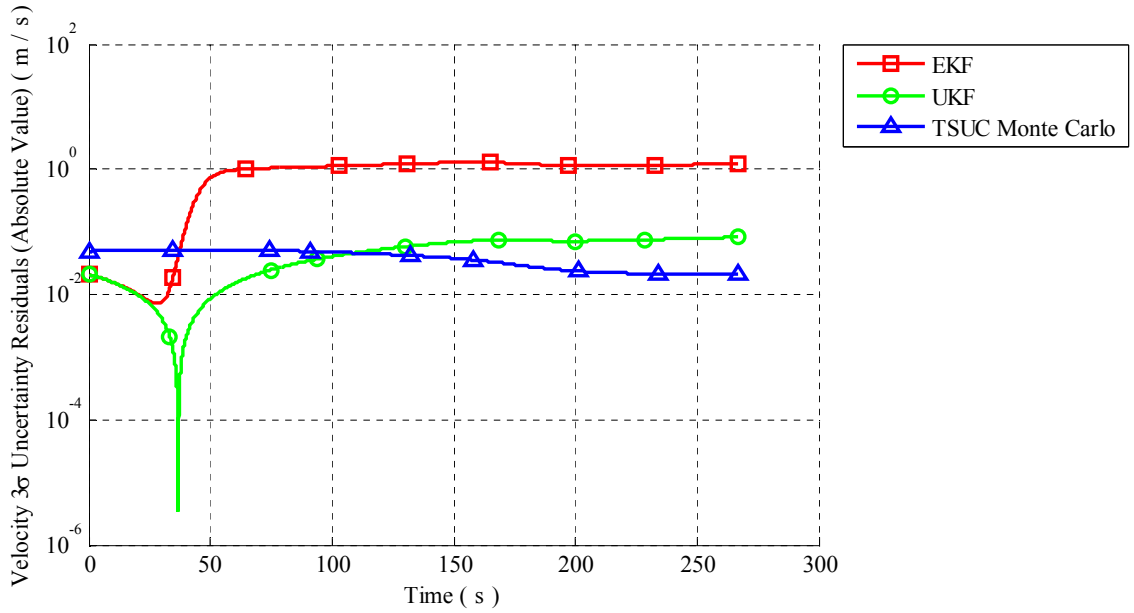

Figure 46: The residuals of the 3σ uncertainty for velocity shown in the previous figure relative to the Monte Carlo simulation's 3σ uncertainty for velocity.

4.3.3 Flight Path Angle

The mean flight path angle from the Monte Carlo simulation is shown in Figure 47 with the best estimate (mean) flight path angle from the Kalman filters. Both Kalman filters discussed in Chapter 3 appear to agree well with the mean Monte Carlo flight path angle, and the residuals of the flight path angle time histories shown in Figure 47 relative to the mean Monte Carlo flight path angle are shown in Figure 48. Note the divergence of the extended Kalman filter from the mean Monte Carlo flight path angle beginning near the time of parachute deployment and the subsequent recovery near the end of the trajectory. The unscented Kalman filter and TSUC maintain good agreement with the simulated sample problem's flight path angle throughout the entire trajectory with some slight variation.

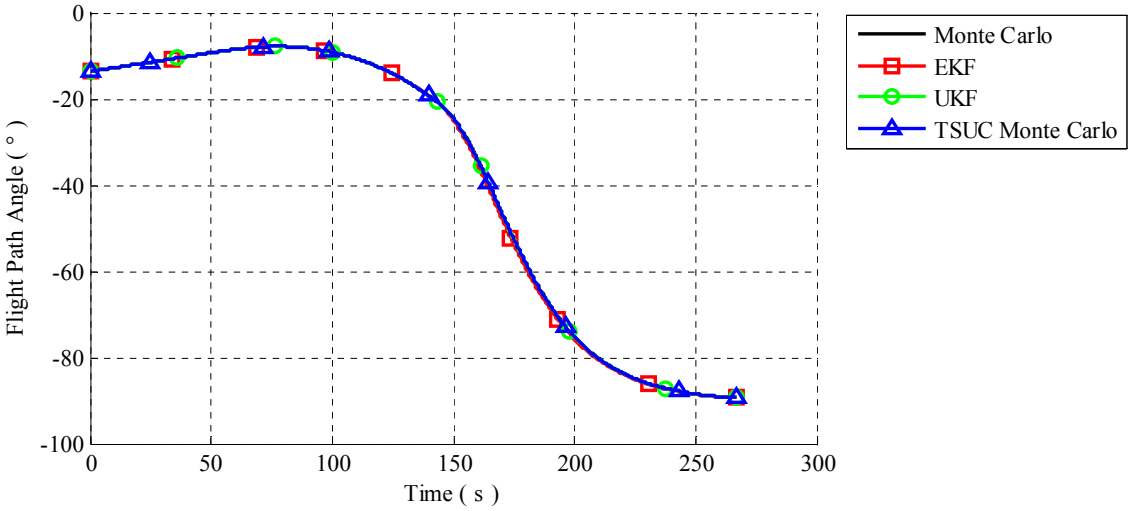

Figure 47: The mean flight path angle from the Monte Carlo simulation is shown with the best estimate (mean) flight path angle from the Kalman filters and TSUC's mean.

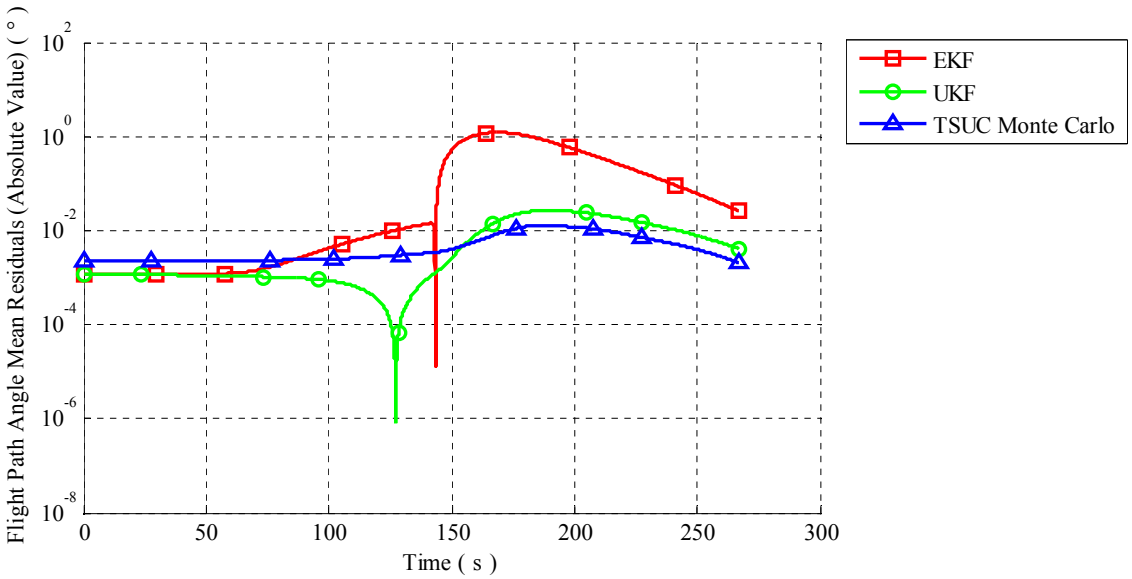

Figure 48: The residuals of the flight path angle time histories shown in the previous figure relative to the mean Monte Carlo flight path angle.

The 3σ uncertainty for flight path angle from the Monte Carlo simulation is shown in Figure 49 with the propagated 3σ uncertainty for flight path angle from the Kalman filters. The prediction of the 3σ uncertainty for flight path angle by the Kalman filters discussed in Chapter 3 agree well with the uncertainty for flight path angle from the Monte Carlo simulation for approximately the first 50 seconds of the trajectory. At that point, the extended Kalman filter's prediction begins to diverge from the Monte Carlo simulation and decreases until it settles near zero. The unscented Kalman filter continues to maintain good agreement with the Monte Carlo simulation's 3σ uncertainty for flight path angle throughout the entire trajectory. TSUC also agrees well with the Monte Carlo. The residuals of the 3σ uncertainty for velocity shown in Figure 49 relative to the Monte Carlo simulation's 3σ uncertainty for velocity are shown in Figure 50.

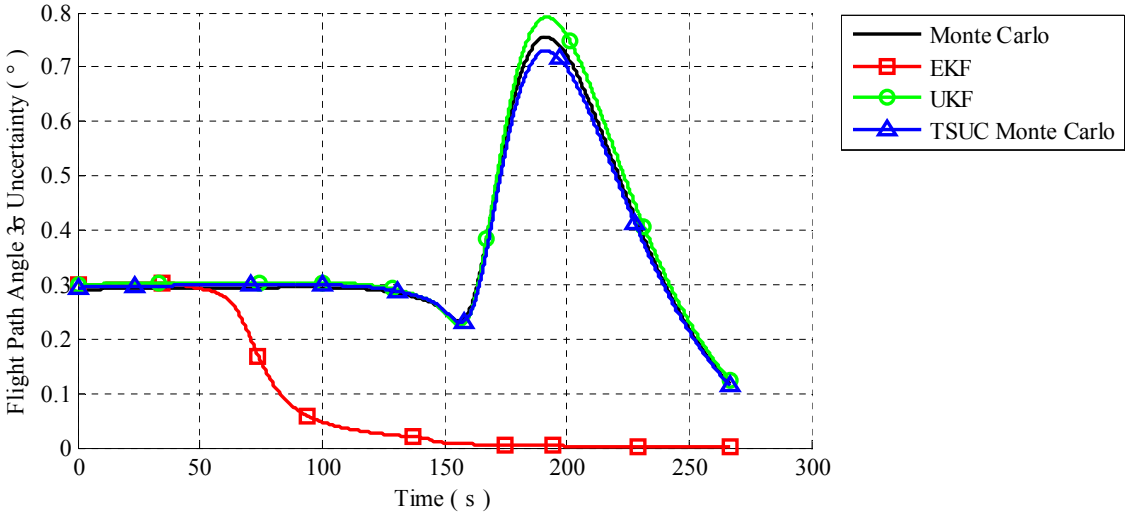

Figure 49: The 3σ uncertainty for flight path angle from the Monte Carlo simulation is shown with the propagated 3σ uncertainty for flight path angle from the Kalman filters and TSUC's 3σ uncertainty.

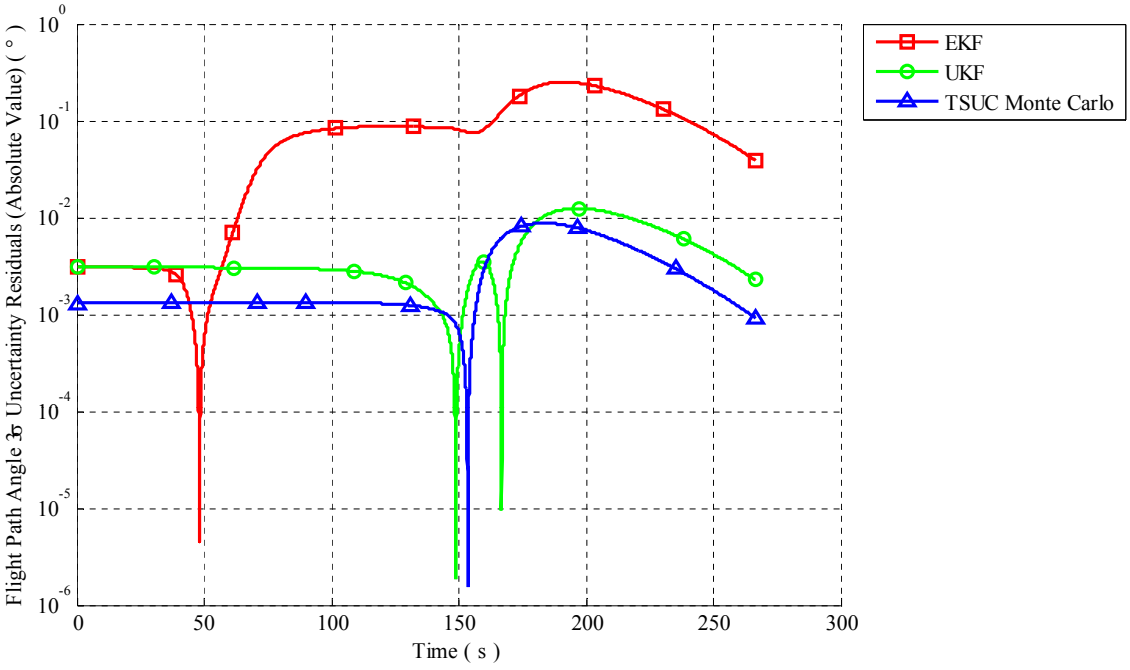

Figure 50: The residuals of the 3σ uncertainty for flight path angle shown in the previous figure relative to the Monte Carlo simulation's 3σ uncertainty for flight path angle.

4.4 Trajectory Performance with Poor Initial Conditions

Finally, a 1,000 run Monte Carlo simulation was performed to determine if each Kalman filter could bound, within its predicted uncertainty bounds, the mean residual (error) between the Kalman filter's best estimate of the trajectory and the simulated sample problem in spite of a poor initial state. This might occur, for example, if the true entry state was different from the mean entry state, as in the real world the true entry state is not known with absolute certainty. The results of this investigation are shown in Figures 51 to Figures 53 for the extended Kalman filter and in Figures 54 to Figures 59 for the unscented Kalman filter.

This Monte Carlo simulation was performed by:

1. Sampling from the initial condition distributions shown in Table 16 on page 100. This initial condition was used to initialize each of the methods discussed in Chapter 3.[3]

2. Each method was then run using the above initial condition and the noisy sample problem accelerometer data discussed above.

3. Once all the Monte Carlo runs were completed, the difference (residual error) between the Monte Carlo run's reconstruction and the true trajectory was computed for each Monte Carlo run.

4. Then, the mean and standard deviation of the residuals was then computed, and they are plotted in the following plots for each method.

[3]Note that since the true entry state for this problem is also the mean entry state given in Table 16, the mean of the "poor" entry states that are sampled from the distribution of the true entry state given in Table 16 will approach the value of the true entry state as the number of Monte Carlo runs increases. In fact with the 1,000 runs done in this study, they appear to be identical, as their difference shown in the following plots appears to be zero.

4.4.1 The Extended Kalman Filter

The Monte Carlo mean residual between the extended Kalman filter's best estimate of altitude and the simulated sample problem's altitude is shown in Figure 51. In spite of a poor initial state, the extended Kalman filter is able to bound the mean Monte Carlo altitude residual within its predicted 3σ uncertainty bounds. Figure 52 shows the Monte Carlo mean residual between the extended Kalman filter's best estimate of velocity and the simulated sample problem's velocity. The poor initial state causes the extended Kalman filter to over predict the accuracy of its best estimate of velocity, as shown in Figure 52 by the mean Monte Carlo velocity residual falling outside the extended Kalman filter's predicted 3σ uncertainty bounds approximately 45 seconds into the trajectory. Figure 53 shows the Monte Carlo mean residual between the extended Kalman filter's best estimate of flight path angle and the simulated sample problem's flight path angle. The poor initial state can cause the extended Kalman filter to over predict the accuracy of its best estimate of flight path angle, as shown in Figure 53 by the mean Monte Carlo flight path angle residual falling outside the extended Kalman filter's predicted 3σ uncertainty bounds approximately 100 seconds into the trajectory.

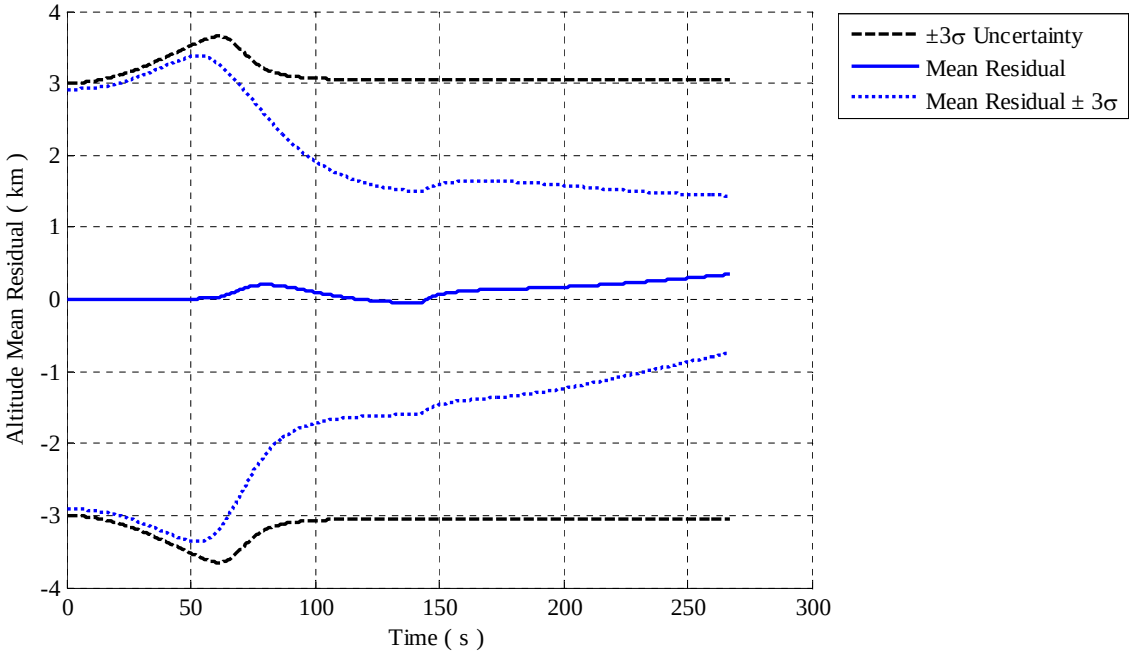

Figure 51: The Monte Carlo mean residual between the extended Kalman filter's best estimate of altitude and the simulated sample problem's altitude.

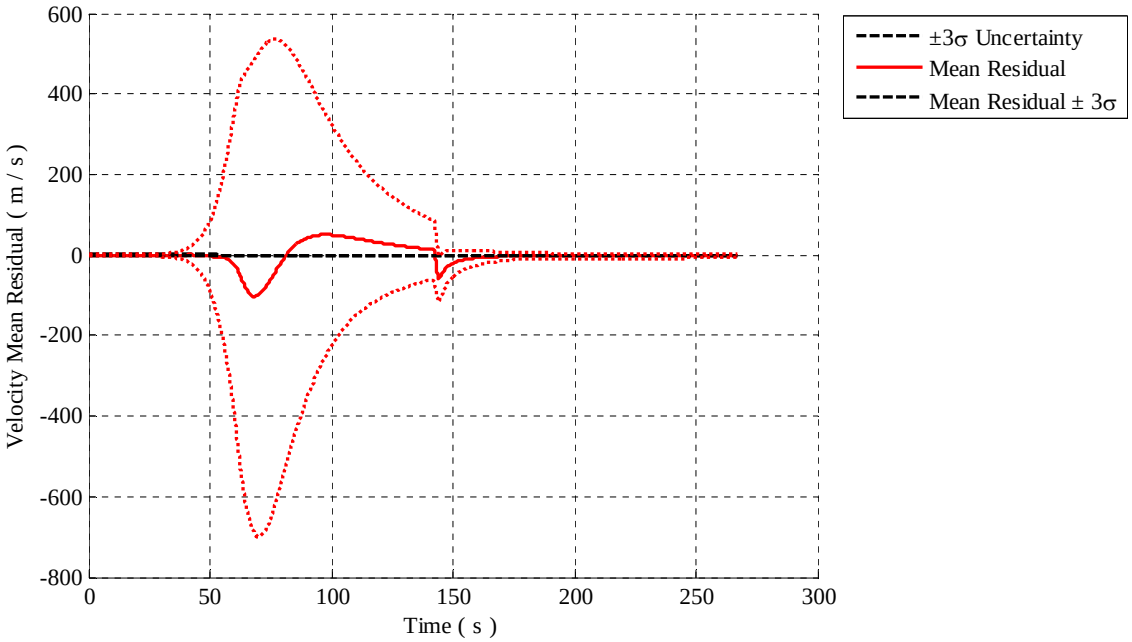

Figure 52: The Monte Carlo mean residual between the extended Kalman filter's best estimate of velocity and the simulated sample problem's velocity.

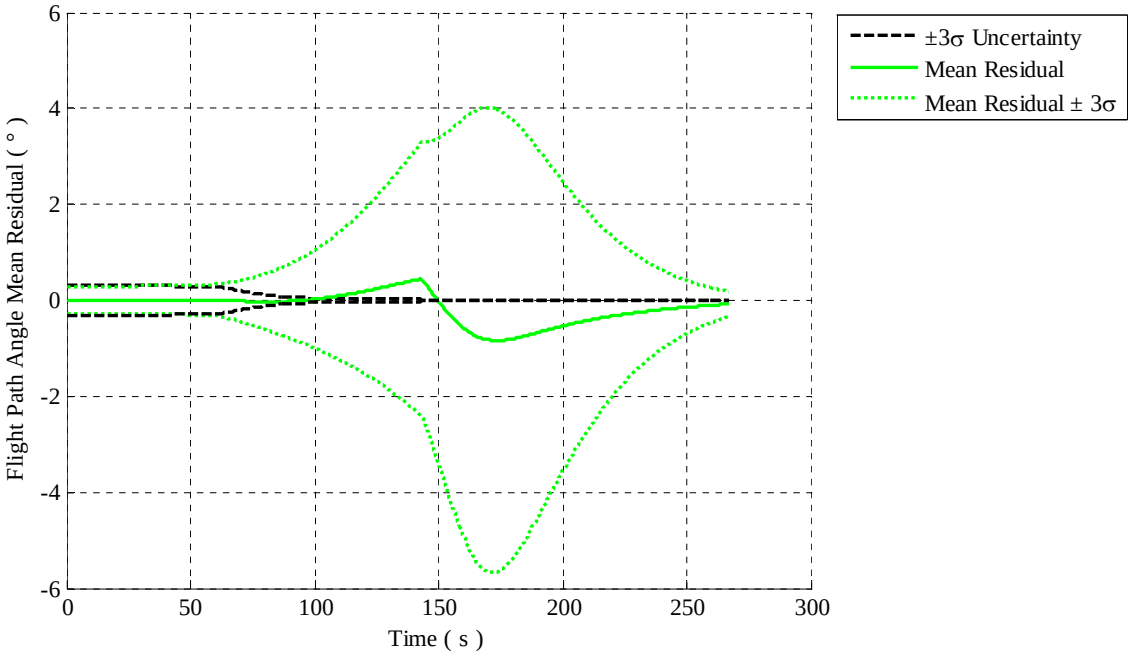

Figure 53: The Monte Carlo mean residual between the extended Kalman filter's best estimate of flight path angle and the simulated sample problem's flight path angle.

4.4.2 The Unscented Kalman Filter

The Monte Carlo mean residual between the unscented Kalman filter's best estimate of altitude and the simulated sample problem's altitude is shown in Figure 54. In spite of a poor initial state, the unscented Kalman filter is able to bound the mean Monte Carlo altitude residual within its predicted 3σ uncertainty bounds.

Figure 55 shows the Monte Carlo mean residual between the unscented Kalman filter's best estimate of velocity and the simulated sample problem's velocity. In spite of a poor initial state, the unscented Kalman filter is able to bound the mean Monte Carlo velocity residual within its predicted 3σ uncertainty bounds approximately 99.7% of the time as shown in Figures 55 to 58 indicating that it does not over predict the accuracy of its best estimate of velocity. Figure 56 shows closer look at the beginning of the trajectory. The unscented Kalman filter is able to bound the mean Monte Carlo velocity residual within its predicted 3σ uncertainty bounds at

the beginning of the trajectory. A closer look near parachute deployment is shown in Figure 57. Near parachute deployment, the mean Monte Carlo velocity residual falls outside the unscented Kalman filter's predicted 3σ uncertainty bounds. This unbounded portion of the residuals represents approximately 0.3% of the trajectory. Hence, in spite of a poor initial state, the unscented Kalman filter is able to bound the mean Monte Carlo velocity residual within its predicted 3σ uncertainty bounds approximately 99.7% of the time indicating that it does not over predict the accuracy of its best estimate of velocity. A closer look at the end of the trajectory is shown in Figure 58, where the unscented Kalman filter is able to bound the mean Monte Carlo velocity residual within its predicted 3σ uncertainty bounds.

The Monte Carlo mean residual between the unscented Kalman filter's best estimate of flight path angle and the simulated sample problem's flight path angle is shown in Figure 59. In spite of a poor initial state, the unscented Kalman filter is able to bound the mean Monte Carlo flight path angle residual within its predicted 3σ uncertainty bounds.

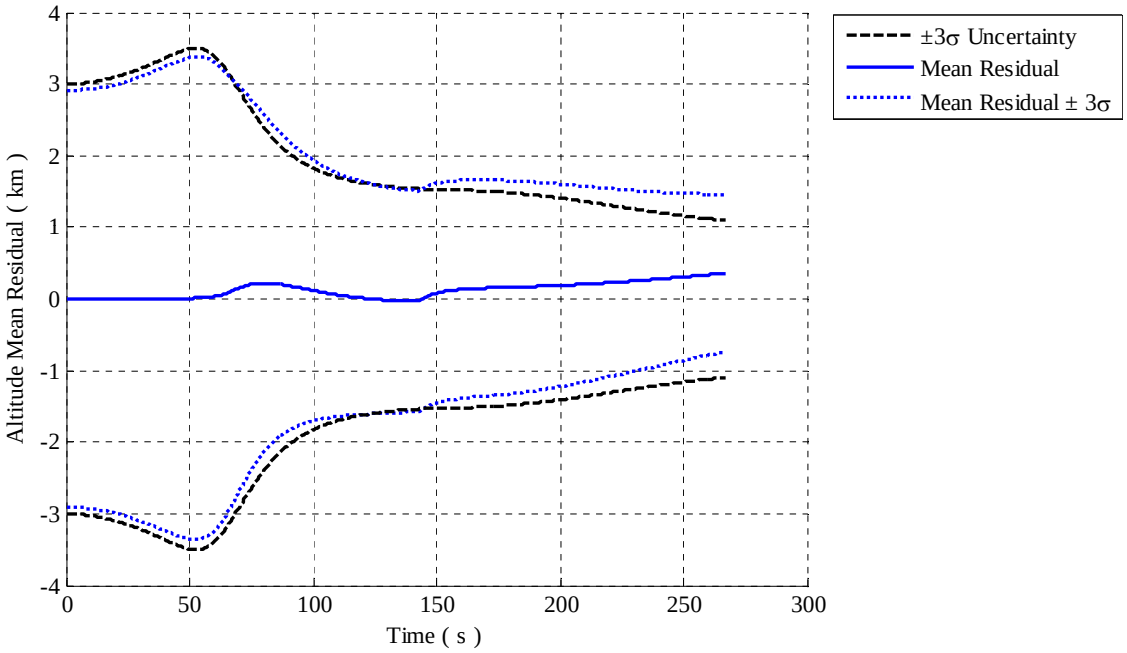

Figure 54: The Monte Carlo mean residual between the unscented Kalman filter's best estimate of altitude and the simulated sample problem's altitude.

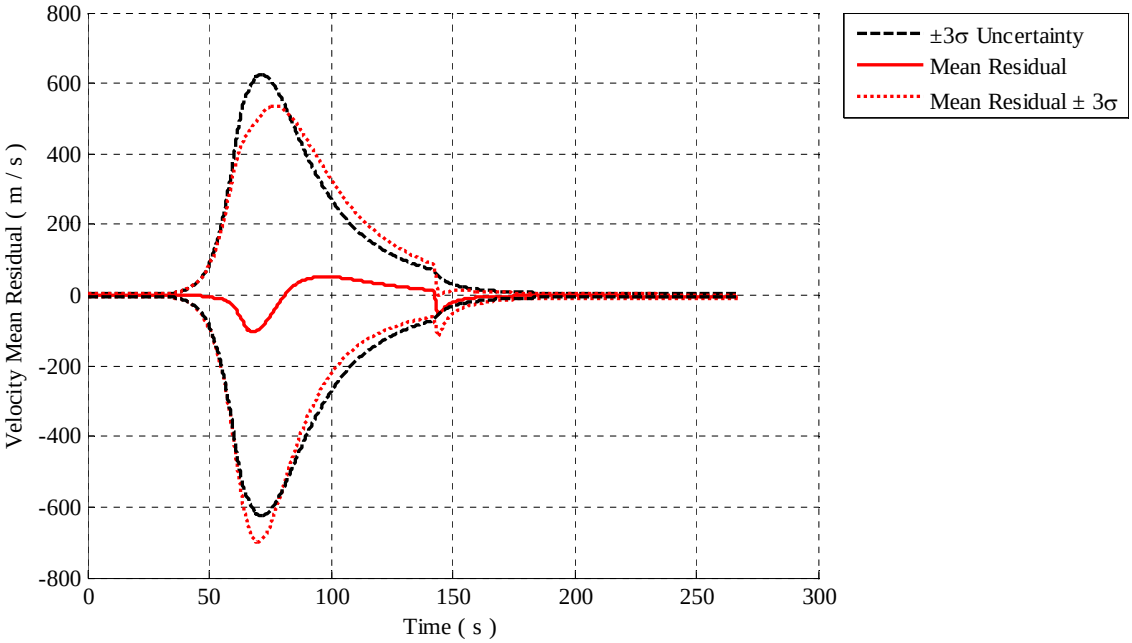

Figure 55: The Monte Carlo mean residual between the unscented Kalman filter's best estimate of velocity and the simulated sample problem's velocity.

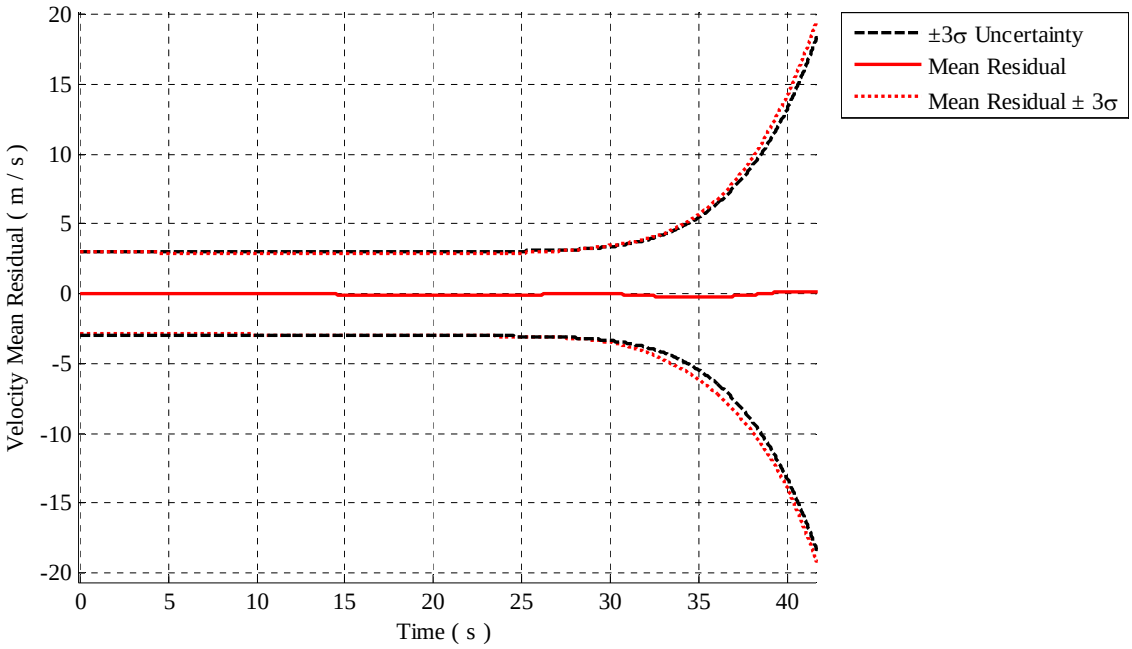

Figure 56: A closer look at the Monte Carlo mean residual between the unscented Kalman filter's best estimate of velocity and the simulated sample problem's velocity.

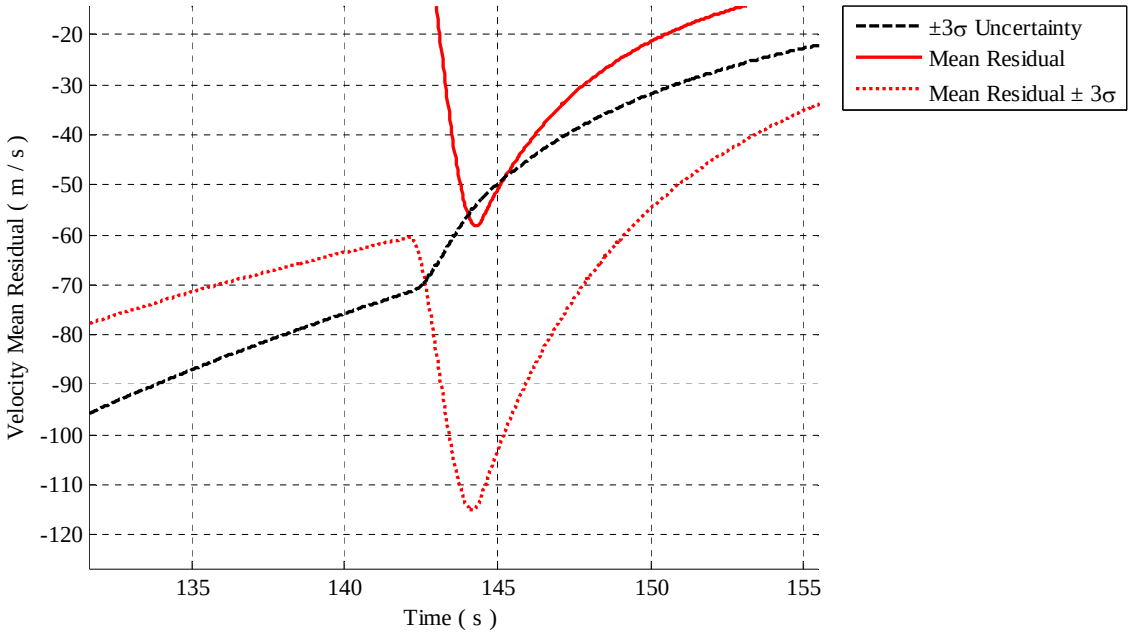

Figure 57: A closer look at the Monte Carlo mean residual between the unscented Kalman filter's best estimate of velocity and the simulated sample problem's velocity. This unbounded portion of the residuals represent approximately 0.3% of the trajectory.

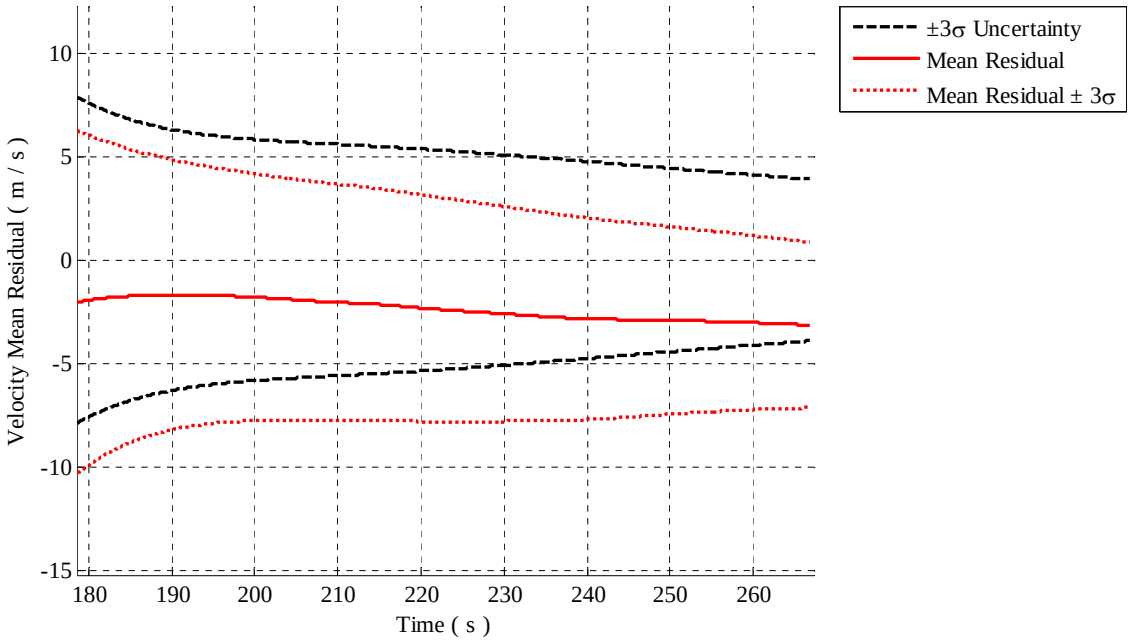

Figure 58: A closer look at the Monte Carlo mean residual between the unscented Kalman filter's best estimate of velocity and the simulated sample problem's velocity.

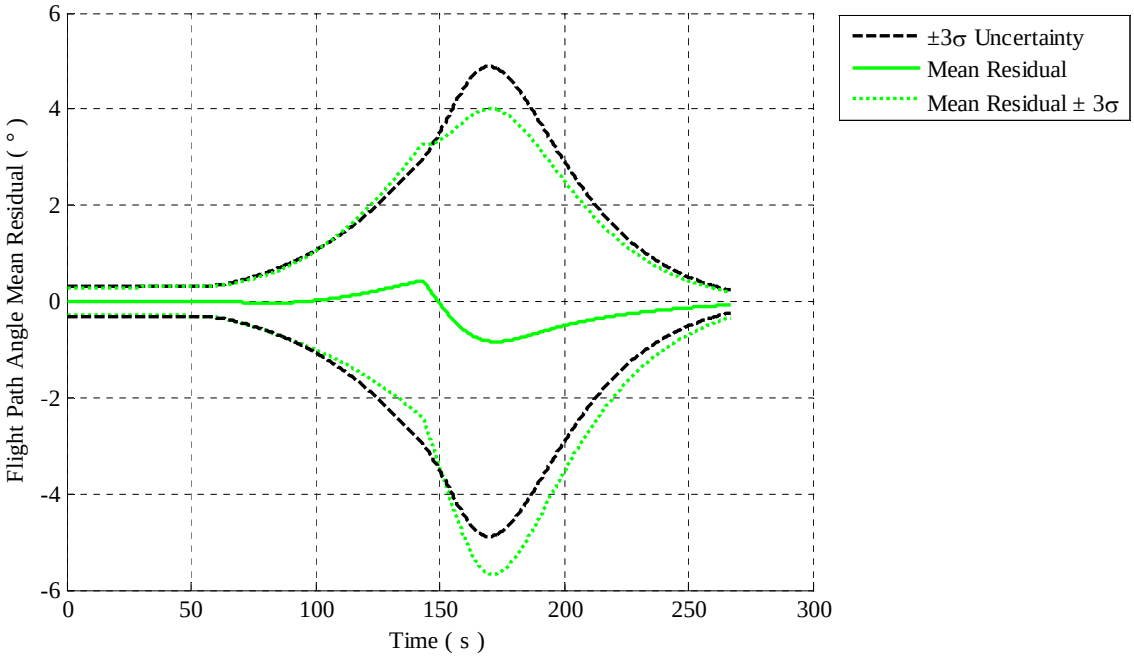

Figure 59: The Monte Carlo mean residual between the unscented Kalman filter's best estimate of flight path angle and the simulated sample problem's flight path angle.

4.4.3 Trajectory Simulation Using Collocation (TSUC)

The Monte Carlo mean residual between TSUC's simulation of altitude and the simulated sample problem's altitude is shown in Figure 60. In spite of a poor initial state, TSUC is able to bound the mean Monte Carlo altitude residual within its simulated 3σ uncertainty bounds.

Figure 61 shows the Monte Carlo mean residual between TSUC's simulation of velocity and the simulated sample problem's velocity. In spite of a poor initial state, TSUC is able to bound the mean Monte Carlo velocity residual within its simulated 3σ uncertainty bounds approximately 99.7% of the time as shown in Figures 61 to 64 indicating that its usefulness for simulating trajectories. TSUC is able to bound the mean Monte Carlo velocity residual within its predicted 3σ uncertainty bounds at the beginning of the trajectory. A closer look near parachute deployment is shown in Figure 63. Near parachute deployment, the mean Monte Carlo velocity residual falls outside TSUC's simulated 3σ uncertainty bounds. This unbounded portion of the residuals represents approximately 0.3% of the trajectory. Hence, in spite of a poor initial state, TSUC is able to bound the mean Monte Carlo velocity residual within its simulated 3σ uncertainty bounds approximately 99.7% of the time indicating that its usefulness for simulating trajectories. A closer look at the end of the trajectory is shown in Figure 64, where TSUC is able to bound the mean Monte Carlo velocity residual within its simulated 3σ uncertainty bounds.

The Monte Carlo mean residual between TSUC's simulation of flight path angle and the simulated sample problem's flight path angle is shown in Figure 65. In spite of a poor initial state, TSUC is able to bound the mean Monte Carlo flight path angle residual within its simulated 3σ uncertainty bounds.

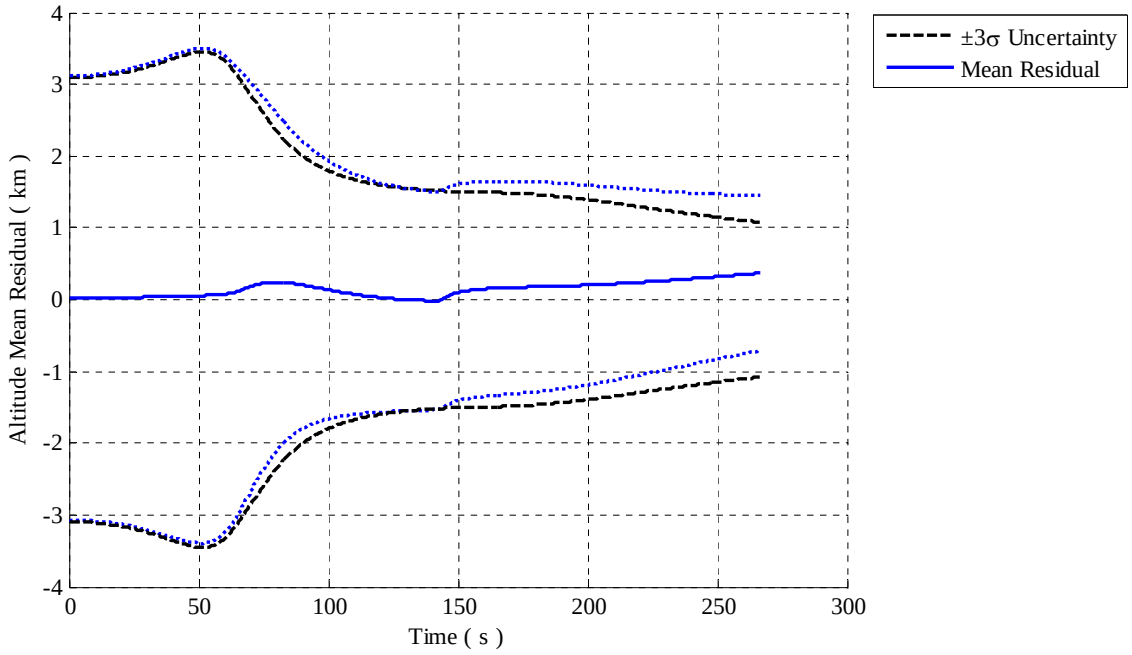

Figure 60: The Monte Carlo mean residual between TSUC's simulation of altitude and the simulated sample problem's altitude.

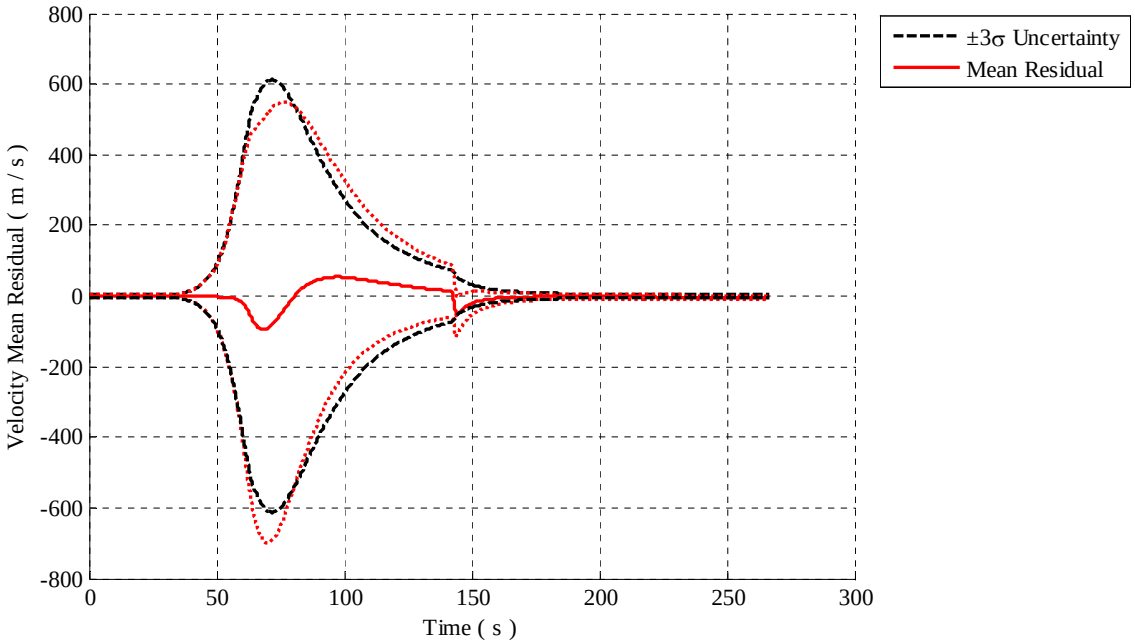

Figure 61: The Monte Carlo mean residual between TSUC's simulation of velocity and the simulated sample problem's velocity.

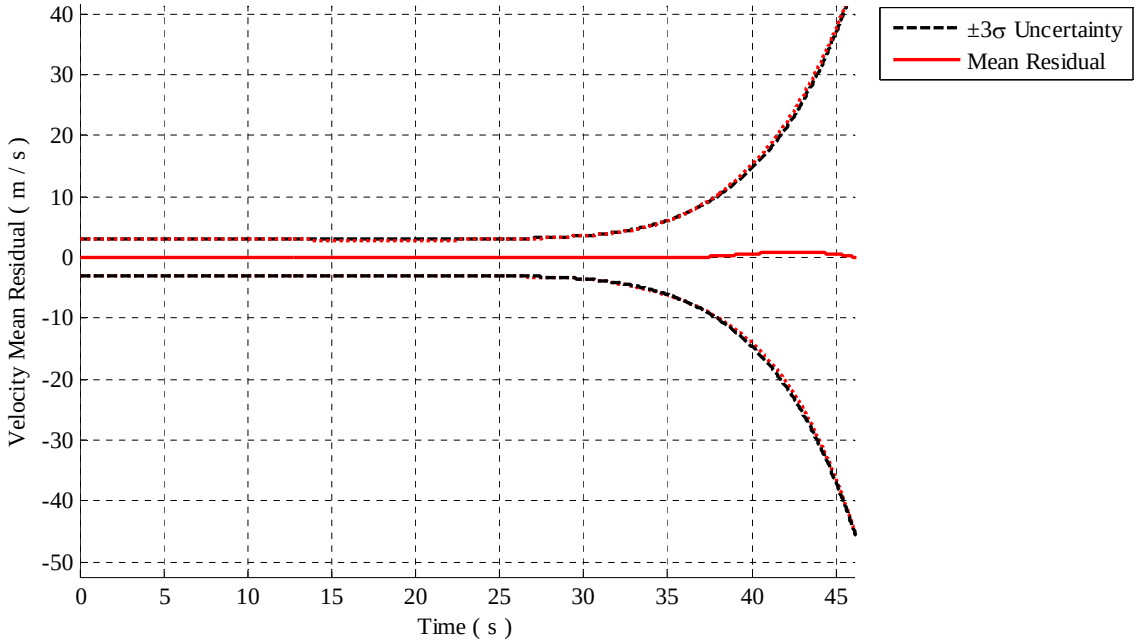

Figure 62: A closer look at the Monte Carlo mean residual between TSUC's simulation of velocity and the simulated sample problem's velocity.

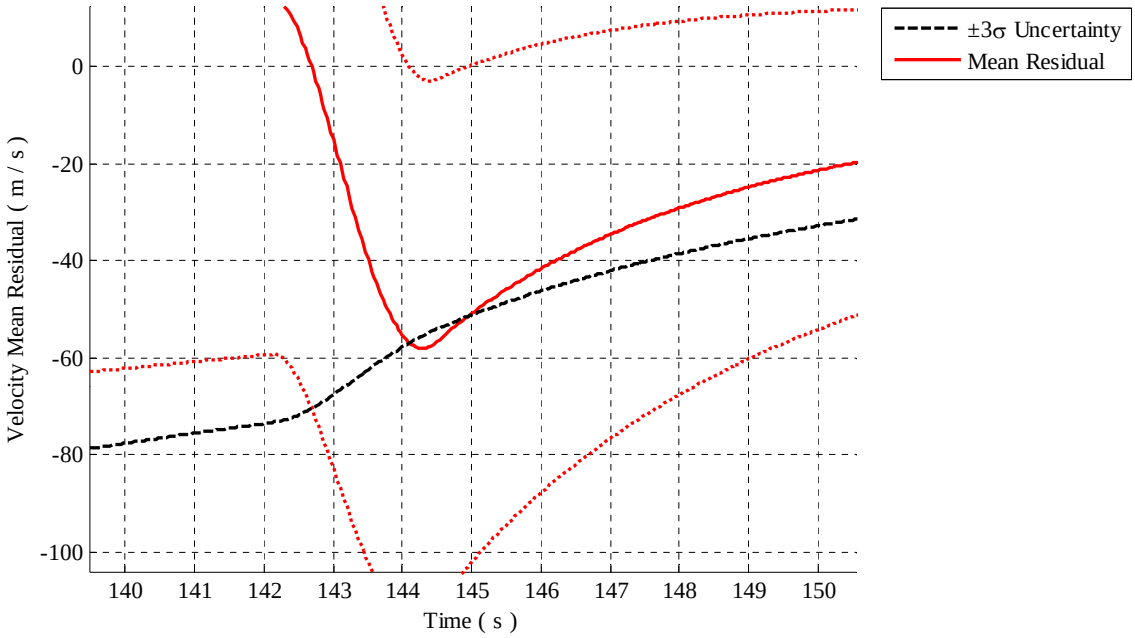

Figure 63: A closer look at the Monte Carlo mean residual between TSUC's simulation of velocity and the simulated sample problem's velocity. This unbounded portion of the residuals represent approximately 0.3% of the trajectory.

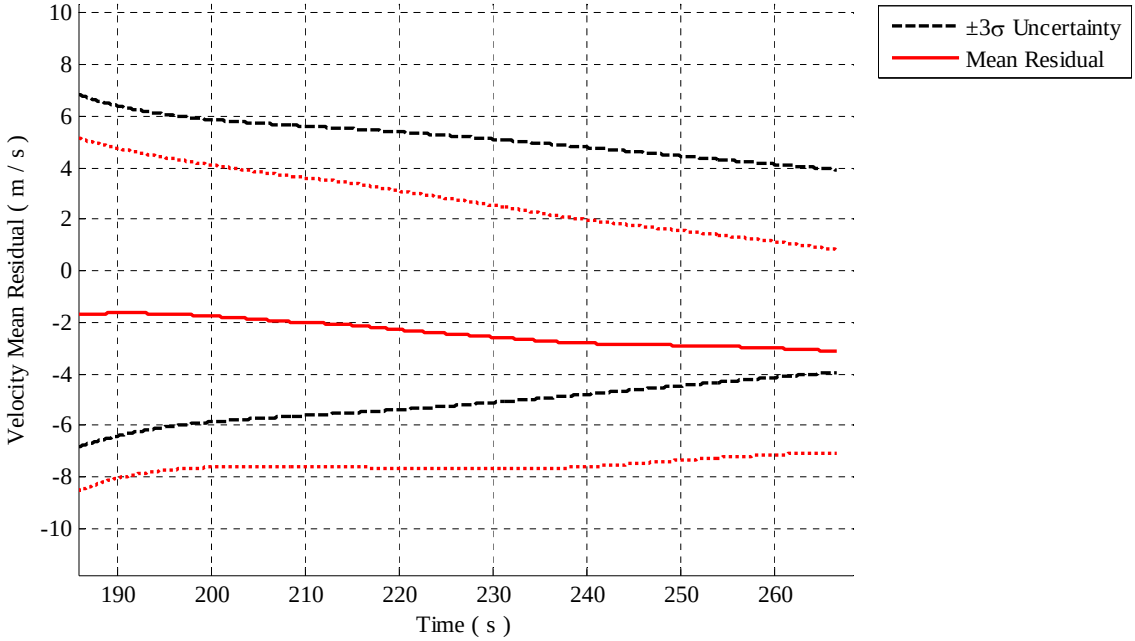

Figure 64: A closer look at the Monte Carlo mean residual between TSUC's simulation of velocity and the simulated sample problem's velocity at the end of the trajectory.

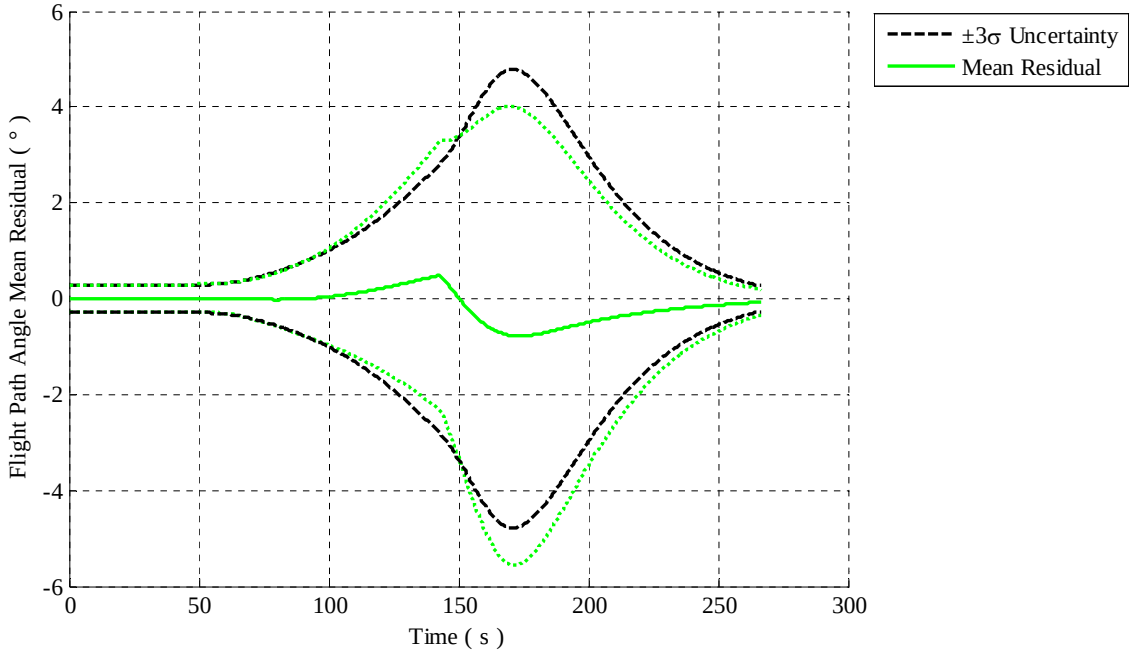

Figure 65: The Monte Carlo mean residual between TSUC's simulation of flight path angle and the simulated sample problem's flight path angle.

4.5 Summary

Both Kalman filters discussed in Chapter 3 were able to reconstruct the mean trajectories nearly equally well. While the extended Kalman filter did demonstrate some difficulties, the unscented Kalman filter had only slight difficulties, and they generally seem identical from the plots. Regarding the estimation of uncertainties, the unscented Kalman filter clearly performed better than the extended Kalman filter and did not over predict the accuracy of their best estimates. Now, we consider these results in the context of the details of each method.[4]

The extended Kalman filter propagates a nominal trajectory that represents a "best guess" of the trajectory based on the process model. The nominal trajectory's estimate of the state is updated at each measurement time using the measurement data to obtain a best estimate of the state at each measurement time, and the nominal

[4]Please see Chapter 3 for the details of each Kalman filter.

trajectory is propagated from that best estimate of the state. There are two items that can explain the extended Kalman filter's difficulties reconstructing a mean trajectory. First, the nominal trajectory is only as good as the process model. If the process model is too poor, then the update of the state using the measurement data may not be big enough to get the nominal trajectory back on track, and the best estimate will drift away from the true trajectory. Second, the update of the state using the measurement data is done with the Kalman gain (please see equation (38i) on page 59). The extended Kalman filter's Kalman gain must take into account both the uncertainty in the state and the measurement noise, where the state uncertainty (the error covariance matrix) is propagated using a linearization of the nonlinear state equations via the state transition matrix (please see Table 11 on page 68). This can result in a poor propagation of the state uncertainty, which results in a poor Kalman gain, a poor state estimate, and poor update of the state uncertainty, especially at highly nonlinear portions of the trajectory such as peak deceleration and parachute deployment. It is possible that through the addition of process noise that the extended Kalman filter would better propagate the initial state uncertainties and bound the residuals between its best estimate and the true trajectory. However, as is discussed below, the unscented Kalman filter can already do this, and it does not require process noise to be added. Additionally, any process noise added to the extended Kalman filter would have to be added to the unscented Kalman filter, so the two Kalman filters could be compared on an equal basis.

In contrast, the unscented Kalman filter performs, what is essentially, a mini–Monte Carlo. The sigma–points are sampled from the initial uncertainty distribution of the state and propagated forward in time using the nonlinear system equations to the next measurement time. The nominal state is the mean of the sigma–points (note that this is not simply a propagation of the previous mean, as in the extended

Kalman filter case), and the error covariance matrix is calculated from the sigma–points, as well. This provides the unscented Kalman filter with a better nominal value of the state to be updated by the measurement data. While the unscented Kalman filter's Kalman gain also takes into account both the uncertainty in the state and the measurement noise, it is found using the sigma points (please see equations (85) to (89) on page 77). As the sigma–points were propagated forward in time using the nonlinear system equations, no linearization was involved. This allows the unscented Kalman filter to obtain a better estimate of both the state and its uncertainty when compared to the extended Kalman filter, as shown in this chapter for entry, descent, and landing trajectory reconstruction.

TSUC's Monte Carlo simulation compared well with the explicit integration Monte Carlo simulation indicating its usefulness for simulating trajectories using the solution procedure in Table 15 on page 98 for determining the values of the state from the controls and parameters of the simulation.

In the next chapter, each Kalman filter will be tested with real–world data, where the true trajectory is unknown.

CHAPTER V

TRAJECTORY RECONSTRUCTION FOR MARS PATHFINDER

As stated earlier, extended Kalman filtering (EKF) has been used extensively in trajectory reconstruction both for orbiting spacecraft and for planetary probes. It forms the standard to which the unscented Kalman filter (UKF) is tested. Additionally, Mars Pathfinder's trajectory will be simulated using collocation.

5.1 Mars Pathfinder

Mars Pathfinder was launched aboard a Delta II rocket [38] in December 4, 1996 [299] and traveled close to 500 million kilometers [191] to reach Mars. It entered the Martian atmosphere on July 4, 1997 [184] and landed approximately five minutes later in the Ares Vallis region of Chryse Planitia [290, 107, 54, 75, 112] at 19.33°N (aerodetic), 326.45°E[1] (see Figure 66). The direct entry method used by Pathfinder to reach the surface of Mars resulted in significant cost–savings since no propellant was needed to capture it into a parking orbit around Mars before landing [310, 202] as with the Viking orbiter–landers [121, 77].

Pathfinder's entry configuration is shown in Figure 19 on page 36. Pathfinder did not have a reaction control system and followed a ballistic flight path. [104] Although Pathfinder's aeroshell is statically unstable for densities less than $2 \times 10^{-7}\ \frac{\text{kg}}{\text{m}^3}$, the gyroscopic stability caused by Pathfinder's two rotations per minute spin mitigated this aerodynamic moment. [191]

[1]Based on landmark recognition. Lander radiometric tracking places the landing site at 19.28°N (aerodetic), 326.48°E, and the best estimate from flight data was 19.09°N (aerocentric), 326.48°E. [269]

Pathfinder's entry, descent, and landing sequence is shown in Figure 67, and the times of several events are listed in Table 17. The spacecraft decelerated with its aeroshell and heatshield, then deployed a supersonic parachute, jettisoned its heatshield, and used retrorockets to minimize its velocity above the surface of Mars. The lander was then separated from the backshell and dropped to the surface protected by airbags. Once the motion of the lander ceased, the lander's petals opened, and it deployed instruments to make in situ science measurements. Three scientific instruments collected data once on the surface: (1) the Imager for Mars Pathfinder [256], (2) the α–proton x–ray spectrometer (APXS) [224], and (3) an atmospheric sTSUCture investigation / meteorology package (ASI/MET) [252]. Mars Pathfinder also deployed a small rover named *Sojourner*. [106, 105, 285]

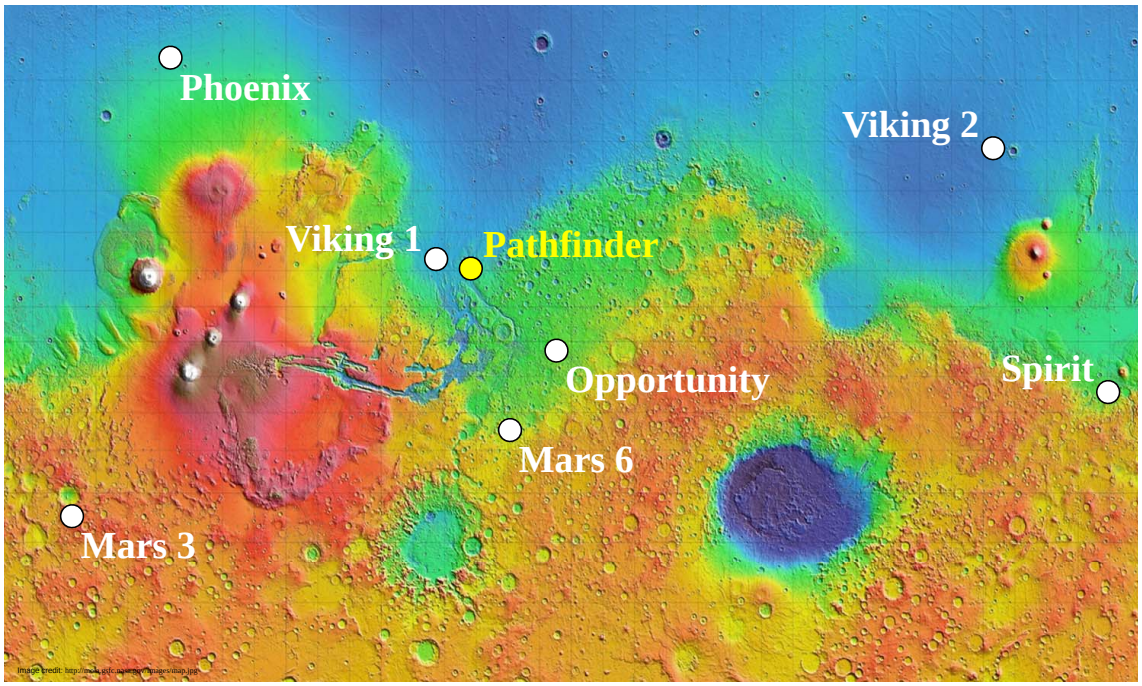

Figure 66: Landing site of Mars Pathfinder. [Image credit: The NASA Goddard Space Flight Center]

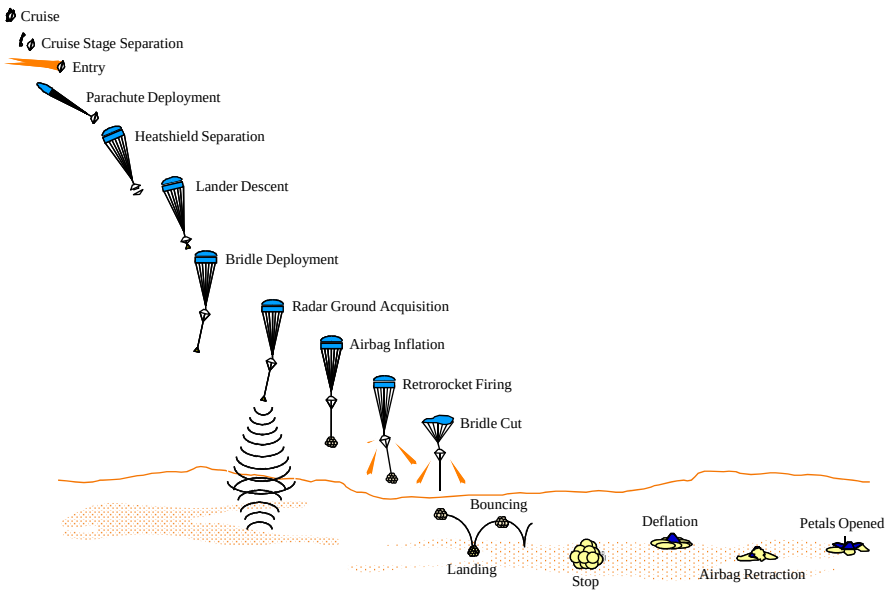

Figure 67: Entry, descent, and landing sequence for Mars Pathfinder. [71, 72, 33]

Table 17: The times of some notable events during Mars Pathfinder's entry, descent, and landing. [269]

Event	Time after Entry (s)
Entry interface	0
Mortar fire	171.4
Parachute open	172.7
Heatshield jettison	192.1
Deployment of lander on bridle	211.4
Airbag inflation	295.2
Rocket deceleration	299.1
Parachute bridle cut	301.3
First bounce	305

5.2 Reconstruction

5.2.1 Initial Conditions

The initial conditions (i.e. the entry state vector $\mathbf{x}_0$) for Mars Pathfinder are listed in Table 18. Both the mean value and the 1σ uncertainty are given for each state variable. These initial values are propagated forward in time until parachute bridle

cut. Time histories of altitude, velocity, and flight path angle are presented below, as well as a density profile of the Martian atmosphere at the time of Mars Pathfinder's entry. A comparison is made with a previous reconstruction [269] of Mars Pathfinder's trajectory that is available in the literature. The previous reconstruction is based on a combination of accelerometer and altimeter measurements using sequential filtering and smoothing techniques.

Table 18: The values of Mars Pathfinder's state variables at entry.

State Variable	Mean [269, 49]	Uncertainty (1σ) [49]
Radius	3 522 200 m	1 700 m
Aerocentric latitude	22.630 3°N	0.04°
Longitude	337.997 6°E	0.01°
Inertial velocity	7 264.2 $\frac{\text{m}}{\text{s}}$	0.7 $\frac{\text{m}}{\text{s}}$
Inertial flight path angle	-14.061 4°	0.02°
Inertial azimuth	253.148 1°	0.02°

5.2.2 Accelerometer Data

During entry, the accelerations experienced by Mars Pathfinder were recorded by accelerometers in Pathfinders atmospheric structure and meteorology instrument. The threshold of acceleration detection due to atmospheric drag was expected to occur at an atmospheric density of 2×10^{-10} $\frac{\text{kg}}{\text{m}^3}$. The acceleration data [164] shown in Figure 68 was stored onboard the spacecraft and later transmitted to Earth. The mean noise level for the simulated acceleration measurements was 0 μg with a standard deviation of 1500 μg [49], and the measurement frequency was 32 Hz [164]. Low–pass filters in the accelerometer electronics attenuated signal frequencies above 5 Hz to suppress the effects of noise and spacecraft dynamic motion. [252] The data was further smoothed to facilitate reconstruction as shown in Figure 69 to remove the spikes in acceleration caused by the gain transitions of the accelerometers.

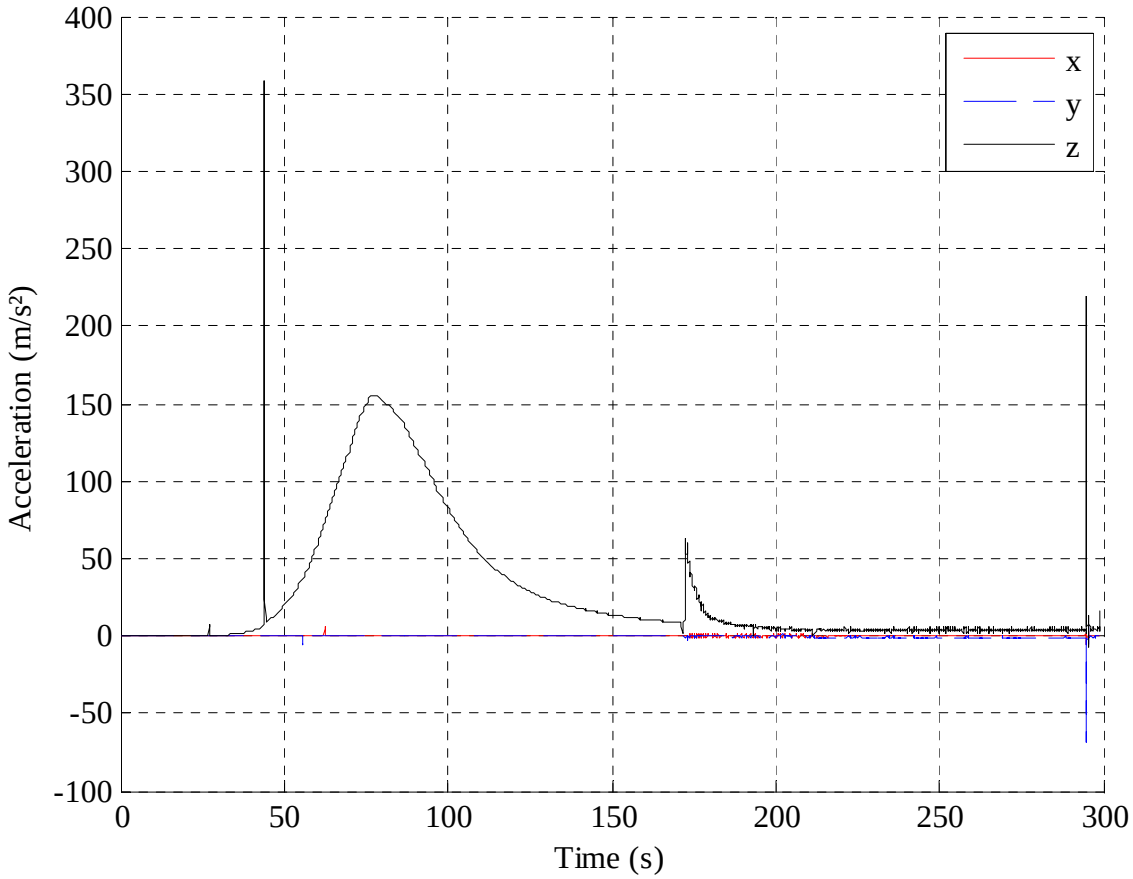

Figure 68: The Mars Pathfinder accelerometer data showing the data spikes from the accelerometers transitioning to different sensitivity levels. [164, 269]

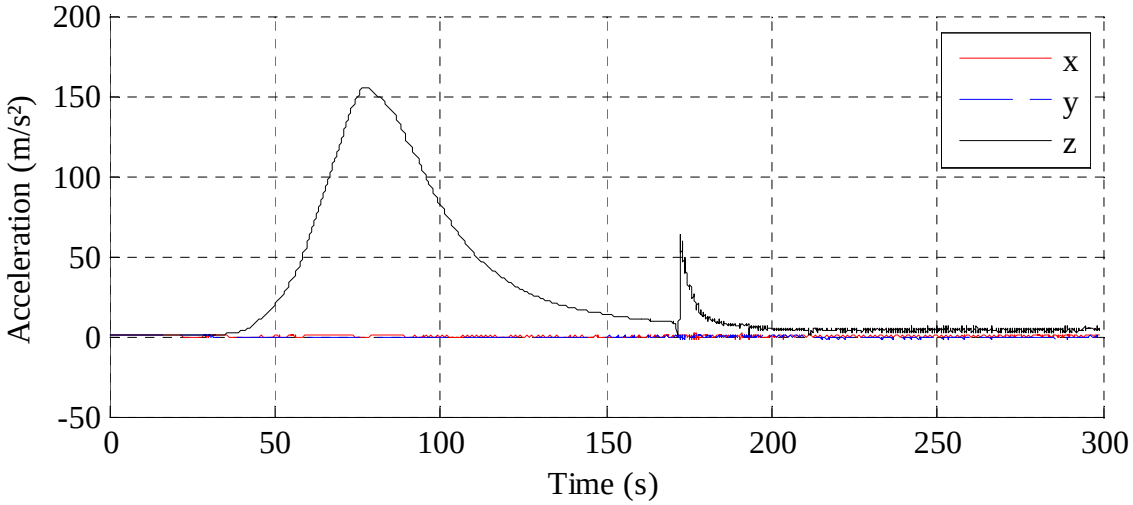

Figure 69: The Mars Pathfinder accelerometer data after smoothing.

5.2.3 Altimeter Data

Near the end of parachute descent, the altitude of Mars Pathfinder was recorded by an altimeter. The noise level for the altimeter measurements was 0.3 m [49] and the measurement frequency was 8 Hz. A plot of the altimeter data [37] is shown in Figure 70.

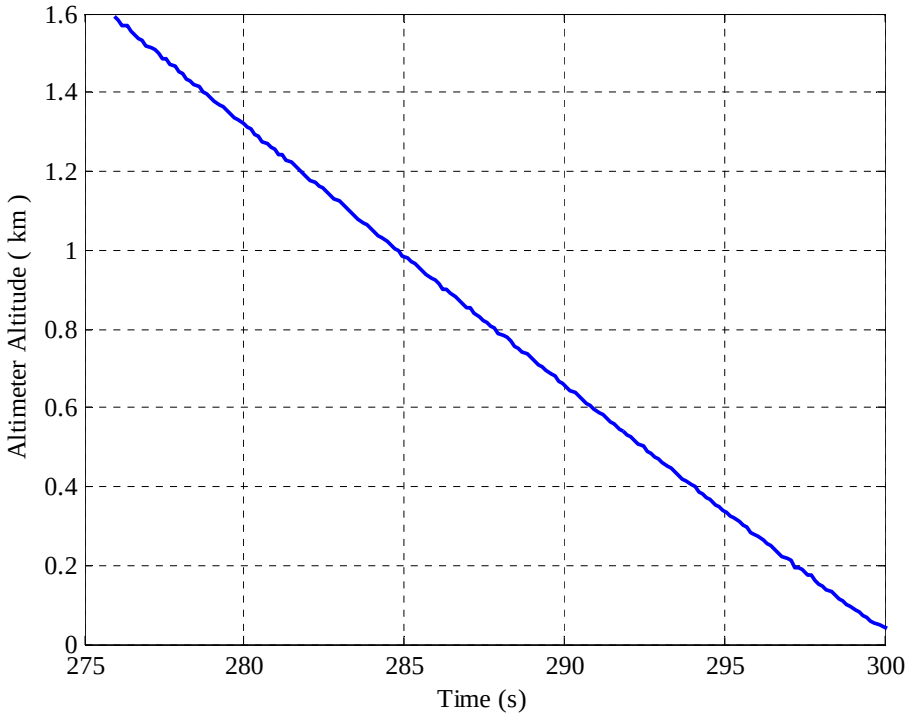

Figure 70: The Mars Pathfinder altimeter data. [37]

5.2.4 Digitized Data

While the Kalman filters discussed in Chapter 3 can be used to reconstruct Mars Pathfinder's entry trajectory and compared against each other, it is also useful to compare the Kalman filters against the "truth". Unfortunately, the true Mars Pathfinder entry trajectory cannot be known, so an independent reconstruction of Mars Pathfinder's entry trajectory was sought for comparison with this investigation. The 1999 Mars Pathfinder entry trajectory reconstruction by David Spencer and others in Reference [269] was selected to provide an independent reconstruction of Mars Pathfinder's entry trajectory. Recall, as discussed in Chapter 2, that the trajectory reconstruction by David Spencer and others [269] used a combination of accelerometer and altimeter measurements using sequential filtering and smoothing techniques [270, 269]. As this is a different process from the Kalman filters discussed in Chapter 3, the results from the Kalman filters discussed in Chapter 3 will differ from the reconstruction by David

Spencer and others [269]. However, the comparison will speak to the general accuracy of the Kalman filters discussed in Chapter 3, while the extended Kalman filter reconstruction, as one accepted standard of trajectory reconstruction[2], will speak to the specific capabilities of the unscented Kalman filter discussed in Chapter 3 for this investigation.

In a discussion with David Spencer regarding the 1999 reconstruction of Mars Pathfinder's trajectory [269], he stated that the data is "long gone" [268], so the altitude, velocity, flight path angle, and density plots shown in Figures 71, 72, and 120 were digitized using the *Engauge Digitizer* digitizing software [186]. For the altitude time history, the resolution of Figure 71 is approximately 0.2 $\frac{\text{km}}{\text{pixel}}$ with a possible error in the digitized altitude of at least 0.8 km based on a four pixel curve width. For the velocity time history, the resolution of Figure 72 is approximately 10.6 $\frac{\text{m/s}}{\text{pixel}}$ with a possible error in the digitized velocity of at least 42.6 $\frac{\text{m}}{\text{s}}$ based on a four pixel curve width. Finally, for the flight path angle time history, the resolution of Figure 72 is approximately 0.106 $\frac{^\circ}{\text{pixel}}$ with a possible error in the digitized flight path angle of at least 0.426° based on a four pixel curve width.

[2]Along with direct integration, as established in Chapter 2.

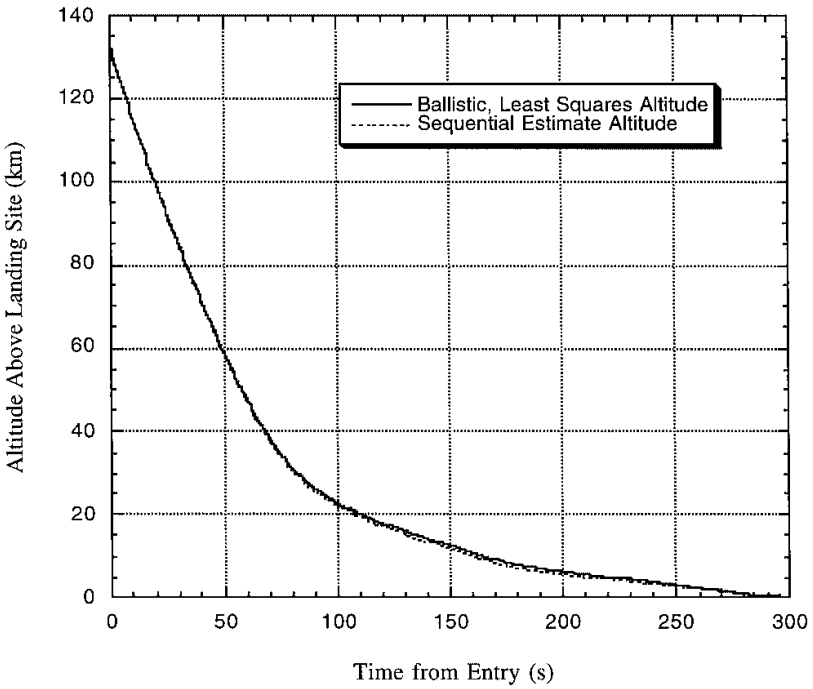

Figure 71: Reconstructed Mars Pathfinder altitude time history from Spencer 1999. [269]

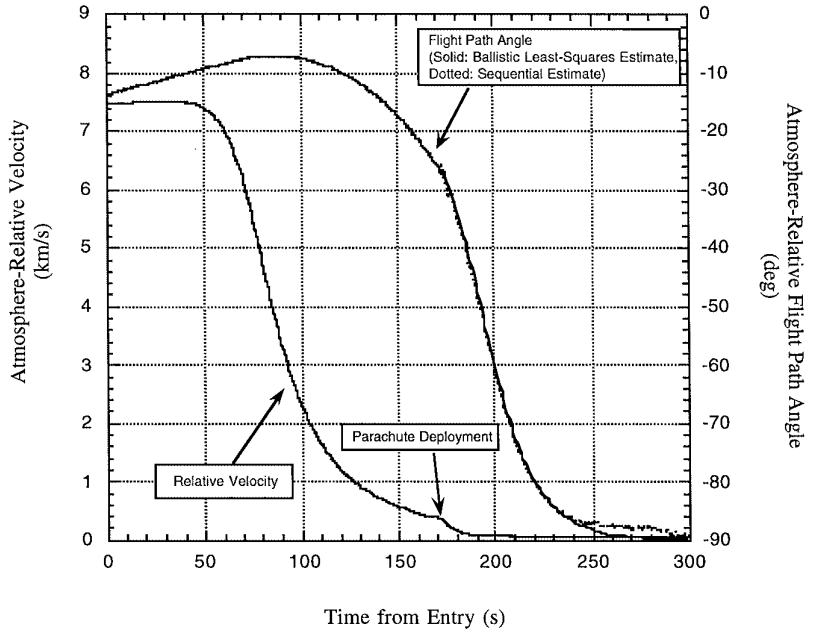

Figure 72: Reconstructed Mars Pathfinder velocity and flight path angle time history from Spencer 1999 [269]

5.2.5 Altitude

Reconstructed with only Acceleration Data

The digitized altitude time history for Mars Pathfinder from Spencer 1999 [269] is shown in Figure 73 with the reconstructions by the Kalman filters discussed in Chapter 3 (using only acceleration data) overlaid. Both Kalman filters discussed in Chapter 3 appear to agree well with the digitized data from Spencer 1999 [269]. The residuals of the altitude time histories shown in Figure 73 relative to the digitized data from Spencer 1999 [269] are shown in Figure 74. Both Kalman filters discussed in Chapter 3 contain the residuals within their 3σ uncertainty bounds. The similarity of the three sets of residuals in Figure 74 indicates that the unscented Kalman filter was able to reconstruct Mars Pathfinder's altitude at least as well as the extended Kalman filter, while TSUC was able to simulate it. While the similarity of the 3σ uncertainty bounds in Figure 74 indicates that neither Kalman filters tends to over predict the accuracy of their best estimate more than the other. Figures 75, 76, and 77 show another look at just the altitude residuals for the extended Kalman filter, the unscented Kalman filter, and TSUC, respectively.

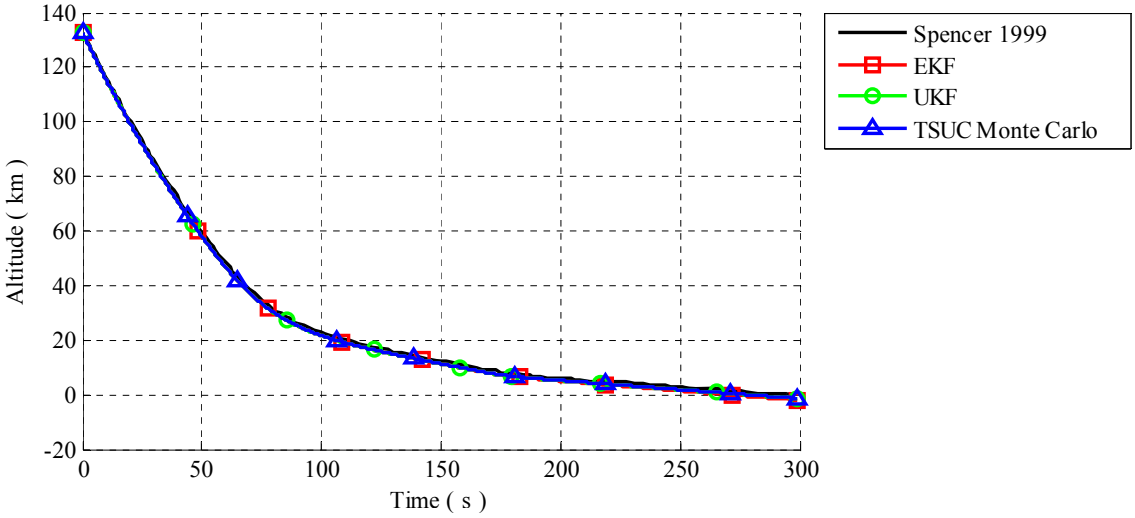

Figure 73: The digitized altitude time history for Mars Pathfinder from Spencer 1999 [269] is shown with the reconstructions (using only acceleration data) and the simulation.

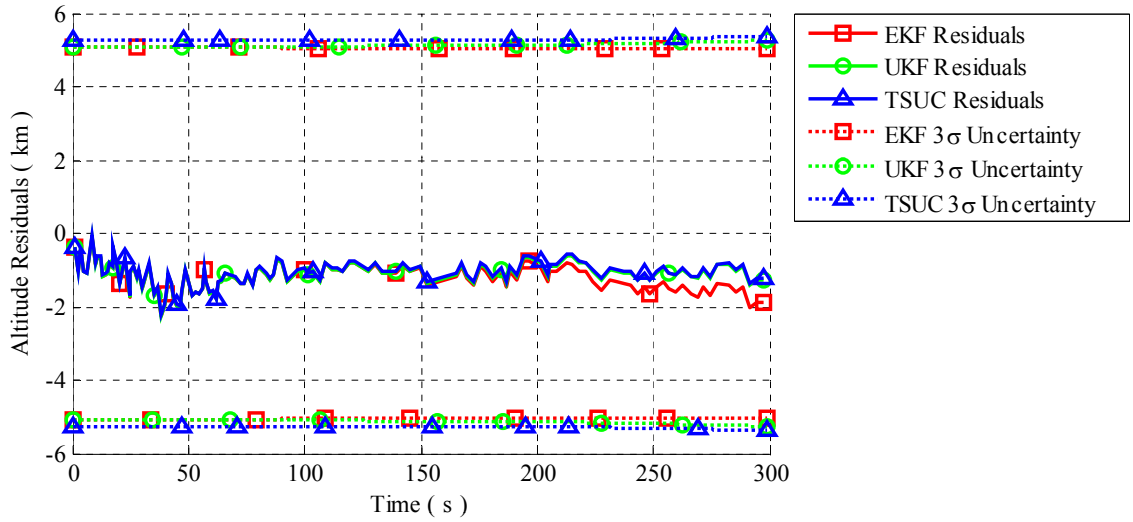

Figure 74: The residuals of the altitude time histories shown in the previous figure relative to the digitized data from Spencer 1999 [269].

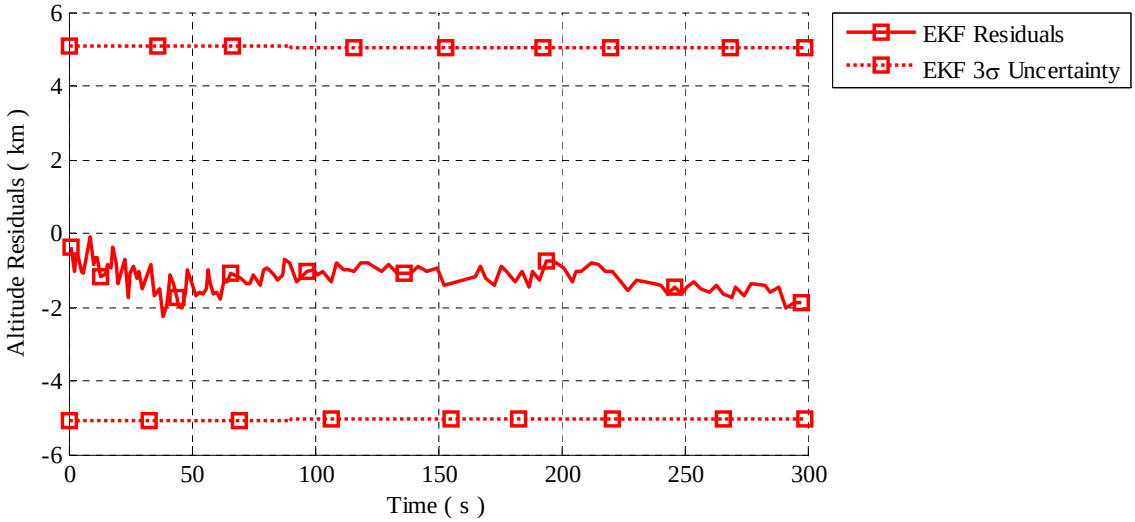

Figure 75: Another look at just the altitude residuals between the extended Kalman filter and the digitized data from Spencer 1999 [269].

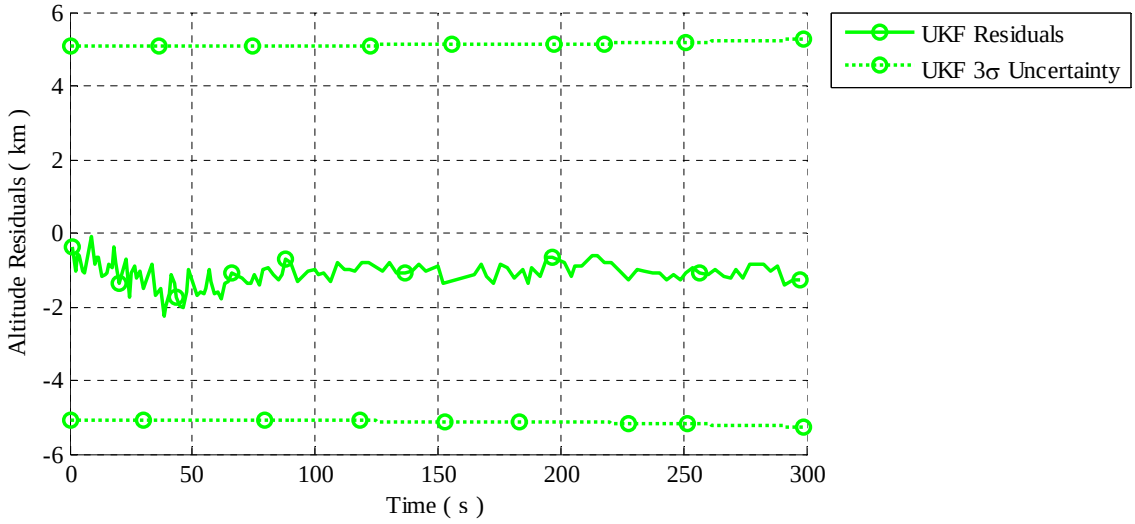

Figure 76: Another look at just the altitude residuals between the unscented Kalman filter and the digitized data from Spencer 1999 [269].

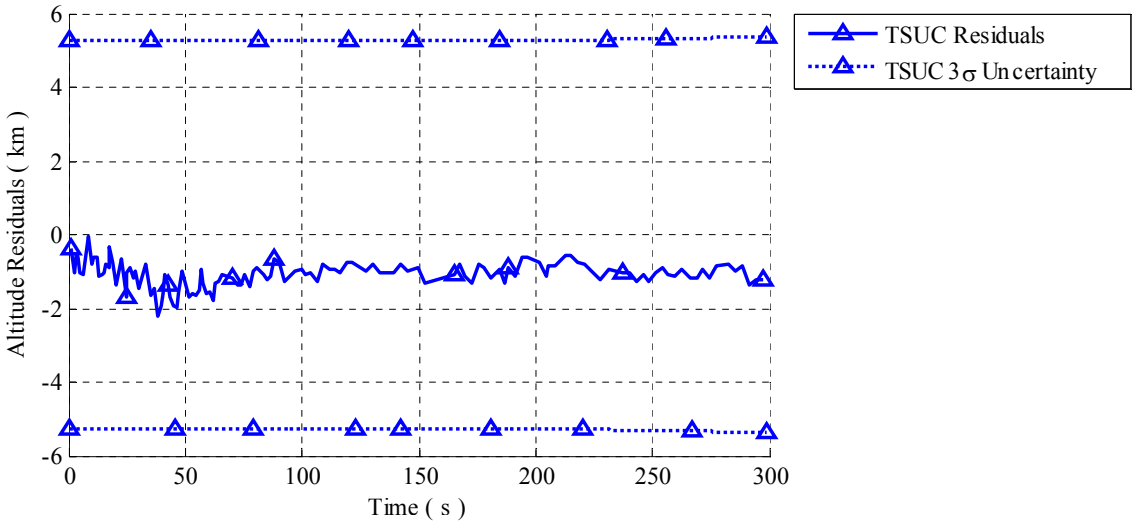

Figure 77: Another look at just the altitude residuals between TSUC and the digitized data from Spencer 1999 [269].

Reconstructed with both Acceleration Data and Altimeter Data

The digitized altitude time history for Mars Pathfinder from Spencer 1999 [269] is shown in Figure 78 with the reconstructions by the Kalman filters discussed in Chapter 3 (using both acceleration data and altimeter data) overlaid. Both Kalman filters discussed in Chapter 3 appear to agree well with the digitized data from Spencer 1999 [269]. A close up view of the change in the altitude estimates shown in Figure 78 when the altimeter acquires the ground is shown in Figure 79. Both Kalman filters discussed in Chapter 3 update their estimates to included the new data.[3] The residuals of the altitude time histories shown in Figure 78 relative to the digitized data from Spencer 1999 [269] are shown in Figure 80. Both Kalman filters discussed in Chapter 3 contain the residuals within their 3σ uncertainty bounds until the altimeter acquires the ground. Then the 3σ uncertainty bounds for the three methods collapses to nearly zero due to the high accuracy of the altimeter measurement. Figures 81, 82, and 83 show another look at just the altitude residuals for the

[3]For TSUC, the altimeter data provides a value of the state and reduces the number of unknown state variables when altimeter data is available.

extended Kalman filter, the unscented Kalman filter, and TSUC, respectively.

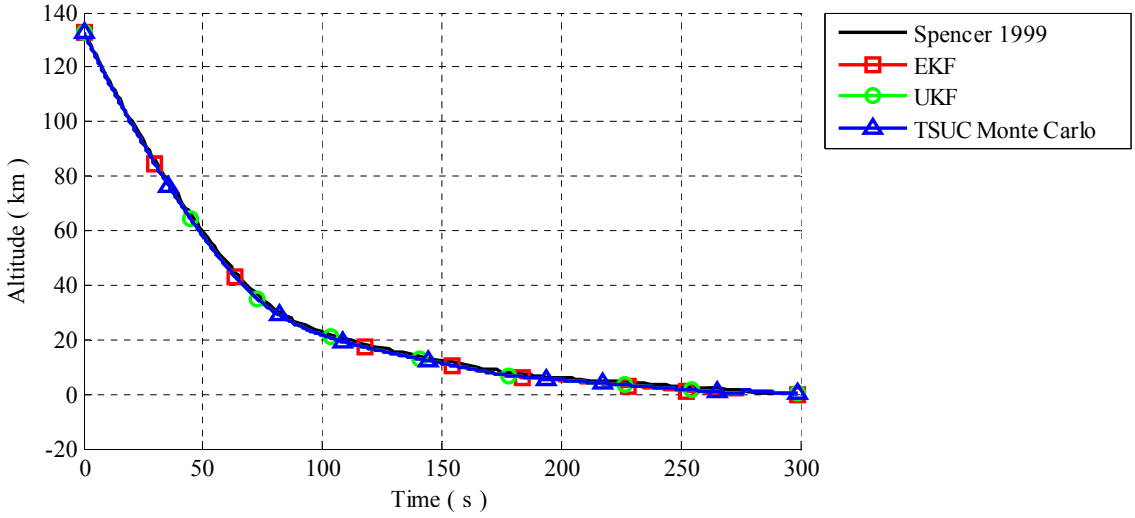

Figure 78: The digitized altitude time history for Mars Pathfinder from Spencer 1999 [269] is shown with the reconstructions (using both acceleration data and altimeter data) and the simulation.

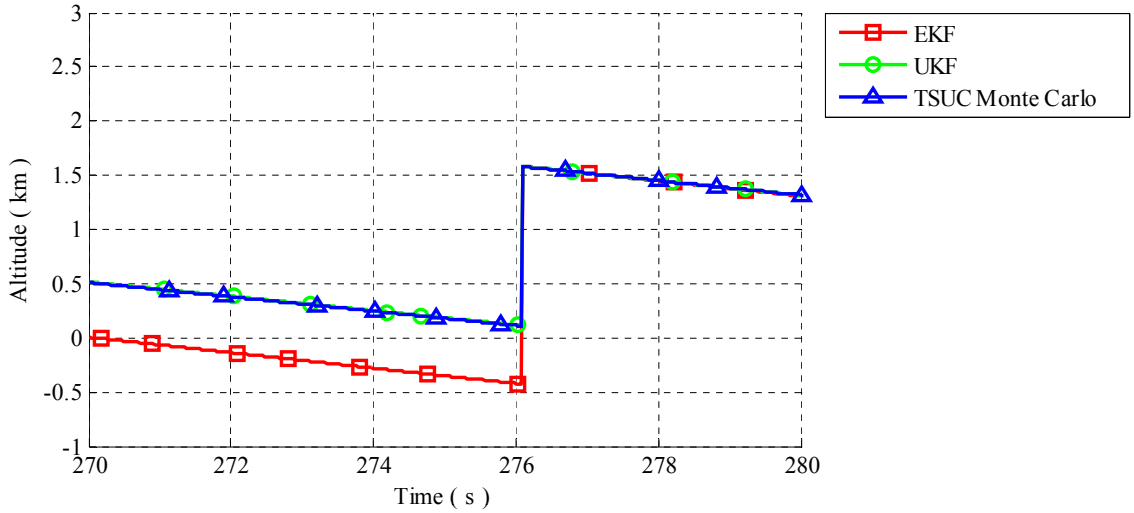

Figure 79: A close up view of the change in the altitude estimates shown in the previous figure when the altimeter acquires the ground. The jump suggests that the true entry state differs from the mean entry state listed in Table 18.

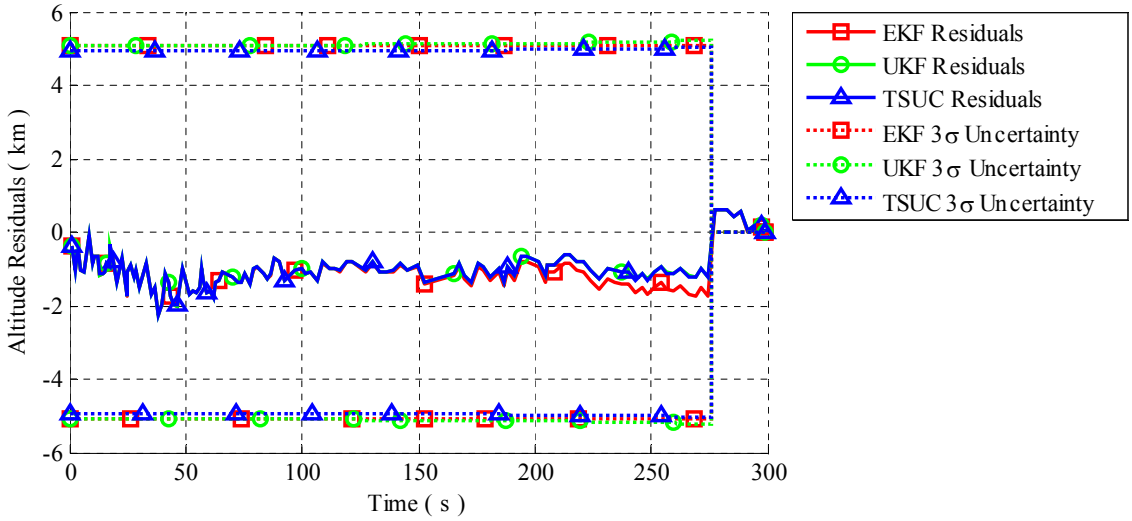

Figure 80: The residuals of the altitude time histories shown in the previous figure relative to the digitized data from Spencer 1999 [269].

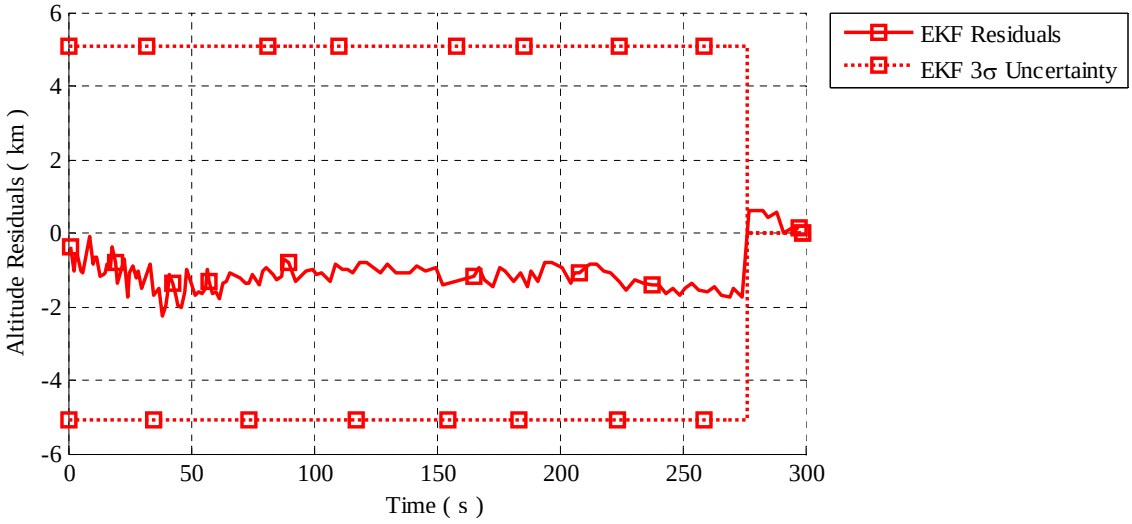

Figure 81: Another look at just the altitude residuals between the extended Kalman filter and the digitized data from Spencer 1999 [269].

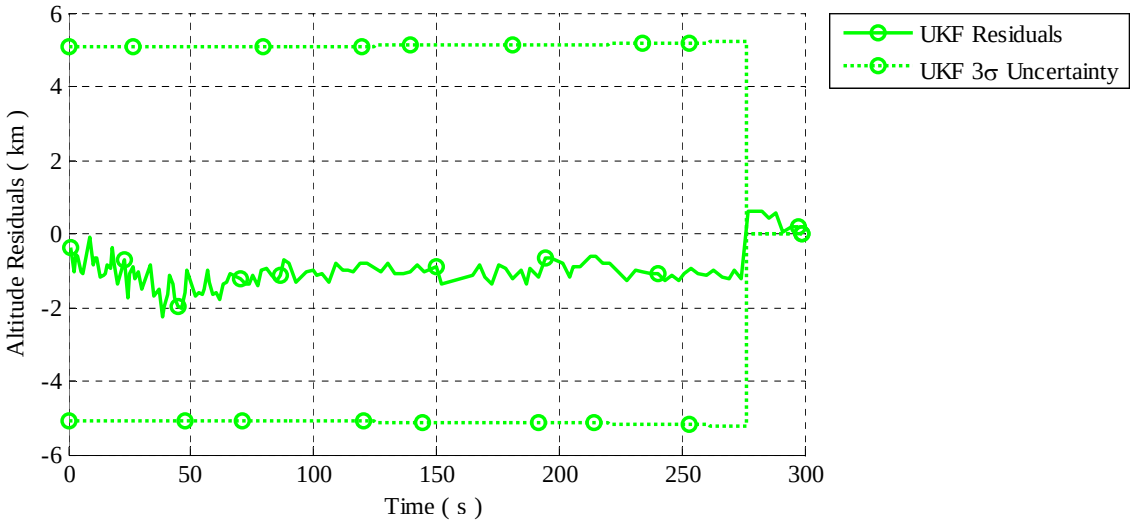

Figure 82: Another look at just the altitude residuals between the unscented Kalman filter and the digitized data from Spencer 1999 [269].

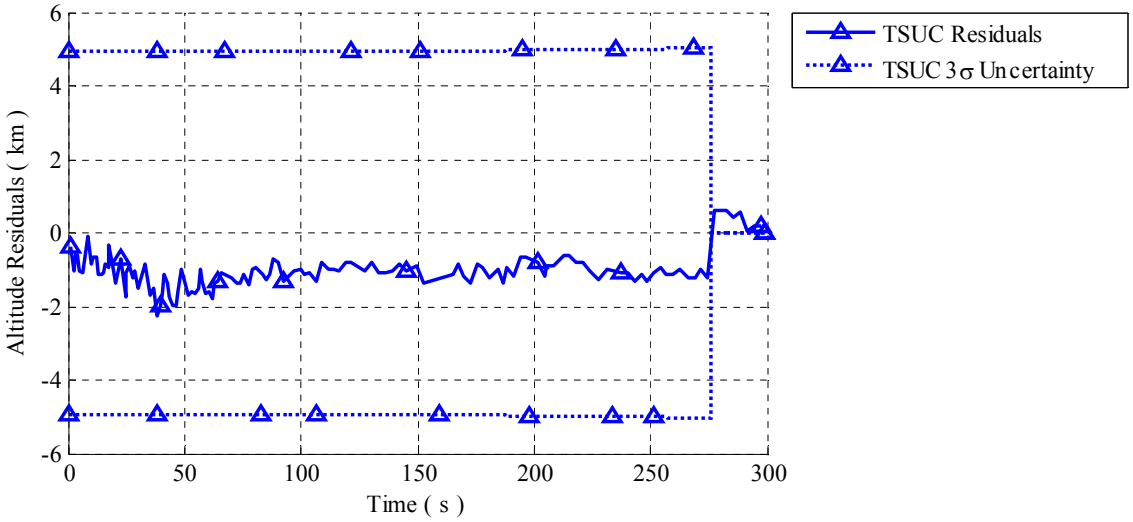

Figure 83: Another look at just the altitude residuals between TSUC and the digitized data from Spencer 1999 [269].

5.2.6 Velocity

Reconstructed with only Acceleration Data

The digitized velocity time history for Mars Pathfinder from Spencer 1999 [269] is shown in Figure 84 with the reconstructions by the Kalman filters discussed in Chapter 3 (using only acceleration data) overlaid. Both Kalman filters discussed in Chapter 3 appear to agree well with the digitized data from Spencer 1999 [269]. The residuals of the velocity time histories shown in Figure 84 relative to the digitized data from Spencer 1999 [269] are shown in Figure 85. Neither Kalman filter discussed in Chapter 3 contains the residuals within their 3σ uncertainty bounds, and the large divergence of the residuals around 75 seconds is due to peak deceleration. However, the similarity of the three sets of residuals in Figure 85 indicates that the unscented Kalman filter was able to reconstruct Mars Pathfinder's trajectory at least as well as the extended Kalman filter. While the similarity of the 3σ uncertainty bounds between the unscented Kalman filter and TSUC in Figure 85 (perhaps better seen in Figure 87) indicates that unscented Kalman filter compares well against a Monte Carlo simulation. Unfortunately, the 3σ uncertainty bounds for the extended Kalman filter rapidly converge to almost zero approximately 50 seconds into the trajectory (perhaps better seen in Figure 86) indicating that the extended Kalman filter tends to over predict the accuracy of its best estimate more than the unscented Kalman filter.

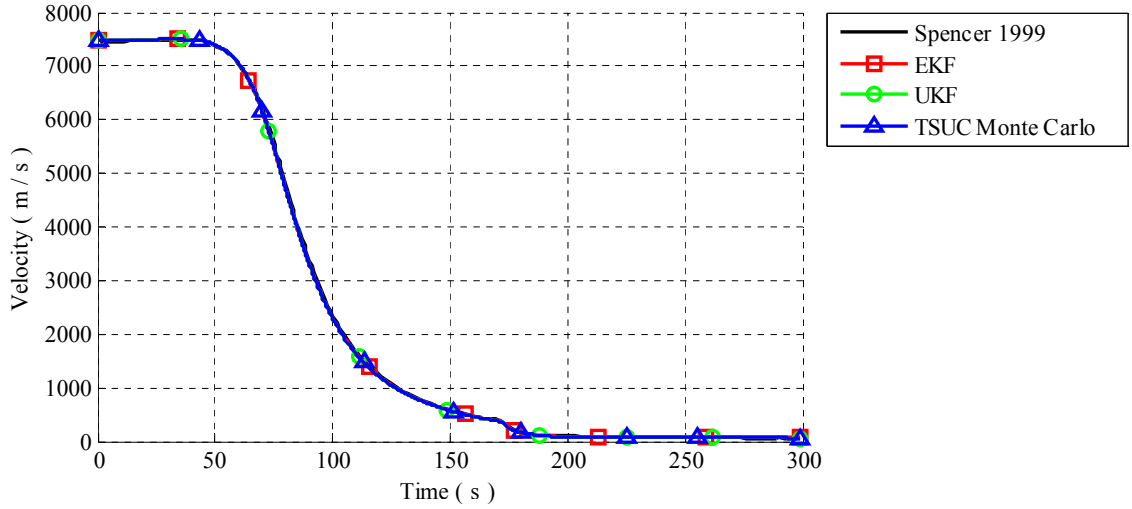

Figure 84: The digitized velocity time history for Mars Pathfinder from Spencer 1999 [269] is shown with the reconstructions (using only acceleration data) and the simulation.

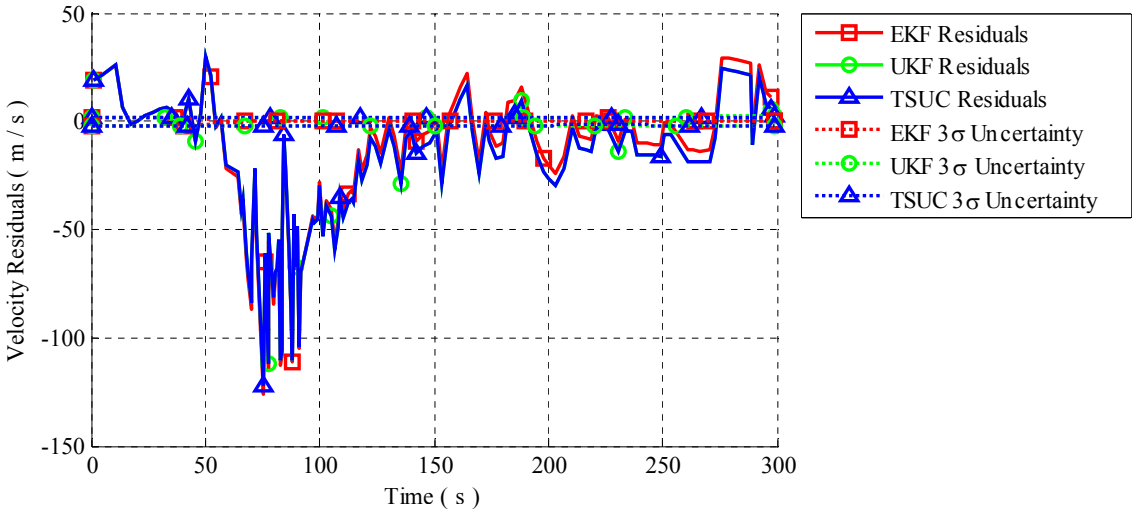

Figure 85: The residuals of the velocity time histories shown in the previous figure relative to the digitized data from Spencer 1999 [269].

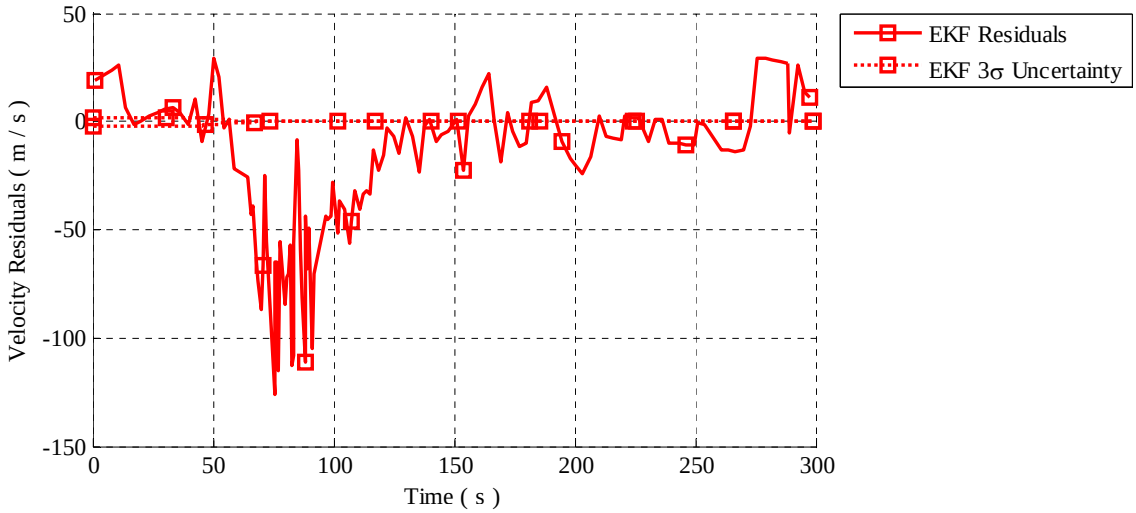

Figure 86: Another look at just the velocity residuals between the extended Kalman filter and the digitized data from Spencer 1999 [269].

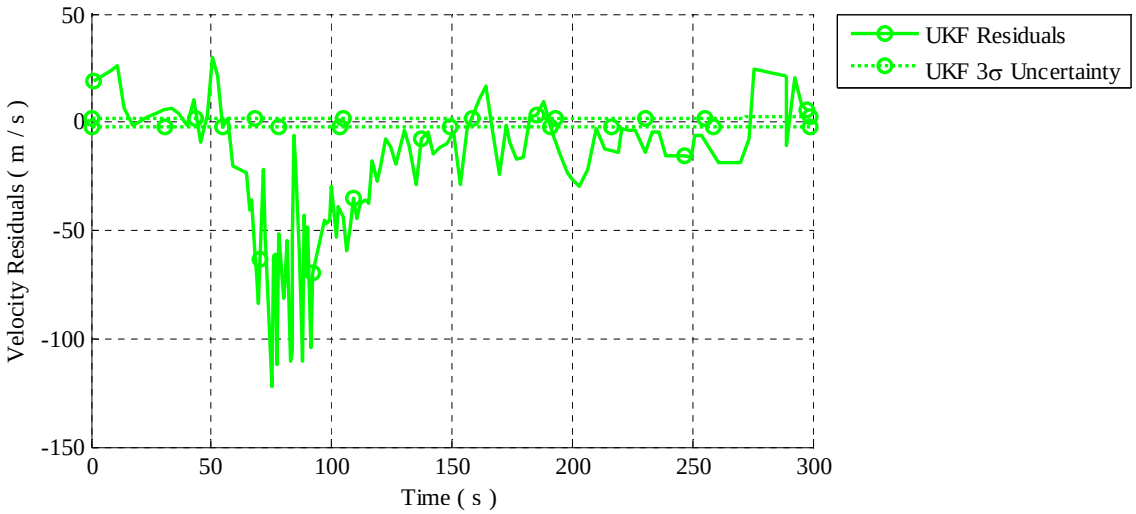

Figure 87: Another look at just the velocity residuals between the unscented Kalman filter and the digitized data from Spencer 1999 [269].

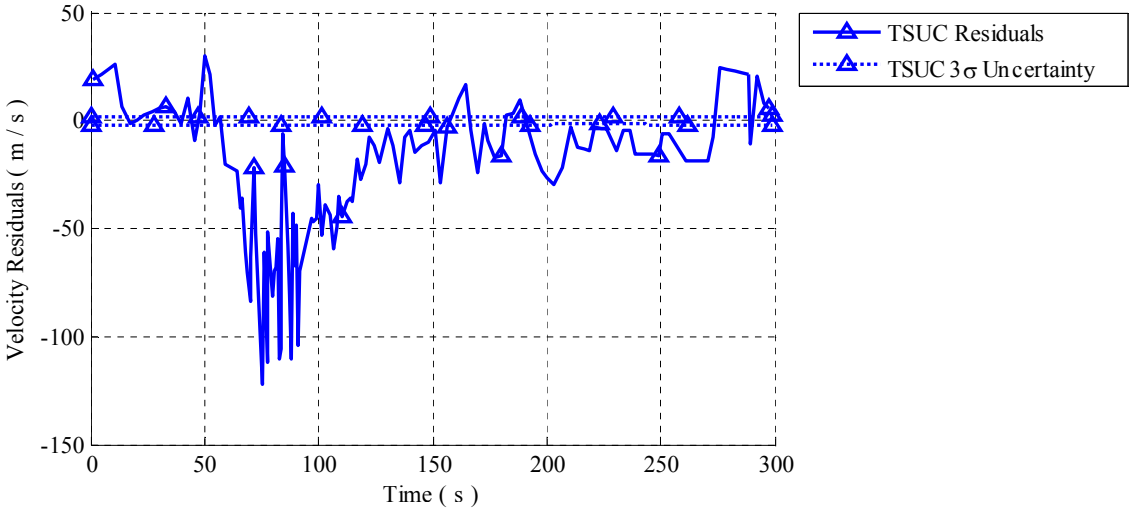

Figure 88: Another look at just the velocity residuals between TSUC and the digitized data from Spencer 1999 [269].

Reconstructed with both Acceleration Data and Altimeter Data

The digitized velocity time history for Mars Pathfinder from Spencer 1999 [269] is shown in Figure 89 with the reconstructions by the Kalman filters discussed in Chapter 3 (using both acceleration data and altimeter data) overlaid. Both Kalman filters discussed in Chapter 3 appear to agree well with the digitized data from Spencer 1999 [269]. The residuals of the velocity time histories shown in Figure 89 relative to the digitized data from Spencer 1999 [269] are shown in Figure 90. Neither Kalman filter discussed in Chapter 3 contains the residuals within their 3σ uncertainty bounds, and the large divergence of the residuals around 75 seconds is due to peak deceleration. However, the similarity of the residuals indicates that the unscented Kalman filter was able to reconstruct Mars Pathfinder's velocity at least as well as the extended Kalman filter. The 3σ uncertainty bounds for the extended Kalman filter rapidly converge to almost zero approximately 50 seconds into the trajectory (perhaps better seen in Figure 91) indicating that the extended Kalman filter tends to over predict the accuracy of its best estimate more than the unscented Kalman filter. The 3σ uncertainty bounds of the unscented Kalman filter (perhaps better seen

in Figure 92) converge rapidly to nearly zero when the altimeter acquires the ground.

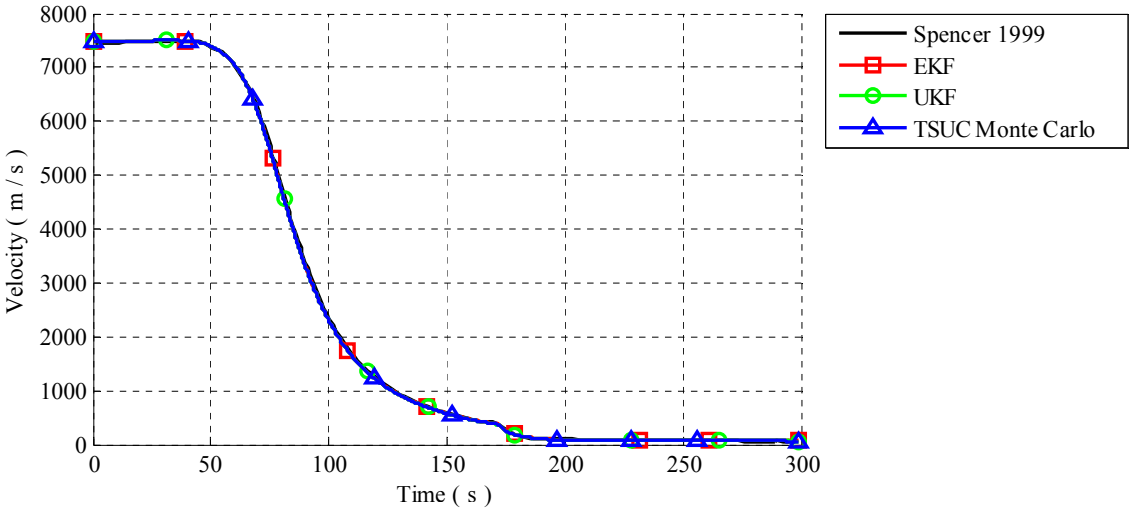

Figure 89: The digitized velocity time history for Mars Pathfinder from Spencer 1999 [269] is shown with the reconstructions (using both acceleration data and altimeter data) and the simulation.

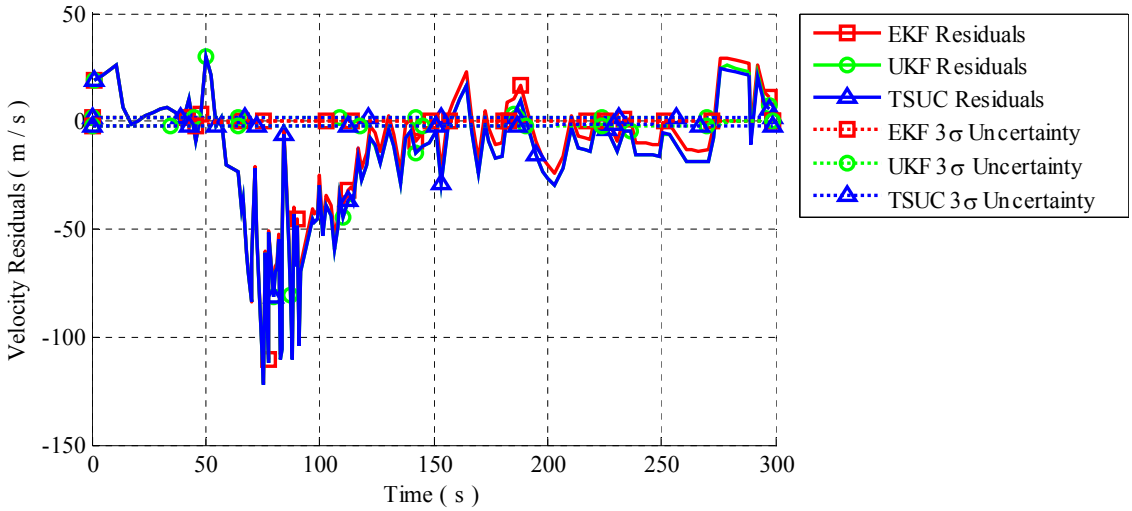

Figure 90: The residuals of the velocity time histories shown in the previous figure relative to the digitized data from Spencer 1999 [269].

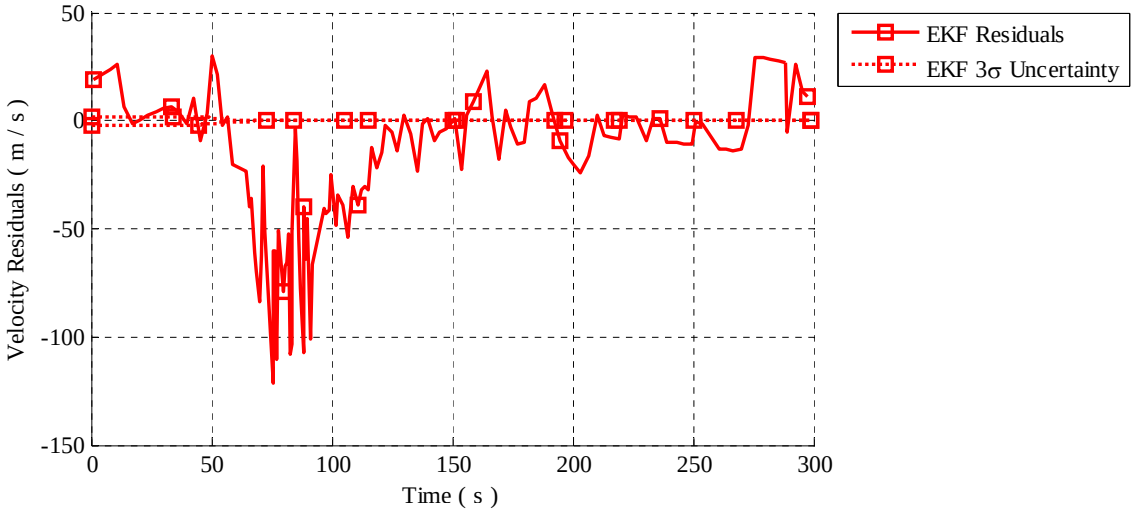

Figure 91: Another look at just the velocity residuals between the extended Kalman filter and the digitized data from Spencer 1999 [269].

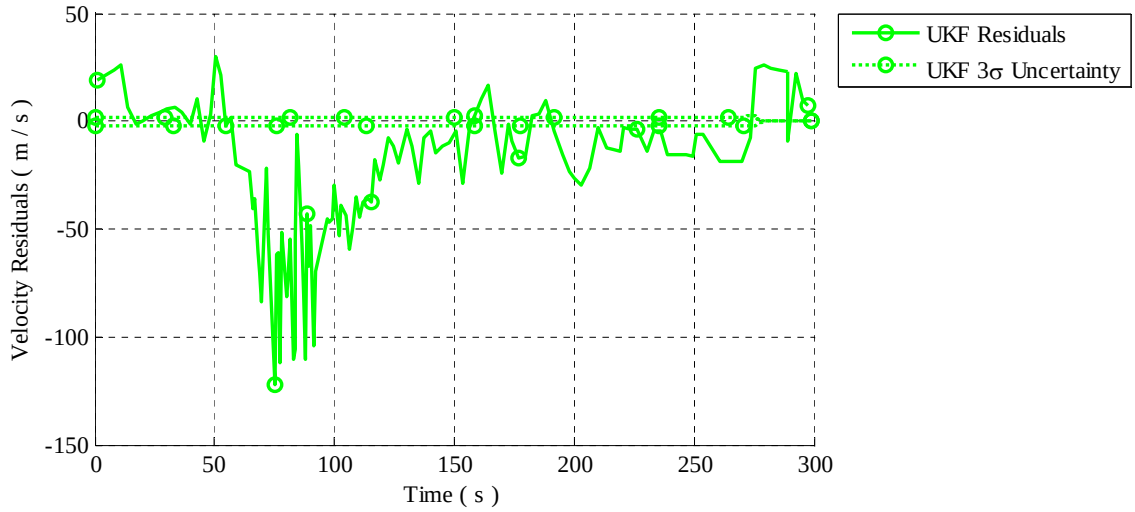

Figure 92: Another look at just the velocity residuals between the unscented Kalman filter and the digitized data from Spencer 1999 [269].

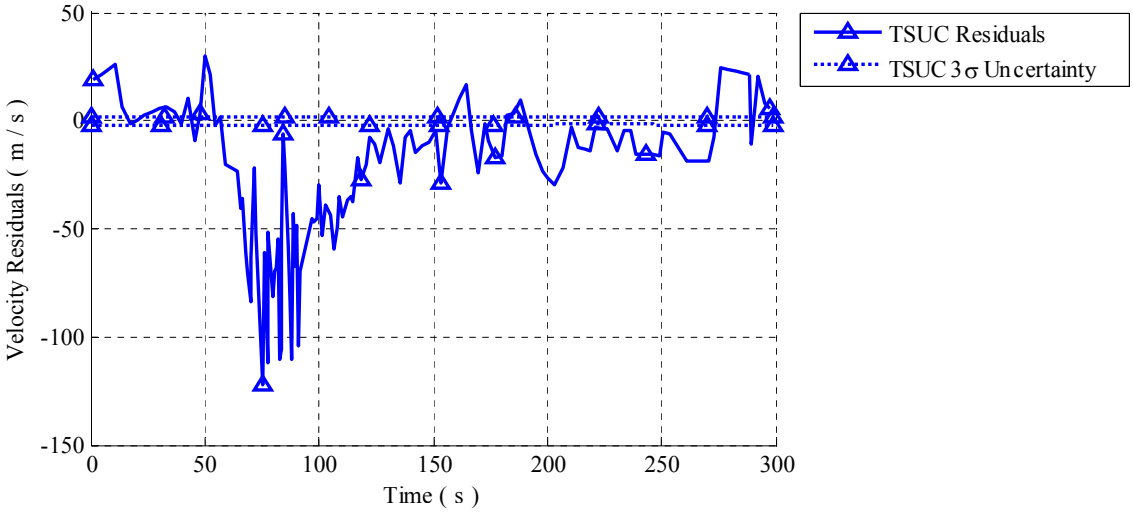

Figure 93: Another look at just the velocity residuals between TSUC and the digitized data from Spencer 1999 [269].

5.2.7 Flight Path Angle

Reconstructed with only Acceleration Data

The digitized flight path angle time history for Mars Pathfinder from Spencer 1999 [269] is shown in Figure 94 with the reconstructions by the Kalman filters discussed in Chapter 3 (using only acceleration data) overlaid. Both Kalman filters discussed in Chapter 3 appear to agree well with the digitized data from Spencer 1999 [269]. The residuals of the flight path angle time histories shown in Figure 94 relative to the digitized data from Spencer 1999 [269] are shown in Figure 95. Neither of the Kalman filters discussed in Chapter 3 contain the residuals within their 3σ uncertainty bounds, and the large divergence of the residuals centered around 210 seconds is due to parachute deployment. However, the better bounding of the residuals by the unscented Kalman filter (perhaps better seen in Figure 97) indicates that it was able to reconstruct Mars Pathfinder's flight path angle somewhat better than the extended Kalman filter. While the similarity of the 3σ uncertainty bounds between the unscented Kalman filter (perhaps better seen in Figures 97 and 98) indicates that the unscented Kalman filter agrees well with the collocation simulation. Unfortunately,

the 3σ uncertainty bounds for the extended Kalman filter are nearly zero before parachute deployment (perhaps better seen in Figure 96) and during parachute deployment, the residuals for the extended Kalman filter are approximately three times larger than the residuals for the unscented Kalman filter indicating that the extended Kalman filter's best estimate of flight path angle is probably worse than the unscented Kalman filter and that the extended Kalman filter tends to over predict the accuracy of its best estimate more than the unscented Kalman filter.

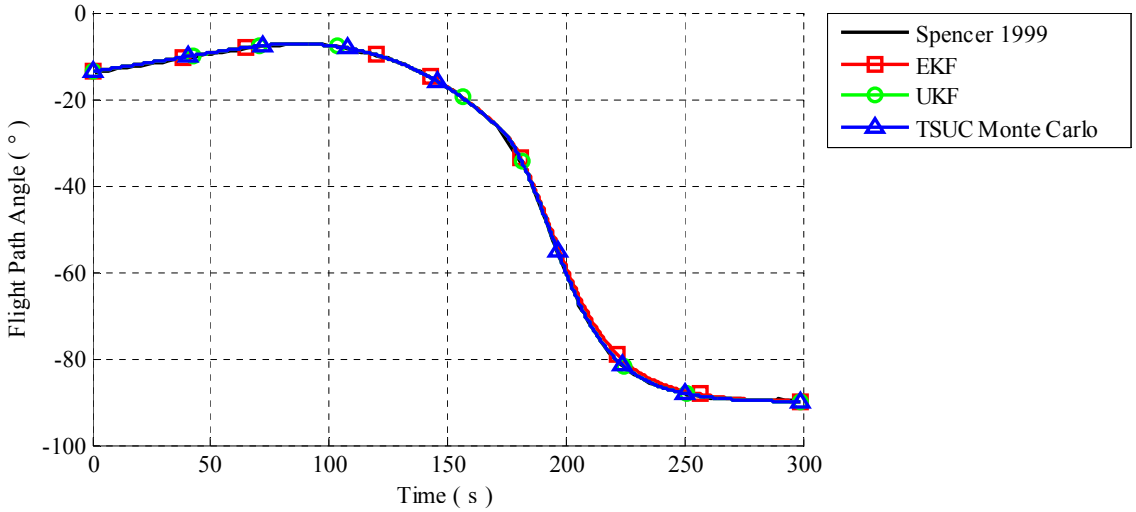

Figure 94: The digitized flight path angle time history for Mars Pathfinder from Spencer 1999 [269] is shown with the reconstructions (using only acceleration data) and the simulation.

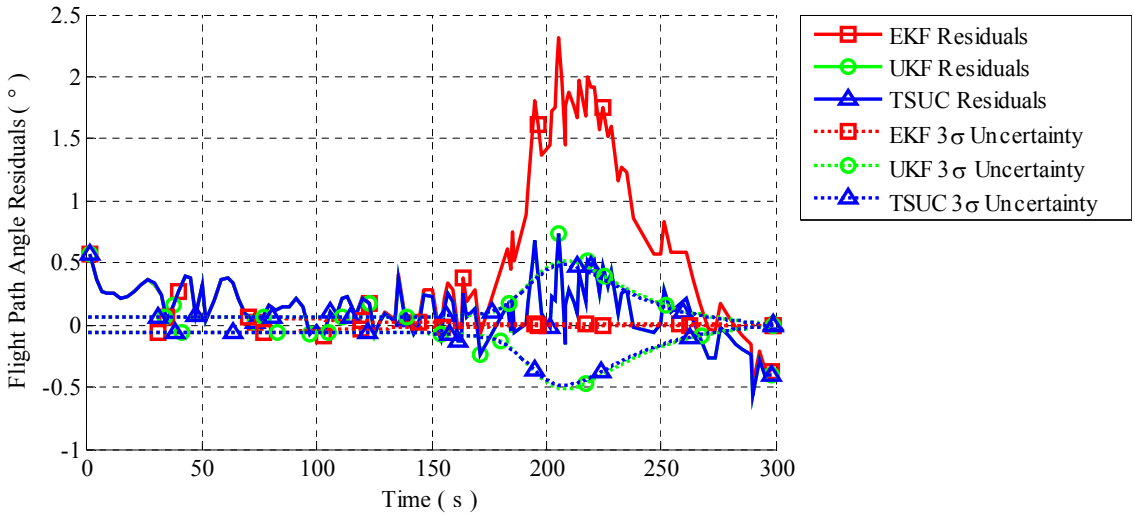

Figure 95: The residuals of the flight path angle time histories shown in the previous figure relative to the digitized data from Spencer 1999 [269].

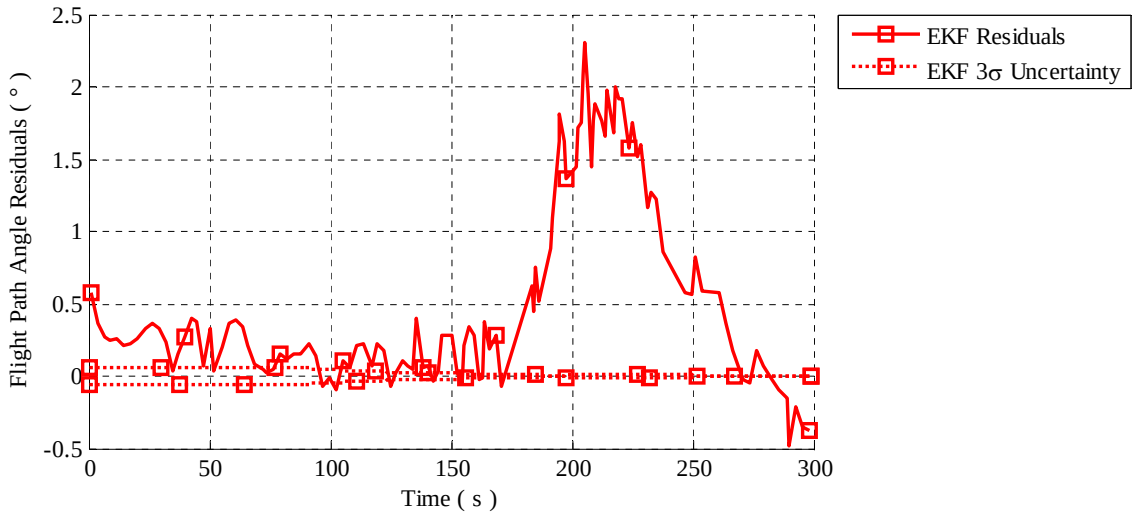

Figure 96: Another look at just the velocity residuals between the extended Kalman filter and the digitized data from Spencer 1999 [269].

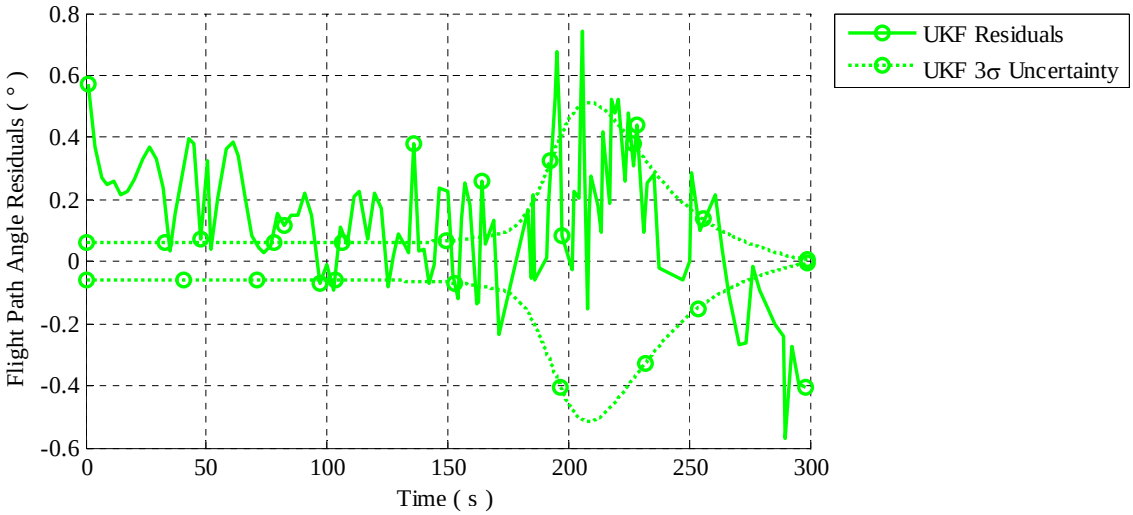

Figure 97: Another look at just the velocity residuals between the unscented Kalman filter and the digitized data from Spencer 1999 [269].

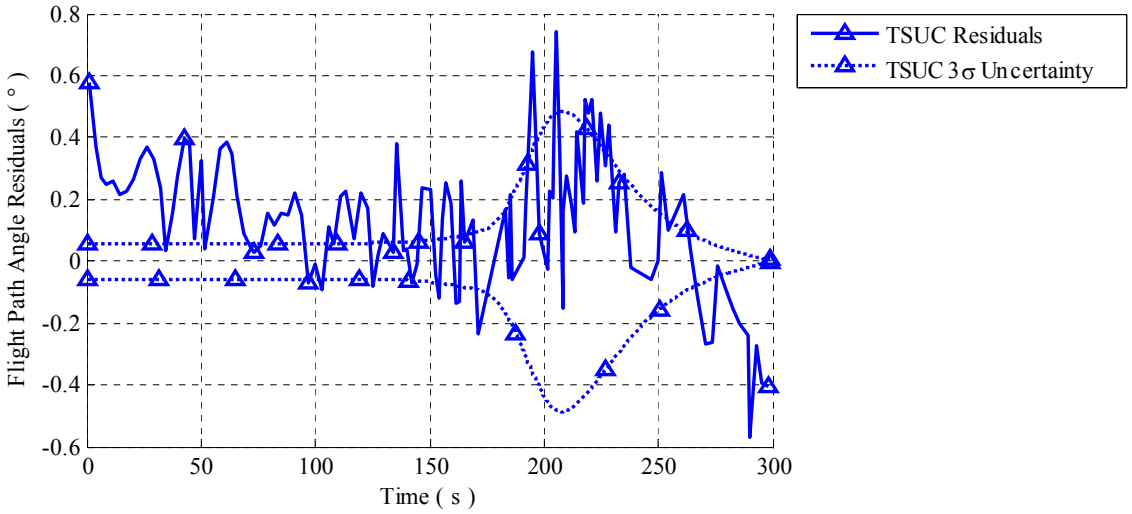

Figure 98: Another look at just the velocity residuals between TSUC and the digitized data from Spencer 1999 [269].

Reconstructed with both Acceleration Data and Altimeter Data

The digitized flight path angle time history for Mars Pathfinder from Spencer 1999 [269] is shown in Figure 99 with the reconstructions by the Kalman filters discussed in Chapter 3 (using both acceleration data and altimeter data) overlaid. Both Kalman

filters discussed in Chapter 3 appear to agree well with the digitized data from Spencer 1999 [269]. The residuals of the flight path angle time histories shown in Figure 99 relative to the digitized data from Spencer 1999 [269] are shown in Figure 100. Neither of the Kalman filters discussed in Chapter 3 contain the residuals within their 3σ uncertainty bounds, and the large divergence of the residuals centered around 210 seconds is due to parachute deployment. However, the better bounding of the residuals by the unscented Kalman filter (perhaps better seen in Figure 102) indicates that it was able to reconstruct Mars Pathfinder's flight path angle somewhat better than the extended Kalman filter. While the similarity of the 3σ uncertainty bounds between the unscented Kalman filter and TSUC (perhaps better seen in Figures 102 and 103) indicates that the unscented Kalman filter agrees well with the collocation simulation. Unfortunately, the 3σ uncertainty bounds for the extended Kalman filter are nearly zero before parachute deployment (perhaps better seen in Figure 101) and during parachute deployment, the residuals for the extended Kalman filter are approximately three times larger than the residuals for the unscented Kalman filter indicating that the extended Kalman filter's best estimate of flight path angle is probably worse than the unscented Kalman filter and that the extended Kalman filter tends to over predict the accuracy of its best estimate more than the unscented Kalman filter. When radar ground acquisition by the altimeter occurs, the extended Kalman filter's 3σ uncertainty bounds are already nearly zero, but ground acquisition causes the unscented Kalman filter to reduce its 3σ uncertainty bounds to nearly zero.

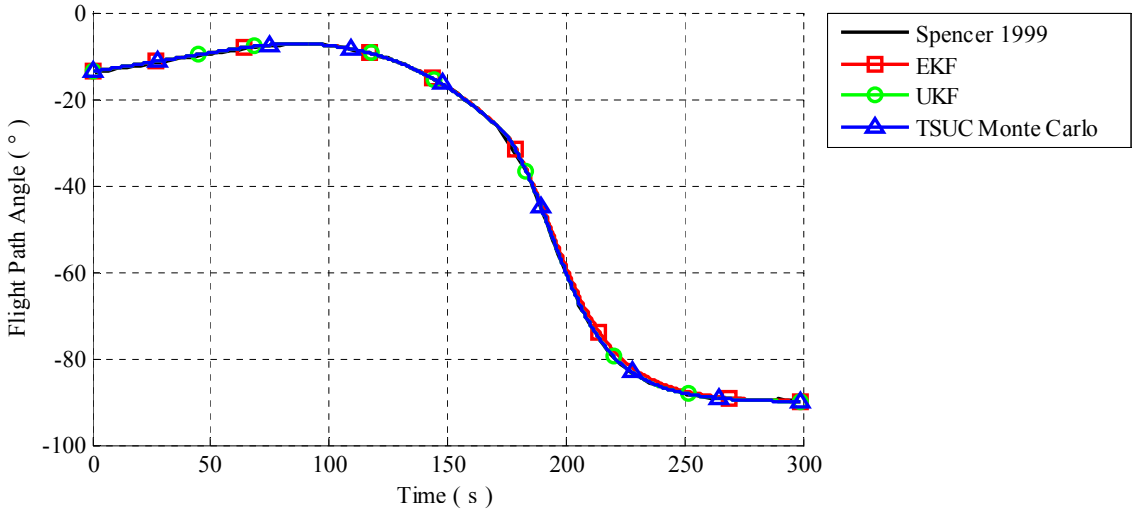

Figure 99: The digitized flight path angle time history for Mars Pathfinder from Spencer 1999 [269] is shown with the reconstructions (using both acceleration data and altimeter data) and the simulation.

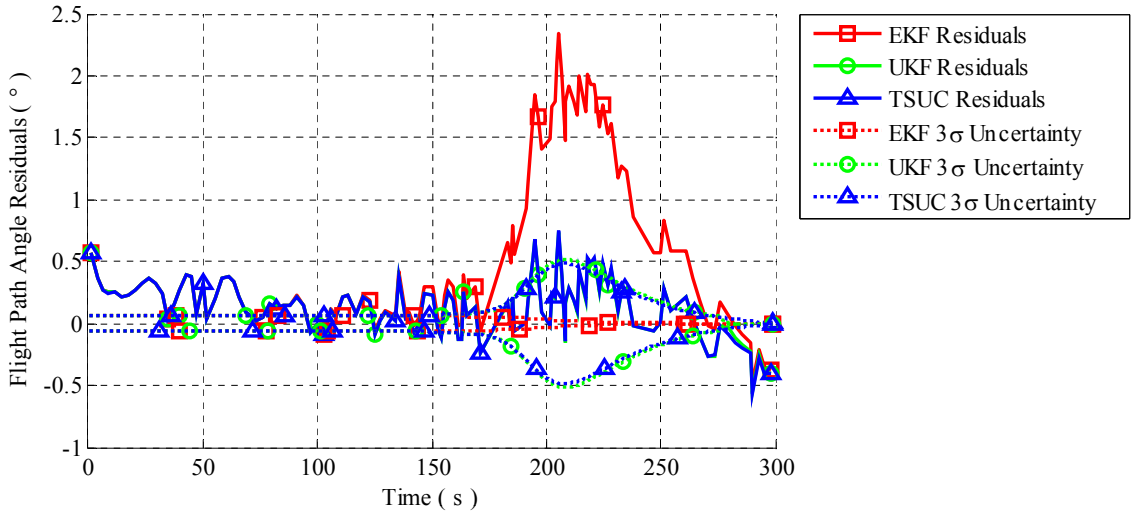

Figure 100: The residuals of the flight path angle time histories shown in the previous figure relative to the digitized data from Spencer 1999 [269].

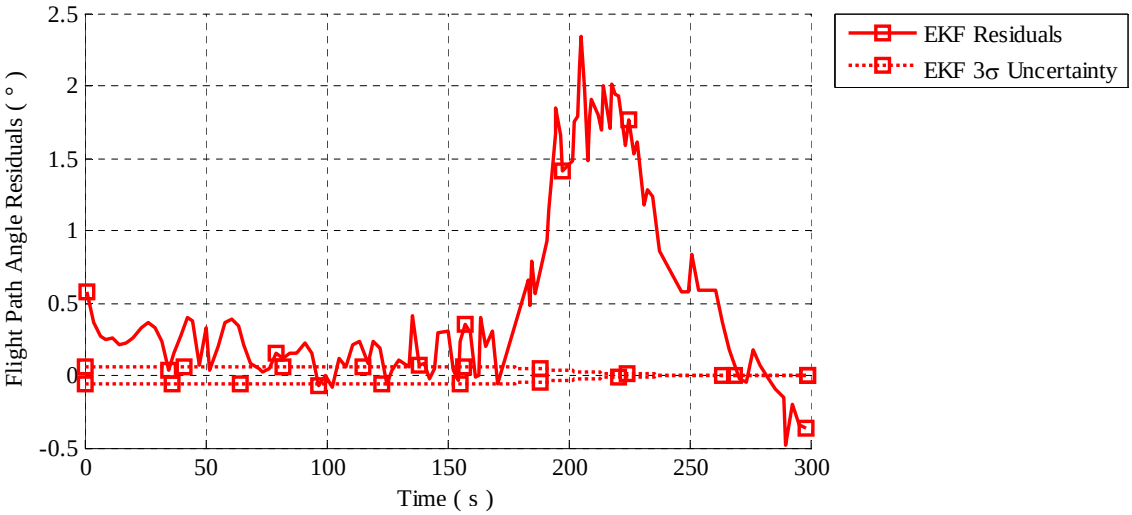

Figure 101: Another look at just the velocity residuals between the extended Kalman filter and the digitized data from Spencer 1999 [269].

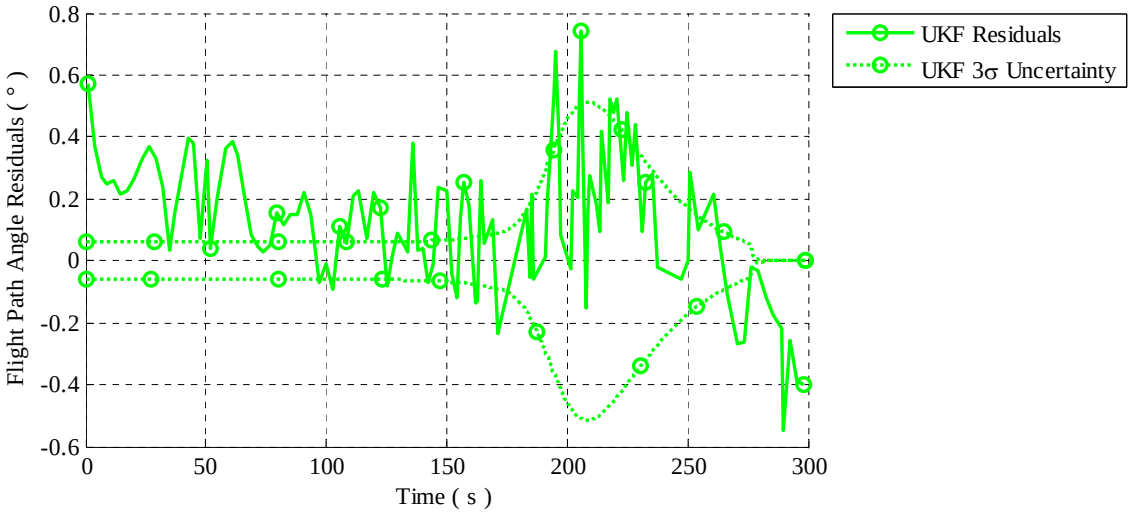

Figure 102: Another look at just the velocity residuals between the unscented Kalman filter and the digitized data from Spencer 1999 [269].

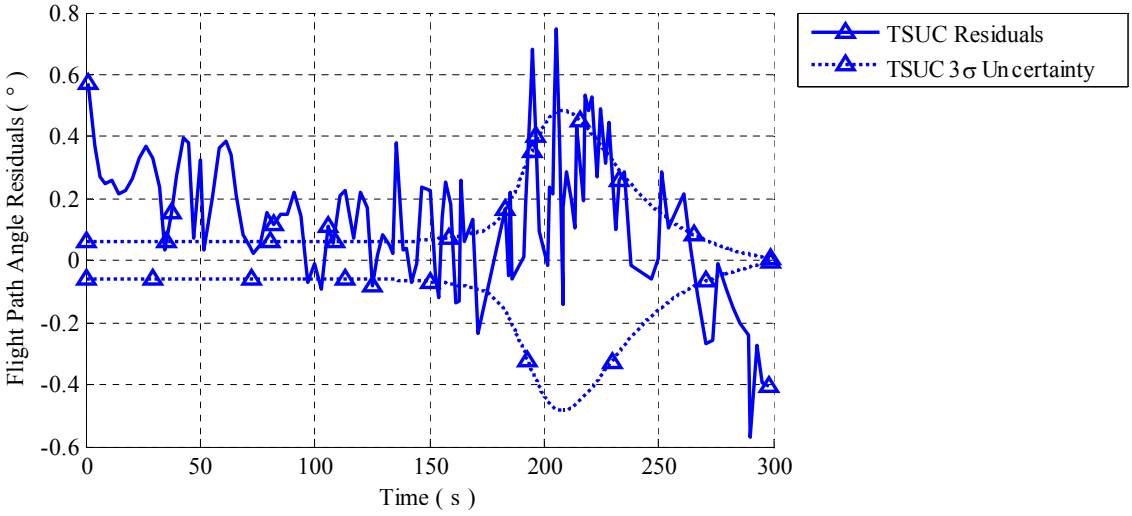

Figure 103: Another look at just the velocity residuals between TSUC and the digitized data from Spencer 1999 [269].

5.2.8 Landing Site

Reconstructed with only Acceleration Data

The landing site for Mars Pathfinder from Spencer 1999 [269] is shown in Figure 104 with the landing site predictions by the Kalman filters discussed in Chapter 3 (using only acceleration data). Both Kalman filters discussed in Chapter 3 appear to agree well with each other from afar. Upon closer examination of the landing site predictions by the Kalman filters discussed in Chapter 3 as shown in Figure 105, the landing site predicted by the unscented Kalman filter is slightly closer to the actual landing site.

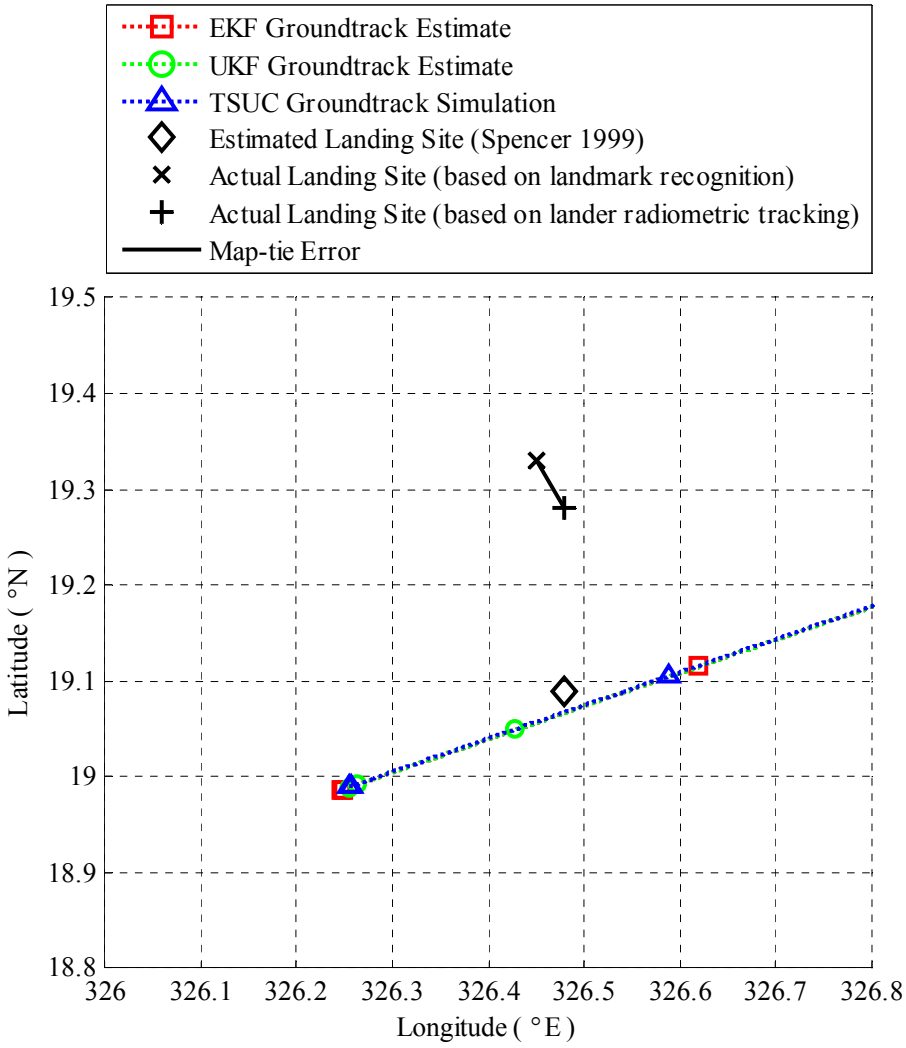

Figure 104: The landing site for Mars Pathfinder from Spencer 1999 [269] is shown with the landing site predictions by the Kalman filters discussed in Chapter 3 (using only acceleration data).

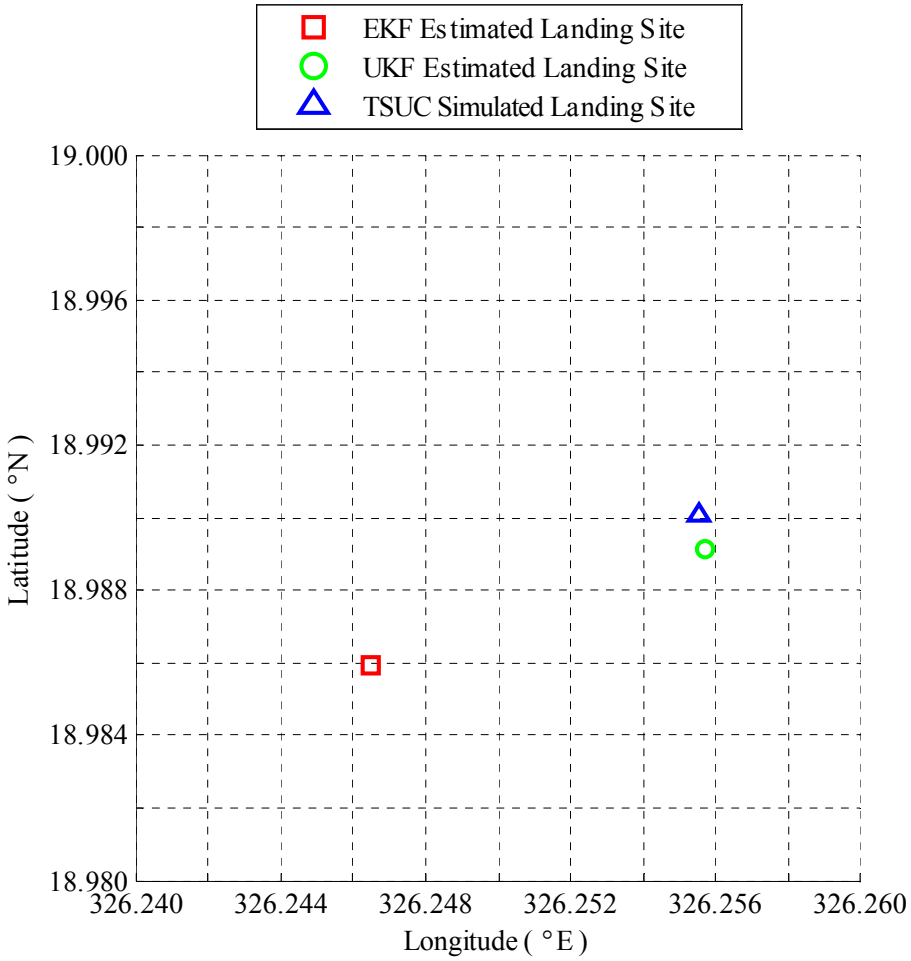

Figure 105: A closer examination of the landing site predictions by the Kalman filters discussed in Chapter 3.

Reconstructed with both Acceleration Data and Altimeter Data

The addition of the altimeter measurement changes the landing site predictions very little as shown in Figures 106 and 107.

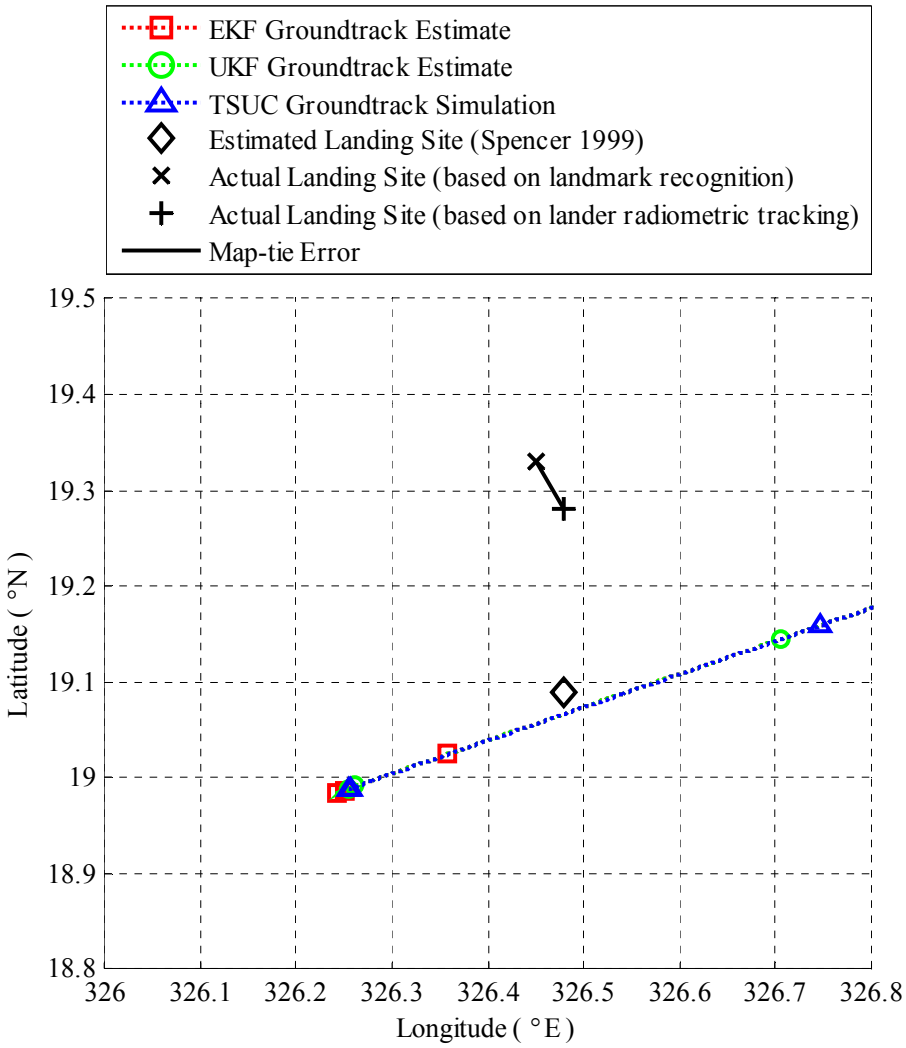

Figure 106: The landing site for Mars Pathfinder from Spencer 1999 [269] is shown with the landing site predictions by the Kalman filters discussed in Chapter 3 (using both acceleration data and altimeter data).

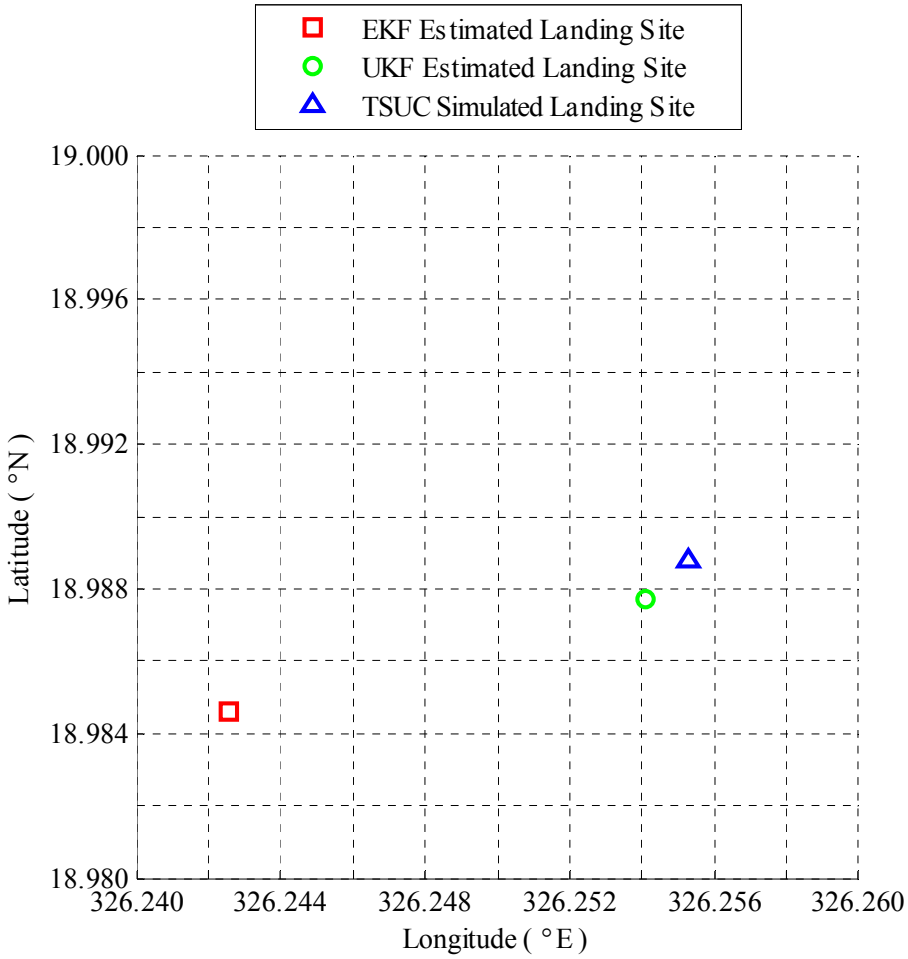

Figure 107: A closer examination of the landing site predictions by the Kalman filters discussed in Chapter 3 (using both acceleration data and altimeter data).

5.3 Summary

Both Kalman filters discussed in Chapter 3 were able to reconstruct the trajectory of Mars Pathfinder nearly equally well. Neither displayed increased residuals in velocity during peak deceleration, though this may have been due to the quality of the digitization of the data from Spencer and others Mars Pathfinder reconstruction [269]. Concerning flight path angle, the extended Kalman filter exhibited residuals during parachute deployment (and later) that were approximately three times larger than those of the unscented Kalman filter. And while the unscented Kalman filter generally

bounded these increased flight path angle residuals, the extended Kalman filter did not. Both Kalman filters were in good agreement in their estimates of altitude, and they were all able to bound their altitude residuals, furthermore, their 3σ uncertainty bounds for altitude were all in good agreement with each other. The addition of the altimeter measurement had a large effect on the estimates of altitude from each of the methods on radar ground acquisition occurred, even though it only slightly affected the estimates of the other state variables. Additionally, their density profiles were in good agreement (please see Appendix E). Regarding the location of Mars Pathfinder's landing site, both Kalman filters agreed with each other when viewed from afar. Upon closer examination, the landing site predicted by the unscented Kalman filter was near TSUC's simulated landing site, while the extended Kalman filter's predicted landing site was approximately 0.01° farther from the actual landing site. These results indicate that TSUC, using the procedure of Table 15 on page 98 to solve for the state variables, is equivalent to explicit integration in performance, and also serves to further validate the results from the unscented Kalman filter.

CHAPTER VI

OBSERVATIONS FROM COMPARING THE TWO KALMAN FILTERS

6.1 Introduction

The following paragraphs discuss the results from the two Kalman filters in terms of their reconstruction results, as well as other aspects of their performance. These other aspects include memory space requirements and the computational time of each method. Additionally, the effects of noise–level and measurement frequency (or sampling rate) are discussed.

6.2 Reconstructed Trajectory Results

Both Kalman filters discussed in Chapter 3 were able to reconstruct the sample problem and Mars Pathfinder's trajectories nearly equally well. While the extended Kalman filter did demonstrate some difficulties, the unscented Kalman filter had only slight difficulties. The unscented Kalman filter showed improved entry, descent, and landing trajectory reconstruction over the extended Kalman filter. For example, the extended Kalman had some difficulty with reconstructing the altitude, velocity, and flight path angle time histories after parachute deployment. This is evident from the residuals of its best estimate trajectory for the sample problem (where the true trajectory is known) as shown in Figure 34 on page 104 (altitude residuals), Figure 36 on page 105 (velocity residuals), and Figure 38 on page 107 (flight path angle residuals). In contrast, for the Mars Pathfinder reconstruction, the unscented Kalman filter had altitude residuals as large as the extended Kalman filter's (see Figure 75 on page 145), and while the extended Kalman filter did demonstrate large velocity residuals in its

reconstruction of Mars Pathfinder's trajectory (see Figure 86 on page 152), it was not alone as the unscented Kalman filter had velocity residuals of similar magnitude (see Figure 85 on page 151).[1] Though the unscented Kalman filter did have lower flight path angle residuals during the parachute phase of Mars Pathfinder's descent as shown in Figure 95 on page 158. Overall, this indicates that the unscented Kalman filter offers better trajectory reconstruction performance with acceleration measurements when the vehicle changes configuration in–flight.[2] Then again, when the state can be observed, the unscented Kalman filter does not have significantly better performance than the extended Kalman filter as shown by the altitude residuals in Figure 80 on page 148 for the reconstruction of Mars Pathfinder's altitude when altimeter measurements are included. However, the extended Kalman filter should not be dismissed, after all: "It has withstood the test of time!" [41]

Regarding the estimation of uncertainties, the unscented Kalman filter clearly performed better than the extended Kalman filter and did not over predict the accuracy of their best estimates as shown by (1) the propagation of the initial uncertainties for the sample problem in Figure 42 on page 111, Figure 46 on page 114, and Figure 50 on page 117 when compared to a Monte Carlo simulation and (2) the trajectory reconstruction with poor initial conditions as discussed in § 4.4 beginning on page 118.

These results are consistent with the literature assertion that unscented Kalman filtering gives improved estimates of the uncertainty over the extended Kalman filter[3], and demonstrates that using TSUC as part of a Monte Carlo simulation allows it to provide estimates of uncertainty on par with those of an explicit integration of the

[1] Also, the large velocity residuals that occurred during peak deceleration were almost certainly due to the quality of the digitization.

[2] Though, as discussed later, the unscented Kalman filter demonstrated a penalty in terms of additional computational time for this improved performance. Additionally, improvements in the model fidelity of the spacecraft configuration changes may allow the extended Kalman filter to achieve results similar to the unscented Kalman filter. However, the unscented Kalman filter offers the improved performance without the need to increase model fidelity, and in the case of the unscented Kalman filter, without the need to add process noise.

[3] In the context of reconstructing entry, descent, and landing trajectories.

dynamics. This result indicates that it is equivalent to explicit integration in performance, and also serves to further validate the results from the unscented Kalman filter. However, as the Monte Carlo for the sample problem in Chapter 4 was only on the initial conditions, the additional sources of uncertainty listed in Chapter 4 would also have to be included in Monte Carlos run for real–world missions.

6.3 Memory Usage

Memory usage[4] is an important consideration if a method is to be used to process measurement data in real–time while in–flight. In terms of program size on a non–volatile hard drive, the storage space required by each Kalman filter was approximately 2,000,000 bytes. In terms of memory usage, the extended Kalman filter is the most efficient, though the unscented Kalman filter has comparable memory usage.

6.4 Computational Time

Computational speed is also an important consideration if a method is to be used to process measurement data in real–time while in–flight. According to the literature [195, 125], the time required for the unscented Kalman filter to compute its best estimate of the trajectory is similar to the time required for the extended Kalman filter to generate its best estimate of the trajectory. This was found to be the case for entry, descent, and landing trajectory reconstruction as the two Kalman filters were within the same order of magnitude as shown in Table 19. However, the unscented Kalman filter was approximately five times slower than the extended Kalman filter, which is similar to what was found for the bearing–only tracking problem [231], and it is better than the 1 (EKF) to 11.5 (UKF) ratio for angle–based relative navigation [272].

[4]All the coding for this research was done in Matlab, so the specific numbers discussed apply only to that coding language.

Table 19: Relative computational times for the extended Kalman filter and the unscented Kalman filter when performing an entry, descent, and landing trajectory reconstruction.

Method	Relative Computational Time
EKF	1
UKF	4.59

6.5 Noise Level and Frequency of Acceleration Measurements

For the extended Kalman filter and the unscented Kalman filter, a study on how the noise level and the frequency of acceleration measurements affected each filter's performance was conducted. In this study, the test criterion was whether or not each Kalman filter could bound the altitude, velocity, and flight path angle residuals between the true trajectory and its best estimate within its predicted 3σ uncertainty bounds. In other words, to pass the test, each Kalman filter must bound the residuals approximately 99.7% of the time. Acceleration noise levels from 10 μg to 1,000,000 μg were tested, and the sampling rate (the frequency at which measurements were taken) was varied from 2^{-8} Hz (one measurement every 256 seconds) to 2^5 Hz (one measurement every $\frac{1}{32}$ of a second). The same random noise was added to the data processed by both filters for each trial, and 100 trials were conducted for each combination of noise level and sampling rate. The results are given below in Figures 108 through 115.

The extended Kalman filter had the least trouble bounding the altitude residuals, the next least trouble bounding the flight path angle residuals, and the most trouble bounding the velocity residuals. The residuals for altitude, velocity, and flight path angle were also harder for the extended Kalman filter to bound as the frequency of measurements increased. As the frequency of measurements increased, the extended Kalman filter was only able to bound the residuals if the noise was substantially reduced. The bounding of the state residuals at low frequencies of measurement by

the extended Kalman filter may be due to the quality of the process model. However, if the unbounded points for altitude, velocity, and flight path angle are expressed as a fraction of the number of measurements, then the extended Kalman filter is unable to bound the residuals within its predicted 3σ limits for noise levels equal to or greater than 10,000 μg for the cases studied (please see Figure 111).

At low frequencies, the extended Kalman filter is just propagating the trajectory for extended periods, and the process model has enough fidelity to ensure that the residuals are bounded. It is expected that increasing the process noise would allow the extended Kalman filter to bound the residuals at higher frequencies of measurement, as higher process noise implies lower model fidelity and lower process noise implies higher model fidelity. Based on the results for the extended Kalman filter, it is not surprising the extended Kalman filter had difficulty bounding the residuals of the sample trajectory and Mars Pathfinder, as the acceleration noise level for these was 1500 μg [49] and the measurement frequency was 32 Hz [164].

The unscented Kalman filter was able to bound the the altitude, velocity, and flight path angle residuals 99.7% of the time for all the cases run. The unscented Kalman filter is, then, a better choice over the extended Kalman filter when uncertainty information is desired and the residuals must be bounded. However, the best estimate of the extended Kalman filter is often as good as the best estimate of the unscented Kalman filter, especially when the state is observable (as in the cases studied here).

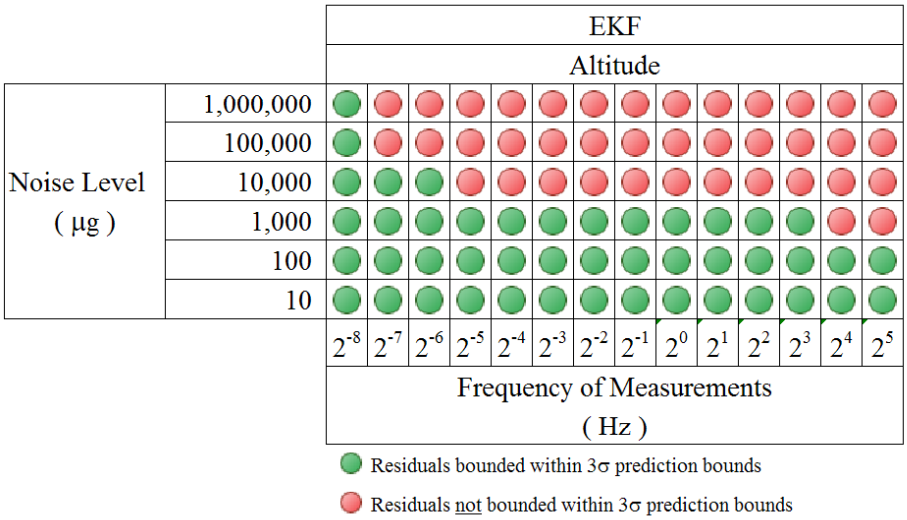

Figure 108: The results of the study on the effect of noise level and frequency of acceleration measurements for the extended Kalman filter's altitude residuals.

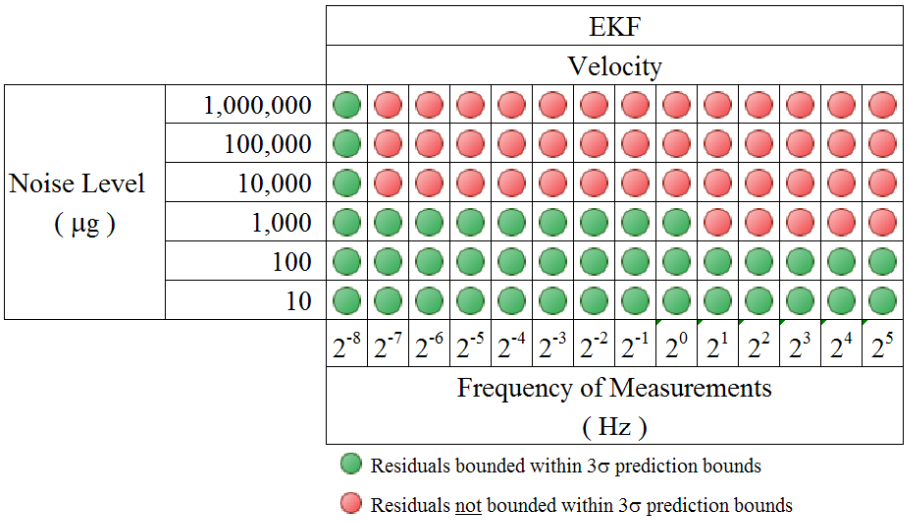

Figure 109: The results of the study on the effect of noise level and frequency of acceleration measurements for the extended Kalman filter's velocity residuals.

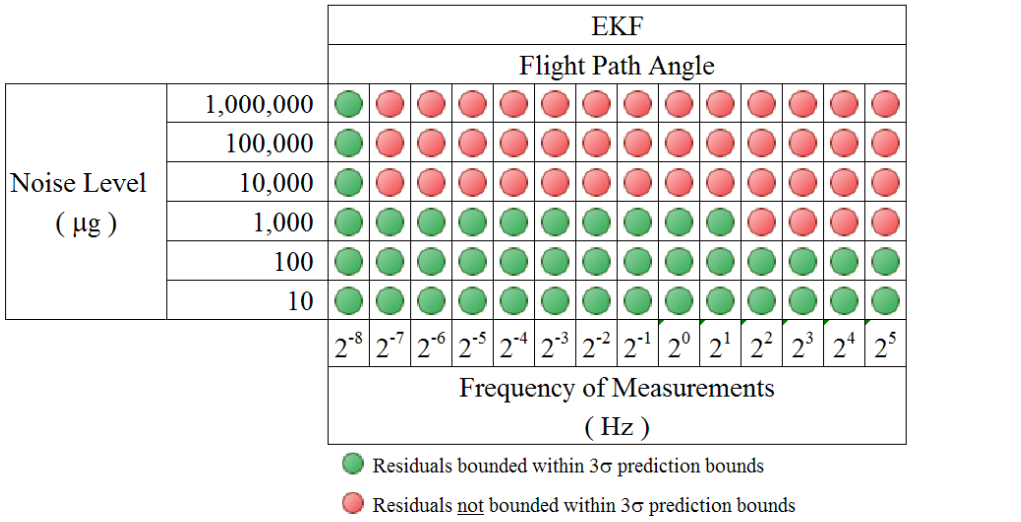

Figure 110: The results of the study on the effect of noise level and frequency of acceleration measurements for the extended Kalman filter's flight path angle residuals.

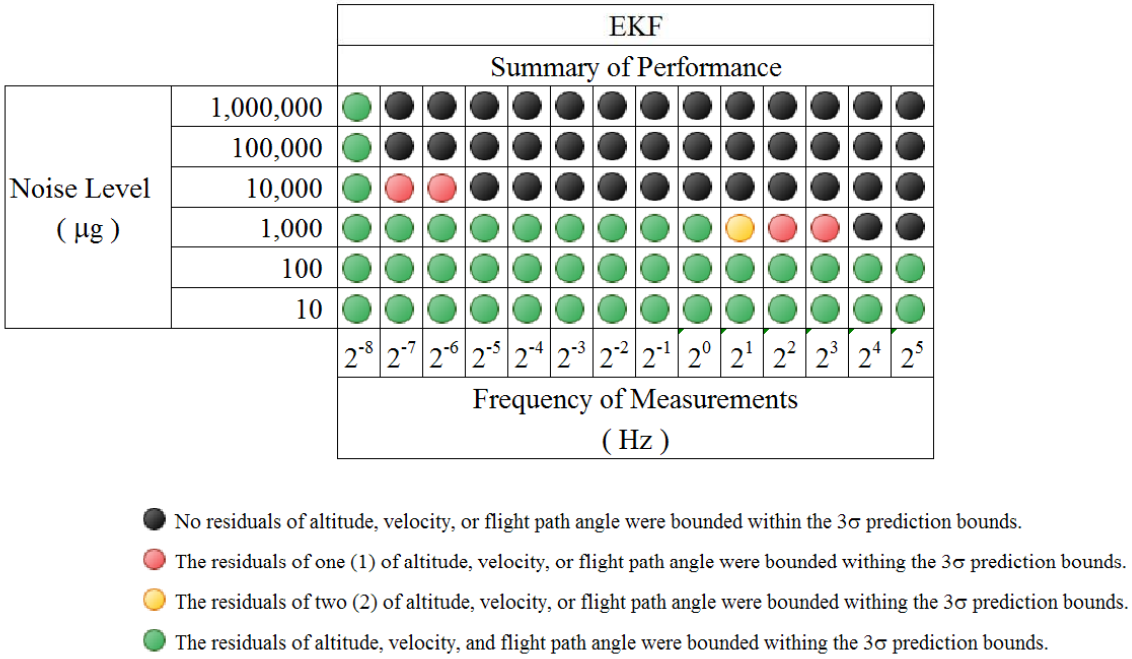

Figure 111: A summary of the results of the study on the effect of noise level and frequency of acceleration measurements for the extended Kalman filter.

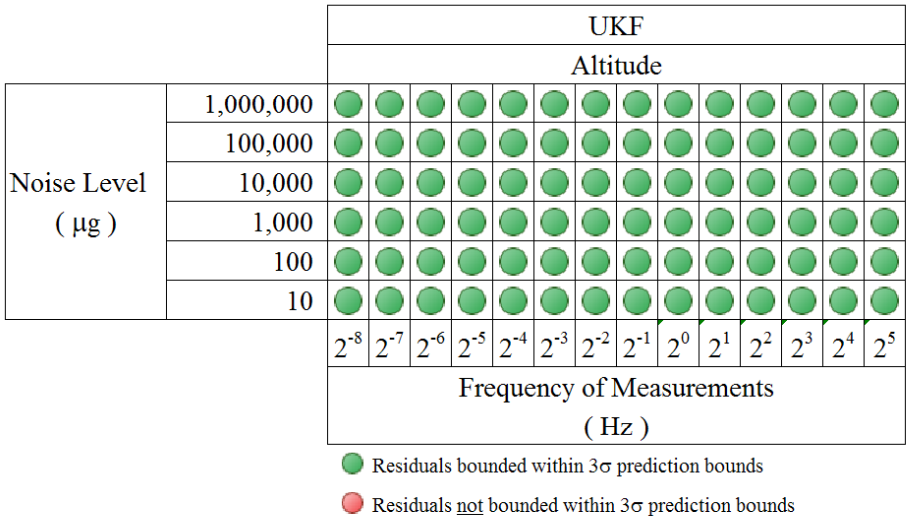

Figure 112: The results of the study on the effect of noise level and frequency of acceleration measurements for the unscented Kalman filter's altitude residuals.

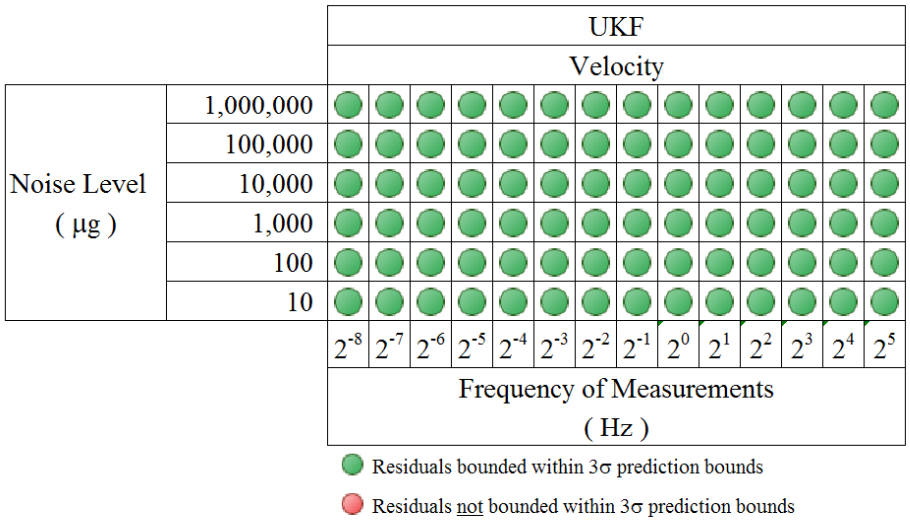

Figure 113: The results of the study on the effect of noise level and frequency of acceleration measurements for the unscented Kalman filter's velocity residuals.

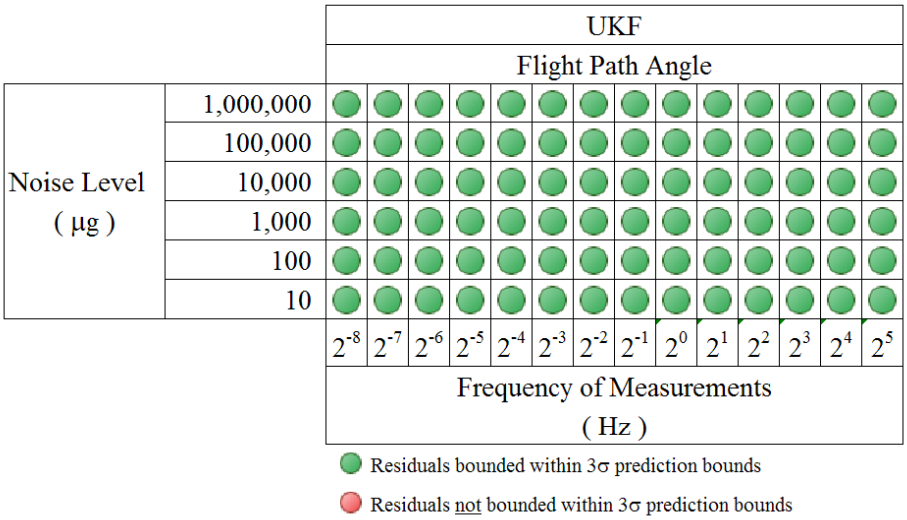

Figure 114: The results of the study on the effect of noise level and frequency of acceleration measurements for the unscented Kalman filter's flight path angle residuals.

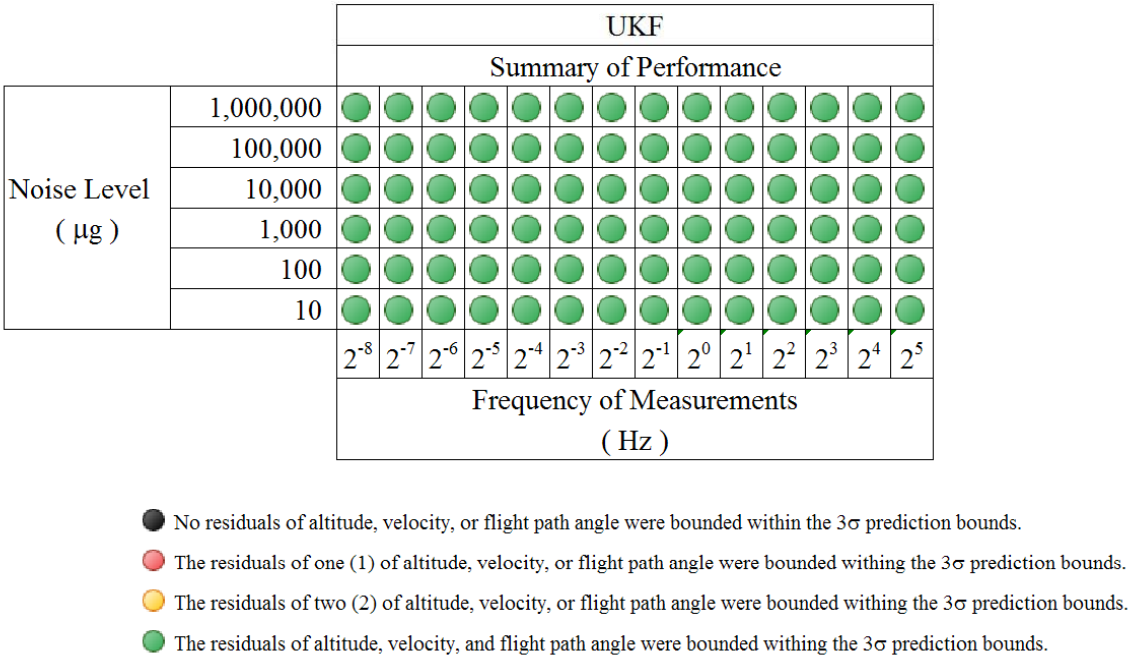

Figure 115: A summary of the results of the study on the effect of noise level and frequency of acceleration measurements for the unscented Kalman filter.

CHAPTER VII

CONCLUSIONS

7.1 Introduction

In the following text, guidelines are suggested on choosing a method for entry, descent, and landing trajectory reconstruction, and this chapter ends with a summary of the research and contributions, as well as suggestions for further research.

7.2 How to Choose a Method for Entry Descent and Landing Trajectory Reconstruction: Suggested Guidelines

Guidelines on how to select a method of entry, descent, and landing trajectory reconstruction are suggested below in Figure 116. The guidelines include trajectory reconstruction using collocation (TRUC) based on its expected capabilities. Figure 116 reflects these important considerations in choosing a method:

1. *Will you need uncertainty information for the state variables?*

   The unscented Kalman filter and TRUC will provide better uncertainty information than the extended Kalman filter. TRUC, however, may require a long run–time, so the unscented Kalman filter may be the best choice.

2. *Will your measurement have extremes in magnitude or is it pretty steady?*

   The best estimate of the extended Kalman filter may stray during events such as peak deceleration and parachute deployment, and the residuals of its best estimate may be unbounded. Although, the best estimates of the unscented Kalman filter and TRUC may stray, they have demonstrated better bounding of the residuals. Once again, however, TRUC may require a long run–time.

3. *How frequently are you taking measurements?*

   Higher frequency measurements tend to be more difficult for the extended Kalman filter to process unless they have very low noise levels. For TRUC, more measurements mean a longer run–time, so the unscented Kalman filter may be the best choice.

4. *Will you have measurements of the state (that is, are the states observable)?*

   If you have direct measurements of the state, the extended Kalman filter is the best choice. It will provide a fast estimate of the state with uncertainties. The unscented Kalman filter can also provide the estimate of the state with uncertainties, but it will be slower. And, if the state is observable, there is little point in using TRUC since the state is most likely well known, and TRUC cannot take into account the measurement noise.

5. *Will you need to take into account measurement noise / error?*

   As stated above, TRUC cannot take into account the measurement noise, so the extended Kalman filter or the unscented Kalman filter are better choices.

6. *Is this a real–time application or post–processing?*

   The quickest real–time response will be with an extended Kalman filter, especially if the state is observable. If a slightly longer processing time can be tolerated, though, the unscented Kalman filter would be a better choice, especially if state is not observable. TRUC should only be used for post–flight processing of data due to its long computational time.

7. *Is the signal–to–noise ratio for your measurements greater than approximately 100?*

   In the study on how the noise level and the frequency of acceleration measurements affected each filter's performance, the extended Kalman filter performed best when the signal–to–noise ratio for the acceleration measurements

was greater than approximately 100. This number also takes into account events in the trajectory such as peak deceleration and parachute deployment in addition to things such as terminal descent on the parachute where the acceleration is relatively steady. Also, when the noise is large compared to the magnitude of the acceleration force being measured, it will be difficult to accurately determine the atmospheric density with any of the methods. And, once again, TRUC cannot take into account the measurement noise, so the unscented Kalman filter is a better choice when noise levels are relatively high.

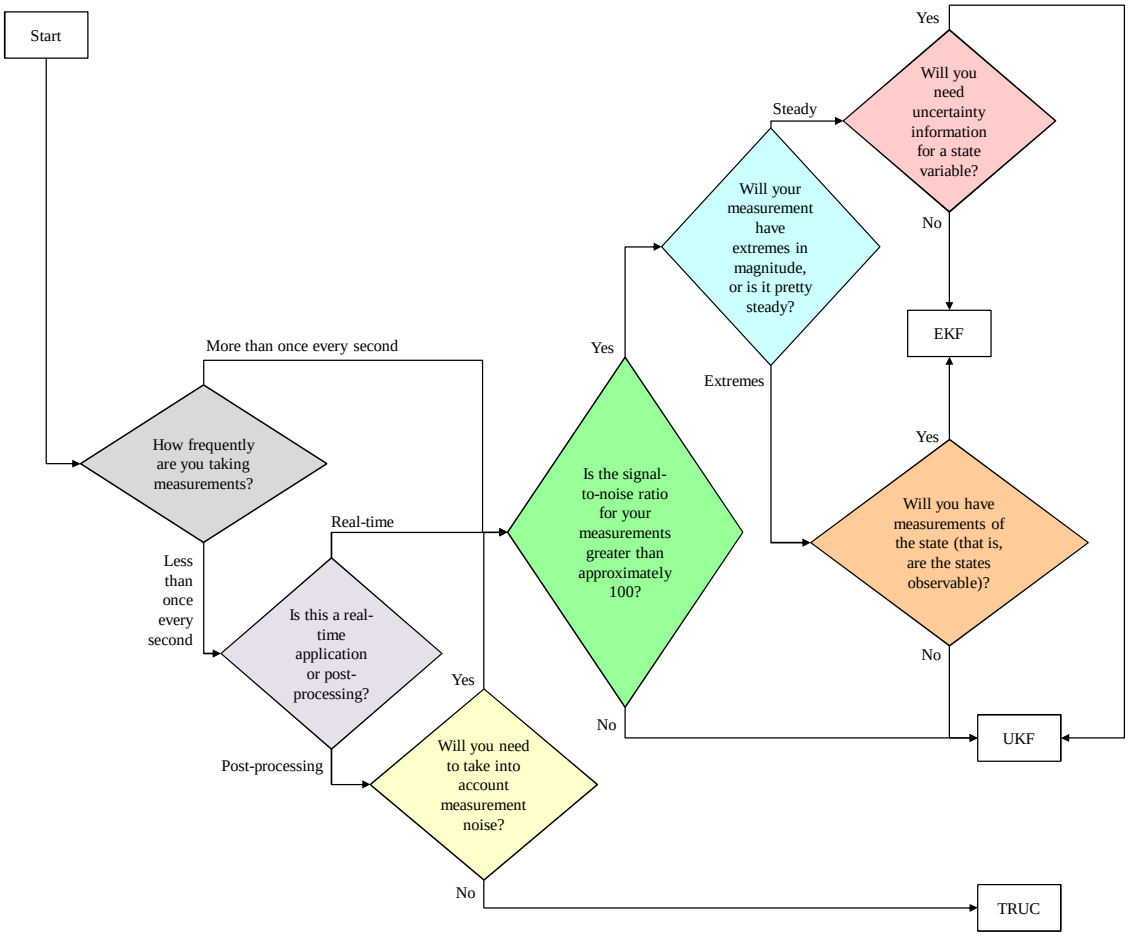

Figure 116: How to Choose a Method for Entry Descent and Landing Trajectory Reconstruction: Suggested Guidelines. The flowchart presumes all three trajectory reconstruction tools: (1) the extended Kalman filter, (2) the unscented Kalman filter, and (3) TRUC exist and are available.

The flowchart in Figure 116 presumes all three trajectory reconstruction tools: (1) the extended Kalman filter, (2) the unscented Kalman filter, and (3) TRUC exist and are available to you. If all three trajectory reconstruction tools are not available to you, then the preferred choice will depend on what you are starting with, especially if you already have an entry, descent, and landing trajectory design tool. For example, if you already have a collocation program for designing entry, descent, and landing trajectories, then TRUC is a straightforward addition that will allow your collocation program to also reconstruct entry, descent, and landing trajectories. However, suppose you have something such as the Program to Optimize Simulated Trajectories (POST) [210], which is not a collocation program. Presumably, you are using it to design your entry, descent, and landing trajectories. If you are starting with the Program to Optimize Simulated Trajectories, it is easier to supplement it with a Kalman filter for trajectory reconstruction (please see reference [277]).

Now, suppose you have nothing.

Starting from scratch, you would like to develop something to design and reconstruct entry, descent, and landing trajectories. With either collocation or Kalman filters, you benefit from having better models of things such as the vehicle's aerodynamics and the planet's (or natural satellite's) atmosphere. If you cannot have the best models, then the Kalman filters allow you to account for this by adding what is called "process noise" (please see Chapter 3). Collocation, and by extension TRUC, does not have something similar.

A key component of a collocation program for designing entry, descent, and landing trajectories is the optimizer, and a key component of a non–collocation program for designing entry, descent, and landing trajectories (which uses a Kalman filter for trajectory reconstruction) is the trajectory integrator. With collocation you must also develop the optimizer or have one already available that you can use. If you have an optimizer already available to you, then a collocation program for designing and

reconstructing entry, descent, and landing trajectories will be faster to develop. With a non–collocation program using either Kalman filter, you must develop a trajectory integrator or have one already available that you can use. If you have a trajectory integrator already available to you, then either Kalman filter will be faster to develop. Additionally, developing a trajectory integrator is easier than developing an optimizer.

Now, the Kalman filters also allow you to account for measurement noise (please see Chapter 3). Collocation cannot, although this may be an area for future research (please see § 7.4). The Kalman filters also provide uncertainty information regarding their estimates of the state with a single run. And, while the unscented Kalman filter was demonstrated to be slower than the extended Kalman filter in this investigation, it gives better estimates of uncertainty. TRUC has to run a Monte Carlo simulation to get the equivalent uncertainty information, which takes more time.

In summary, if you already have a collocation trajectory design program, then adding TRUC will readily allow you to reconstruct entry, descent, and landing trajectories. If you have a non–collocation program that uses trajectory integration, then Kalman filters are a better choice. And, finally, if you are starting from scratch, and you want the most benefit with the shortest development time, then the unscented Kalman filter is the best choice.

7.3 Summary of Contributions

The contributions of this research, as discussed in detail above, are:

(1) The extended Kalman filter was originally developed for signal processing applications and only later applied to trajectory reconstruction. Similarly, unscented Kalman filtering was developed for signal processing applications, and this work represents its first application to the reconstruction of entry, descent, and landing trajectories.

(2) The reformulation of the entry, descent, and landing trajectory reconstruction problem using collocation has been demonstrated by the author. This approach dubbed "TRUC", after "trajectory reconstruction using collocation" posits that entry, descent, and landing trajectory design tools using collocation may also be used for entry, descent, and landing trajectory reconstruction. As a first step, the performance of entry, descent, and landing trajectory simulation using collocation (TSUC) has been demonstrated by the author. Additionally, a solution procedure for determining the state values that satisfy the defect constraints has been developed. This procedure allows the trajectory to be determined from the controls and parameters of the simulation in a deterministic way.[1]

(3) Trajectory reconstruction results from the unscented Kalman filter were compared against the trajectory reconstruction done using the extended Kalman filter. From this, guidance on choosing a method for the reconstruction of future trajectories was established. This guidance included trajectory reconstruction using collocation based on its expected capabilities.

7.4 Suggestions for Future Research

First, there are literally tens[2] of additional methods that may also be used for trajectory reconstruction. Some of them are discussed in § 3.3 on page 69, though they were not selected for this research. Each may have something to offer. Ultimately, though, better trajectory reconstruction will come through more frequent, more accurate measurements.

Second, demonstrating trajectory reconstruction using collocation (TRUC) using

[1]The review of the literature for this research indicates that collocation has not been used for entry, descent, and landing trajectory reconstruction, so this solution procedure has not been used for entry, descent, and landing trajectory reconstruction using collocation.

[2]Perhaps hundreds, when variations on each method are taken into account, along with the different settings that may be involved with any single method.

the solution procedure for the state variables given in Table 15 on page 98 (or one of the other solution procedures discussed in Chapter 3) is an area of future research. Such an approach could allow one to utilize the same collocation trajectory design tools for the subsequent reconstruction.

Third, investigating the possibility of incorporating of measurement noise into TRUC is an area of future research. The inability of the method, as presently formulated, to incorporate measurement noise is a distinct disadvantage. As such, the Kalman filters are better choices when measurement noise must be taken into account, and the unscented Kalman filter is the best choice for higher noise levels.

Fourth, applying TRUC to a six–degree–of–freedom trajectory reconstruction with gyroscope data is an area of future research. For this case, the angle of attack α, the side–slip angle β, and the bank angle σ for the spacecraft could be control variables.

Fifth, it may be possible to reconstruct the atmospheric density profile using TRUC by making the atmospheric density a control variable, and it may also be possible to determine atmospheric winds in this manner. In doing this, the aerodynamic coefficient uncertainties and the uncertainties of the atmospheric conditions cannot be separated unless separate measurements are made of either the actual flight atmospheric conditions or the pressure distribution around the spacecraft in–flight.

Sixth, using the solution procedure in Table 15 on page 98 to calculate values of the state that satisfy collocation's defect equations may allow the algebraic constraints produced from using collocation to be solved while using only the control variables as the independent variables in general optimal control problems, significantly reducing the number of independent variables.

Seventh, the bounding of the state residuals at low frequencies of measurement by the extended Kalman filter may be due to the quality of the process model. At low frequencies, the extended Kalman filter is just propagating the trajectory for extended periods. Varying the fidelity of the model and the amount of process noise

to investigate filter performance is an area of further research.[3]

Finally, in lieu of one highly accurate method[4] of determining location, there is a need to blend data from different instruments in order to obtain the best estimate of a spacecraft's position and velocity in three-dimensional space, hence the blending of additional data types should be considered for future research. Ultimately, trajectory reconstruction should occur in real–time, so that the information can be used for pinpoint landing on the terrestrial bodies of the solar system. As such, incorporating trajectory reconstruction, with data blending, into the guidance of landers is an area of further research.

[3]Luckily, measurement accuracy is improving and sampling rates are increasing, which will aid trajectory reconstruction.

[4]The global positioning system is one example of a highly accurate method of position determination. However, financial constraints prevent us from setting up global positioning systems around all the bodies in the solar system we would like to explore.

APPENDIX A

EQUATIONS OF MOTION

For the trajectories in this research, a three-degree-of-freedom simulation was used. The translational motion is described by the state equation given in equation (155), where the state variables radius r, latitude ϕ, and longitude θ give the three components of position, and the state variables velocity v, flight path angle γ, and azimuth ψ give the three components of velocity. The expressions for the state derivatives are given in equations (156) through (161)). [60]

$$\dot{\mathbf{x}} = \mathbf{f}(\mathbf{x}) = \begin{bmatrix} \dot{r} \\ \dot{\phi} \\ \dot{\theta} \\ \dot{v} \\ \dot{\gamma} \\ \dot{\psi} \end{bmatrix} \tag{155}$$

$$\dot{r} = v \sin\gamma \tag{156}$$

$$\dot{\phi} = \frac{v \cos\gamma \cos\psi}{r} \tag{157}$$

$$\dot{\theta} = \frac{v \cos\gamma \sin\psi}{r \cos\phi} \tag{158}$$

$$\begin{aligned} \dot{v} = {} & \frac{1}{m}(Y \sin\beta - D \cos\beta) \\ & - g \sin\gamma \\ & + \Omega^2 r \cos\phi(\sin\gamma \cos\phi - \cos\gamma \sin\phi \cos\psi) \end{aligned} \tag{159}$$

$$\begin{aligned}\dot{\gamma} = &\frac{1}{mv}(L\cos\sigma - D\sin\beta\sin\sigma - Y\cos\beta\sin\sigma) \\ &+ \left(\frac{v}{r} - \frac{g}{v}\right)\cos\gamma \\ &+ 2\Omega\cos\phi\sin\psi \\ &+ \frac{\Omega^2 r}{v}\cos\phi(\cos\gamma\cos\phi + \sin\gamma\sin\phi\cos\psi)\end{aligned} \tag{160}$$

$$\begin{aligned}\dot{\psi} = &\frac{1}{mv\cos\gamma}(L\sin\sigma + D\sin\beta\cos\sigma + Y\cos\beta\cos\sigma) \\ &+ \frac{v\cos\gamma}{r}\sin\psi\tan\phi \\ &- 2\Omega(\cos\phi\cos\psi\tan\gamma - \sin\phi) \\ &+ \frac{\Omega^2 r}{v\cos\gamma}\cos\phi\sin\phi\sin\psi\end{aligned} \tag{161}$$

where

- C_D is the drag coefficient of the spacecraft. It is a function of the angle of attack α and Mach number M of the of the spacecraft: $C_D = C_D(\alpha, M)$.
- C_L is the lift coefficient of the spacecraft. It is a function of the angle of attack α and Mach number M of the spacecraft: $C_L = C_L(\alpha, M)$.
- C_Y is the side force coefficient of the spacecraft. It is a function of the side-slip angle β and Mach number M of the spacecraft: $C_Y = C_Y(\beta, M)$.
- D is the aerodynamic drag force acting on the spacecraft. $D = \frac{1}{2}\rho v^2 S C_D$ where the drag coefficient C_D is a function of the angle of attack α and Mach number M of the spacecraft: $C_D = C_D(\alpha, M)$.
- g is the local acceleration of gravity at the spacecraft's position.
- L is the aerodynamic lift force acting on the spacecraft. $L = \frac{1}{2}\rho v^2 S C_L$ where

the lift coefficient C_L is a function of the angle of attack α and Mach number M of the spacecraft: $C_L = C_L(\alpha, M)$.

- m is the mass of the spacecraft.
- M is the Mach number of the spacecraft.
- r is the spacecraft's local radius measured from the center of the planet at which entry is taking place.
- S is the aerodynamic reference area of the spacecraft.
- t is time.
- v is the spacecraft's velocity.
- Y is the aerodynamic side force acting on the spacecraft. $Y = \frac{1}{2}\rho v^2 S C_Y$ where the side force coefficient C_Y is a function of the side-slip angle β and Mach number M of the spacecraft: $C_Y = C_Y(\beta, M)$.
- α is the angle of attack of the spacecraft. For the studies conducted in this investigation, the angle of attack was set to zero for the duration of the trajectory.
- β is the side-slip angle of the spacecraft. For the studies conducted in this investigation, the side-slip angle was set to zero for the duration of the trajectory.
- γ is the spacecraft's flight path angle, which is positive above the local horizontal.
- θ is the spacecraft's longitude.
- ρ is the local atmospheric density at the spacecraft's position.

- σ is the bank angle of the spacecraft. For the studies conducted in this investigation, the bank angle was set to zero for the duration of the trajectory.
- ϕ is the spacecraft's latitude.
- ψ is the spacecraft's azimuth, which is positive when measured clockwise from north.
- Ω is the rotation rate of the planet at which entry is taking place.

and these variables may be categorized into state variables and parameters as shown in Table 20.

Table 20: Categorization of the variables in the equations of motion into state variables and parameters.

State Variables	Parameters
r	C_D
ϕ	C_L
θ	C_Y
v	D
γ	g
ψ	L
	m
	S
	Y
	α
	β
	ρ
	σ
	Ω

APPENDIX B

ELEMENTS OF THE JACOBIAN

For trajectories with the translational motion described by the six differential equations beginning on page 186 (equations (156) through (161)) the following equations (equations (162) through (197)) give the elements of their Jacobian matrix.

$$\frac{\partial \dot{r}}{\partial r} = 0 \tag{162}$$

$$\frac{\partial \dot{r}}{\partial \phi} = 0 \tag{163}$$

$$\frac{\partial \dot{r}}{\partial \theta} = 0 \tag{164}$$

$$\frac{\partial \dot{r}}{\partial v} = \sin\gamma \tag{165}$$

$$\frac{\partial \dot{r}}{\partial \gamma} = v\cos\gamma \tag{166}$$

$$\frac{\partial \dot{r}}{\partial \psi} = 0 \tag{167}$$

$$\frac{\partial \dot{\phi}}{\partial r} = -\frac{v \cos\gamma \cos\psi}{r^2} \tag{168}$$

$$\frac{\partial \dot{\phi}}{\partial \phi} = 0 \tag{169}$$

$$\frac{\partial \dot{\phi}}{\partial \theta} = 0 \tag{170}$$

$$\frac{\partial \dot{\phi}}{\partial v} = \frac{\cos\gamma \cos\psi}{r} \tag{171}$$

$$\frac{\partial \dot{\phi}}{\partial \gamma} = -\frac{v \sin\gamma \cos\psi}{r} \tag{172}$$

$$\frac{\partial \dot{\phi}}{\partial \psi} = -\frac{v \cos\gamma \sin\psi}{r} \tag{173}$$

$$\frac{\partial \dot{\theta}}{\partial r} = -\frac{v \cos\gamma \sin\psi}{r^2 \cos\phi} \tag{174}$$

$$\frac{\partial \dot{\theta}}{\partial \phi} = -\frac{v \cos\gamma \sin\psi}{r \cos\phi} \cdot \frac{\sin\phi}{\cos^2\phi} \tag{175}$$

$$\frac{\partial \dot{\theta}}{\partial \theta} = 0 \tag{176}$$

$$\frac{\partial \dot{\theta}}{\partial v} = \frac{\cos\gamma \sin\psi}{r \cos\phi} \tag{177}$$

$$\frac{\partial \dot{\theta}}{\partial \gamma} = -\frac{v \sin\gamma \sin\psi}{r \cos\phi} \tag{178}$$

$$\frac{\partial \dot{\theta}}{\partial \psi} = \frac{v \cos\gamma \cos\psi}{r \cos\phi} \tag{179}$$

$$\frac{\partial \dot{v}}{\partial r} = -\frac{\partial g}{\partial r}\sin\gamma + \Omega^2 \cos\phi(\sin\gamma\cos\phi - \cos\gamma\sin\phi\cos\psi) \tag{180}$$

$$\begin{aligned}\frac{\partial \dot{v}}{\partial \phi} = &-\frac{\partial g}{\partial \phi}\sin\gamma \\ &- 2\Omega^2 r\sin\phi\cos\phi\sin\gamma \\ &+ \Omega^2 r\sin^2\phi\cos\gamma\cos\psi \\ &- \Omega^2 r\cos^2\phi\cos\gamma\cos\psi\end{aligned} \tag{181}$$

$$\frac{\partial \dot{v}}{\partial \theta} = -\frac{\partial g}{\partial \theta}\sin\gamma \tag{182}$$

$$\frac{\partial \dot{v}}{\partial v} = 0 \tag{183}$$

$$\begin{aligned}\frac{\partial \dot{v}}{\partial \gamma} = &-g\cos\gamma \\ &+ \Omega^2 r\cos^2\phi\cos\gamma \\ &+ \Omega^2 r\sin\phi\cos\phi\sin\gamma\cos\psi\end{aligned} \tag{184}$$

$$\frac{\partial \dot{v}}{\partial \psi} = \Omega^2 r\sin\phi\cos\phi\cos\gamma\sin\psi) \tag{185}$$

$$\begin{aligned}\frac{\partial\dot{\gamma}}{\partial r} = &-\frac{v}{r^2} \\ &- \frac{\partial g}{\partial r}\cdot\frac{\cos\gamma}{v} \\ &+ \frac{\Omega^2}{v}\cos\phi(\cos\gamma\cos\phi + \sin\gamma\sin\phi\cos\psi)\end{aligned} \tag{186}$$

$$\begin{aligned}\frac{\partial\dot{\gamma}}{\partial\phi} = &-\frac{\partial g}{\partial\phi}\cdot\frac{\cos\gamma}{v} \\ &- 2\Omega\sin\phi\sin\psi \\ &- 2\frac{\Omega^2 r}{v}\sin\phi\cos\phi\cos\gamma \\ &- \frac{\Omega^2 r}{v}\sin^2\phi\sin\gamma\cos\psi \\ &+ \frac{\Omega^2 r}{v}\cos^2\phi\sin\gamma\cos\psi\end{aligned} \tag{187}$$

$$\frac{\partial\dot{\gamma}}{\partial\theta} = 0 \tag{188}$$

$$\begin{aligned}\frac{\partial\dot{\gamma}}{\partial v} = &-\frac{1}{mv^2}(L\cos\sigma - D\sin\beta\sin\sigma - Y\cos\beta\sin\sigma) \\ &+ \left(\frac{1}{r} + \frac{g}{v^2}\right)\cos\gamma \\ &- \frac{\Omega^2 r}{v^2}\cos\phi(\cos\gamma\cos\phi + \sin\gamma\sin\phi\cos\psi)\end{aligned} \tag{189}$$

$$\begin{aligned}\frac{\partial\dot{\gamma}}{\partial\gamma} = &-\left(\frac{v}{r}-\frac{g}{v}\right)\sin\gamma \\ &-\frac{\Omega^2 r}{v}\cos^2\phi\sin\gamma \\ &+\frac{\Omega^2 r}{v}\sin\phi\cos\phi\cos\gamma\cos\psi\end{aligned} \tag{190}$$

$$\begin{aligned}\frac{\partial\dot{\gamma}}{\partial\psi} = &\ 2\Omega\cos\phi\cos\psi \\ &-\frac{\Omega^2 r}{v}\sin\phi\cos\phi\sin\gamma\sin\psi\end{aligned} \tag{191}$$

$$\begin{aligned}\frac{\partial\dot{\psi}}{\partial r} &= -\frac{v\cos\gamma}{r^2}\sin\psi\tan\phi \\ &\quad + \frac{\Omega^2}{v\cos\gamma}\cos\phi\sin\phi\sin\psi\end{aligned} \tag{192}$$

$$\begin{aligned}\frac{\partial\dot{\psi}}{\partial\phi} &= \frac{v\cos\gamma}{r}\frac{\sin\psi}{\cos^2\phi} \\ &\quad + 2\Omega\sin\phi\cos\psi\tan\gamma - \sin\phi \\ &\quad + 2\Omega\cos\phi \\ &\quad + \frac{\Omega^2 r}{v\cos\gamma}\sin\psi(1-2\sin^2\phi)\end{aligned} \tag{193}$$

$$\frac{\partial\dot{\psi}}{\partial\theta} = 0 \tag{194}$$

$$\begin{aligned}\frac{\partial\dot{\psi}}{\partial v} &= -\frac{1}{mv^2\cos\gamma}(L\sin\sigma + D\sin\beta\cos\sigma + Y\cos\beta\cos\sigma) \\ &\quad + \frac{\cos\gamma}{r}\sin\psi\tan\phi \\ &\quad - \frac{\Omega^2 r}{v^2\cos\gamma}\cos\phi\sin\phi\sin\psi\end{aligned} \tag{195}$$

$$\begin{aligned}\frac{\partial\dot{\psi}}{\partial\gamma} = &-\frac{\sin\gamma}{mv\cos^2\gamma}(L\sin\sigma + D\sin\beta\cos\sigma + Y\cos\beta\cos\sigma) \\ &- \frac{v\sin\gamma}{r}\sin\psi\tan\phi \\ &- 2\Omega\frac{\cos\phi\cos\psi}{\cos^2\gamma} \\ &+ \frac{\Omega^2 r\sin\gamma}{v\cos^2\gamma}\sin\phi\cos\phi\sin\psi\end{aligned} \tag{196}$$

$$\begin{aligned}\frac{\partial\dot{\psi}}{\partial\psi} = &\frac{v\cos\gamma}{r}\cos\psi\tan\phi \\ &+ 2\Omega\cos\phi\sin\psi\tan\gamma \\ &+ \frac{\Omega^2 r}{v\cos\gamma}\cos\phi\sin\phi\cos\psi\end{aligned} \tag{197}$$

APPENDIX C

PARAMETERS FOR THE EXTENDED KALMAN FILTER

The parameters for the extended Kalman filter are listed below. The state vector and the equations of motion are given in Appendix A.

$$\mathbf{x} = \begin{bmatrix} r \\ \phi \\ \theta \\ v \\ \gamma \\ \psi \end{bmatrix} \tag{198}$$

$$\mathbf{F} = \begin{bmatrix} \frac{\partial \dot{r}}{\partial r} & \frac{\partial \dot{r}}{\partial \phi} & \frac{\partial \dot{r}}{\partial \theta} & \frac{\partial \dot{r}}{\partial v} & \frac{\partial \dot{r}}{\partial \gamma} & \frac{\partial \dot{r}}{\partial \psi} \\ \frac{\partial \dot{\phi}}{\partial r} & \frac{\partial \dot{\phi}}{\partial \phi} & \frac{\partial \dot{\phi}}{\partial \theta} & \frac{\partial \dot{\phi}}{\partial v} & \frac{\partial \dot{\phi}}{\partial \gamma} & \frac{\partial \dot{\phi}}{\partial \psi} \\ \frac{\partial \dot{\theta}}{\partial r} & \frac{\partial \dot{\theta}}{\partial \phi} & \frac{\partial \dot{\theta}}{\partial \theta} & \frac{\partial \dot{\theta}}{\partial v} & \frac{\partial \dot{\theta}}{\partial \gamma} & \frac{\partial \dot{\theta}}{\partial \psi} \\ \frac{\partial \dot{v}}{\partial r} & \frac{\partial \dot{v}}{\partial \phi} & \frac{\partial \dot{v}}{\partial \theta} & \frac{\partial \dot{v}}{\partial v} & \frac{\partial \dot{v}}{\partial \gamma} & \frac{\partial \dot{v}}{\partial \psi} \\ \frac{\partial \dot{\gamma}}{\partial r} & \frac{\partial \dot{\gamma}}{\partial \phi} & \frac{\partial \dot{\gamma}}{\partial \theta} & \frac{\partial \dot{\gamma}}{\partial v} & \frac{\partial \dot{\gamma}}{\partial \gamma} & \frac{\partial \dot{\gamma}}{\partial \psi} \\ \frac{\partial \dot{\psi}}{\partial r} & \frac{\partial \dot{\psi}}{\partial \phi} & \frac{\partial \dot{\psi}}{\partial \theta} & \frac{\partial \dot{\psi}}{\partial v} & \frac{\partial \dot{\psi}}{\partial \gamma} & \frac{\partial \dot{\psi}}{\partial \psi} \end{bmatrix} \tag{199}$$

$$\mathbf{H}_{\text{acceleration}} = \begin{bmatrix} 0 & 0 & 0 & \frac{\rho v S C_L}{2m} & 0 & 0 \\ 0 & 0 & 0 & \frac{\rho v S C_Y}{2m} & 0 & 0 \\ 0 & 0 & 0 & -\frac{\rho v S C_D}{2m} & 0 & 0 \end{bmatrix} \tag{200}$$

$$\mathbf{H}_{\text{altimeter}} = \begin{bmatrix} 1 & 0 & 0 & 0 & 0 & 0 \end{bmatrix} \tag{201}$$

$$\mathbf{Q} = \begin{bmatrix} 0 & 0 & 0 & 0 & 0 & 0 \\ 0 & 0 & 0 & 0 & 0 & 0 \\ 0 & 0 & 0 & 0 & 0 & 0 \\ 0 & 0 & 0 & 0 & 0 & 0 \\ 0 & 0 & 0 & 0 & 0 & 0 \\ 0 & 0 & 0 & 0 & 0 & 0 \end{bmatrix} \tag{202}$$

$$\mathbf{R}_{\text{altimeter}} = \begin{bmatrix} 0.3^2 \end{bmatrix} \tag{203}$$

$$\mathbf{R}_{\text{acceleration}} = \begin{bmatrix} ((1500)(9.80665))^2 & 0 & 0 \\ 0 & ((1500)(9.80665))^2 & 0 \\ 0 & 0 & ((1500)(9.80665))^2 \end{bmatrix} \tag{204}$$

APPENDIX D

PARAMETERS FOR THE UNSCENTED KALMAN FILTER

The parameters for the unscented Kalman filter are listed below. The state vector and the equations of motion are given in Appendix A.

$$\mathbf{x} = \begin{bmatrix} r \\ \phi \\ \theta \\ v \\ \gamma \\ \psi \end{bmatrix} \tag{205}$$

$$L = 6 \tag{206}$$

$$\alpha = 0.5 \tag{207}$$

$$\beta = 2 \tag{208}$$

$$\kappa = 3 - L \tag{209}$$

$$\mathbf{h}_{\text{acceleration}}(\mathcal{X}) = \begin{bmatrix} 0 & 0 & 0 & \frac{\rho v^2 S C_L}{2m} & 0 & 0 \\ 0 & 0 & 0 & \frac{\rho v^2 S C_Y}{2m} & 0 & 0 \\ 0 & 0 & 0 & \frac{\rho v^2 S C_D}{2m} & 0 & 0 \end{bmatrix} \tag{210}$$

$$\mathbf{h}_{\text{altimeter}}(\mathcal{X}) = \begin{bmatrix} h & 0 & 0 & 0 & 0 & 0 \end{bmatrix} \tag{211}$$

$$\mathbf{Q} = \begin{bmatrix} 0 & 0 & 0 & 0 & 0 & 0 \\ 0 & 0 & 0 & 0 & 0 & 0 \\ 0 & 0 & 0 & 0 & 0 & 0 \\ 0 & 0 & 0 & 0 & 0 & 0 \\ 0 & 0 & 0 & 0 & 0 & 0 \\ 0 & 0 & 0 & 0 & 0 & 0 \end{bmatrix} \tag{212}$$

$$\mathbf{R}_{\text{altimeter}} = \begin{bmatrix} 0.3^2 \end{bmatrix} \tag{213}$$

$$\mathbf{R}_{\text{acceleration}} = \begin{bmatrix} ((1500)(9.80665))^2 & 0 & 0 \\ 0 & ((1500)(9.80665))^2 & 0 \\ 0 & 0 & ((1500)(9.80665))^2 \end{bmatrix} \tag{214}$$

APPENDIX E

ATMOSPHERIC DENSITY RECONSTRUCTION

E.1 Reconstruction Process

As mentioned in Chapter 2, detailed procedures for obtaining the density profile of a planetary atmosphere from measurements of accelerations experienced by a vehicle making a ballistic entry into the atmosphere of a planet are given in [238, 204]. Atmospheric density ρ is determined from the axial acceleration a_A experienced by the entry vehicle assuming: the vehicle's aerodynamic properties (specifically, the axial coefficient C_A or the drag coefficient C_D[1], aerodynamic reference area S, the speed of the entry vehicle v, and its mass m using equation (216).

$$ma_A = \frac{1}{2}\rho v^2 C_A S \tag{215}$$

$$\rho = \frac{2ma}{v^2 C_A S} \tag{216}$$

The values of the variables on the right–hand–side of equation (216) are obtained in different ways. The following paragraphs discuss how these values are obtained.

The spacecraft's aerodynamic coefficients are obtained from computational fluid dynamics simulations of the spacecraft and wind tunnel test data. These aerodynamic coefficients are not perfectly predicted (in the case of computational fluid dynamics simulations) or measured (in the case of wind tunnel tests), so they have uncertainties associated with them. Because the procedures for obtaining the atmospheric density profile given in [238, 204] require the aerodynamic coefficients (specifically, the axial

[1] $C_A = C_D$ when the angle of attack is zero ($\alpha = 0$).

coefficient), the aerodynamic coefficient uncertainties and the uncertainties of the atmospheric conditions cannot be separated unless separate measurements are made of either the actual flight atmospheric conditions or the pressure distribution around the spacecraft in–flight. However, these aerodynamic properties are the best information available for the spacecraft. In this analysis, a nominal aerodynamic drag coefficient of 1.68 is used.

The aerodynamic reference area can be obtained from the computer aided design models of the spacecraft, or it can be obtained from measuring the actual spacecraft. Generally, because it is needed long before the spacecraft is completely built, it is obtained from the computer aided design models of the spacecraft.

The mass of the spacecraft can also be determined from the computer aided design models, or it can be obtained from weighing the actual spacecraft. Since weighing the spacecraft is not practical (or a safe process for the spacecraft), the spacecraft's mass is obtained from the computer aided design models of the spacecraft. However, during assembly, each piece of the spacecraft is weighed to obtain an accurate "as–built" mass of the spacecraft. A complication arises with the mass of the spacecraft because of ablation of the heatshield during entry. The ablation results in mass loss, and depending on the planet at which entry is occurring, it can be significant. During Galileo's entry at Jupiter, it lost approximately 80 kg [185].

Finally, the velocity of the spacecraft is obtained from the trajectory reconstruction process. Since the value of everything on the right–hand–side of equation (216) is known at each measurement time, the atmospheric density at each measurement time can be calculated from equation (216). The densities can then be plotted against the reconstructed altitude time history to obtain an atmospheric density profile along the spacecraft's trajectory.

E.2 Sample Problem Atmospheric Density Reconstruction

Since the sample problem discussed in Chapter 4 is simulated data, the true atmospheric density profile is known. The density profile of the Martian atmosphere for the sample problem discussed in Chapter 4 is shown in Figure 117.

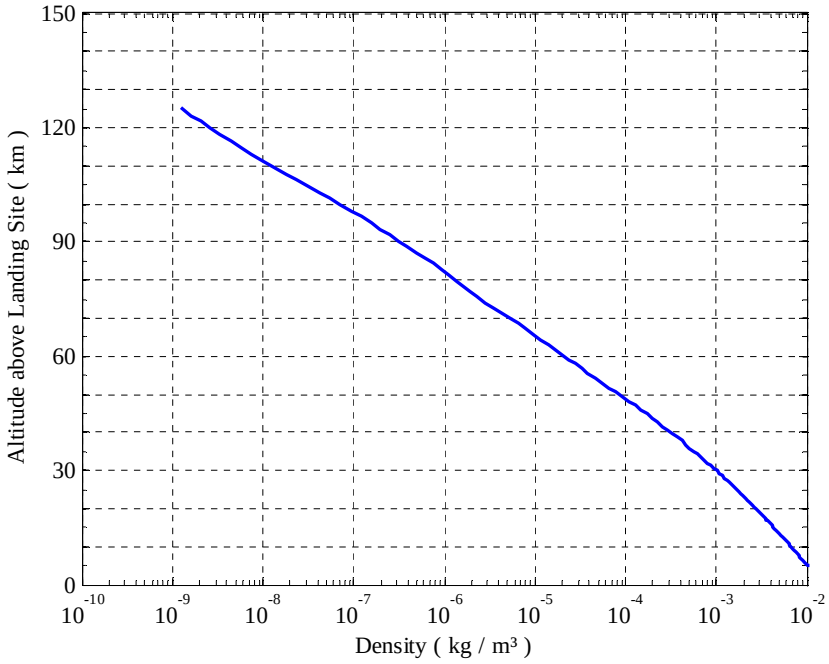

Figure 117: Sample problem atmospheric density profile.

The density profile of the sample problem is shown in Figure 118. The sample problem density profile is shown with the Kalman filter reconstructions overlaid, as well as the collocation simulation. The Kalman filters discussed in Chapter 3 appear to agree well with the simulated sample problem, even though the noise in the acceleration data at the beginning of the trajectory prevents a better reconstruction of the density profile at very high altitudes. This is because the noise is close in magnitude to the accelerations. The residuals of the sample problem density profile and the reconstructions shown in Figure 118 are shown in Figure 119. The effect of the noise in the acceleration data at very high altitudes is evident.

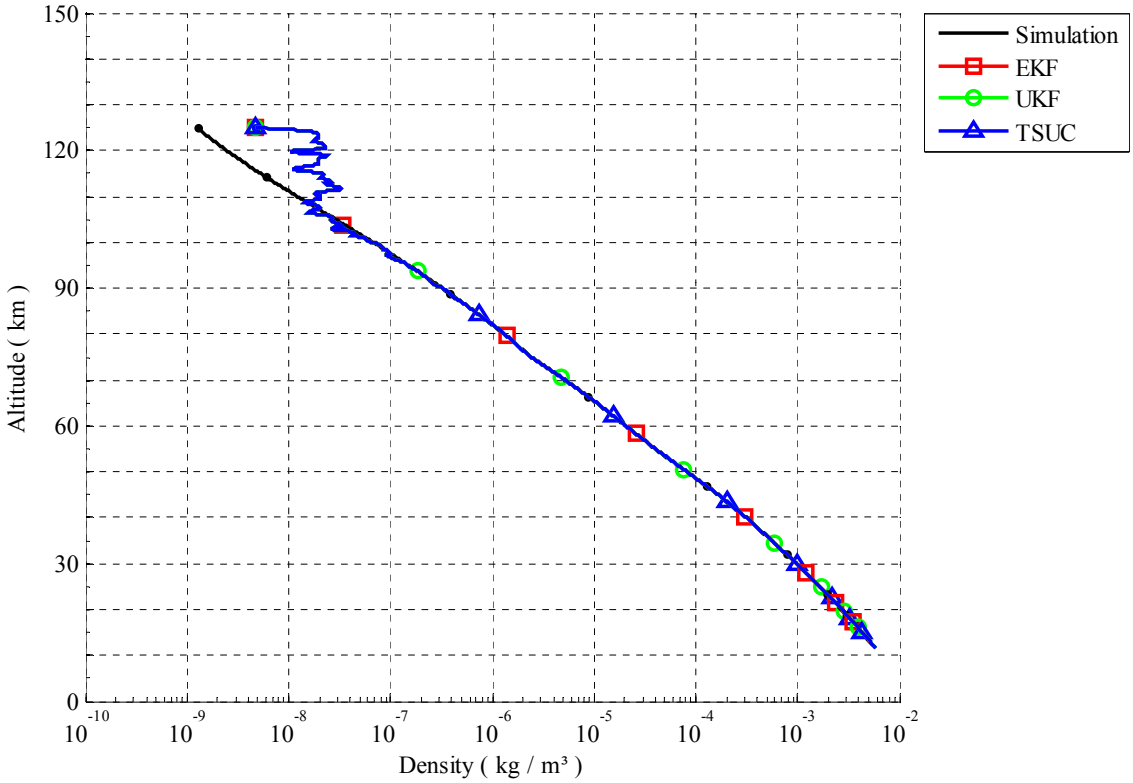

Figure 118: The density profile of the sample problem is reconstructed using the Kalman filters discussed in Chapter 3. The sample problem density profile is shown with the reconstructions overlaid.

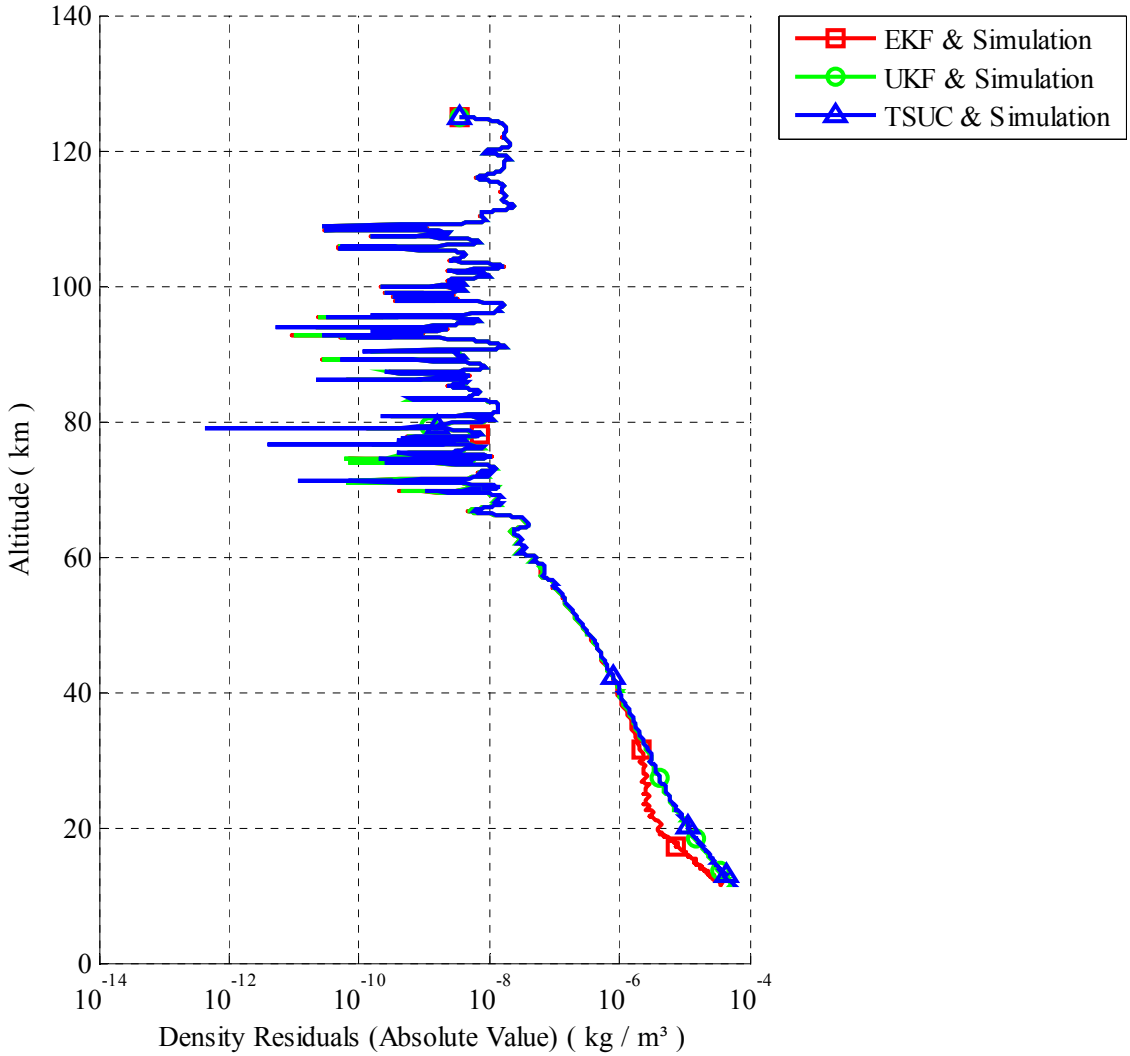

Figure 119: The residuals of the sample problem density profile and the reconstructions shown in the previous figure.

E.3 Mars Pathfinder

E.3.1 Digitized Data

Unfortunately, the true atmospheric density profile experienced by Mars Pathfinder during its entry cannot be known, so an independent reconstruction of Mars Pathfinder's entry trajectory was sought for comparison with this investigation. As with the altitude, velocity and flight path angle time histories, the 1999 Mars Pathfinder entry trajectory reconstruction by David Spencer and others in Reference [269] was selected

to provide an independent reconstruction of the atmospheric density profile experienced by Mars Pathfinder during its entry. Recall, as discussed in Chapter 2, that the trajectory reconstruction by David Spencer and others [269] used a combination of accelerometer and altimeter measurements using sequential filtering and smoothing techniques [270, 269]. As this is a different process from the methods discussed in Chapter 3, the results from the Kalman filters discussed in Chapter 3 will differ from the reconstruction by David Spencer and others [269]. However, the comparison will speak to the general accuracy of the Kalman filters discussed in Chapter 3, while the extended Kalman filter reconstruction, as one accepted standard of trajectory reconstruction[2], will speak to the specific capabilities of the unscented Kalman filter discussed in Chapter 3 for this investigation.

The density plot shown in Figures 120 was digitized using the *Engauge Digitizer* digitizing software [186]. The resolution of Figure 120 in density is approximately 0.0079 $\frac{\text{decades}}{\text{pixel}}$ with a possible error in the digitized density profile of at least 0.032 decades based on a four pixel curve width. Additionally, the resolution of Figure 120 in altitude is approximately 0.18 $\frac{\text{km}}{\text{pixel}}$ with a possible error in the digitized altitude of at least 0.71 km based on a four pixel curve width.

[2]Along with direct integration, as established in Chapter 2.

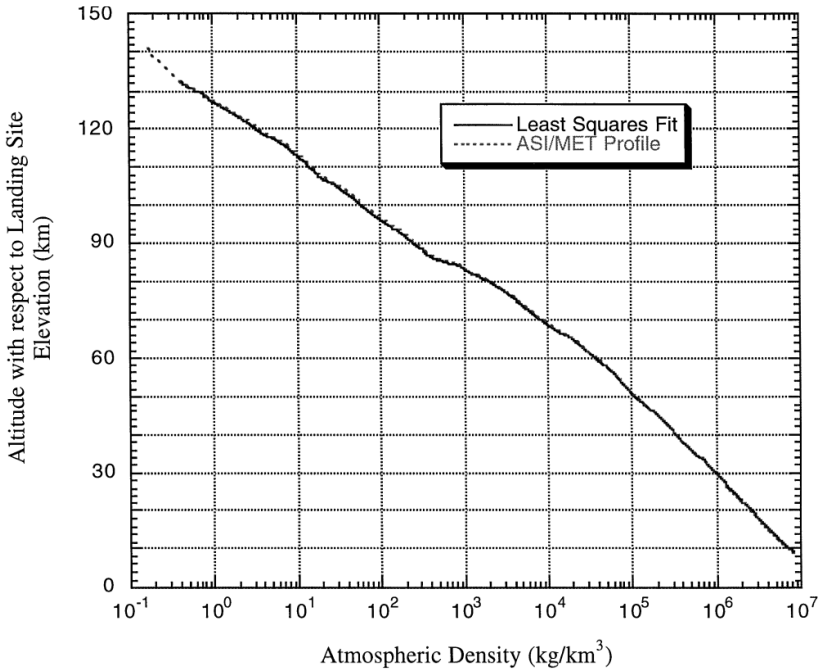

Figure 120: Reconstructed Mars Pathfinder atmospheric density profile from Spencer 1999. [269]

E.3.2 Reconstructed Atmospheric Density Profile

The digitized atmospheric density profile for Mars Pathfinder from Spencer 1999 [269] is shown in Figure 121 with the atmospheric density reconstructions by the Kalman filters discussed in Chapter 3, as well as the collocation simulation, overlaid. Both Kalman filters discussed in Chapter 3 appear to agree well with the digitized data from Spencer 1999 [269]. The residuals of the atmospheric density profiles shown in Figure 121 relative to the digitized data from Spencer 1999 [269] are shown in Figure 122. The similarity of the three sets of residuals indicates that the unscented Kalman filter was able to reconstruct Mars Pathfinder's atmospheric density profile at least as well as the extended Kalman filter.

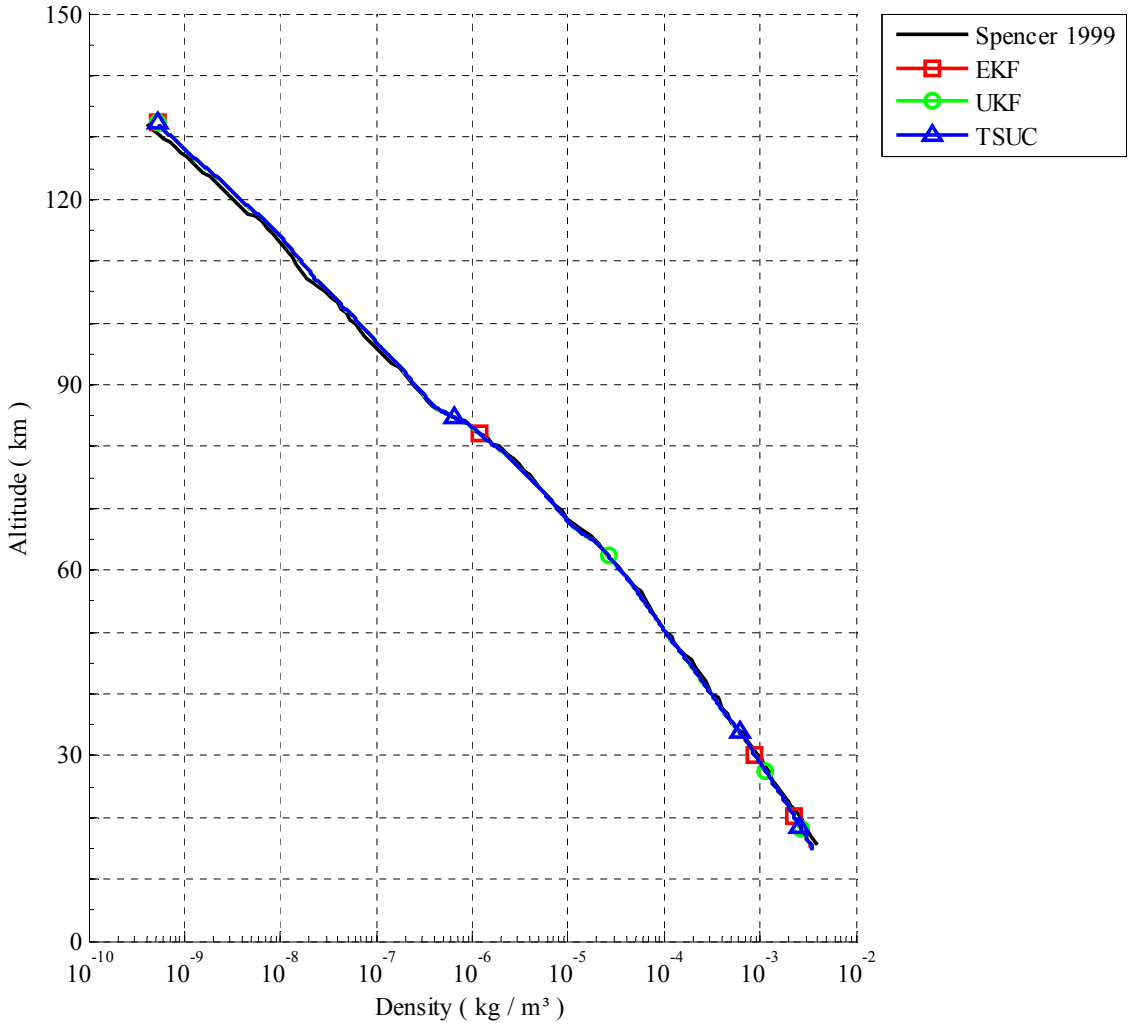

Figure 121: The digitized atmospheric density profile for Mars Pathfinder from Spencer 1999 [269] is shown with the atmospheric density reconstructions by the Kalman filters discussed in Chapter 3 overlaid.

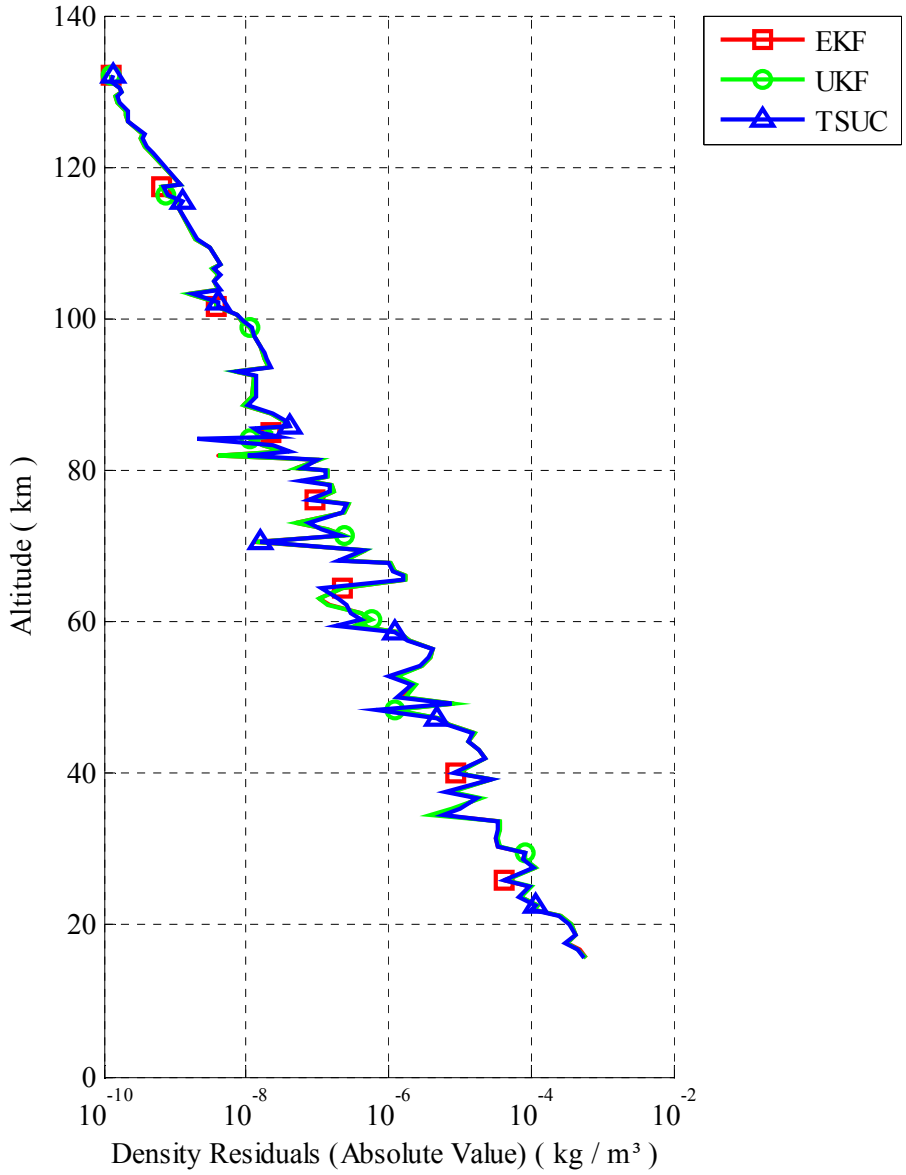

Figure 122: The residuals of the atmospheric density profiles shown in the previous figure relative to the digitized data from Spencer 1999 [269].

APPENDIX F

LITERATURE CONTRIBUTIONS

F.1 Journal Articles

F.1.1 Relevant Journal Articles

1. "Instrumentation for Entry, Descent, and Landing Trajectory Reconstruction and Atmospheric Studies at Earth, Venus, Mars, and Titan: A Review," *Journal of Spacecraft and Rockets*, (to be submitted).

2. "A Comparison of Entry, Descent, and Landing Trajectory Reconstruction by Extended and Unscented Kalman Filters," *IEEE Transactions on Aerospace and Electronic Systems*, (to be submitted).

F.1.2 Other Journal Articles

1. Christian, J., Wells, G., Lafleur, J., Verges, A., Braun, R., "Sizing of an Entry, Descent, and Landing System for Human Mars Exploration," *Journal of Spacecraft and Rockets*, Vol. 45, No. 1, pp. 130–141, January–February 2008.

F.2 Conference Papers

F.2.1 Relevant Conference Papers

1. Wells, G., Dutta, S., Mattson, S., Lisano, M., "Phoenix Location Determination Using HiRISE Imagery," IPPW–7–340, *International Planetary Probe Workshop 7*, Barcelona, Spain, June 2010.

2. Wells, G., Braun, R., "Trajectory Reconstruction of a Martian Planetary Probe Mission: Reconstruction of the Spirit Mars Exploration Rover Entry, Descent,

and Landing Performance," AA–3–2008–16, *2nd International ARA Days*, Arcachon, France, October 2008.

F.2.2 Other Conference Papers

1. Christian, J., Manyapu, K., Wells, G., Lafleur, J., Verges, A., Braun, R., "Sizing of an Entry, Descent, and Landing System for Human Mars Exploration," AIAA–2006–7427, *AIAA Space 2006 Conference*, San Jose, California, September 2006.

2. Alemany, K., Braun, R., Clark, I., Theisinger, J., Wells, G., "Mars Entry, Descent, and Landing Parametric Sizing and Design Space Visualization," AIAA–2006–6022, *AIAA Astrodynamics Specialist Conference*, Keystone, Colorado, August 2006.

3. Clark, I., Wells, G., Theisinger, J., Braun, R., "An Evaluation of Ballute Entry Systems for Lunar Return Missions," AIAA–2006–6276, *AIAA Atmospheric Flight Mechanics Conference*, Keystone, Colorado, August 2006.

4. Wells, G., Braun, R., "An Entry Handbook for the Conceptual Design of Mars Missions," AA2006–1–34, *1st International ARA Days*, Arcachon, France, July 2006.

5. Wells, G., Lafleur, J., Verges, A. Lewis, C., Christian, J., Manyapu, K., Braun, R. "Entry Descent and Landing Challenges of Human Mars Exploration," AAS–06–072, *29th AAS Guidance and Control Conference*, Breckenridge, Colorado, February 2006.

6. Kipp, D., Dec, J., Wells, G., and Braun, R. "Development of a Planetary Entry System Synthesis Tool for Conceptual Design and Analysis," *Proceedings of the 3rd International Planetary Probe Workshop*, Athens, Greece, June 2005.

7. Clark, I., Francis, S., Otero, R., Wells, G. "Reusable Exploration Vehicle (REV): Orbital Space Tourism Concept," *2005 RASC-AL Design Competition*, Coco Beach, Florida, May 2005.

REFERENCES

[1] Aboudan, A., Colombatti, G., Ferri, F., and Angrilli, F., "Huygens Probe Entry Trajectory and Attitude Estimated Simultaneously with Titan Atmospheric Structure by Kalman Filtering," *Planetary and Space Science*, vol. 56, pp. 573–585, April 2008.

[2] Aitken, M., Busnardo, D., Tolson, R., Amzajerdian, F., and Pierrottet, D., "High Speed Lunar Navigation for Crewed and Remotely Piloted Vehicles," *i–SAIRAS 2010: 10th International Symposium on Artificial Intelligence, Robotics and Automation in Space*, NASA ARC–E–DAA–TN 2071, Sapporo, Japan, August 29, – September 1, 2010.

[3] Aitken, M., Busnardo, D., Tolson, R., Amzajerdian, F., and Pierrottet, D., "LIDAR–Aided Inertial Navigation with Extended Kalman Filtering for Pinpoint Landing over Rough Terrain," *49th AIAA Aerospace Sciences Meeting including the New Horizons Forum and Aerospace Exposition*, AIAA–2011–0428, Orlando, Florida, January 4–7, 2011.

[4] Allen, R. and Copeland, G., "NASA Three–Laser Airborne Differential Absorption LIDAR System Electronics," Tech. Rep. NASA–CR–174293, NASA, December 1984.

[5] Andrade–Cetto, J., "The Kalman Filter," Tech. Rep. IRI–DT–02–01, Institut de Robòtica i Informàtica Industrial, UPC CSIC, Barcelona, Spain, May 2005.

[6] Andreev, B., Guslyakov, V., Kerzhanovich, V., Kruglov, Y., Lysov, V., Marov, M., Onishchenko, L., Rozhdestvenskii, M., Sorokin, V., and Shnygin, Y., "Venera 8 Wind-Velocity Measurements in the Atmosphere of Venus," *Cosmic Research*, vol. 12, pp. 238–245, March–April 1974.

[7] Andreev, B., Guslyakov, V., Kerzhanovich, V., Kruglov, Y., Lysov, V., Marov, M., Onishchenko, L., Rozhdestvenskii, M., Sorokin, V., and Shnygin, Y., "Venera 8 Wind-Velocity Measurements in the Atmosphere of Venus," *Cosmic Research*, vol. 12, pp. 385–393, May–June 1974.

[8] Antsibor, N., Bakit'ko, R., Ginzburg, A., Guslyakov, V., Kerzhanovich, V., Makarov, Y., Marov, M., Molotov, E., Rogal'skii, V., Rozhdestvenskii, M., Sopokin, V., and Shnygin, Y., "Estimates of Wind Velocity and Turbulence from Relayed Doppler Measurements of the Velocity of Instruments Dropped from Venera 9 and Venera 10," *Cosmic Research*, vol. 14, pp. 625–631, September–October 1976.

[9] Apostol, T., *Calculus: Multi–Variable Calculus and Linear Algebra, with Applications to Differential Equations and Probability*, ch. 8, pp. 269–271. Volume 2, 2nd edition, John Wiley & Sons, New York, 1969.

[10] Arulampalam, S., Maskell, S., Gordon, N., and Clapp, T., "A Tutorial on Particle Filters for Online Nonlinear / Non–Gaussian Bayesian Tracking," *IEEE Transactions on Signal Processing*, vol. 50, pp. 174–188, February 2002.

[11] Arvidson, R., Anderson, R., Haldemann, A., Landis, G., Li, R., Lindemann, R., Matijevic, J., Morris, R., Richter, L., Squyres, S., Sullivan, R., and Snider, N., "Physical Properties and Localization Investigations Associated with the 2003 Mars Exploration Rovers," *Journal of Geophysical Research: Planets*, vol. 108, no. E12, 2003.

[12] Ascher, U., Mattheij, R., and Russell, R., *Numerical Solution of Boundary Value Problems for Ordinary Differential Equations*, ch. 5, pp. 218–219. Prentice–Hall Inc., 1988.

[13] Atkinson, D., Kazeminejad, B., Gaborit, V., Ferri, F., and Lebreton, J., "Huygens Probe Entry and Descent Trajectory Analysis and Reconstruction Techniques," *Planetary and Space Science*, vol. 53, pp. 586–593, April 2005.

[14] Atkinson, D., Pollack, J., and Seiff, A., "Galileo Doppler Measurements of the Deep Zonal Winds at Jupiter," *Science*, vol. 272, pp. 842–843, May 10, 1996.

[15] Atkinson, D., Pollack, J., and Seiff, A., "The Galileo Probe Doppler Wind Experiment: Measurement of the Deep Zonal Winds on Jupiter," *Journal of Geophysical Research*, vol. 103, no. E10, pp. 22911–22928, 1998.

[16] Avduevskii, V., Akim, E., Aleshin, V., Borodin, N., Kerzhanovich, V., Malkov, Y., Marov, M., Morozov, S., Rozhdestvenskii, M., Ryabov, O., Subbotin, M., Suslov, V., Cheremukhina, Z., and Shkirina, V., "Martian Atmosphere in the Vicinity of the Landing Site of the Descent Vehicle Mars-6 (Preliminary Results)," *Cosmic Research*, vol. 13, pp. 18–27, January–February 1975.

[17] Avduevskii, V., Borodin, N., Burtsev, V., Malkov, Y., Marov, M., Morozov, S., Rozhdestvenskii, M., Romanov, R., Sokolov, S., Fokin, V., Cheremukhina, Z., and Shkirina, V., "Automatic Stations Venera 9 and Venera 10 - Functioning of Descent Vehicles and Measurement of Atmospheric Parameters," *Cosmic Research*, vol. 14, pp. 577–586, September–October 1976.

[18] Avduevskii, V., Dobrov, A., Ivanov, N., Karyagin, V., Kuznetsov, V., Martirosov, M., Mottsulev, B., Pichkhadze, K., Polyakov, V., Antsibor, N., Barkhatova, L., and Kerzhanovich, V., "Analysis of the

Trajectories of the Venera 13 and Venera 14 Entry Probes in the Atmosphere of Venus," *Cosmic Research*, vol. 21, pp. 111–118, March–April 1983.

[19] Avduevskii, V., Godnev, A., Semenchenko, V., Uspenskii, G., and Cheremukhina, Z., "Stratosphere of Venus according to the Data of the Accelerometer Measurements of the Venera-11 and Venera-12 Spacecraft," *Cosmic Research*, vol. 20, pp. 649–655, November–December 1982.

[20] Avduevskii, V., Godnev, A., Semenchenko, V., Uspenskii, G., and Cheremukhina, Z., "Characteristics of the Stratosphere of Venus from Measurements of the Overloads during the Braking of the Venera 13 and Venera 14 Spacecraft," *Cosmic Research*, vol. 21, pp. 149–154, March–April 1983.

[21] Avduevskii, V., Ivanov, N., Mot-tsulev, B., Polyakov, V., and Tikhonov, V., "A Method for a Complex Post-Flight Ballistic Analysis of the Descent Trajectories for "Venera"-type Landers," *Cosmic Research*, vol. 21, pp. 39–48, January–February 1983.

[22] Avduevsky, V., Marov, M., Rozhdestvensky, M., Borodin, N., and Kerzhanovich, V., "Soft Landing of Venera 7 on the Venus Surface and Preliminary Results of Investigations of the Venus Atmosphere," *Journal of the Atmospheric Sciences*, vol. 28, pp. 263–269, March 1971.

[23] Banani, S. and Masnadi–Shirazi, M., "A New Version of Unscented Kalman Filter," *Proceedings of the World Academy of Science, Engineering, and Technology*, vol. 20, pp. 192–197, April 2007.

[24] Battin, R., *An Introduction to the Mathematics and Methods of Astrodynamics*. AIAA Education Series, American Institute of Aeronautics and Astronautics, Inc., New York, 1987.

[25] Bayes, T., "An Essay towards Solving a Problem in the Doctrine of Chances," *communicated by Richard Price, in a letter to John Canton*, http://www.stat.ucla.edu/history/essay.pdf, December 23, 1763.

[26] Bekkeng, J. and Psiaki, M., "Attitude Estimation for Sounding Rockets Using Microelectromechanical System Gyros," *Journal of Guidance, Control, and Dynamics*, vol. 31, pp. 533–542, May–June 2008.

[27] Bell, II, E. and Grayzeck, E., "Galileo Probe Entry Timeline," *National Space Science Data Center*, http://nssdc.gsfc.nasa.gov/planetary/galileo_probe_time.html, NSSDC ID: 1973–052A, June 14, 1996.

[28] Belton, M., "Theory of the Curve Growth and Phase Effects in a Cloudy Atmosphere: Applications to Venus," *Journal of the Atmospheric Sciences*, vol. 25, pp. 596–609, July 1968.

[29] Beneš, V., "Exact Finite–Dimensional Filters for Certain Diffusions with Nonlinear Drift," *Stochastics*, vol. 5, no. 1, pp. 62–95, 1981.

[30] Benoit, C., "Sur une méthode de résolution des équations normales provenant de l'application de la méthode des moindes carrés a un système d'équations linéaires en numbre inférieur a celui des inconnues – application de la méthode a la résolution d'un système defini d'équations linéaires (Procédé du Commandant Andre–Louis Cholesky)," *Bulletin Géodêsique et Géophysique Internationale*, vol. 2, pp. 67–77, Toulouse, France, 1924.

[31] Berg, R., "Estimation and Prediction for Maneuvering Target Trajectories," *IEEE Transactions on Automatic Control*, vol. AC–28, pp. 294–304, March 1983.

[32] Bird, M., Allison, M., Asmar, S., Atkinson, D., Avruch, I., Dutta–Roy, R., Dzierma, Y., Edenhofer, P., Folkner, W., Gurvits, L., Johnston, D., Plettemeier, D., Pogrebenko, S., Preston, R., and Tyler, G., "The Vertical Profile of Winds on Titan," *Nature*, vol. 438, pp. 800–802, December 8, 2005.

[33] Blanchard, R., "Entry Descent and Landing Trajectory and Atmosphere Reconstruction for the Mars Exploration Rovers Missions A and B." The George Washington University, performed under NASA–JPL subcontract CCNS20568F, April 15, 2008.

[34] Blanchard, R., "Mars Phoenix Mission Entry, Descent, and Landing Trajectory and Atmosphere Reconstruction." The George Washington University, performed under NASA grant award CCLS20458F, January 2009.

[35] Brammer, R., Pass, R., and White, J., "Bathymetric and Oceanographic Applications of Kalman Filtering," *IEEE Transactions on Automatic Control*, vol. AC–28, pp. 363–371, March 1983.

[36] Braun, R. *Personal Communication*, 2007.

[37] Braun, R., "Mars Pathfinder Altimeter Data," *Personal Communication*, January 11, 2008.

[38] Braun, R., Powell, R., Engelund, W., Gnoffo, P., Weilmuenster, K., and Mitcheltree, R., "Mars Pathfinder Six–Degree–of–Freedom Entry Analysis," *Journal of Spacecraft and Rockets*, vol. 32, pp. 993–1000, November–December 1995.

[39] Brown, R. and Hwang, P., *Introduction to Random Signals and Applied Kalman Filtering*, ch. 2, p. 99. 2nd edition, John Wiley & Sons, Inc., New York, 1992.

[40] Brown, R. and Hwang, P., *Introduction to Random Signals and Applied Kalman Filtering*, ch. 5, pp. 218–236. 2nd edition, John Wiley & Sons, Inc., New York, 1992.

[41] Brown, R. and Hwang, P., *Introduction to Random Signals and Applied Kalman Filtering*, ch. 5, p. 236. 2nd edition, John Wiley & Sons, Inc., New York, 1992.

[42] Brunke, S. and Campbell, M., "Square Root Sigma Point Filtering for Real–Time, Nonlinear Estimation," *Journal of Guidance, Control, and Dynamics*, vol. 27, no. 2, pp. 314–317, 2004.

[43] Bucy, R. and Joseph, P., *Filtering for Stochastic Processes with Applications to Guidance*, ch. 16, pp. 175–6. Interscience Publishers (a division of John Wiley & Sons), New York, 1968.

[44] Butler, C., "Development and Operation of a Real–time Data Acquisition System for the NASA–LaRC Differential Absorption LIDAR," Tech. Rep. NASA–CR–174384, NASA, January 1985.

[45] Campbell, J., Synnott, S., and Bierman, G., "Voyager Orbit Determination at Jupiter," *IEEE Transactions on Automatic Control*, vol. AC–28, pp. 256–268, March 1983.

[46] Castano, A., Fukunaga, A., Biesiadecki, J., Neakrase, L., Whelley, P., Greeley, R., Lemmon, M., Castano, R., and Chien, S., "Automatic Detection of Dust Devils and Clouds on Mars," *Machine Vision and Applications*, vol. 19, pp. 467–482, October 2008.

[47] Champion, K. and Faire, A., "Falling Sphere Measurements of Atmospheric Density, Temperature, and Pressure, up to 115 km," Tech. Rep. AFCRL 64–554, Air Force Cambridge Research Laboratory, July 1964.

[48] Chatzi, E. and Smyth, A., "The Unscented Kalman Filter and Particle Filter Methods for Nonlinear Structural System Identification with Non–collocated Heterogeneous Sensing," *Structural Control and Health Monitoring*, vol. 16, pp. 99–123, February 2009.

[49] Christian, J., Verges, A., and Braun, R., "Statistical Reconstruction of Mars Entry, Descent, and Landing Trajectories and Atmospheric Profiles," *AIAA Space 2007 Conference and Exposition*, AIAA–2007–6192, Long Beach, California, September 18–20, 2007.

[50] Colin, L. and Hunten, D., "Pioneer Venus Experiment Descriptions," *Space Science Reviews*, vol. 20, pp. 451–525, June 1977.

[51] Crassidis, J., Lai, K., and Harman, R., "Magnetometer–Based Attitude and Rate Estimation for Spacecraft with Wire Booms," *Journal of Guidance, Control, and Dynamics*, vol. 28, pp. 584–593, July–August 2005.

[52] Crassidis, J., Lai, K., and Harman, R., "Real–Time Attitude–Independent Three–Axis Magnetometer Calibration," *Journal of Guidance, Control, and Dynamics*, vol. 28, pp. 115–120, January–February 2005.

[53] Crisp, J., Adler, M., Matijevic, J., Squyres, S., Arvidson, R., and Kass, D., "Mars Exploration Rover Mission," *Journal of Geophysical Research: Planets*, vol. 108, October 24, 2003.

[54] Crumpler, L., "Geotraverse from Xanthe Terra to Chryse Planitia: Viking 1 Lander Region, Mars," *Journal of Geophysical Research*, vol. 102, pp. 4201–4218, February 25, 1997.

[55] Daum, F., *Bayesian Analysis of Time Series and Dynamic Models*, ch. 8, pp. 199–226. Marcel Drekker, Inc., 1988.

[56] Daum, F. and Fitzgerald, R., "Decoupled Kalman Filters for Phased Array Radar Tracking," *IEEE Transactions on Automatic Control*, vol. AC–28, pp. 269–283, March 1983.

[57] Daum, F. and Fitzgerald, R., "Modeling and System Identification of a Life–Size Brake–Actuated Manipulator," *IEEE Transactions on Robotics*, vol. 25, pp. 481–491, June 2009.

[58] de Vaucouleurs, G. and Menzel, D., "Results of the Occultation of Regulus by Venus, July 7, 1959," *Nature*, vol. 188, pp. 28–33, October 1, 1960.

[59] Deryugin, V., Dolgopolov, V., Karyagin, V., Kovtunenko, V., Kremnev, R., Pichkhadze, K., Rogovskii, G., and Sagdeev, R., "Vega-1 and Vega-2 Spacecraft: Operation of the Landers in the Venusian Atmosphere," *Cosmic Research*, vol. 25, pp. 494–498, September–October 1987.

[60] Desai, P., *Improved Collocation Methods with Application to Six–Degree–of–Freedom Trajectory Optimization*. PhD thesis, University of Illinois at Urbana–Champaign, March 30, 2005.

[61] Desai, P., Blanchard, R., and Powell, R., "Entry Trajectory and Atmosphere Reconstruction Methodologies for the Mars Exploration Rover Mission," *European Space Agency Special Publication (ESA SP 544)*, pp. 213–220, February 2004.

[62] Desai, P. and Knocke, P., "Mars Exploration Rovers Entry, Descent, and Landing Trajectory Analysis," *AIAA / AAS Astrodynamics Specialist Conference and Exhibit*, AIAA–2004–5092, Providence, Rhode Island, August 16–19, 2004.

[63] Desai, P. and Knocke, P., "Entry, Descent, and Landing Scenario for the Mars Exploration Rover Mission," *Journal of the Astronautical Sciences*, vol. 55, pp. 421–430, October–December 2007.

[64] Desai, P. and Knocke, P., "Mars Exploration Rovers Entry, Descent, and Landing Trajectory Analysis," *Journal of the Astronautical Sciences*, vol. 55, pp. 311–323, July–September 2007.

[65] Desai, P. and Lyons, D., "Entry, Descent, and Landing Operations Analysis for the Genesis Entry Capsule," *Journal of Spacecraft and Rockets*, vol. 45, pp. 27–32, January–February 2008.

[66] Desai, P., Mitcheltree, R., and Cheatwood, F., "Entry Dispersion Analysis for the Stardust Comet Sample Return Capsule," *Journal of Spacecraft and Rockets*, vol. 36, pp. 463–469, May–June 1999.

[67] Desai, P., Prince, J., McQueen, E., Cruz, J., and Grover, M., "Entry, Descent, and Landing Performance of the Mars Phoenix Lander," *AIAA Guidance, Navigation, and Control Conference*, AIAA–2008–7346, Honolulu, Hawaii, August 18–21, 2008.

[68] Desai, P. and Qualls, G., "Stardust Entry Reconstruction," *46th AIAA Aerospace Sciences Meeting and Exhibit*, AIAA–2008–1198, Reno, Nevada, January 7–10, 2008.

[69] Desai, P., Qualls, G., and Schoenenberger, M., "Reconstruction of the Genesis Entry," *Journal of Spacecraft and Rockets*, vol. 45, pp. 33–38, January–February 2008.

[70] Desai, P., Schoenenberger, M., and Cheatwood, F., "Mars Exploration Rover Six-Degree-of-Freedom Entry Trajectory Analysis," *Journal of Spacecraft and Rockets*, vol. 43, pp. 1019–1025, September–October 2006.

[71] Desai, P., Schofield, J., and Lisano, M., "Flight Reconstruction of the Mars Pathfinder Disk–Gap–Band Parachute Drag Coefficients," *17th AIAA Aerodynamic Decelerator Systems Technology Conference and Seminar*, Monterey, California, May 19–22, 2003.

[72] Desai, P., Schofield, J., and Lisano, M., "Flight Reconstruction of the Mars Pathfinder Disk–Gap–Band Parachute Drag Coefficients," *Journal of Spacecraft and Rockets*, vol. 42, pp. 672–676, July–August 2005.

[73] Dorfman, S., "The Pioneer Venus Spacecraft Program," *Journal of Spacecraft and Rockets*, vol. 14, pp. 683–689, November 1977.

[74] Dzierma, Y., Bird, M., Dutta–Roy, R., Pérez–Ayúcar, M., Plettemeier, D., and Edenhofer, P., "Huygens Probe Descent Dynamics Inferred from Channel B Signal Level Measurements," *Planetary and Space Science*, vol. 55, pp. 1886–1895, November 2007.

[75] Edgett, K. and Christensen, P., "Rocks and Aeolian Features in the Mars Pathfinder Landing Site Region: Viking Infrared Thermal Mapper Observations," *Journal of Geophysical Research*, vol. 102, pp. 4107–4116, February 25, 1997.

[76] Edquist, K., "Computations of Viking Lander Capsule Hypersonic Aerodynamics with Comparisons to Ground and Flight Data," *AIAA Atmospheric Flight Mechanics Conference and Exhibit*, AIAA–2006–6137, Keystone, Colorado, August 21–24, 2006.

[77] Edquist, K., Wright, M., and Allen, G., "Viking Afterbody Heating Computations and Comparisons to Flight Data," *44th AIAA Aerospace Sciences Meeting and Exhibit*, AIAA–2006–0386, Reno, Nevada, January 9–12, 2006.

[78] Edwards, C. and Penney, D., *Differential Equations & Linear Algebra*, ch. 8, pp. 476–513. Prentice Hall, Upper Saddle River, New Jersey, 2001.

[79] Euler, E., Adams, G., and Hopper, F., "Design and Reconstruction of the Viking Lander Descent Trajectories," *Journal of Guidance, Control, and Dynamics*, vol. 1, pp. 372–378, September–October 1978.

[80] Evensen, G., "Using the Extended Kalman Filter with a Multilayer Quasi–Geostrophic Ocean Model," *Journal of Geophysical Research: Oceans*, vol. 97, pp. 17905–17924, November 15, 1992.

[81] Evensen, G., "Open Boundary Conditions for the Extended Kalman Filter with a Quasi–Geostrophic Ocean Model," *Journal of Geophysical Research: Oceans*, vol. 98, pp. 16529–16546, September 15, 1993.

[82] Evensen, G., "Sequential Data Assimilation with a Nonlinear Quasi–Geostrophic Model Using Monte Carlo Methods to Forecast Error Statistics," *Journal of Geophysical Research: Oceans*, vol. 99, pp. 10143–10162, May 15, 1994.

[83] Evensen, G., *Data Assimilation: The Ensemble Kalman Filter*, ch. 1–17, pp. 1–330. 2nd edition, Springer–Verlag, Berlin / Heidelberg, Germany, 2009.

[84] Farina, A., Ristic, B., and Benvenuti, D., "Tracking a Ballistic Target: Comparison of Several Nonlinear Filters," *IEEE Transactions on Aerospace and Electronic Systems*, vol. 38, pp. 854–867, July 2002.

[85] Fay, J. and Riddell, F., "Theory of Stagnation Point Heat Transfer in Dissociated Air," *Journal of the Aeronautical Sciences*, vol. 25, pp. 73–85, 121, February 1958.

[86] Findlay, J. and Blanchard, R., "Proposed Methods for the Reconstruction of the Pioneer Venus Probe Entry Trajectories," *17th Aerospace Sciences Meeting*, AIAA–1979–0259, New Orleans, Louisiana, January 15–17, 1979.

[87] Findlay, J. and Kelly, G., "A Recommended Entry Reconstruction Process for the Pioneer Venus Multi-Probe Mission," Tech. Rep. NASA–CR–158962, AMA–78–18, November 1, 1978.

[88] Fisher, J. and Vadali, S., "Gyroless Attitude Control of Multi–Body Satellites Using an Unscented Kalman Filter," *AIAA / AAS Astrodynamics Specialist Conference and Exhibit*, AIAA–2006–6163, Keystone, Colorado, August 21–24, 2006.

[89] Fjeldbo, G. and Eshleman, V., "The Atmosphere of Mars Analyzed by Integral Inversion of the Mariner IV Occultation Data," *Planetary Space Science*, vol. 16, pp. 1035–1059, 1968.

[90] Fjeldbo, G. and Eshleman, V., "Atmosphere of Venus as Studied with the Mariner 5 Dual Radio-Frequency Occultation Experiment," *Radio Science*, vol. 4, pp. 879–897, October 1969.

[91] Fjeldbo, G., Kliore, A. J., and Eshleman, V. R., "The Neutral Atmosphere of Venus as Studied with the Mariner V Radio Occultation Experiments," *Astronomical Journal*, vol. 76, pp. 123–140, 1971.

[92] Fjeldbo, G., Sweetnam, D., Brenkle, J., Christensen, E., Farless, D., Mehta, J., and Seidel, B., "Viking Radio Occultation Measurements of the Martian Atmosphere and Topography: Primary Mission Coverage," *Journal of Geophysical Research*, vol. 82, pp. 4317–4324, September 30, 1977.

[93] Frost, W. and Huang, K., "Doppler LIDAR Signal and Turbulence Study," Tech. Rep. NASA–CR–170976, NASA, December 1983.

[94] Fulchignoni, M., "The Atmosphere of Titan and the Huygens Atmospheric Structure Instrument," *Il Nuovo Cimento*, vol. 15C, pp. 1163–1177, November–December 1992.

[95] Fulchignoni, M., Ferri, F., Angrilli, F., Ball, A., Bar-Nun, A., Barucci, M., Bettanini, C., Bianchini, G., Borucki, W., Colombatti, G., Coradini, M., Coustenis, A., Debei, S., Falkner, P., Fanti, G., Flamini, E., Gaborit, V., Grard, R., Hamelin, M., Harri, A., Hathi, B., Jernej, I., Leese, M., Lehto, A., Stoppato, P., López-Moreno, J., Mäkinen, T., McDonnell, J., McKay, C., Molina-Cuberos, G., Neubauer, F., Pirronello, V., Rodrigo, R., Saggin, B., Schwingenschuh, K., Seiff, A., Simões, F., Svedhem, H., Tokano, T., Towner, M., Trautner, R., Withers, P., and Zarnecki, J., "In Situ Measurements of the Physical Characteristics of Titan's Environment," *Nature*, vol. 438, pp. 785–791, December 8, 2005.

[96] Gannot, S. and Moonen, M., "On the Application of the Unscented Kalman Filter to Speech Processing," *international Workshop on Acoustic Echo and Noise Control (IWAENC)*, Kyoto, Japan, September 2003.

[97] Gavss, J. C. F., *Theoria Motvs Corporvm Coelestivm in Sectionibvs Conicis Solem Ambientivm*, ch. 2.3, p. 249. Hamburg, F. Perthes and I.H. Besser, 1809.

[98] Gelb, A., *Applied Optimal Estimation*, ch. 4, p. 156. MIT Press, Cambridge, Massachusetts, 1974.

[99] Gelb, A., *Applied Optimal Estimation*, ch. 4, pp. 107–113. MIT Press, Cambridge, Massachusetts, 1974.

[100] Gelb, A., *Applied Optimal Estimation*, ch. 6, p. 188. MIT Press, Cambridge, Massachusetts, 1974.

[101] Georgiev, S., "A Feasibility Study of an Experiment for Determining the Properties of the Mars Atmosphere," Tech. Rep. NASA CR–530, NASA, Government Printing Office, Washington, DC, July 1967.

[102] Gingerich, O., "The Computer versus Kepler," *American Scientist*, vol. 52, pp. 218–226, 1964.

[103] Gnoffo, P., Braun, R., Weilmuenster, K., Mitcheltree, R., Engelund, W., and Powell, R., "Prediction and Validation of Mars Pathfinder Hypersonic Aerodynamic Database," *Journal of Spacecraft and Rockets*, vol. 36, pp. 367–373, May–June 1999.

[104] Gnoffo, P., Weilmuenster, K., Braun, R., and Cruz, C., "Influence of Sonic-Line Location on Mars Pathfinder Aerothermodynamics," *Journal of Spacecraft and Rockets*, vol. 33, pp. 169–177, March–April 1996.

[105] Golombek, M., "The Mars Pathfinder Mission," *Journal of Geophysical Research – Planets*, vol. 102, pp. 3953–3965, February 25, 1997.

[106] Golombek, M., Cook, R., Economou, T., Folkner, W., Haldemann, A., Kallemeyn, P., Knudsen, J., Manning, R., Moore, H., Parker, T., Rieder, R., Schofield, J., Smith, P., and Vaughan, R., "Overview of the Mars Pathfinder Mission and Assessment of Landing Site Predictions," *Science*, vol. 278, pp. 1743–1748, December 5, 1997.

[107] Golombek, M., Cook, R., Moore, H., and Parker, T., "Selection of the Mars Pathfinder Landing Site," *Journal of Geophysical Research – Planets*, vol. 102, pp. 3967–3988, February 25, 1997.

[108] Grayzeck, E. and Bell, E., "Mars 3 Lander," *National Space Science Data Center*, http://nssdc.gsfc.nasa.gov/nmc/masterCatalog.do?sc=1971-049F, October 8, 2010.

[109] Grewal, M. and Andrews, A., *Kalman Filtering: Theory and Practice Using MATLAB*, ch. 5, pp. 183–186. 3rd edition, Wiley-Interscience, 2008.

[110] Grewal, M. and Andrews, A., *Kalman Filtering: Theory and Practice Using MATLAB*, ch. 4, p. 139. 3rd edition, Wiley-Interscience, 2008.

[111] Grewal, M. and Andrews, A., *Kalman Filtering: Theory and Practice Using MATLAB*, ch. 8, pp. 393–403. 3rd edition, Wiley-Interscience, 2008.

[112] Haldemann, A., Mitchell, D., Jurgens, R., Slade, M., and Muhleman, D., "Mars Pathfinder Landing Site Assessment with Goldstone Delay–Doppler and CW Radar Experiments," *Journal of Geophysical Research*, vol. 102, pp. 4097–4106, February 25, 1997.

[113] Hanessian, Jr., J. and Guttmacher, I., "Experimental Results of the U. S. Rocket Program for the International Geophysical Year to 1 July 1958," National Academy of Science – National Research Council, Washington, DC, IGY Rocket Report Serial No. 1, July 30, 1958.

[114] Hargraves, C. and Paris, S., "Direct Trajectory Optimization Using Nonlinear Programming and Collocation," *Journal of Guidance, Control, and Dynamics*, vol. 10, pp. 338–342, July–August 1987.

[115] Haykin, S., *Kalman Filtering and Neural Networks*, ch. 1, p. 5. John Wiley & Sons, Inc., New York, 2001.

[116] Haykin, S., *Kalman Filtering and Neural Networks*, ch. 1, pp. 5–20. John Wiley & Sons, Inc., New York, 2001.

[117] Haykin, S., *Kalman Filtering and Neural Networks*, ch. 1, p. 17. John Wiley & Sons, Inc., New York, 2001.

[118] Haykin, S., *Kalman Filtering and Neural Networks*, ch. 7, p. 221. John Wiley & Sons, Inc., New York, 2001.

[119] Haykin, S., *Kalman Filtering and Neural Networks*, ch. 7, pp. 234–239. John Wiley & Sons, Inc., New York, 2001.

[120] Holman, F. and Kennet, H., "Planetary Atmospheric Determination Utilizing a Semipassive Probe," *Journal of Spacecraft*, vol. 3, pp. 651–658, May 1966.

[121] Hopper, F., "Trajectory, Atmosphere, and Wind Reconstruction from Viking Entry Measurements," *AAS/AIAA Astrodynamics Specialist Conference*, AAS 75–068, AAS Microfiche Series Vol. 26, Nassau, Bahamas, July 28–30, 1975.

[122] Hu, G., Ong, C., and Teo, C., "Direct Collocation and Nonlinear Programming for Optimal Control Problem Using an Enhanced Transcribing Scheme," *Proceedings of the 1999 IEEE International Symposium on Computer Aided Control System Design*, Kohala Coast – Island of Hawaii, Hawaii, August 22–27, 1999.

[123] Ingoldby, R., Michel, F., Flaherty, T., Doty, M., Preston, B., Villyard, K., and Steele, R., "Entry Data Analysis for Viking Landers 1 and 2 Final Report," Tech. Rep. NASA CR–159388, NASA, November 1976.

[124] Istomin, V., Grechnev, K., Ozerov, L., Slutskii, M., Pavlenko, V., and Tsvetkov, V., "Experiment to Measure the Atmospheric Composition of Mars on the Mars 6 Entry Capsule," *Cosmic Research*, vol. 13, pp. 13–17, January–February 1975.

[125] Ito, K. and Xiong, K., "Gaussian Filters for Nonlinear Filtering Problems," *IEEE Transactions on Automatic Control*, vol. 45, pp. 910–927, May 2000.

[126] Ivankov, A., Williams, D., and Grayzeck, E., "Mars 6," *National Space Science Data Center*, http://nssdc.gsfc.nasa.gov/nmc/spacecraftDisplay.do?id=1973-052A, NSSDC ID: 1973–052A, August 5, 2008.

[127] Jah, M., *Mars Aerobraking Spacecraft State Estimation by Processing Inertial Measurement Unit Data*. PhD thesis, University of Colorado at Boulder, 2005.

[128] Jah, M., Lisano, M., Born, G., and Axelrad, P., "Mars Aerobraking Spacecraft State Estimation by Processing Inertial Measurement Unit Data," *SpaceOps 2006 Conference*, Rome, Italy, June 19–23, 2006.

[129] Jah, M., Lisano, M., Born, G., and Axelrad, P., "Mars Aerobraking Spacecraft State Estimation by Processing Inertial Measurement Unit Data," *Journal of Guidance, Control, and Dynamics*, vol. 31, pp. 1802–1812, November–December 2008.

[130] James, C. and Smith, W., "Experimental Studies of Static Stability and Radiative Heating Associated with Mars and Venus Entry," *Presented at the 31st Annual Meeting of the IAS*, New York, New York, January 21–23, 1963.

[131] Jaw, L., "Recent Advancements in Aircraft Engine Health Management (EHM) Technologies and Recommendations for the Next Step," *Proceedings of GT2005, ASME Turbo Expo 2005: Power for Land, Sea, and Air*, Reno, Nevada, June 6–9, 2005.

[132] Jenkins, J. M., *Variations in the 13 cm opacity below the main cloud layer in the atmosphere of Venus inferred from Pioneer–Venus radio occultation studies 1978-1987*. PhD thesis, Georgia Institute of Technology, May 1992.

[133] Jenkins, K., "Empirical Comparisons of Meteorological Rocket Wind Sensors," *Journal of Applied Meteorology*, vol. 1, pp. 196–202, June 1962.

[134] Johnson, N. L., "Soviet Atmospheric and Surface Venus Probes," *Spaceflight*, vol. 20, pp. 224–228, June 1978.

[135] Julier, S., "A Skewed Approach to Filtering," *SPIE Conference on Signal and Data Processing of Small Targets*, Orlando, Florida, April 1998.

[136] Julier, S., "The Scaled Unscented Transformation," *American Control Conference*, Anchorage, Alaska, May 8–10 2002.

[137] Julier, S. and Uhlmann, J., "A General Method for Approximating Nonlinear Transformations of Probability Distributions," tech. rep., The Robotics Research Group, Department of Engineering Science, The University of Oxford, Oxford, United Kingdom, November 1, 1996.

[138] Julier, S. and Uhlmann, J., "A New Extension of the Kalman Filter to Nonlinear Systems," *International Symposium on Aerospace/Defense Sensing, Simulation, and Controls*, Orlando, Florida 1997.

[139] Julier, S. and Uhlmann, J., "Unscented Filtering and Nonlinear Estimation," *Proceedings of the IEEE*, vol. 92, March 2004.

[140] Julier, S., Uhlmann, J., and Durrant-Whyte, H., "A New Method for the Nonlinear Transformation of Means and Covariances in Filters," *IEEE Transactions on Automatic Control*, vol. 45, pp. 477–482, March 2000.

[141] Julier, S., Uhlmann, J., and Whyte, H. D., "A New Approach for Filtering Nonlinear systems," *Proceedings of the American Control Conference*, Seattle, Washington, June 1995.

[142] Kailath, T., "A View of Three Decades of Linear Filtering Theory," *IEEE Transactions on Information Theory*, vol. IT–20, no. 2, pp. 146–181, 1974.

[143] Kalman, R., "A New Approach to Linear Filtering and Prediction Problems," *Journal of Basic Engineering*, vol. 82, pp. 34–45, March 1960.

[144] Kalman, R., "New Methods and Results in Linear Prediction and Filtering Theory," Tech. Rep. 61–1, Research Institute for Advanced Studies (RIAS), Martin Co., Baltimore, Maryland, 1961.

[145] Kalman, R. and Bucy, R., "New Results in Linear Filtering and Prediction Theory," *Journal of Basic Engineering*, vol. 83, pp. 95–108, March 1961.

[146] Karkoschka, E., Tomasko, M., Doose, L., See, C., McFarlane, E., Schröder, S., and Rizk, B., "DISR Imaging and the Geometry of the Descent of the Huygens Probe within Titan's Atmosphere," *Planetary and Space Science*, vol. 55, pp. 1896–1935, November 2007.

[147] Karyagin, V., Kremnev, R., Pichkhadze, K., Sklovskaya, A., and Yaroshevskii, V., "Investigation of Aerodynamics and Dynamics of Venera 9 and Venera 10 during Motion in the Atmosphere," *Cosmic Research*, vol. 14, pp. 741–747, November–December 1976.

[148] Kass, D., Schofield, J., Crisp, J., Bailey, E., Konefat, E., Lee, W., Litty, E., Manning, R., Martin, A. S., Willis, J., Beebe, R., Murphy, J., and Huber, L., "MER1/MER2–M–IMU–4–EDL–V1.0," *NASA Planetary Data System*, 2004.

[149] Kazeminejad, B., *Methodology Development for the Reconstruction of the ESA Huygens Probe Entry and Descent Trajectory*. PhD thesis, Karl–Franzens University Graz, January 2005.

[150] Kazeminejad, B. and Atkinson, D., "The ESA Huygens Probe Entry and Descent Trajectory Reconstruction," *European Space Agency Special Publication (ESA SP 544)*, pp. 213–220, February 2004.

[151] Kazeminejad, B., Atkinson, D., Pérez–Ayúcar, M., Lebreton, J., and Sollazzo, C., "Huygens' Entry and Descent through Titan's Atmosphere: Methodology and Results of the Trajectory Reconstruction," *Planetary and Space Science*, vol. 55, pp. 1845–1876, November 2007.

[152] Kerzhanovich, V., "Mars 6: Improved Analysis of the Descent Module Measurements," *Icarus*, vol. 30, pp. 1–25, January 1977.

[153] Kerzhanovich, V., Antsibor, N., Bakit'ko, R., Lysov, V., Molotov, E., Puchkov, V., Rutkovskii, A., Tikhonov, V., and Pichkhadze, K., "Vega-1 and Vega-2: Vertical Wind Speed Profiles from Doppler Measurements aboard the Descent Vehicles," *Cosmic Research*, vol. 25, pp. 513–516, September-October 1987.

[154] Kerzhanovich, V., Antsibor, N., Kustodiev, V., Makarov, Y., Matsygorin, I., Molotov, E., Sorokin, V., Sukhanov, K., Tikhonov, V., Karyagin, V., and Mottsulev, B., "Vertical Profile of the Wind Speed in the Atmosphere of Venus from Doppler Measurements on Venera 13 and Venera 14," *Cosmic Research*, vol. 21, pp. 155–161, March–April 1983.

[155] Kerzhanovich, V., Gotlib, V., Chetyrkin, N., and Andreev, B., "Results of Determining the Dynamics of the Atmosphere of Venus from Data of Measurements of the Radial Velocity of the Interplanetary Probe "Venera-4"," *Cosmic Research*, vol. 7, pp. 536–540, July–August 1969.

[156] Kirk, D., Intrieri, P., and Seiff, A., "Aerodynamic Behavior of the Viking Entry Vehicle – Ground Test and Flight Results," *Atmospheric Flight Mechanics Conference*, AIAA–1977–1160, Hollywood, Florida, August 8–10, 1977.

[157] Kirk, D., Intrieri, P., and Seiff, A., "Aerodynamic Behavior of the Viking Entry Vehicle – Ground Test and Flight Results," *Journal of Spacecraft and Rockets*, vol. 15, pp. 208–212, July–August 1978.

[158] Kolmogorov, A., "Interpolation und extrapolation von stationaren zufalligen folgen," *Bulletin of the Academy of Science of the USSR, Series on Mathematics*, vol. 5, pp. 3–14, 1941.

[159] Kondratyev, K., "Meteorological Investigations with Rockets and Satellites," Tech. Rep. NASA–TT–F–115, NASA, September 1, 1963.

[160] Kovtunenko, V., Sagdeev, R., and Barsukov, V., "Vega Project: Re–entry Vehicle of "Vega" Spacecraft," *Acta Astronautica*, vol. 13, no. 6/7, pp. 425–432, 1986.

[161] Kun, D., Kaijun, L., and Qunsheng, X., "Application of Unscented Kalman Filter for the State Estimation of Anti–lock Braking System," *IEEE International Conference on Vehicular Electronics and Safety (ICVES)*, Beijing, China, December 13–15, 2006.

[162] Lacey, T. and Thacker, N., "TINA Algorithms Guide," Tech. Rep. Chapter 11 Tutorial: The Kalman Filter, Electronic Systems Group, University of Sheffield, 1997.

[163] Lange, R., "Cassini–Huygens Mission Overview and Recent Science Results," *IEEE Aerospace Conference*, Paper 1598, Big Sky, Montana, March 1–8, 2008.

[164] Law, E. and Sauchanka–Davis, M., "Mars Pathfinder," *NASA Planetary Data System*, http://starbrite.jpl.nasa.gov/pds/viewDataset.jsp?dsid=MPFL-M-ASIMET-4-DDR-EDL-V1.0, July 25, 2003.

[165] Lebreton, J., Witasse, O., Sollazzo, C., Blancquaert, T., Couzin, P., Schipper, A., Jones, J., Matson, D., Gurvits, L., Atkinson, D., Kazeminejad, B., and Pérez–Ayúcar, M., "An Overview of the Descent and Landing of the Huygens Probe on Titan," *Nature*, vol. 438, pp. 758–764, December 8, 2005.

[166] Lee, C. and Salcic, Z., "A Fully-Hardware-Type Maximum-Parallel Architecture for Kalman Tracking Filter in FPGAs," *International Conference on Information, Communications and Signal Processing*, Singapore, September 9–12, 1997.

[167] Lee, Y., *A Fault Diagnosis Technique for Complex Systems Using Bayesian Data Analysis*. PhD thesis, Georgia Institute of Technology, April 2008.

[168] Leith, C., "Theoretical Skill of Monte Carlo Forecasts," *Monthly Weather Review*, vol. 102, pp. 409–418, June 1974.

[169] Linkin, V., Blamont, J., Devyatkin, S., Ignatova, S., Kerzhanovich, V., Lipatov, A., Malik, K., Stadnyk, B., Sanotskii, Y., Stolyarchuk, P., Terterashvili, A., Frank, G., and Khlyustova, L., "Thermal Structure of the Atmosphere of Venus from the Results of Measurements Taken by Landing Vehicle Vega-2," *Cosmic Research*, vol. 25, pp. 501–512, September–October 1987.

[170] Lisano, M., "Nonlinear Consider Covariance Analysis Using a Sigma-Point Filter Formulation," *29th Annual AAS Guidance and Control Conference*, AAS 06–035, Breckinridge, Colorado, February 4–8, 2006.

[171] Lisano, M., "Comparing Consider–Covariance Analysis with Sigma–Point Consider Filter and Linear–Theory Consider Filter Formulations," *Proceedings of the 20th International Symposium on Space Flight Dynamics*, Annapolis, Maryland, September 24–28, 2007.

[172] Lisano, M., Kruizinga, G., and Portock, B., "The NASA Phoenix 2007 Mars Lander Thruster Calibration Estimator: Design and Validation," *AIAA / AAS Astrodynamics Specialist Conference and Exhibit*, AIAA–2008–7217, Honolulu, Hawaii, August 18–21, 2008.

[173] Lovett, R., "North Magnetic Pole Moving Due to Core Flux," *National Geographic Daily News*, http://news.nationalgeographic.com/news/2009/12/091224-north-pole-magnetic-russia-earth-core.html, December 24, 2009.

[174] Lumelsky, V., "Estimation and Prediction of Unmeasurable Variables in the Steel Mill Soaking Pit Control System," *IEEE Transactions on Automatic Control*, vol. AC–28, pp. 388–400, March 1983.

[175] Magalhães, J., Schofield, J., and Seiff, A., "Results of the Mars Pathfinder Atmospheric Structure Investigation," *Journal of Geophysical Research - Planets*, vol. 104, pp. 8943–8955, April 25, 1999.

[176] Marinai, L., Probert, D., and Singh, R., "Prospects for Aero Gas–Turbine Diagnostics: A Review," *Applied Energy*, vol. 79, pp. 109–126, September 2004.

[177] Marov, M., "Venus: A perspective at the beginning of planetary exploration," *Icarus*, vol. 16, pp. 415–461, June 1972.

[178] McCormick, M., "The Use of LIDAR for Stratospheric Measurements," Tech. Rep. NASA–TM–74085, NASA, September 1977.

[179] McIlrath, T., "Atmospheric LIDAR Research Applying to H2O, O2, and Aerosols," Tech. Rep. NASA–CR–155798, NASA, December 1977.

[180] Meditch, J., "A Survey of Data Smoothing for Linear and Nonlinear Dynamic Systems," *Automatica*, vol. 9, pp. 151–162, March 1973.

[181] Metzger, J., Wisotzky, K., Wendel, J., and Trommer, G., "Sigma–Point Filter for Terrain Referenced Navigation," *AIAA Guidance, Navigation, and Control Conference and Exhibit*, AIAA–2005–6068, San Francisco, California, August 15–18, 2005.

[182] Michael, W., Tolson, R., Brenkle, J., Cain, D., Fjeldbo, G., Stelzried, C., Grossi, M., Shapiro, I., and Tyler, G., "The Viking Radio Science Investigations," *Journal of Geophysical Research*, vol. 82, pp. 4293–4295, September 30, 1977.

[183] Mihos, C., "Soviet Craft – Mars (1960–1974)," http://burro.astr.cwru.edu/stu/advanced/20th_soviet_mars.html, January 11, 2006.

[184] Milos, F., Chen, Y., Congdon, W., and Thornton, J., "Mars Pathfinder Entry Temperature Data, Aerothermal Heating, and Heatshield Material Response," *Journal of Spacecraft and Rockets*, vol. 36, pp. 380–391, May–June 1999.

[185] Milos, F., Chen, Y., Squire, T., and Brewer, R., "Analysis of Galileo Probe Heatshield Ablation and Temperature Data," *Journal of Spacecraft and Rockets*, vol. 36, pp. 298–306, May–June 1999.

[186] Mitchell, M., "Engauge Digitizer," http://digitizer.sourceforge.net/ 2004.

[187] Montenbruck, O. and Gill, E., *Satellite Orbits: Models, Methods, and Applications*, ch. 8, p. 282. Springer, Berlin, 2000.

[188] Montenbruck, O. and Gill, E., *Satellite Orbits: Models, Methods, and Applications*, ch. 8, pp. 281–282. Springer, Berlin, 2000.

[189] Moroz, V., "Preliminary Results of Studies Conducted on the Soviet Automatic Stations Mars 4, Mars 5, Mars 6, and Mars 7," *Cosmic Research*, vol. 13, pp. 1–6, January–February 1975.

[190] Moroz, V. and Zasova, L., "VIRA–2: A Review of Inputs for Updating the Venus International Reference Atmosphere," *Advances in Space Research*, vol. 19, no. 8, pp. 1191–1201, 1997.

[191] Moss, J., Blanchard, R., Wilmouth, R., and Braun, R., "Mars Pathfinder Rarefied Aerodynamics - Computation and Measurements," *Journal of Spacecraft and Rockets*, vol. 36, pp. 330–339, May–June 1999.

[192] Müller–Eigner, R., Koppenwallner, G., and Fritsche, B., "Pressure and Heat Flux Measurement with RAFLEX II during MIRKA Re–Entry," *Third European Symposium on Aerothermodynamics for Space Vehicles, European Space Agency Special Publication (ESA SP–426)*, pp. 685–694, Noordwijk, The Netherlands, January 1999.

[193] Mutch, T., Grenander, S., Jones, K., Patterson, W., Arvidson, R., Guinness, E., Avrin, P., Carlston, C., Binder, A., Sagan, C., Dunham, E., Fox, P., Pieri, D., Huck, F., Rowland, C., Taylor, G., Wall, S., Kahn, R., Levinthal, E., S. Liebes, J., Tucker, R., Morris, E.,

Pollack, J., Saunders, R., and Wolf, M., "The Surface of Mars: The View from the Viking 2 Lander," *Science*, vol. 194, pp. 1277–1283, December 17, 1976.

[194] Nier, A., Hanson, W., Seiff, A., McElroy, M., Spencer, N., Duckett, R., Knight, T., and Cook, W., "Composition and Structure of the Martian Atmosphere - Preliminary Results from Viking 1," *Science*, vol. 193, pp. 786–788, August 27, 1976.

[195] Nørgaard, M., Poulsen, N., and Ravn, O., "New Developments in State Estimation for Nonlinear Systems," *Automatica*, vol. 36, pp. 1627–1638, November 2000.

[196] Novak, F., Hutchinson, M., Mitchell, M., Munk, M., and Parker, P., "Mars Entry Atmospheric Data System (MEADS) Requirements and Design for the Mars Science Laboratory (MSL)," *6th International Planetary Probe Workshop*, Atlanta, Georgia, June 23–27, 2008.

[197] Obukhov, A. and Golitsyn, G., "Dynamics of the Descent of Space Probes in the Atmospheres of Planets as a Means of Controlling Measured Data," *Cosmic Research*, vol. 7, pp. 135–140, January–February 1969.

[198] Owen, T. and Biemann, K., "Composition of the Atmosphere at the Surface of Mars: Detection of Argon–36 and Preliminary Analysis," *Science*, vol. 193, pp. 801–803, August 27, 1976.

[199] Paris, S., Hargraves, C., and others, "Optimal Trajectories by Implicit Simulation (Version 1.2)," Tech. Rep. TR–88–3057, Vols. I–IV, Wright Research and Development Center, November 1988.

[200] Park, C., Kim, K., and Kang, W., "UKF Based In–Flight Alignment Using Low Cost IMU," *AIAA Guidance, Navigation, and Control Conference and Exhibit*, AIAA–2006–6353, Keystone, Colorado, August 21–24, 2006.

[201] Park, E., Park, S., Roh, K., and Choi, K., "Satellite Orbit Determination Using a Batch Filter Based on the Unscented Transformation," *Aerospace Science and Technology*, doi:10.1016/j.ast.2010.03.007, in Press, online April 1, 2010.

[202] Pastor, P., Bishop, R., and Striepe, S., "Evaluation of Mars Entry Reconstructed Trajectories Based on Hypothetical 'Quick–Look' Entry Navigation Data," in *Advances in the Astronautical Sciences*, vol. 105 II, pp. 1473–1490, 2000. AAS 00–197.

[203] Perminov, V., "The Difficult Road to Mars: A Brief History of Mars Exploration in the Soviet Union," Tech. Rep. Monographs in Aerospace History (Number 15), NP–1999–06–251–HQ, A joint publication of the NASA History Division, the Office of Policy and Plans, and the Office of Space Science, July 1999.

[204] Peterson, V., "A Technique for Determining Planetary Atmosphere Structure from Measured Accelerations of an Entry Vehicle," Tech. Rep. NASA TN D–2669, NASA, February 1965.

[205] Peterson, V., "Analysis of the Errors Associated with the Determination of Planetary Atmosphere Structure from Measured Accelerations of an Entry Vehicle," Tech. Rep. NASA TR R–225, NASA, July 1965.

[206] Pham, D., "Stochastic Methods for Sequential Data Assimilation in Strongly Nonlinear Systems," *Monthly Weather Review*, vol. 129, pp. 1194–1207, May 2001.

[207] Pham, D., Verron, J., and Gordeau, L., "Filtres de Kalman Singuliers Évolutif pour l'Assimilation de Données en Océnographie.," *Comptes Rendus de l'Académie des Sciences: Sciences de la Terre et des Planètes*, vol. 326, pp. 255–260, 1998.

[208] Pham, D., Verron, J., and Roubaud, M., "A Singular Evolutive Extended Kalman Filter for Data Assimilation," *Journal of Marine Systems*, vol. 16, pp. 323–340, October 1998.

[209] Plett, G., DeLima, P., and Pack, D., "Target Localization Using Multiple UAVs with Sensor Fusion via Sigma-Point Kalman Filtering," *AIAA Infotech@Aerospace Conference and Exhibit*, AIAA–2007–2845, Rohnert Park, California, May 7–10, 2007.

[210] Powell, R., Striepe, S., Desai, P., Braun, R., Brauer, G., Cornick, D., Olson, D., Petersen, F., and Stevenson, R., *Program to Optimize Simulated Trajectories (POST) Version 5.1.* NASA Langley Research Center, Hampton, Virginia, and Martin Marietta Corporation, Denver, Colorado, March 1997.

[211] Psiaki, M., "Attitude–Determination Filtering via Extended Quaternion Estimation," *Journal of Guidance, Control, and Dynamics*, vol. 23, pp. 206–214, March–April 2000.

[212] Psiaki, M., "The Super–Iterated Extended Kalman Filter," *AIAA Guidance, Navigation, and Control Conference and Exhibit*, AIAA–2004–5418, Providence, Rhode Island, August 16–19, 2004.

[213] Psiaki, M., "Backward–Smoothing Extended Kalman Filter," *Journal of Guidance, Control, and Dynamics*, vol. 28, no. 5, pp. 885–894, 2005.

[214] Psiaki, M., "Estimation of a Spacecraft's Attitude Dynamics Parameters by Using Flight Data," *Journal of Guidance, Control, and Dynamics*, vol. 28, pp. 594–603, July–August 2005.

[215] Psiaki, M., Klatt, E., Kintner, P., and Powell, S., "Attitude Estimation for a Flexible Spacecraft in an Unstable Spin," *Journal of Guidance, Control, and Dynamics*, vol. 25, pp. 88–95, January–February 2002.

[216] Psiaki, M., Martel, F., and Pal, P., "Three–Axis Attitude Determination via Kalman Filtering of Magnetometer Data," *Journal of Guidance, Control, and Dynamics*, vol. 13, pp. 506–514, May–June 1990.

[217] Psiaki, M. and Wada, M., "Derivation and Simulation Testing of a Sigma–Points Smoother," *AIAA Guidance, Navigation, and Control Conference and Exhibit*, AIAA–2006–6349, Keystone, Colorado, August 21–24, 2006.

[218] Psiaki, M. and Wada, M., "Derivation and Simulation Testing of a Sigma–Points Smoother," *Journal of Guidance, Control, and Dynamics*, vol. 30, no. 1, pp. 78–86, 2007.

[219] Rahideh, A. and Shaheed, M., "Output Feedback Nonlinear Model Predictive Control of a Twin Rotor MIMO System," *Eleventh International Conference on Climbing and Walking Robots and the Support Technologies for Mobile Machines*, Coimbra, Portugal, September 8–10, 2008.

[220] Rea, D., "The Atmosphere and Surface of Mars – A Selective Review," *Proceedings of the Caltech-JPL Lunar and Planetary Conference*, Jet Propulsion Laboratory, Pasadena, California, September 13–18, 1965.

[221] Remsberg, E., "LIDAR Support for the LACATE Balloon Experiment," Tech. Rep. NASA–TM–X–72956, NASA, January 1975.

[222] Research, C., "Measurement of Radiosignal Parameters from the Descent Vehicle of the Space Probe Mars 6 by the Retranslation Method," *Cosmic Research*, vol. 14, pp. 527–536, July–August 1976.

[223] Ribeiro, M., "Kalman and Extended Kalman Filters: Concept, Derivation, and Properties," tech. rep., Institute for Systems and Robotics, Instituto Superior Técnico, February 2004.

[224] Rieder, R., Wänke, H., Economou, T., and Turkevich, A., "Determination of the Chemical Composition of Martian Soil and Rocks: The Alpha Proton X Ray Spectrometer," *Journal of Geophysical Research – Planets*, vol. 102, pp. 4027–4044, February 25, 1997.

[225] Riehl, J., Paris, S., and Sjauw, W., "Comparison of Implicit Integration Methods for Solving Aerospace Trajectory Optimization Problems," *AIAA / AAS Astrodynamics Specialist Conference and Exhibit*, AIAA–2006–6033, Keystone, Colorado, August 21–24, 2006.

[226] Riehl, J., Sjauw, W., Falck, R., Hargraves, C., and Paris, S., "OTIS: Optimal Trajectories by Implicit Simulation," http://otis.grc.nasa.gov/index.html May 2008.

[227] Ristic, B., Farina, A., Benvenuti, D., and Arulampalam, M., "Performance Bounds and Comparison of Nonlinear Filters for Tracking a Ballistic Object on Re-entry," *IEE Proceedings – Radar, Sonar, and Navigation*, pp. 65–70, April 2003.

[228] Russell, R. *Personal Communication*, March 26, 2010.

[229] Russell, S. and Norvig, P., *Artificial Intelligence: A Modern Approach*, ch. 15, pp. 566–603. 3rd edition, Prentice Hall, 2009.

[230] Sabin, M., "Linear Filtering of Ballistic–Entry Probe Data for Atmospheric Reconstruction," *Journal of Spacecraft and Rockets*, vol. 12, pp. 66–73, February 1975.

[231] Sadhu, S., Mondal, S., Srinivasan, M., and Ghoshal, T., "Sigma Point Kalman Filter for Bearing only Tracking," *Signal Processing*, vol. 86, pp. 3769–3777, December 2006.

[232] Sagdeev, R., Linkin, V., Kerzhanovich, V., Lipatov, A., Shurupov, A., Blamont, J., Crisp, D., Ingersoll, A., Elson, L., Preston, R., Hildebrand, C., Ragent, B., Seiff, A., Young, R., Petit, G., Boloh, L., Alexandrov, Y., Armand, N., Bakitko, R., and Selivanov, A., "Overview of Vega Venus Balloon in Situ Meteorological Measurements," *Science*, vol. 231, pp. 1411–1414, March 21, 1986.

[233] Sameni, R., Shamsollahi, M., and Jutten, C., "Filtering Electrocardiogram Signals using the Extended Kalman Filter," *27th Annual IEEE Engineering in Medicine and Biology Conference*, Shanghai, China, September 1–4, 2005.

[234] Schei, T., "A Finite–Difference Method for Linearization in Nonlinear Estimation Algorithms," *Automatica*, vol. 33, no. 11, pp. 2053–2058, 1997.

[235] Schipper, A. and Lebreton, J., "The Huygens Probe – Space History in Many Ways," *Acta Astronautica*, vol. 59, pp. 319–334, July–September 2006.

[236] Schlee, F., Standish, C., and Toda, N., "Divergence in the Kalman Filter," *AIAA Journal*, vol. 5, pp. 1114–1120, June 1967.

[237] Schofield, J., Barnes, J., Crisp, D., Haberle, R., Larsen, S., Magalhães, J., Murphy, J., Seiff, A., and Wilson, G., "The Mars Pathfinder Atmospheric Structure Investigation/Meteorology (ASI/MET) Experiment," *Science*, vol. 278, pp. 1752–1758, December 5, 1997.

[238] Seiff, A., "Some Possibilities for Determining the Characteristics of the Atmospheres of Mars and Venus from Gas Dynamic Behavior of a Probe Vehicle," Tech. Rep. NASA TN D–1770, NASA, April 1963.

[239] Seiff, A., "The Viking Atmosphere Structure Experiment – Techniques, Instruments, and Expected Accuracies," *Space Science Instrumentation*, vol. 2, pp. 381–423, September 1976.

[240] Seiff, A., "Entry–Probe Studies of the Atmospheres of Earth, Mars, and Venus: A Review," *28th Aerospace Sciences Meeting*, AIAA–1990–0765, Reno, Nevada, January 8–11, 1990.

[241] Seiff, A., "Mars Atmospheric Winds Indicated by Motion of the Viking Landers during Parachute Descent," *Journal of Geophysical Research*, vol. 98, pp. 7461–7474, April 1993.

[242] Seiff, A. and Kirk, D., "Structure of Mars' Atmosphere up to 100 km from the Entry Measurements of Viking 2," *Science*, vol. 194, pp. 1300–1303, December 17, 1976.

[243] Seiff, A. and Kirk, D., "Structure of the Atmosphere of Mars in Summer at Mid–Latitudes," *Journal of Geophysical Research*, vol. 82, pp. 4364–4378, September 30, 1977.

[244] Seiff, A., Kirk, D., Knight, T., Mihalov, J., Blanchard, R., Young, R., Schubert, G., von Zahn, U., Lehmacher, G., Milos, F., and Wang, J., "Structure of the Atmosphere of Jupiter: Galileo Probe Measurements," *Science*, vol. 272, pp. 844–845, May 10, 1996.

[245] Seiff, A., Kirk, D., Knight, T., Mihalov, J., Blanchard, R., Young, R., Schubert, G., von Zahn, U., Lehmacher, G., Milos, F., and Wang, J., "Thermal Structure of Jupiter's Atmosphere near the Edge of a 5–μm Hot Spot in the North Equatorial Belt," *Journal of Geophysical Research*, vol. 103, no. E10, pp. 22857–22889, 1998.

[246] Seiff, A., Kirk, D., Sommer, S., Young, R., Blanchard, R., Juergens, D., Lepetich, J., Intrieri, P., Findlay, J., and Derr, J., "Structure of the Atmosphere of Venus up to 110 Kilometers: Preliminary Results from the Four Pioneer Venus Entry Probes," *Science*, vol. 203, pp. 787–790, February 23, 1979.

[247] Seiff, A., Kirk, D., Young, R., Blanchard, R., Findlay, J., Kelly, G., and Sommer, S., "Measurements of Thermal Structure and Thermal Contrasts in the Atmosphere of Venus," *Journal of Geophysical Research*, vol. 85, pp. 7903–7933, December 30, 1980.

[248] Seiff, A. and Knight, T., "The Galileo Probe Atmosphere Structure Instrument," *Space Science Reviews*, vol. 60, pp. 203–232, May 1992.

[249] Seiff, A. and Reese, D., "Use of Entry Vehicle Responses to Define the Properties of the Mars Atmosphere," in *Advances in the Astronautical Sciences*,

vol. 19, pp. 419–445, 1965. AAS 65–24, Proceedings of the American Astronautical Society Symposium on Unmanned Exploration of the Solar System, Denver, Colorado, February 8–10, 1965.

[250] Seiff, A., Reese, D., Sommer, S., Kirk, D., Whiting, E., and Niemann, H., "PAET, An Entry Probe Experiment in the Earth's Atmosphere," *Icarus*, vol. 18, pp. 525–563, 1973.

[251] Seiff, A., Sromovsky, L., Borucki, W., Craig, R., Juergens, D., Young, R., and Ragent, B., "Pioneer Venus 12.5 km Anomaly Workshop Report (Volume 1)," *NASA Conference Publication 3303*, Moffett Field, California, September 28–29, 1993.

[252] Seiff, A., Tillman, J., Murphy, J., Schofield, J., Crisp, D., Barnes, J., LaBaw, C., Mahoney, C., Mihalov, J., Wilson, G., and Haberle, R., "The Atmosphere Structure and Meteorology Instrument on the Mars Pathfinder Lander," *Journal of Geophysical Research – Planets*, vol. 102, pp. 4045–4056, February 25, 1997.

[253] Shoenenberger, M., "MER Flight Data," *Personnel Correspondence*, October 1, 2008.

[254] Singh, U., Yu, J., Petros, M., Chen, S., Kavaya, M., Trieu, B., Bai, Y., Petzar, P., Modlin, E., Koch, G., and Beyon, J., "Advances in High Energy Solid–State 2–micron Laser Transmitter Development for Ground and Airborne Wind and CO2 Measurements," *i–SAIRAS 2010: 10th International Symposium on Artificial Intelligence, Robotics and Automation in Space*, AIAA–2011–0428, Toulouse, France, September 20–23, 2010.

[255] Smith, P., "The Phoenix Mission to Mars," *Proceedings of SPIE - The International Society for Optical Engineering, Instruments, Methods, and Missions for Astrobiology X*, vol. 6694, pp. 6694P 1–7, October 1, 2007.

[256] Smith, P., Tomasko, M., Britt, D., Crowe, D., Reid, R., Keller, H., Thomas, N., Gliem, F., Rueffer, P., Sullivan, R., Greeley, R., Knudsen, J., Madsen, M., Gunnlaugsson, H., Hviid, S., Goetz, W., Soderblom, L., Gaddis, L., and Kirk, R., "The Imager for Mars Pathfinder Experiment," *Journal of Geophysical Research – Planets*, vol. 102, pp. 4003–4025, February 25, 1997.

[257] Sofair, I., "Improved Method for Calculating Exact Geodetic Latitude and Altitude," *Journal of Guidance, Control, and Dynamics*, vol. 20, pp. 824–826, July–August 1997.

[258] Sofair, I., "Improved Method for Calculating Exact Geodetic Latitude and Altitude Revisited," *Journal of Guidance, Control, and Dynamics*, vol. 23, p. 369, March–April 2000.

[259] Soffen, G. and Snyder, C., "The First Viking Mission to Mars," *Science*, vol. 193, pp. 759–766, August 27, 1976.

[260] Soken, H. and Hajiyev, C., "Pico Satellite Attitude Estimation via Robust Unscented Kalman Filter in the Presence of Measurement Faults," *ISA Transactions*, vol. 49, pp. 249–256, May 8, 2010.

[261] Sokolov, S., Fokin, V., Burtsev, V., Romanov, R., Rozhdestvenskii, M., Karyagin, V., Borodin, N., Ivannikov, V., Shkirina, V., Nikolaenko, L., Kerzhanovich, V., and Kotov, B., "Operation of the Mars 6 Entry Capsule in the Atmosphere of Mars," *Cosmic Research*, vol. 13, pp. 7–12, January–February 1975.

[262] Sommer, S., Boissevain, A., Yee, L., and Hedlund, R., "The Structure of an Atmosphere from On–board Measurements of Pressure, Temperature, and Acceleration," Tech. Rep. NASA TN D–3933, NASA, April 1967.

[263] Sommer, S. and Yee, L., "An Experiment to Determine the Structure of a Planetary Atmosphere," *Journal of Spacecraft and Rockets*, vol. 6, pp. 704–710, June 1969.

[264] Sorenson, H., *Advances in Control System Theory*, ch. Kalman Filtering Techniques, pp. 219–292. vol. 3, Academic Press Inc., 1966.

[265] Sorenson, H., "Least–Squares Estimation: From Gauss to Kalman," *IEEE Spectrum*, vol. 7, pp. 63–68, 1970.

[266] Sorenson, H., *Kalman Filtering: Theory and Application*, ch. 1, p. 1. IEEE Press, 1985.

[267] Spear, A. and Golombek, M., "Mars Pathfinder Project Progress Report," *Acta Astronautica*, vol. 39, pp. 91–99, July–August 1996.

[268] Spencer, D. *Personal Communication*, September 7, 2010.

[269] Spencer, D., Blanchard, R., Braun, R., Kallemeyn, P., and Thurman, S., "Mars Pathfinder Entry, Descent, and Landing Reconstruction," *Journal of Spacecraft and Rockets*, vol. 36, pp. 357–366, May–June 1999.

[270] Spencer, D., Blanchard, R., Thurman, S., Braun, R., Peng, C., and Kallemeyn, P., "Mars Pathfinder Atmospheric Entry Reconstruction," in *Advances in the Astronautical Sciences*, vol. 99–1, pp. 663–692, 1998. AAS 98–146.

[271] Stark, H. and Woods, J., *Probability and Random Processes with Applications to Signal Processing*. 3rd edition, Prentice Hall, Upper Saddle River, New Jersey, 2002.

[272] Stastny, N., Bettinger, R., and Chavez, F., "Comparison of the Extended and Unscented Kalman Filters for Angles Based Relative Navigation," *AIAA / AAS Astrodynamics Specialist Conference and Exhibit*, AIAA-2008-7083, Honolulu, Hawaii, August 18–21, 2008.

[273] Stenger, B., Mendonca, P., and Cipolla, R., "Model–Based Hand Tracking Using an Unscented Kalman Filter," in *Proceedings of the British Machine Vision Conference, Volume I*, pp. 63–72, 2001.

[274] Strang, G., *Linear Algebra and its Applications*, ch. 3, pp. 195–197. Brooks/Cole Thomson Learning Inc., United States, 1988.

[275] Stratonovich, R., "Application of the Theory of Markoff Processes for Optimum Filtration of Signals," *Radio Engineering and Electronics Physics*, vol. 1, pp. 1–19, November 1960.

[276] Stratonovich, R., "Detection and Estimation of Signals in Noise when One or Both are Non–Gaussian," *Proceedings of the IEEE*, vol. 58, pp. 670–679, May 1970.

[277] Striepe, S., *Huygens Probe Entry, Descent, and Landing Trajectory Reconstruction Using the Program to Optimize Simulated Trajectories II*. PhD thesis, The University of Texas at Austin, December 2007.

[278] Striepe, S. *Personal Communication*, March 26, 2010.

[279] Striepe, S., Blanchard, R., Kirsch, M., and Fowler, W., "Huygens Titan Probe Trajectory Reconstruction Using Traditional Methods and the Program to Optimize Simulated Trajectories II," *17th AAS/AIAA Space Flight Mechanics Meeting*, AAS–07–226, Sedona, Arizona, January 28–February 1, 2007.

[280] Swerling, P., "A Proposed Stagewise Differential Correction Procedure for Satellite Tracking and Prediction," *Journal of the Astronautical Sciences*, vol. 6, pp. 46–52, 1959.

[281] Swerling, P., "First–Order Error Propagation in a Stagewise Smoothing Procedure for Satellite Observations," Tech. Rep. RM–2329, The RAND Corporation, June 15, 1959.

[282] Tapley, B., Schutz, B., and Born, G., *Statistical Orbit Determination*, ch. 4, pp. 199–211. Elsevier Academic Press, New York, 2004.

[283] Tapley, B., Schutz, B., and Born, G., *Statistical Orbit Determination*, ch. 1, pp. 11–13. Elsevier Academic Press, New York, 2004.

[284] Teixeira, B., Tôrres, L., Iscold, P., and Aguirre, L., "Flight Path Reconstruction - A Comparison of Nonlinear Kalman Filter and Smoother Algorithms," *Aerospace Science and Technology*, vol. 15, pp. 60–71, January–February 2011.

[285] The Rover Team, "The Pathfinder Microrover," *Journal of Geophysical Research – Planets*, vol. 102, pp. 3989–4001, February 25, 1997.

[286] Tichavský, P., Muravchik, C., and Nehorai, A., "Reconstructing the Weather on Mars at the Time of the MERs and Beagle 2 Landings," *Geophysical Research Letters*, vol. 33, pp. L19202–1 – L19202–5, doi:10.1029/2006GL026565, May 2006.

[287] Tolson, R., Willcockson, W., Desai, P., and Thomas, P., "Anomalistic Disturbance Torques during the Entry Phase of the Mars Exploration Rover Missions – A Telemetry and Mars–Surface Investigation," in *Advances in the Astronautical Sciences*, vol. 125, pp. 507–525, 2006. AAS 06–087.

[288] Tomasko, M., Archinal, B., Becker, T., Bézard, B., Bushroe, M., Combes, M., Cook, D., Coustenis, A., de Bergh, C., Dafoe, L., Doose, L., Douté, S., Eibl, A., Engel, S., Gliem, F., Grieger, B., Holso, K., Howington-Kraus, E., Karkoschka, E., Keller, H., Kirk, R., Kramm, R., Küppers, M., Lanagan, P., Lellouch, E., Lemmon, M., Lunine, J., McFarlane, E., Moores, J., Prout, G., Rizk, B., Rosiek, M., Rueffer, P., Schröder, S., Schmitt, B., See, C., Smith, P., Soderblom, L., Thomas, N., and West, R., "Rain, Winds and Haze during the Huygens Probe's Descent to Titan's Surface," *Nature*, vol. 438, pp. 765–778, December 8, 2005.

[289] Tortora, P., Oshman, Y., and Santoni, F., "Spacecraft Angular Rate Estimation from Magnetometer Data Only Using an Analytic Predictor," *Journal of Guidance, Control, and Dynamics*, vol. 27, pp. 365–373, May–June 2004.

[290] Treiman, A., "Near–Surface Geologic Units Exposed Along Ares Vallis and in Adjacent Areas: A Potential Source of Sediment at the Mars Pathfinder Landing Site," *Journal of Geophysical Research*, vol. 102, pp. 4219–4229, February 25, 1997.

[291] Tylee, J., "On–Line Failure Detection in Nuclear Power Plant Instrumentation," *IEEE Transactions on Automatic Control*, vol. AC–28, pp. 406–415, March 1983.

[292] Uchiyama, M. and Hakomori, K., "Measurement of Instantaneous Flow Rate through Estimation of Velocity Profiles," *IEEE Transactions on Automatic Control*, vol. AC–28, pp. 380–388, March 1983.

[293] van der Merwe, R., *Sigma-Point Kalman Filters for Probabilistic Inference in Dynamic State-Space Models*. PhD thesis, OGI School of Science & Engineering, Oregon Health & Science University, April 2004.

[294] van der Merwe, R., Doucet, A., de Freitas, N., and Wan, E., "The Unscented Particle Filter," Tech. Rep. CUED/F–INFENG/TR 380, Cambridge University Engineering Department, August 16, 2000.

[295] van der Merwe, R. and Wan, E., "Efficient Derivative–free Kalman Filters for Online Learning," *Proceedings of the European Symposium on Artificial Neural Networks (ESANN)*, Bruges, Belgium, April 2001.

[296] van der Merwe, R. and Wan, E., "The Square–Root Unscented Kalman Filter for State– and Parameter–Estimation," *IEEE International Conference on Acoustics, Speech, and Signal Processing (ICASSP)*, Salt Lake City, Utah, May 2001.

[297] van der Merwe, R. and Wan, E., "Sigma-Point Kalman Filters for Probabilistic Inference in Dynamic State-Space Models," *Proceedings of the Workshop on Advances in Machine Learning*, Montreal, Canada, June 2003.

[298] Van Trees, H. and Bell, K., eds., *Bayesian Bounds for Parameter Estimation and Nonlinear Filtering / Tracking*, ch. 1, p. 1. Wiley–IEEE Press, ISBN–13: 978–0470120958, August 2007.

[299] Vaughan, R., Kallemeyn, P., Spencer, D., and Braun, R., "Mars Pathfinder Atmospheric Entry Navigation Operations," *Journal of Spacecraft and Rockets*, vol. 36, pp. 340–347, May–June 1999.

[300] Vlases, W., Paris, S., Lajoie, R., Martens, P., and Hargraves, C., "Optimal Trajectories by Implicit Simulation Ver. 2.0 User's Manual," Tech. Rep. TR–90–3056, Wright Research and Development Center, 1990.

[301] Wagner, W., "Re-Entry Filtering, Prediction, and Smoothing," *Journal of Spacecraft and Rockets*, vol. 3, pp. 1321–1327, September 1966.

[302] Wagner, W. E. and Serold, A. C., "Utilization Report on Statistical Trajectory Estimation Programs," Tech. Rep. NASA CR–66837, Martin Marietta Corporation for NASA, June 1, 1969.

[303] Wagner, W. E. and Serold, A. C., "Formulation on Statistical Trajectory Estimation Programs," Tech. Rep. NASA CR–1482, Martin Marietta Corporation for the Langley Research Center, January 1970.

[304] Wallace, J. and Clarke, R., "The Application of Kalman Filtering Estimation Techniques in Power Station Control Systems," *IEEE Transactions on Automatic Control*, vol. AC–28, pp. 416–427, March 1983.

[305] Wan, E. and van der Merwe, R., "The Unscented Kalman Filter for Nonlinear Estimation," *IEEE Adaptive Systems for Signal Processing, Communications, and Control Symposium*, Chateau Lake Louise, Lake Louise, Alberta, Canada, October 1–4, 2000.

[306] Wan, E., van der Merwe, R., and Nelson, A., *Advances in Neural Information Processing Systems 12*, ch. "Dual Estimation and the Unscented Transformation", pp. 666–672. S. Solla, T. Leen, K.–R. Müller (editors), MIT Press, Cambridge, Massachusetts, 2000.

[307] Welch, G. and Bishop, G., "An Introduction to the Kalman Filter," Tech. Rep. TR 95–041, University of North Carolina at Chapel Hill, July 24, 2006.

[308] Wells, G., "Trajectory Reconstruction of a Martian Planetary Probe Mission: Reconstruction of the Spirit Mars Exploration Rover Entry, Descent, and Landing Performance," *2nd International ARA Days*, AA–3–2008–16, October 21–23, 2008.

[309] Wiener, N., *The Extrapolation, Interpolation and Smoothing of Stationary Time Series*, ch. 1–5, pp. 1–163. John Wiley & Sons, Inc., New York, New York, 1949.

[310] Willcockson, W., "Mars Pathfinder Heatshield Design and Flight Experience," *Journal of Spacecraft and Rockets*, vol. 36, May–June 1999.

[311] Withers, P. and Catling, D., "The Phoenix Atmospheric Structure Experiment (ASE) - Data Processing and Scientific Results," *International Planetary Probe Workshop (IPPW–7)*, Barcelona, Spain, June 14–18, 2010.

[312] Withers, P. and Smith, M., "Atmospheric Entry Profiles from the Mars Exploration Rovers Spirit and Opportunity," *Icarus*, vol. 185, pp. 133–142, November 2006.

[313] Withers, P., Towner, M., Hathi, B., and Zarnecki, J., "Analysis of Entry Accelerometer Data: A Case Study of Mars Pathfinder," *Planetary and Space Science*, vol. 51, pp. 541–561, August–September 2003.

[314] Withers, P., Towner, M., Hathi, B., and Zarnecki, J., "Review of the Trajectory and Atmospheric Structure Reconstruction for Mars Pathfinder," *European Space Agency Special Publication (ESA SP 544)*, pp. 163–174, February 2004.

[315] Woo, R., "Observations of Turbulence in the Atmosphere of Venus using Mariner 10 Radio Occultation Measurements," *Journal of the Atmospheric Sciences*, vol. 32, pp. 1085–1090, June 1975.

[316] Yakolev, O., Efimov, A., Timofeeva, T., Yakovleva, G., Chub, E., Tikhonov, V., and Shtrykov, V., "Preliminary Radio Transmission Data and the Venusian Atmosphere from Venera 9 and Venera 10," *Cosmic Research*, vol. 14, pp. 632–637, September–October 1976.

[317] Young, R. and Magalhães, J., "In memoriam: Alvin seiff (1922–2000)," *Icarus*, vol. 152, pp. 1–3, July 2001.

[318] Young, R., Smith, M., and Sobeck, C., "Galileo Probe: In Situ Observations of Jupiter's Atmosphere," *Science*, vol. 272, pp. 837–838, May 10, 1996.

[319] Yunck, T., "An Overview of Atmospheric Radio Occultation," *Journal of Global Positioning Systems*, vol. 1, no. 1, pp. 58–60, 2002.

[320] Zadeh, L. and Ragazzini, J. R., "An Extension of Wiener's Theory of Prediction," *Journal of Applied Physics*, vol. 21, pp. 645–655, 1950.

[321] Zarchan, P. and Musoff, H., *Fundamentals of Kalman Filtering: A Practical Approach*, ch. 7, p. 265. Progress in Astronautics and Aeronautics, Vol. 190, AIAA, Reston, Virginia, 2000.

[322] Zarchan, P. and Musoff, H., *Fundamentals of Kalman Filtering: A Practical Approach*, ch. 7, p. 257. Progress in Astronautics and Aeronautics, Vol. 190, AIAA, Reston, Virginia, 2000.

[323] Zhang, S. and Hu, G., "Variations of Unscented Kalman Filter with their Applications in Target Tracking on Re-entry," *2006 Chinese Control Conference*, August 7–11, 2006.

[324] Zhang, S., Hu, G., and Liu, S., "New Development of UKF and its Applications in Target Tracking on Re-entry," *Control Theory & Applications*, vol. 23, pp. 569–574, August 2006.

[325] Zuppardi, G. and Gianpaolo, V., "Improved Fay–Riddell Procedure to Compute the Stagnation Point Heat Flux," *Journal of Spacecraft and Rockets*, vol. 35, pp. 403–405, May–June 1998.

[326] zur Nieden, P. and Olivier, H., "Determination of Atmospheric Densities from Reentry Flight Data," *Journal of Spacecraft and Rockets*, vol. 44, pp. 332–337, March–April 2007.